



The
University
Of
Sheffield.

Dynamics of Premixed Flames in Tube

By:

Celestine Ebieto **EBIETO**

A thesis submitted in partial fulfilment of the requirements for the
degree of Doctor of Philosophy

*The University of Sheffield
Faculty of Engineering
Department of Mechanical Engineering*

November 2017

ACKNOWLEDGEMENT

I am most grateful to Almighty God for the strength and courage to start this work and have brought me thus far.

I want to appreciate my supervisor, Dr Robert Woolley for allowing me to learn/train under him. Your contributions, criticisms and painstakingly editing of this work gave it the much-needed standard. A big thank you to my second supervisor, Dr Anton Krynkina for the useful discussions we had concerning this work.

My Special gratitude goes to my Laboratory Technicians, Mr Malcolm Nettleship and Mr Oliver Cooper, thank you for being there anytime I needed your attention. To my colleague and friend, Mr Nazrein Amaludin, for your useful contribution and support with the experimental data collection, data processing and analysis. My gratitude also goes to Dr Zhen Ma and Mr Houshi Jiang, for their useful help with some aspects of the experiment.

Special appreciation to my wife, for enduring with me even in the difficult times you have stayed strong with me. I will not forget my kids, friends and family for your continued support and encouragements, God bless you all. Special gratitude to my uncle and colleague at the University of Port Harcourt, Nigeria, Prof Lucky Akaruese for facilitating the sponsorship for this research.

Finally, my appreciation goes to The Federal Government of Nigeria through the Office of the Special Adviser to the President on Niger Delta and the University of Port Harcourt, Nigeria, for the sponsorship opportunity to undergo this study. This kind gesture has been worthwhile.

ABSTRACT

Experimental work is reported for premixed flames propagating in tubes. The flames were ignited with a pilot flame and the flame propagation captured with high-speed cameras. Initial measurements were performed characterising the rig. These included investigations of the end configuration (open, closed, orifice plate) and whether the tube was horizontal or vertical. For horizontal tube open at both ends, the pressure signal of the propagating flame was recorded and the flame temperature distribution along the tube length was found by observation of a thin silicon carbide filament. The flame propagated steadily immediately after ignition with a curved front, then was subjected to oscillations at the middle of the tube. At the end of the tube, it regained its stability. The pressure and temperature of the propagating flame were highest at the middle point where the flame oscillated. Methane-air flames enriched with hydrogen were studied. As the hydrogen concentration was increased the acoustic pressure initially increased and then decreased this was found to be associated with the presence of Rayleigh-Taylor instabilities. For downwardly propagating flames to a closed end, methane and propane were studied. The flames initially propagated steadily, then at approximately a third of the way down the tube, the primary acoustic oscillation sets in resulting to change in the flame shape. This was then followed by a plateau of variable length before a more violent secondary acoustic oscillation. In some circumstances, flames were observed to rotate due to the primary acoustic instability. Some of the flames were subjected to Rayleigh Taylor instabilities associated with large pressure oscillations. The flame front position growth rate for both methane and propane were similar despite the differences in the fuels. There was a strong correlation between the flame oscillations and changes in CH^* and C_2^* as well as the flame surface area.

TABLE OF CONTENTS

Title Page	i
Acknowledgement	ii
Abstract	iii
Table of Contents	iv
List of Figures	vii
List of Tables	xii
Nomenclature	xiii
CHAPTER 1: Introduction	
1.1 Background	1
1.2 Motivation	3
1.3 Objectives of the study	4
1.4 Structure of dissertation	5
CHAPTER 2: Literature Review	
2.1 Laminar premixed flame propagation in tubes	7
2.1.1 Propagation in a tube closed at both ends	8
2.1.2 Propagation in a tube open at both ends	10
2.1.3 Propagation in a tube open at the ignition end, closed at the other end	11
2.2 Laminar burning characteristics	13
2.2.1 Laminar burning velocity	13
2.2.2 Factors influencing laminar burning velocity	14
2.2.3 Flammability limit	17
2.3 Flame instability	18
2.4 Flame oscillations in premixed combustion	23
2.4.1 Cellular flame	24
2.4.2 Rotating/spinning flame	25
2.5 Flame growth rate	26
2.5.1 Flame acoustic losses	28

2.6	Temperature measurement technique	29
2.6.1	Pyrometer	30
2.6.2	Two-colour method	31

CHAPTER 3: Research Methodologies

3.1	Experimental facilities	33
3.1.1	Flames in tube test rig	33
3.1.2	High-speed cameras	37
3.1.3	Pressure sensor	38
3.1.4	Gas, syringe and gas bag	38
3.2	Experimental procedure	39
3.2.1	Calibration	39
3.2.2	Computing of required volume of fuel	40
3.3	Python code and PCC application	44
3.3.1	Pressure data and high-speed image synchronisation	44
3.4	Flame oscillation signal processing and analysis	45
3.4.1	Scidavis and origin software	45
3.4.2	Data filtering	46
3.5	Laminar flame speed	48
3.5.1	Flame surface area	48
3.5.2	Rotational speed of the flame	50
3.6	The two colour method technique	51
3.6.1	Thermal behaviour of filaments	51
3.7	Measurements, processing and data analysing errors	53

CHAPTER 4: Methane and Propane Flame Propagation in Tube

4.1	Introduction	55
4.2	Horizontal propagating flame	55
4.2.1	Horizontal propagating methane/air mixture	55
4.2.2	Horizontal propagating propane/air mixture	57
4.3	Vertically downward propagating flame	59

4.3.1	Downward propagating methane/air mixture	59
4.3.2	Downward propagating propane/air mixture	62
4.4	Flame comparison, flammability limits and gravity effect	64
4.5	Flame acoustic pressure	66
4.6	Flame intensity and temperature profile	69

CHAPTER 5: Hydrogen enriched Flame in Open Ended Tube

5.1	Introduction	78
5.2	Flame speed of methane/hydrogen/air mixture	78
5.3	Methane Hydrogen/air flame analysis for open ended tube	79
5.4	Flame oscillation analysis	83
5.4.1	Rayleigh Taylor impact on the flame oscillation	90
5.5	Flame propagation in longer tube	94

CHAPTER 6: Downwardly Propagating Flame towards a closed end

6.1	Introduction	97
6.2	Flame behaviour and Characteristics	97
6.2.1	Flame rotational behaviour	106
6.2.2	Flame Rayleigh Taylor analysis	108
6.2.3	Flame pressure and frequency characterisation	112
6.3	Flame growth rate and acoustic loss	114
6.4	Flame oscillation analysis	120
6.5	Flame chemiluminescence	123

CHAPTER 7: Conclusions and Recommendations

7.1	Conclusions	128
7.2	Recommended future work	131

REFERENCES	132
-------------------	-----

APPENDICES	143
-------------------	-----

LIST OF FIGURES

- Figure 2.1:** Stroboscopic flame records. Mixture: 10 parts CO + 1 part O₂ saturated with water vapour at 15°C. tube closed at both ends; diameter 5 cm; length: (a) 19.5 cm (b) 17 cm (c) 12 cm (d) 9.5 cm.
- Figure 2.2:** Pressure record of acoustic instability of a premixed propane-air flame
- Figure 2.3:** Variations of burning velocity and equivalence ratio for methane and propane
- Figure 2.4:** Graph showing the effect of temperature and pressure on burning velocity for methane, propane and hydrogen.
- Figure 2.5:** Deviation of flow lines leading to the Darrieus-Landau instability
- Figure 2.6:** Visualisation of an unstable RTI configuration
- Figure 2.7:** Schematics of an incident shock wave
- Figure 2.8:** Self-turbulising cellular flame dynamically stabilised in a uniform laminar flow
- Figure 2.9:** Peak-to-peak pressure amplitude of flame as a function of time
- Figure 3.1a:** First experimental test rig
- Figure 3.1b:** Experimental test rig with vacuum pump and pressure transducer
- Figure 3.2:** 5mm orifice plate fitted to the end of the rig
- Figure 3.3:** Effect of Ignition source on flame speed
- Figure 3.4a:** Rig schematics for flame temperature measurement
- Figure 3.4b:** Schematics of the downwardly propagating rig
- Figure 3.5:** Pressure-Time graph for rig volume calculation
- Figure 3.6:** Filtering Methods
- Figure 3.7:** Flame Schematics (a) side view (b) front view
- Figure 3.8:** Frustum of a right circular cone
- Figure 3.9:** schematics of a curved flame
- Figure 4.1:** Flame front position against time for horizontally propagating methane flame
- Figure 4.2:** Speed against ϕ for horizontally propagating methane flame
- Figure 4.3:** Flame front position against time for horizontally propagating propane flame
- Figure 4.4:** Speed against ϕ for horizontally propagating propane flame
- Figure 4.5:** Flame front position against time for downwardly propagating methane flame
- Figure 4.6:** Speed versus ϕ for downwardly propagating methane flame
- Figure 4.7:** Comparison of speed versus ϕ for downwardly propagating methane flame

Figure 4.8: Flame front position against time of downwardly propagating propane flame

Figure 4.9: Speed versus ϕ of downwardly propagating propane flame

Figure 4.10: Comparison of horizontal and downward propagating flame for methane

Figure 4.11: Comparison of horizontal and downward propagating flame for methane

Figure 4.12: Comparison of flame pressure oscillation for pressure sensor at the middle and the end of the tube (Results from two experiments combined).

Figure 4.13: Horizontally propagating flames in open ends tube (a) early stage (b) Intermediate stage (c) final stage

Figure 4.14: Pressure variation and relative flame position as a function of time

Figure 4.15: The glowing fibre as the flame crossed through tube middle section and time-dependent pixel brightness intensity response.

Figure 4.16: Time-dependent gas temperature variation at equivalence ratio = 1.1. (a) Temperature variation at the left end of the tube near ignition place, (b) Temperature variation at the middle of the tube, (c) Temperature variation at the right end of the tube.

Figure 4.17: Pressure oscillation of the flame in the tube at equivalence ratio = 1.1

Figure 4.18: a,b and c Experimental heat-up and cool-down cycle at Left-end, Middle and Right end of the tube, d,e and d present the main frequency of intensity oscillation at the corresponding positions of the tube, using FFT.

Figure 4.19: The average temperature of flame travelling through the fibre at different equivalence ratios

Figure 4.20: Flame velocity varying with equivalence ratio

Figure 4.21: Flame speed and temperature for faster methane flames versus equivalence ratio

Figure 4.22: Middle of tube time-dependent gas temperature variation at different equivalence

Figure 5.1: Flame speed of Methane/Hydrogen/Air mixture against equivalence at different *RH*

Figure 5.2: Methane flame propagation at 1.2 equivalence ratio (a) *RH* = 0 (b) *RH* = 0.1

Figure 5.3: Methane flame propagation at 1.2 equivalence ratio (a) *RH* = 0.2 (b) *RH* = 0.3

Figure 5.4: Methane flame propagation at 1.2 equivalence ratio (a) $RH = 0.4$ (b) $RH = 0.5$

Figure 5.5: Methane/Hydrogen flame propagation at $\phi=1.2$ and different RH

Figure 5.6: $CH_4 - H_2$ - air flame at $\phi = 1.2$ for $RH = 0$ and $RH = 0.1$: (a) x in the flame front position (b) P_f is the flame pressure amplitude (c) a is the flame amplitude (d) u_{fft} is the FFT filtered flame speed (e) n_f is the flame size approximated by the number of pixels

Figure 5.7: $CH_4 - H_2$ - air flame at $\phi = 1.2$ for $RH = 0.2$ and $RH = 0.3$: (a) x in the flame front position (b) P_f is the flame pressure amplitude (c) a is the flame amplitude (d) u_{fft} is the FFT filtered flame speed (e) n_f is the flame size approximated by the number of pixels

Figure 5.8: $CH_4 - H_2$ - air flame at $\phi = 1.2$ for $RH = 0.4$ and $RH = 0.5$: (a) x in the flame front position (b) P_f is the flame pressure amplitude (c) a is the flame amplitude (d) u_{fft} is the FFT filtered flame speed (e) n_f is the flame size approximated by the number of pixels

Figure 5.9: $CH_4 - H_2$ - air flame at $\phi=1.2$ $RH = 0.6$ and $RH = 0.7$: (a) x in the flame front position (b) P_f is the flame pressure amplitude (c) a is the flame amplitude (d) u_{fft} is the FFT filtered flame speed (e) n_f is the flame size approximated by the number of pixels

Figure 5.10: Frequency of the flames at the different hydrogen addition (RH)

Figure 5.11a: An example flame characteristic behaviours with and without RT instabilities

Figure 5.11b: An example flame characteristic behaviours with and without RT instabilities

Figure 5.11c: An example flame characteristic behaviours with and without RT instabilities

Figure 5.12: Flame growth rate at the different hydrogen addition (RH)

Figure 5.13: Propane/Hydrogen flame propagation at $\phi=1.2$ and $RH = 0.1$

Figure 5.14: Propane/Hydrogen flame propagation frequency at $\phi=1.2$ and $RH = 0.1$

Figure 5.15: Propane/Hydrogen flame propagation oscillation amplitude at $\phi=1.2$ and $RH = 0.1$

Figure 6.1: Propagating flame behaviour in the different regime. (a) Curved flame (b) Flat flame during the low-level acoustical instability (c) cellular flame (d) shaken flame

Figure 6.2(a): Relative flame position (x) and pressure variation (P_f) as a function of time

Figure 6.2(b): Relative flame position (x) and pressure variation (P_f) as a function of time

Figure 6.2(c): Relative flame position (x) and pressure variation (P_f) as a function of time

Figure 6.2(d): Relative flame position (x) and pressure variation (P_f) as a function of time

Figure 6.3: Pressure variation and relative flame position as a function of time for primary acoustically unstable flames at equivalence ratio of 0.7 and flame speed = 0.221 ms^{-1} . (a) Curved flame (b) Flat flame

Figure 6.4: Pressure variation and relative flame position as a function of time for secondary acoustically unstable flames at equivalence ratio of 0.8 and flame speed = 0.318 ms^{-1} . (a) Curved flame (b) Flat flame (c) Cellular flame (d) Shaken flame

Figure 6.5: Pressure variation and relative flame position as a function of time for flame with continuous transition from primary to secondary acoustically unstable flames at equivalence ratio of 1.0 and flame speed = 0.429 ms^{-1} . (a) Curved flame (b) Cellular flame (c) Shaken flame

Figure 6.6: Downwardly propagating cellular flame rotating clockwise

Figure 6.7: Downwardly propagating cellular flame rotating anti-clockwise

Figure 6.8a: Downwardly propagating cellular flame subjected to R-T instability

Figure 6.8b: Downwardly propagating cellular flame subjected to R-T instability

Figure 6.9: Downwardly propagating cellular flame subjected to R-T instability

Figure 6.10: Downwardly propagating cellular flame subjected to R-T instability

Figure 6.11a: Maximum pressure of flame primary acoustic oscillation against ϕ .

Figure 6.11b: Maximum pressure of flame secondary acoustic oscillation against ϕ .

Figure 6.12: Oscillating frequency against ϕ for propane and methane.

Figure 6.13a: Pressure growth rate for methane-air flame against equivalence ratio

Figure 6.13b: Flame front position growth rate for methane-air flame against equivalence ratio

Figure 6.13c: Pressure growth rate for propane-air flame against equivalence ratio

Figure 6.13d: Flame front position growth rate for propane-air flame against equivalence ratio

Figure 6.14: Comparison between the characteristic times for acoustic losses measured for propane and methane versus equivalence ratio (a) radiative losses and (b) wall losses.

Figure 6.15: Comparison between the characteristic times for total acoustic losses measured for propane and methane versus equivalence ratio.

Figure 6.16: Comparison between the characteristic times for total acoustic losses measured for propane and methane versus acoustic angular speed.

Figure 6.17: Propane-air flame at $\phi=0.7, 0.8$ and 1.0 (a) x in the flame front position (b) P_f is the flame pressure amplitude (c) φ is the flame position and pressure amplitude phase difference (d) a is the flame amplitude (e) u_{fft} is the FFT filtered flame speed (f) n_f is the flame size approximated by the number of pixels

Figure 6.18a: Coloured image sequences without oscillation of propane-air flame recorded at 1000 fps

Figure 6.18b: Coloured image sequences with oscillation of propane-air flame recorded at 1000 fps

Figure 6.19a: Acoustic pressure and $CH^*/C2^*$ against time for propane-air flame at $\phi = 0.8$

Figure 6.19b: Acoustic pressure and $CH^*/C2^*$ against time for propane-air flame at $\phi = 1.0$

Figure 6.20a: Frequency of the pressure oscillation for downwardly propagating flame

Figure 6.20b: Frequency of the CH^* for downwardly propagating flame

Figure C1: Flame surface Area at varying equivalence ratio and RH

LIST OF TABLES

Table 3.1: Rig Volume calculation

Table 3.2: Methane-Hydrogen-air mixture characteristics

Table 3.3: Measurements, Processing and Data Analyzing Errors

Table 4.1: Horizontal propagating methane flame shape at different equivalence ratio

Table 4.2: Horizontal propagating propane flame shape at different equivalence ratio

Table 4.3: Downward propagating methane flame shape at different equivalence ratio

Table 4.4: Horizontal propagating propane flame shape at different equivalence ratio

Table 4.5: Flammability limit data for downwardly propagating methane flame

Table 4.6: Flammability limit data for downwardly propagating propane flame

Table 6.1: Characteristic behaviour of propane and methane at both lean and rich conditions

NOMENCLATURE

S_l	Laminar burning velocity
R_f	Radius of flame front
P	Pressure of the combustion bomb
R, r	Radius
h	Height/heat transfer coefficient
S_f	Flame front velocity with respect to tube or flame speed
S_{ug}	Unburnt gas velocity
A_f	Flame area
D	Mass diffusivity
ρ	Density
λ	Heat conductivity of mixture
V_T	Specific heat capacity
ω	Vorticity/Angular speed
τ_{rad}	Radiative losses
τ_{rad}	Losses
L	Tube length
c	Speed of sound
ν	Kinematic viscosity
α	Thermal diffusivity
V_T	Total volume of the rig
\bar{M}_a	Molecular weight of air
\bar{M}_f	Molecular weight of the fuel
$(A/F)_{stoic}$	Stoichiometric air-fuel ratio.
C_F	Mole fraction of fuel
C_H	Mole fraction of hydrogen
C_A	Mole fraction of air
ϕ_F	Effective equivalence ratio of the main fuel
RH	Amount of hydrogen addition
C_2	Second Planck's constant

$G(\lambda, T)$	Grey level of image
S	Instrument factor of imaging system
λ_R	Wavelength in R channel of the imaging system
λ_G	Wavelength in G channel of the imaging system
ε	SiC fibre emissivity
σ	Stefan-Boltzman constant
T_a	Ambient temperature
T_f	Fibre temperature
T_g	Gas temperature
T	Surface temperature
V	Average fluid velocity
D_f	SiC fibre diameter
μ	Dynamic viscosity
k	Thermal conductivity of fluid
Le	Lewis number
Pr	Prandtl number
Re	Reynolds number
Nu	Nusselt number
α	Temperature exponent (constant)
β	Pressure exponent (constant)
ϕ	Equivalence ratio
γ_u	Specific heat ratio of unburnt gas

Abbreviation

$D - L$	Darrieus-Landau
RTI	Rayleigh-Taylor Instabilities
RMI	Richtmyer-Meshkov Instabilities
LFL	Lower Flammability Limit
UFL	Upper Flammability Limit

CHAPTER ONE

INTRODUCTION

1.1 Background

Global demand for energy has increased over the last 100 years and it is projected to increase [1]. Our modern civilization is built on combustion both for heat and electrical power. At present, 80% of our worldwide energy demand is met by combustion and it has played a crucial role in driving the human race towards the path of prosperity and progress [2]. Despite the continuous search for alternative sources of energy, combustion will remain relevant for the foreseeable future. However, there is likely to be a wider range of fuels burnt with a wider range of properties such as the laminar burning, Lewis number and density ratio. It is necessary to revisit flame dynamics or unsteady flame propagation. One way of carrying out these studies is to observe flame propagation in tubes. A flame is the result of a self-sustained chemical reaction taking place at the flame front. Flames are classified as premixed flames or non-premixed (diffusion)/partially premixed flames. In a premixed flame, prior to the occurrence of any substantial chemical reaction, the fuel and an oxidizer are mixed, while, in a diffusion flame, mixing and reaction between the fuel and the oxidizer take place simultaneously. Flames are either laminar or turbulent in nature. The laminar combustion properties of fuels are fundamental properties necessary for analysing and predicting the performance of internal combustion engines and power plants. The study of laminar premixed flames has been a focal point to research on premixed combustion, ever since it was acknowledged that flames propagate at a characteristic rate known as the *laminar burning velocity* [3]. The laminar burning velocity is one of the fundamental characteristics of any premixed combustible mixture. *It is the relative velocity of a gaseous mixture normal to the flame front through which unburnt gases are transformed into combustible products* [4]. When flames propagate in tubes or other confinements, acoustic instabilities are generated and in some conditions, they are extremely enhanced as a result of heat release rate fluctuation in phase with pressure fluctuation. Research on such phenomena has been conducted for more than a century [5-8] and some flame instability mechanisms affecting the phenomena have been previously studied; for example,

hydrodynamic instability [9], thermal diffusive instability [10, 11], and body-force instability also known as the Rayleigh-Taylor instability [12-14].

Rayleigh [15] had proposed a mechanism where the fluctuating heat release in a combustion system acts as an acoustic source when there is a coupling between the heat source and the pressure wave to form a self-induced excitation which depends on the type burner used. Although excitation of the heat released in combustion systems are inevitable and contribute to the resultant instability in the system, they cannot act alone but form a part of a self-exciting mechanism to successfully initiate instability in the system. Fluctuation in the pressure, velocity, temperature, and fuel concentration of the combustion system can also cause heat release excitations and consequently the pressure waves, which then feedback energy into the initial disturbance to sustain the instability mechanism. Though the global mechanism responsible for flame instabilities is known, identifying the initial mechanisms responsible for actuating the process has uncertainties. Many authors such as Mallard and Le Chatelier [5], Wheeler [16], Coward and Hartwell [17, 18], Guenoche [8] and Searby [6, 7], have looked at this problem but there have been a relatively little consensus as a wide range of experimental configurations have been used. A further understanding of the characteristics of such propagating flames is vital in order to design proper energy systems such as the rocket engines, gas turbine combustor and industrial furnaces that often suffer from flame instabilities brought about by the interactions between the unstable heat release and the acoustic oscillations.

1.2 Motivation

Flame acoustic oscillations have the potential to significantly alter the behaviour of the flame. If the flame is confined, these interactions can lead to intense instabilities sufficient enough to damage the combustion chamber. This phenomenon is of fundamental importance since an initial deflagration (a subsonic combustion driven by heat transfer) wave can transform to detonation or knocking of the engine when there are continuous instabilities. In the current research, experimental work has been carried out for horizontally propagating flame in an open-ended tube and downwardly propagating flames starting at an open end and moving towards the closed end. The main aim of this research is to observe, measure, and characterize the impact of self-generated pressure waves in premixed flame propagating in tubes with different configurations.

The research work originally started with studying acoustic flame propagation interactions in a horizontal tube opened at both ends. The results of the experiment lead us to compare the vertical and horizontal propagation with orifice plate at both ends. With the results of these experiments, there was an attempt to create a simplified flame acoustic model to further explain the flame interaction which was not successful so was abandoned. Finally, following discussions with other researchers in the area combustion instability which suggested igniting the fuel mixture from an open end towards a closed end with the tube in the vertical position, there was then need to change the configuration to downward propagation towards a closed end.

1.3 Objectives of the study

The objectives of the present research work are:

- To study the effect of gravity, flammability limit and laminar burning speed in the two different configurations for both propane and methane.
- Show the effect/correlation of temperature on the flame acoustic behaviour
- To show the impact of hydrogen addition on the flame propagation.
- To show the influence of hydrogen addition on the acoustic behaviour of propagating flames
- To show the impact of Rayleigh Taylor instabilities on propagating flame
- To carry out Chemiluminescence (CH^* and C_2^* emission) test to ascertain the effect of flame chemistry on the flame oscillations.
- Characterization of the acoustic oscillations oscillation on a propagating flame.

1.4 Structure of Dissertation

A direct identification of the onset of flame acoustic instabilities remains difficult. Although numerical simulations have been carried out as seen in literature to explain the phenomenon of flame acoustic oscillations in different configuration of tubes (open both ends, open ignition end with the other end closed and open ignition end but allowing a small opening at the other end), there is little or no experimental analysis to validate these results. Therefore, there is a need for a comprehensive understanding of the prevailing fluid dynamic and thermochemical driving mechanisms which influence this process as a proactive measure to prevent and to control as many as possible combustion related instabilities.

This thesis is divided into 7 chapters and appendices. The first chapter (CHAPTER ONE) gives a brief background into the research and the aims and objectives. The second chapter (CHAPTER TWO) provide detailed literature used for the research.

CHAPTER THREE contains the description of the experimental rig and the necessary operational procedures. Contains descriptions of other equipment used as part of the experimental process. The data processing and analysis technique for obtaining the flame speed and the laminar burning velocity was discussed and the technique applied to determine the flame surface area was also discussed. The chapter also provides detailed data processing and analysis technique for the acoustic pressure. It also gives the detailed data processing and analysis of the temperature measurement technique. Finally, the measurement and analysis errors were discussed.

CHAPTER FOUR contains experimental results for horizontally and vertically downward propagating flame in a tube with a 5mm orifice plate at both ends and without orifice plates at both ends. It covers comparison of propane-air and methane-air flame speed and flammability limits in both the horizontal and vertical configuration. Flame acoustic pressure was also discussed which covers experiment to determine the position to place the pressure sensor on the tube and the region of possible flame acoustic oscillation. Finally, the chapter ends with flame temperature measurement.

CHAPTER FIVE contains experimental results for a horizontally propagating flame enriched with hydrogen in a tube opened at both ends. It covers the resultant effect of

adding hydrogen (i.e. increasing the burn speed of the fuel) to the main fuel. This chapter ends with the effect of changing the tube length on the acoustic oscillation.

CHAPTER SIX contains experimental results for a downwardly propagating flame towards a closed. It gives a detailed description of the flame behaviour in this configuration and also a detailed comparison between a lighter fuel and a relatively heavier fuel in this configuration.

CHAPTER SEVEN provides a brief summary of the conclusions drawn from the thesis, covering the main achievements of the thesis, and the recommended future work.

Journal publications and conference papers of relevance to this thesis either published or under review are listed below.

Ebieto, C. E., Amaludin, N. A. and Woolley, R "*Methane/Hydrogen/Air Flame Oscillations in Open Ended Tubes*", 25th International Colloquium on the Dynamics of Explosions and Reactive Systems (ICDERS), Leeds, United Kingdom.

Ma.Z., Ebieto.C.E., Zhang Y., and Woolley R "*Measuring the temperature of a flame propagating through a quartz tube using high speed colour imaging and thin SiC filament based two colour method*", 12th International Conference on Heat Transfer, Fluid Mechanics and Thermodynamics (HEFAT2016). 2016: Costa Del Sol, Spain.

Ebieto, C. E., Amaludin, N. A., and Woolley, R "*Downwardly propagating flames to a closed end*" (under review).

Amaludin, N. A., Ebieto, C. E., and Woolley, R " Rayleigh Taylor instabilities in the propagation of premixed flames in open-ended tubes" (under review).

CHAPTER TWO

LITERATURE REVIEW

Examples of combustion processes are power generation, propulsion systems, heating systems. However, these processes exhibit a wide range of dynamics which can stimulate the coupling between pressure fields and uneven combustion processes in the combustion chamber, leading to continuous large amplitude oscillations known as thermoacoustic instabilities [19]. These system instabilities enhance heat transfer at the wall of the combustor, deteriorate the efficiency of the combustion and increase pollutant emission. In extreme circumstances, these instabilities could lead to structural damages resulting in the loss of control of the propulsion system or power plant.

2.1 Laminar Premixed Flame Propagation in Tubes

If an ignition source (spark or flame) dissipates sufficient energy into a premixed fuel/air mixture, a flame will be formed that begins to propagate. In the initial stages the flame will propagate as a sphere, however, the walls of the vessel soon affect both the expanding burnt gases and the velocity of the unburnt gases changing the flame shape.

In 1883, Mallard and Le Chatelier [5] performed experiments on the propagation of premixed flames with a horizontal tube opened at the point of ignition and closed at the far-off end. The flames were generally observed to oscillate as they propagated down the tube and the flame front shape became irregular (unstable). In their experiment, they measured a characteristic burning speed of the flame to be the speed when the flame stabilised. Subsequently, other researchers, for example Wheeler [16], Coward and Hartwell [17, 18], Fiock [20] Gerstein et al. [21, 22], Guenoche [8], Fuller et al. [23] and recently Fouzi [3] have used this method to obtain burning velocities as well as study combustion instabilities. To stabilise the flame propagation, the tube diameter has been varied, different combinations of open and closed ends including the use of orifice at one or both ends of the tube have all been implemented. Guenoche [8] outlined four possible tube configurations: tube closed at both ends, tube opened at both ends, tube opened at one end with ignition at the closed end, and finally, tube opened at one end with ignition at the open end. He found that in all four configurations, shortly after ignition and a brief period of acceleration, the

flame decelerated. He also found that although the configuration greatly affected the propagation of the flame front, some form of flame oscillation occurred in each. Guenoche [8] concluded that the onset of flame oscillation in a tube is the result of the coupled interaction between the acoustic oscillations in the gas and the flame front.

In recent years, significant progress has been made in understanding the nature and characteristics of combustion/acoustic instability in premixed flames. One of the main difficulties encountered has been to interpret the interactions between the heat release fluctuation and the disturbances that initiate them (i.e. the boundary conditions). The heat release fluctuation may be due to the changes in the pressure, temperature, velocity, or reactants composition, these may be present simultaneously.

Though fluctuations in the flow and pressure may be present, there are two major conditions which must be met for an instability to occur. First, the fluctuations in the heat release and the acoustic pressure must be in phase so that the heat release is modulated (i.e. Rayleigh's criterion) [24] and the other is that the rate of energy gain must surpass the rate of energy loss in the system. A modified form of the Rayleigh's criterion is given by Zinn [25], as shown in Equation (2.1).

$$\int_V \int_T p'(x, t) Q'(x, t) dt dV \geq \int_V \int_T \sum_i L_i(x, t) dt dV \quad (2.1)$$

Where $L_i(x, t)$ is the total loss in the system in time and space.

2.1.1 Propagation in a tube closed at Both Ends

The study of flames in tubes closed at both ends is of major interest because of the understanding they offer into the burning process and the interaction between flames and their underlying flow velocity. According to Ellis [26], flames in a closed tube undergo two phases, the first phase is immediately after ignition and the second phase happens at the side walls. Figure 2.1 shows the stroboscopic records of premixed flames ignited in tubes of the same diameter but different lengths.

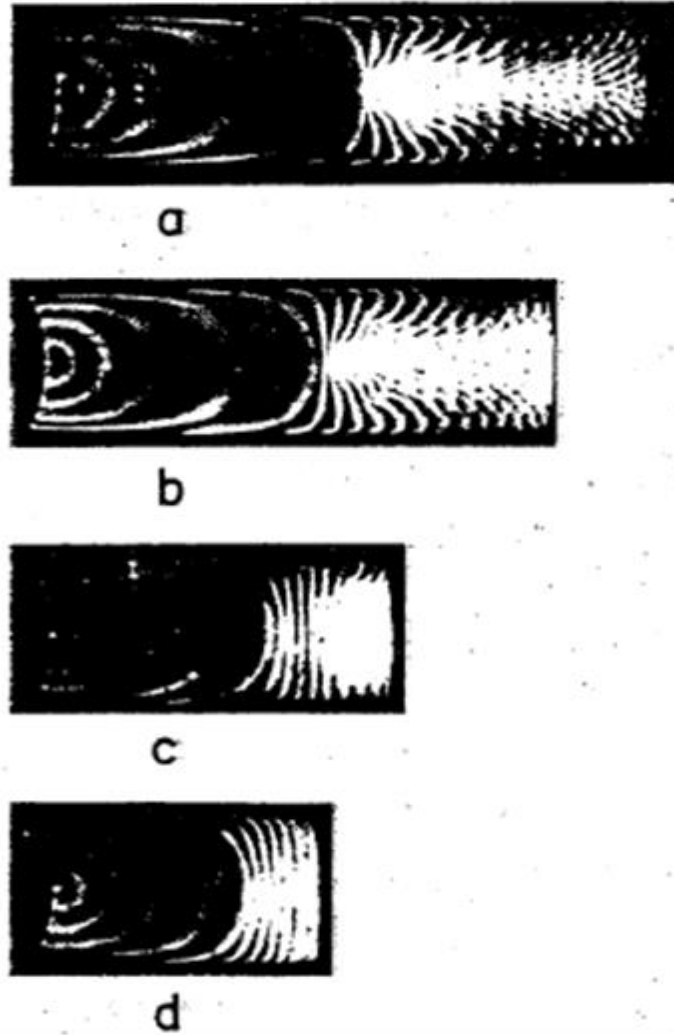


Figure 2.1: Stroboscopic flame records. Mixture: 10 parts CO + 1 part O₂ saturated with water vapour at 15°C. tube closed at both ends; diameter 5 cm; length: (a) 19.5 cm (b) 17 cm (c) 12 cm (d) 9.5 cm. Reproduced from [8]

In Figure 2.2a the flame grows out from ignition as a hemisphere at the left end wall, then as it moved towards the side wall of the tube, it was elongated into a finger-shaped flame looking like a semi-ellipsoid; this was the first phase of the propagation. The second phase starts as the flame makes contact with the side wall which causes the flame to quench. The quenching process speedily flattens the flame before it was inverted (convex towards the burnt gas). The flame then remains inverted throughout the rest of the combustion process. This observation is analogous to the flame propagation phases refer to by Clanet and Searby [27].

According to Guenoche [8], in a short tube, the flame assumes a shorter elongated shape, a lesser axial flame velocity and a smaller flame surface area than in a longer tube. Therefore, if the tube is sufficiently long, the flame development will be the same regardless of the tube length. If a large ignition source is used, the flame will reach the side walls more rapidly, so that the maximum flame surface area will be smaller than in the case of a point source. The speed of displacement of the flame will, therefore, be greater with a point source ignition.

2.1.2 Propagation in a tube Open at both Ends

The tube configuration which is potentially the most dangerous or destructive in industrial application are either tube with both ends open or flame propagation from a closed to an open end. For a flame propagating in a tube open at both ends, the flame begins by assuming a stable/uniform shape, convex towards the unburnt gases, almost instantaneously after ignition (1 or 2 tube diameters of propagation). As the flame propagates, the burned gases set the unburned gas in motion, since they (unburned gases) can also expand in the downstream end. This result in flame propagation at a higher velocity compared to that in a tube closed at the downstream end. The flame accelerates as it propagates until somewhere between one-third and the middle of the tube, the shape of the flame flattens followed by a decrease in its propagation velocity and finally flame begins to oscillate [8]. During the oscillation, the mean velocity of propagation increases either constantly with a smooth acceleration to the end of the tube or with oscillating characteristics [28]. It has been shown that the period of uniform movement of the flame starts when the motion of the unburned gases caused by the initial disturbance has been damped, and the flame propagates in a medium at rest and that the time required for the damping increases with the tube length [29-31].

Partially or wholly removing the oscillation requires maintaining a constant pressure in the unburned gas greater than the pressure of the burned gas. One way of achieving this is by terminating the tube with matching the impedance at the downstream end or both ends of the tube. Coward and Hartwell [32], achieved a steady movement of their flame by placing a glass-wool pad at the ignition end. Guenoche and Jouy [33] achieved the same result by placing an orifice plate at the ends of the tube. A reduction in the diameter of the orifice, caused the flame to propagate uniformly towards the tube end after oscillation and the

distance over which the flame remains uniform is increased. Guenoche [8] showed that the oscillations of the propagating flame in this configuration occurred towards the end of the tube when the orifice diameter was smaller than the diameter required for the maximum distance covered by the uniform/steady flame and that these oscillations increased in amplitude and time as the orifice diameter tended to zero.

Kurdyumov and Matalon [34], performed a 2-D numerical simulation of a premixed flame propagating in long narrow tubes with adiabatic walls opened at both ends where the flame was ignited at one end and allowed to propagate to the other end. The resulting flow was retarded on the walls due to viscous drag and accelerated in the central part of the tube. As a consequence, the pressure gradient produced a thrust that created Poiseuille flow in the unburned gases, in the direction away from the flame. The flame accelerated as it travelled down the tube, and analytical expressions were obtained for the flame speed and total travel time, in the limit of the narrow tube. In 2015, Kurdyumov and Matalon [35] extended their work further showing that during the initial stages of propagation, the flame accelerated almost at a constant rate, not depending on the tube diameter. For narrower tubes, the flame propagated at a constant acceleration until it got to the tube end while in wider tubes; the flame propagated with a constant acceleration, but after a certain distance, the flame acceleration was nearly at an exponential rate, reaching extremely large speeds at the tube end. Their conclusion was that the flame self-acceleration was as a result of the mutual impact of gas expansion (arising from the heat release) and lateral confinement. The pressure gradient and frictional forces on the side walls induce a gas motion that develops and propels the unburnt gas towards the tube end.

2.1.3 Propagation in a tube Open at the Ignition End, Closed at the other End

Flame propagation in tubes closed at the far end and opened at the ignition end have been frequently used since it provides the simplest propagation condition to model and also in this configuration, the flame propagates at a constant speed for the longest time, making it possible to measure the laminar burning velocity of the flame [8, 36]. It has been observed that the oscillatory behaviour arises from the growth of an ignition disturbance that causes expansion in the pressure waves for the entire gaseous medium. The amplification of this

ignition disturbance was linked to the changes in the flame structure which results from the repeated interaction of the pressure disturbance with the flame front.

Experimental observations by Searby [7], may be considered to be the continuation of work of Markstein [8, 37, 38], Kaskan [39], and Leyer [40, 41]. Searby reported four different regimes of instability for a premixed flame propagating downwards from the open end of a vertical tube to the closed end. These flames were classified according to their burning rate: (1) below 16cm/s, the flame was curved and propagated to the bottom end of the tube steadily and noiseless (2) between 16cm/s and 25cm/s, the flame propagated with no sound in the upper portion of the tube, then a primary acoustic instability sets in as the flame was in the lower half of the tube (3) above 25cm/s, flame propagated steadily this was followed by a primary acoustic instability, which then developed into a much more violent secondary acoustic instability before extinction and (4) for faster flames, the developed secondary acoustic instability reach a great acoustic level which then degenerated into a rambling turbulent wave followed by a fall in sound level. A typical result from Searby's work showing the pressure record of acoustic instability of a premixed propane-air flame propagating in a tube is shown in Figure 2.2.

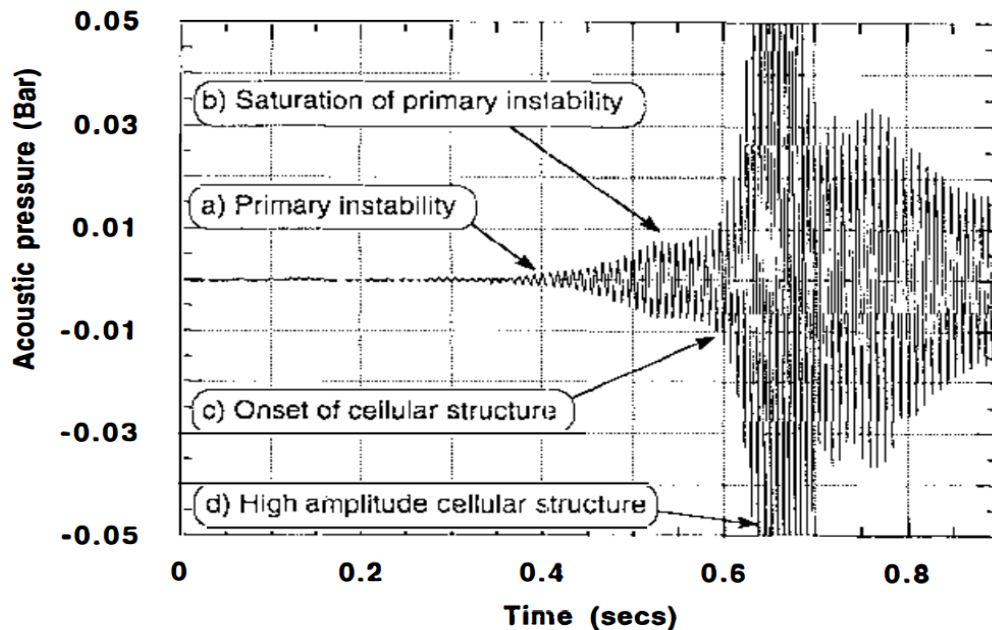


Figure 2.2: Pressure record of acoustic instability of a premixed propane-air flame propagating in a tube. Equivalence ratio = 0.82: Reproduced from [42]

Initial theoretical work by Dunlap [43] showed that the periodic change in the adiabatic temperature of a propagating flame would modulate the local rate of heat release of the flame in phase with acoustic pressure with the result that the acoustic pressure fluctuation increases the reaction rate. Clavin et al. [44], using Dunlop's mechanism, gave an analytical expressions showing the linear growth rate for the mechanism. He proposed that the growth rate of the primary acoustic instability be proportional to a coupling constant, βM . where β , is a dimensionless measure of the sensitivity of the reaction rate to variation in temperature. Clanet et al. [45] have also shown that the instabilities in flames resulted from a coupling between the acoustic acceleration field and the flame front geometry separating the less dense burnt gases from the denser unburnt gases, though with a stronger primary acoustic instability.

More recently Yoon, et al. [46] has demonstrated that the dissimilarity in the flame surface area (flame geometry) do not always result in spontaneous formation of the primary acoustic instability in initially non-oscillating flames and that even in initially oscillating flat flames, the growth rate of the primary acoustic instabilities are not linked to the increase or decrease of the surface area of the flame. There is, therefore, need to investigate experimentally, how the mixture composition changes the primary acoustic instability growth rate.

2.2 Laminar Burning Characteristics

2.2.1 Laminar Burning Velocity

The laminar burning velocity is one of the important intrinsic properties of a premixed flame and its reliable data are continuously needed for combustion applications. The correct understanding of the laminar burning velocity is crucial for designing of engines, turbulent combustion modelling, and chemical kinetic mechanisms validation. Furthermore, burning velocity is very important for the calculations used in fuel tank venting and explosion protection. Burning velocity is the linear velocity, relative to and normal to the flame front, with which unburnt gases travel into the flame front and is changed into products, or it can also be defined as the volume of unburnt gas used up per unit time divided by the flame front area used up.

Laminar burning velocity is highly dependant on pressure, temperature and composition of the gas mixture (equivalence ratio), hence, plays a vital role in determining combustion parameters. However, the laminar burning flame obtained experimentally using the tube method is always subjected to stretch (stretched flame front). Since the propagating flame has a stretched flame front, further analysis is always required to calculate the adiabatic laminar burning velocity which is the same as the un-stretched laminar burning velocity. One of the analysis method commonly applied to obtain an un-stretched laminar burning velocity from a stretched flame is by extrapolating to zero stretch rate on a plot of laminar burning velocity versus the stretch rate [47]. Shown in Figure 2.3 is a graph of how the laminar burning velocity varies with equivalence ratio.

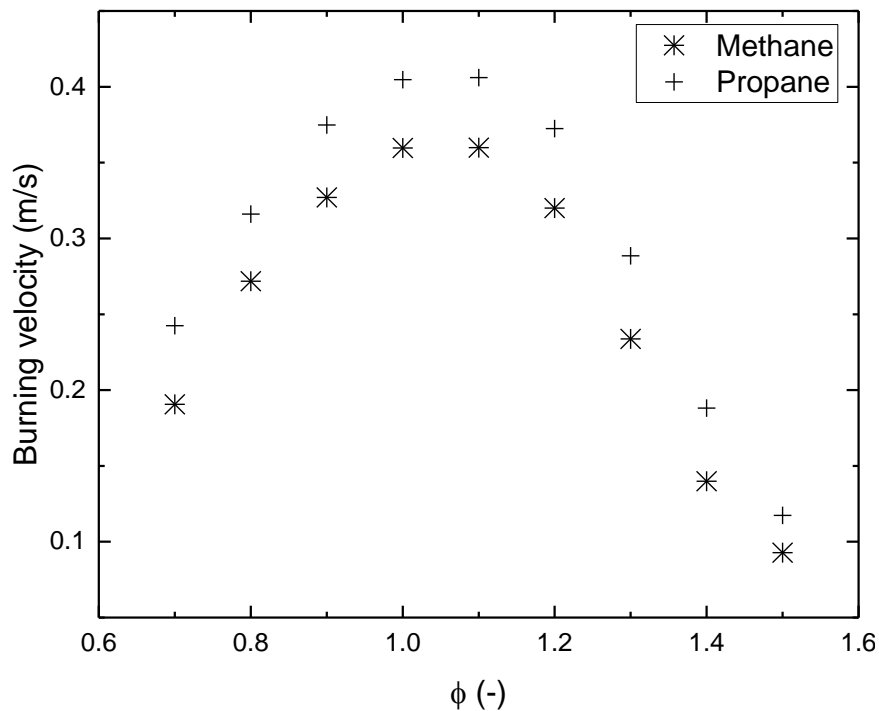


Figure 2.3: Variations of burning velocity and equivalence ratio for methane and propane (Source: Chemkin)

2.2.2 Factors Influencing Laminar Burning Velocity

Temperature and Pressure: The laminar burning velocity of a premixed combustible mixture may increase with an increase in the temperature and decreased as the temperature decrease at constant pressure. The increase or decrease in the laminar burning velocity as

the temperature increased or decreased respectively is as a result of the increase or decrease in the rate of the chemical reaction in the preheat zone. In the combustion process, during hydrocarbon oxidation, hydrogen atoms undergo two competing reactions. These are the chain-branching reaction primarily caused by the diffusion of the hydrogen atom into the preheat zone and the recombination reaction. The chain-branching reaction has high-pressure sensitivity and a large activation energy resulting in a rapid increase in the rate of chemical reaction at a slight increase in the temperature. The recombination reaction, on the other hand, has low-pressure sensitivity with no temperature sensitivity. In the hot region of burning the chain-branching reaction dominates while in the colder region, the recombination reaction dominates. Therefore, for a flame with low burning velocity and a low flame temperature, increasing the pressure level with which the flame is burning would increase the rate of the recombination reactions relative to the chain-branching reactions, hence reducing the burning velocity [48]. For a flame at low temperature, increasing the initial temperature should greatly increase the burning velocity and this is more so for flames at lower burning velocities and have no effect for flames with higher burning velocity because of the competition between the recombination and chain branching reactions in the preheat zone. The effects of temperature and pressure on the laminar burning velocity of gaseous mixture have been measured using data fitted to a power law of the general form [49-51]:

$$S_l = S_{l,o} \left(\frac{T_i}{T_o} \right)^\alpha \left(\frac{P_i}{P_o} \right)^\beta \quad (2.2)$$

Where

$T_o = 298K$ and $P_o = 1atm$ are the reference temperature and pressure.

$S_{l,o}$, α and β are constants for a given fuel.

Figure 2.4 shows how the laminar burning velocity varies with temperature and pressure for propane, methane and hydrogen. For the case of methane and propane, the burning velocity increases with increase in temperature at a constant pressure but immediately the pressure starts increasing, there was a decrease in the burning velocity and vice versa for a decrease in pressure. However, for hydrogen, though the burning velocity increases as the temperature increases at constant pressure, an increase or decrease in the pressure, gives a corresponding increase or decrease respectively in the burning velocity.

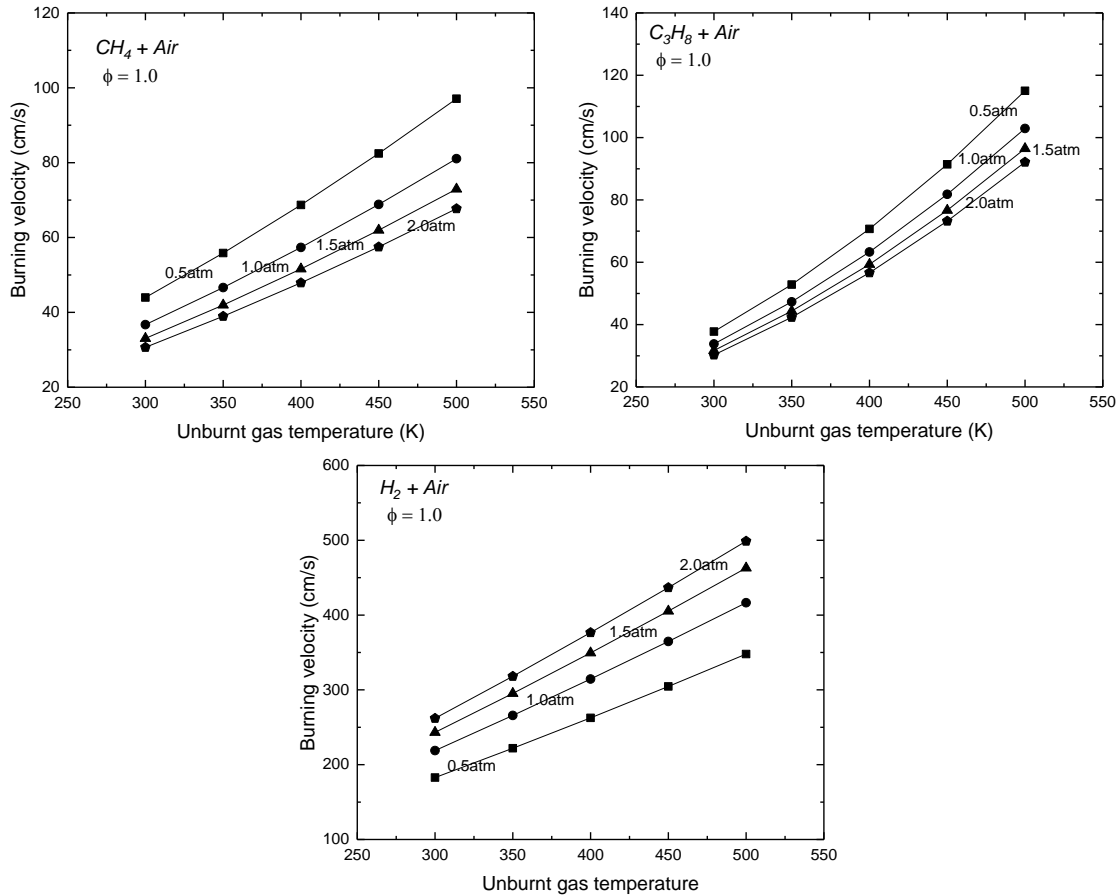


Figure 2.4: Graph showing the effect of temperature and pressure on burning velocity for methane, propane and hydrogen.

Equivalence Ratio: The fuel/air ratio or air/fuel ratio is not the best parameter for defining mixture composition because the composition of the products of combustion varies significantly for fuel-rich and fuel-lean mixtures, and the stoichiometric fuel/air ratio is determined from the composition of the fuel. Therefore, the equivalence ratio (ϕ) which is the ratio of the actual fuel/air ratio to the stoichiometric fuel/air ratio is a more useful parameter for defining the composition of mixtures. The laminar burning velocity increases with equivalence ratio up to a maximum, usually for most hydrocarbons, between equivalence ratio of 1.0 and 1.1. This behaviour is common for all fuels at different temperature and pressure. Fuels with equivalence ratios to the left of the stoichiometric equivalence ratio are considered lean fuel while fuels with equivalence ratios to the right are considered rich fuel. A fuel-air mixture that is rich or lean tends to decrease the laminar

burning velocity. This decrease in the laminar burning velocity as the mixture becomes lean is because there is not enough fuel for the combustion reaction, therefore less heating value per unit mass of the mixture necessary to speed up the reaction is generated which in turn reduces the burning speed of the flame. Similarly, the decrease in the laminar burning velocity as the fuel becomes rich is because there is too much fuel and less air to sustain the complete combustion reaction, hence, less heating value per unit mass of the mixture necessary to speed up the reaction is generated which in turn reduces the burning speed of the flame. Therefore, the proportional reduction in laminar burning velocity is independent of the unburnt mixture temperature, pressure and equivalence ratio [52].

2.2.3 Flammability Limit

Experiments have shown that the ratio of fuel and oxygen which can support a flame varies with each combustible gas or vapour and determines the propagation of the flame. A flammable mixture could be rendered non-flammable by dilution with one of its constituents (either the fuel or oxygen) or with another gas. The limit of dilution such that the flame remains flammable is called the flammability limit. The minimum amount of fuel required to support the formation of a flame in air is the Lower Flammability limits (LFL). Similarly, the maximum amount of fuel required to support the formation of a flame in air is the Upper Flammability limits (UFL), and above this amount, the mixture is considered too rich to burn. In between the LFL and the UFL is known as the flammable region for the fuel. Flammability limits are characterised using a percentage by volume of the amount of fuel contained in air or by the fuel-air mixture equivalence ratio. Flammability limits are determined in tubes, where the criterion is the ability of a combustion wave to traverse a long tube from one end to the other, and it varies in the direction the flame propagates in the tube [53, 54]. For a tube mounted vertically with the mixture ignited at the lower end (upward propagation), it is possible to go richer or leaner than when the mixture is ignited at the upper end (downward propagation) and for a tube mounted horizontally, the limits are usually between the limits for downward and upward propagation [53].

Strehlow *et al.* [55] have shown that for a vertical tube, the flammability limit at fuel lean is higher for downward propagation than that for upward propagation. Jarosinski [54] has also shown that as the deviation from stoichiometric mixture increases, the differences between the downward and upward flammability limits increase. He opined that this

difference arose from the difference in the time taken for the flame extinction. Therefore, since the downward and upward propagating flame has different flame extinguishment process/time, then the difference in flammability limit is inevitable.

Burning at LFL is advantageous in the application of the lean combustion technology. Since at the LFL, the combustible mixtures are burnt in abundant air which allows for complete combustion, thus reducing toxic emission such as NO_x into the atmosphere. Also burning at the LFL decreases the temperature of the burned gas, therefore, increasing the specific heat ratio.

2.3 Flame Instability

There are different sources of instabilities in a combustion chamber. These instabilities could be due to the peculiarity of the chamber, or due to instabilities from the complete system and finally instabilities from the reacting gases [56]. The instabilities due to the chamber peculiarity and that due to the complete system are from external influences such as shock waves, acoustic waves, and the establishment of the patterns of flow in the chamber. The instabilities due to the reacting gases are not from external influence but from the instabilities generated by the reactants. Common examples are thermo-diffusive, Darrieus-Landau and acceleration or buoyancy instabilities.

Darrieus-Landau Instabilities: A flame front could become suddenly curved because of the hydrodynamic nature of the mixture. This was first discovered independently just before the World War II by Darrieus and Landau [9, 57, 58], and it is the major reason why the flame fronts observed in several flame propagation experiments have curved shapes. Figure 2.5 shows flow lines deviation leading to the formation of Darrieus-Landau instability. If a flame front is considered as a zero thickness surface separating the unburned and the burned gas propagating at a constant velocity with respect to the unburned gas, the gas expansion produced by the heat release will deviate flow lines across the front towards the normal to the flame. As the tangential component of the fluid velocity continues over the disturbed flame front, the streamlines diverge in front of the flame and converge on the burnt gas side of the flame, for the sections of the flame that are convex towards the unburnt mixture; which in turn result to an increase in the flame instability.

From mass conservation law, ρuA is constant. As the fluid flow cross section area increased, (i.e. the stream lines diverge, at the sections where the flame is convex towards the unburnt gas), the gas flow velocity is decreased with a constant burning velocity, therefore the sections of the flame that are convex towards the unburnt gas tend to move further upstream.

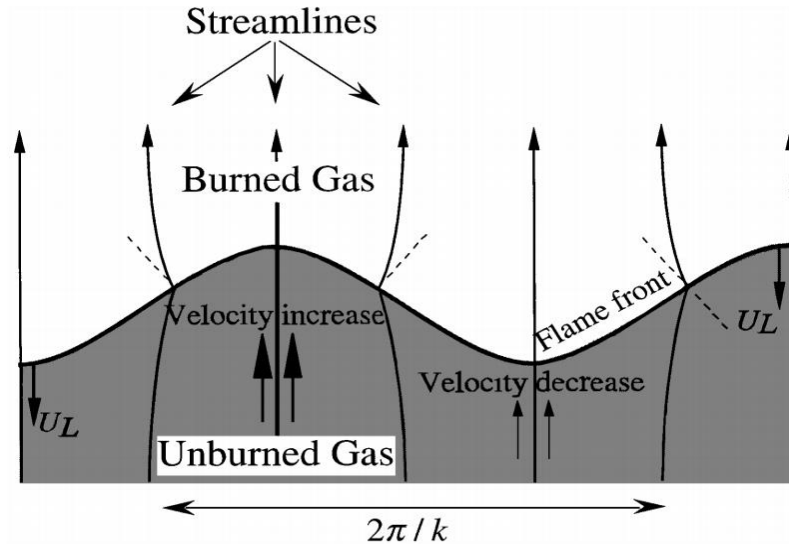


Figure 2.5: Deviation of flow lines leading to the Darrieus-Landau instability: Reproduced from [9]

The same analogy can be used for the part of the flame that is concave towards the unburnt gas, where the flame front is considered moving further downstream. The flame instability is increased by the simultaneous upstream and downstream movement of the different parts of the flame.

Thermo-Diffusive Instabilities: This mechanism occurs as a consequence of the competition between the thermal and mass diffusivity of the premixed gas. Referring to Figure 2.5, when there is thermal diffusion dominance, there are two possible processes; the first is the thermal diffusion of hot gases into the cold gas where there is convergence in front of the flame for the part of the flame concave towards the unburnt mixture making that part warmer and divergence for the part of the flame convex towards the unburnt mixture causing a drop in temperature of the part of the flame that is concave towards the burnt mixture. If this warming and cooling continue, there comes a time when the temperature of the burned and unburnt mixture comes to equilibrium, therefore stabilising the flame. The second process is the mass diffusion of the deficient molecules into the

flame front, hence increasing the concentration of the molecule on the part of the flame that is convex towards the unburnt mixture and decreasing the concentration on the part that is concave to the unburnt mixture. These two simultaneous processes can either calm or disrupt the reaction zone of the propagating flame and can be described quantitatively using the Lewis number which is the ratio of the thermal diffusivity of the total mixture to the mass diffusivity of the deficient reactants and can be expressed as [59].

$$Le = \frac{\alpha}{D} = \frac{\lambda}{D\rho c_p} \quad (2.3)$$

For a flame convex towards the unburnt gas, the conductive heat loss to the unburnt gas increases. For a unit Lewis number, the normal components of the thermal and mass diffusivities of the flame are equal, meaning there would be a balance between the heat loss at the convex part of the flame and the increase in the rate of diffusion of the reactants into the flame. The result is a constant flame temperature and burning speed. Therefore if $Le > 1$ (i.e. reactants diffusing weakly), the heat generated from the reactant diffusion is less than the heat loss by the flame, resulting in a drop in the flame temperature, reduced burning, and a corresponding reduction in the instability. However if $Le < 1$ (i.e. reactants diffusing strongly), the heat generated from the reactant diffusion would be greater than the heat loss by the flame, resulting in an increased flame temperature, increased burning, and a corresponding increase in the instability. In general, a propagating planar flame is stable if $Le \geq 1$ and unstable if $Le < 1$, hence, thermo-diffusive instability can only occur in a limited range of premixed flames with very low Lewis number or low gas expansion. Typical Lewis number for Methane-air flame at $\phi = 0.8, 1.0$ and 1.2 can be found in [60]. There have been quite a lot of numerical simulations related to the thermo-diffusive instability mechanism such as Sivashinsky [61], Kailasanath et al. [62] and Denet and Haldenwang [63]. Thermo-diffusive instability gives a possible explanation of the formation of cellular structures in premix flames of some gases. Such instabilities, in conjunction with the flame stretch effect, are somehow vital when it comes to flame extinction [64]. Therefore, the thermo-diffusive instabilities are of great concern in the design of efficient and reliable combustion systems.

Rayleigh-Taylor Instabilities (RTI): Rayleigh [14] studied the stability of certain fluid motion in a gravitational field. Subsequently, Taylor [13] further applied Rayleigh's

findings to accelerating fluids. According to the Rayleigh-Taylor instabilities, if two fluids with dissimilar densities accelerating in a direction perpendicular to their boundary, the conditions for the boundary to be steady or unsteady depends on the acceleration direction. If the acceleration direction is from the heavier fluid to the lighter fluid, the surface would be steady, otherwise, the surface would be unsteady. Therefore, for instability to develop, $\nabla p \cdot \nabla \rho < 0$. An example of Rayleigh-Taylor instabilities is the behaviour of water on oil in the gravity of earth when the interface is disturbed or perturbed. Rayleigh-Taylor instabilities are gravitation driven, as opposed to the mathematically similar Kelvin-Helmholtz instability that is shear driven. Rayleigh-Taylor instabilities are the result of the pressure torque produced by the difference in the density and pressure gradients at the disturbed boundary as represented in Equation (2.4).

$$\frac{D\omega}{Dt} = \frac{1}{\rho^2} \nabla \rho \times \nabla p \quad (2.4)$$

For this case, the pressure gradient that is dominant is the hydrostatic generated by the acceleration. If the system becomes unsteady, for a certain harmonic component of the first perturbation, the generated torque on the interface produces vorticity that tends to increase the difference in the gradient vectors which then creates supplementary vorticity, leading to an additional difference in the gradient vector. This is shown in Figure 2.6, where the two counter-rotating vortices have velocity fields that sum up at the trough and peak of the disturbed interface [65]. In the stable configuration, the vorticity, and thus the induced velocity field, will be in a direction that decreases the difference in the gradient vectors and therefore stabilizes the system[66].

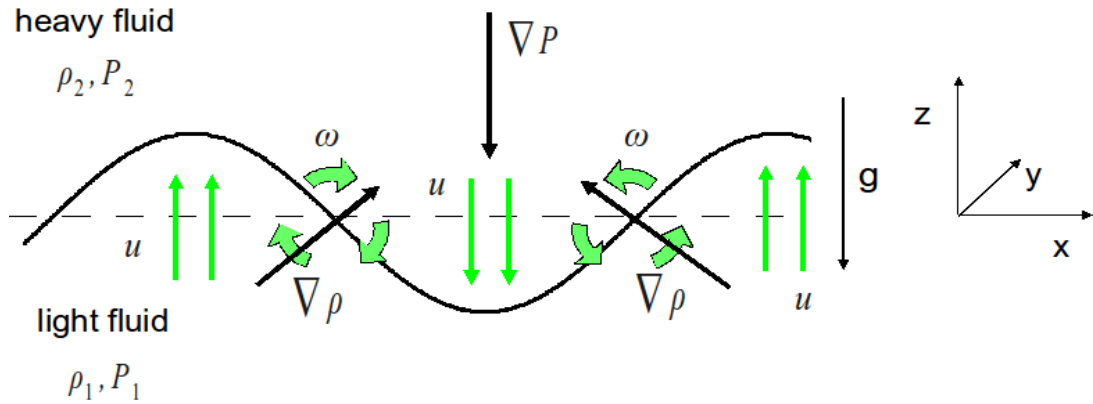


Figure 2.6: Visualisation of an unstable RTI configuration: Reproduced from [65]

Richtmyer-Meshkov Instabilities (RMI): This instability mechanism was first theoretically postulated by Richtmyer [67] and was experimentally studied by Meshkov [68]. When two fluids of different densities accelerate, the difference in the density and pressure gradients result in the fluids interface being unstable and ultimately produced a turbulent interaction of the fluids. If the acceleration is sustained, it is termed the Rayleigh–Taylor instability, but if the acceleration, however, is impulsive (i.e. shock wave driven), it is called the Richtmyer-Meshkov instability [69]. The Richtmyer-Meshkov instability differs qualitatively from the Rayleigh-Taylor instability because it makes the interface unstable in both the situation of shock wave driven acceleration from a lighter fluid to a heavier fluid and from the heavier fluid to the lighter fluid.

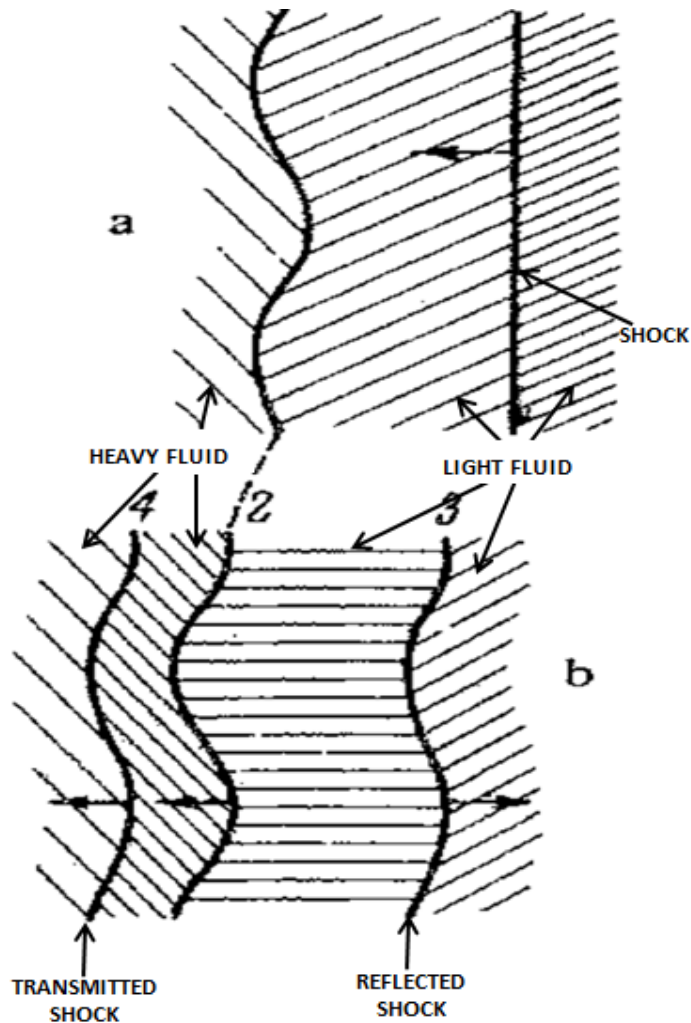


Figure 2.7: Schematics of an incident shock wave: Reproduced from [68]

Figure 2.7(a) shows a schematic of an incident shock wave 1 traversing the interface 2 from a light fluid towards a heavier fluid. The shock wave is refracted at the interface 2, forming a reflected shock 3 and a transmitted shock 4, which is slightly disturbed as shown in Figure 2.7(b). The transmitted and reflected wave diverges and converges weakly respectively at the interface disturbance trough, which creates pressure gradients normal to the interface. The analogous behaviour develops in the crest interface disturbance, but with an opposite sign pressure gradient. The pressure gradient at the trough and crest generate forces which lead to the continuous growth of the interface disturbance.

2.4 Flame Oscillations in Premixed Combustion

Flames are combustion waves driven by an exothermic chemical reaction. Flames can spontaneously produce acoustic oscillations in tubes or any other confined space [5]. Once an oscillation occurs, a feedback process can be created where the acoustic field modulates the heat release from the flame, which in turn feedback energy into the acoustic wave. According to the Rayleigh's criterion [70], the acoustic wave will be amplified if the fluctuations in the heat release and the acoustic pressure are in phase. Previous researchers such as Markstein [8, 37, 38, 71], Kaskan [39], Leyer [41], Clavin et al. [44] and Searby [6, 7] have adopted different mechanisms to explain this phenomenon. Faster flames create stronger acoustic waves and generate intense turbulent burning in tubes [7]. Flame interaction with the tube walls leads to oscillation regime of burning which causes variation in the shape and velocity of the flame. The oscillation parameter (oscillation period and frequency) depends on the tube width and controls the flows Reynolds number. In narrower tubes, the flame oscillations are weaker, while in wider tubes, the flame oscillations become stronger with well pronounced nonlinear effects. The oscillation period increased for wider tubes while it decreased for narrower tubes and the average flame front surface area, the flame burning rate slightly depends on the tube width. However, the oscillation does not depend/weakly depend on the length of the tube, the Prandtl number and the Mach number [72].

Petchenko et al. [73] in their work on violent folding of a flame front in a flame-acoustic resonance, got result similar with [7] such as the extra-large increase in the flame speed and the extra-strong acoustic waves for wider tubes, but concluded that because of limited

parameter domain for their simulation, their results do not quantitatively compare to the experimental result of [7]. Similarly, Petchenko et al. [74] observe that flame-sound interaction strongly influences oscillations of flame front (flame sound interaction increases the oscillation amplitude). Shalaby et al. [75] approached the problem differently, they simulate the response of curved lean premixed flame dynamically to sinusoidal acoustic waves at varying single frequencies and frequencies of wideband excitation. Results from the study showed that the mass burning flux of the flame increased as the amplitude of the acoustic wave was increased. However, the result also showed that an increase in the frequency does not lead to increased rate of fuel consumption and for the four single frequencies tested, the maximum rate of fuel consumption occurred at 500 Hz. Furthermore, the study also identified that once the acoustic waves were simulated as oblique waves in the place of round waves, the fuel consumption rate increased due to the formation of vortexes around the surface of the flame by significant baroclinic torque as identified by Xiao et al. [76, 77]. In summary, their study showed that planar flames are less sensitive to acoustic excitations when compared to curved flames.

Although numerical simulations have been carried out as seen in literature to explain the phenomenon of flame oscillation in different configuration of tubes (open both ends, open ignition end and open ignition end but allowing a small opening at the other end), there is little or not enough experimental analysis to validate these results.

2.4.1 Cellular Flame

At certain mixture conditions, complex flame structures break up and are subjected to flame instabilities resulting in the formation of numerous cells which form the initial stage of the flame transition from laminar flame to turbulent flame propagation (Figure 2.8) [58]. Cellular flames are formed intermittently with peaks directed towards the burnt gas when the Lewis number L_e and the flame front radius are respectively lesser than and greater than a certain critical value [78, 79]. At the crest, the flame seemed darker than at the trough indicating a lower temperature at the crest compared to the other parts of the cell [78].

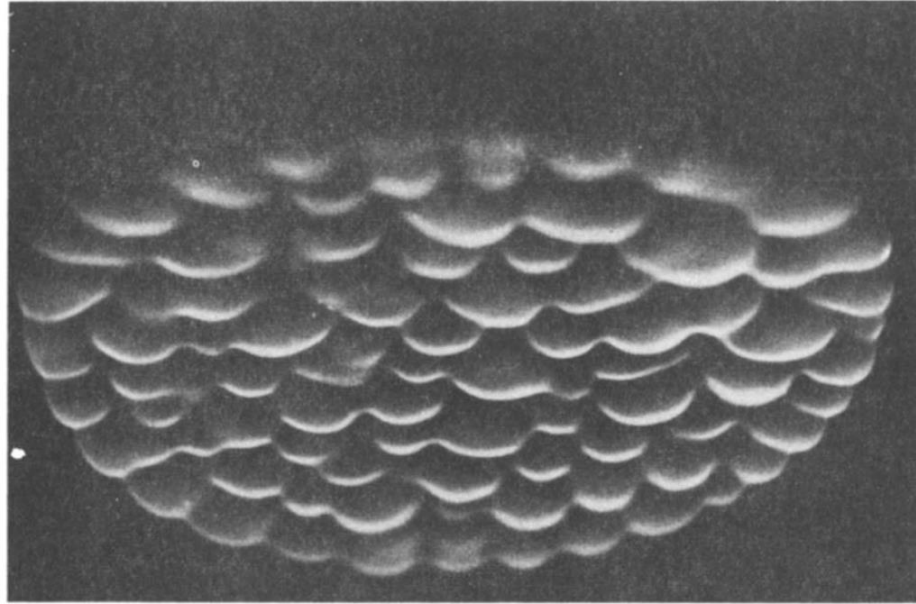


Figure 2.8: Self-turbulising cellular flame dynamically stabilised in a uniform laminar flow: Reproduced from [58]

The surface area, depth, cell size, and flame speed, are determined by the flame temperature, Lewis number, and flame acceleration, which constitute the thermal-diffusive and hydrodynamic effect. There is the likelihood of a stationary flame being formed after successive cellular flame if the inlet velocity is not the same as that of the cellular flame velocity [79, 80]. Matkowsky et al. [78], in considering two-dimensional problem of the stability of a stationary cylindrical flame front produced by a point source, showed that the flame fronts that became stable for $L_e > L_c$, and were probably unstable for $L_e < L_c$. For cases where $L_e < L_c$, there was a possibility of stability if $R < R_c$ or instability when $R > R_c$ where R is the flame front radius and the subscript c is a critical value. These instabilities would progress into a cellular structure over time.

2.4.2 Rotating/Spinning Flame

In 1985, Sohrab and Law [81], by varying mixture concentration and flame velocity in a burner, identified rotating, stationary and unstable polyhedral flames and was able to measure the rotational velocity, the temperature in the trough and crest and the periodic temperature fluctuations of the gases through which the flame rotates. Bayliss and

Matkowsky [80] solved numerically flame stabilisation in the cellular regime (i.e. when the Lewis number is lesser than one) and found that as the Lewis number decrease, there was a successive transition from stationary axisymmetric solution, to a stationary four-cell solution and finally to a spinning four-cell solution. Their spinning four-cell solution was a very slowly travelling waves that occur due to an infinite period and symmetry breaking bifurcation. Spinning flames similar to the rotating polyhedral flame identified by Kwon et al.[82] in a sudden expansion tube; this they assert was caused by heat loss, preferential diffusion and hydrodynamic effects. Many other studies have been carried out where spinning and pulsating flames were reported [83-85]. In 2007, Xu and Yu [86], observed spinning flame for the first time in a divergent mesoscale channel for methane and propane in both lean and rich conditions. Their results showed that the flame starts to spin if the flow rate goes above a critical value and that the frequency of spinning was proportional to the flame speed. However, the spinning of the flame only occurred after the switch from a fast flame regime to a slow flame regime and either rotate in the counterclockwise or clockwise direction with equal possibility. Kurata [87] observed the presence of X-shaped flames in a coaxial burner operated near blowout for methane-air. Kurata's X-flame rotates with a slanted flamelet, shaped liked an asymmetric triangle with a curved surface. The flame had a rotational frequency of about 30Hz, which strongly depends on the gas velocity and the mixture composition (i.e., increases with increasing fuel-air ratio) and made no sound. Deshpande and Kumar [88], recently reported the presence of spinning flame in a stepped micro-combustor for both lean and rich regime. The spinning frequency of these flames was almost twice that observed by previous research and the spinning flame formation depends on the equivalence ratio, mixture flow rate and the number of steps in the micro-combustor.

2.5 Flame Growth Rate

The rate of growth of the primary acoustic instability is proportional to $(ak)^2$, where a and k are the amplitude and wave number of the flame respectively [89]. This expression assumes that the flame has constant amplitude and does not take into account that flame amplitude by D-L instability changes nonlinearly. Clanet and Searby [9] measured their flame growth rate by taking the peak-to-peak amplitude of the flame front position of the

wrinkling flame while Searby [7] measured the same growth rate by taking the peak-to-peak amplitude of the flame front position of the flame .

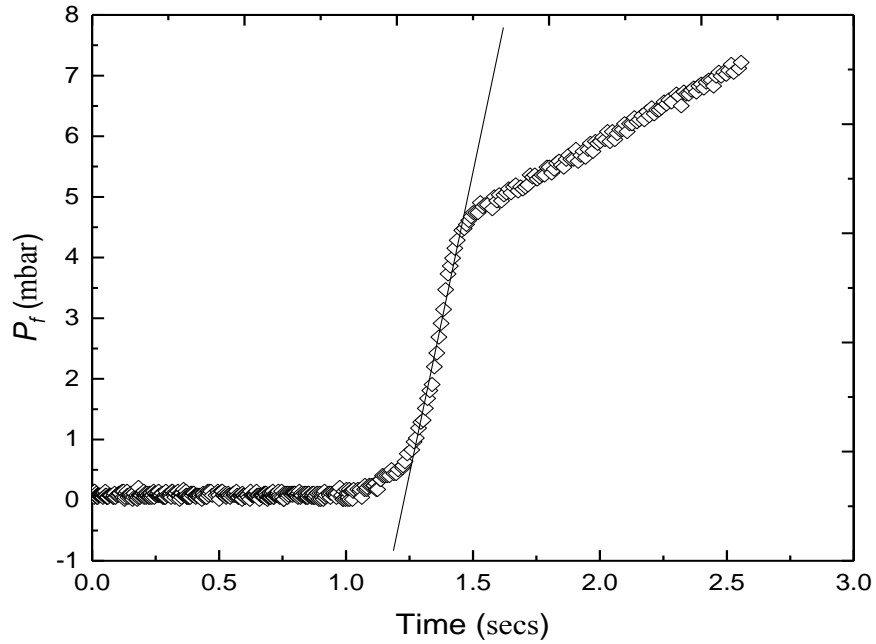


Figure 2.9: Peak-to-peak pressure amplitude of flame as a function of time

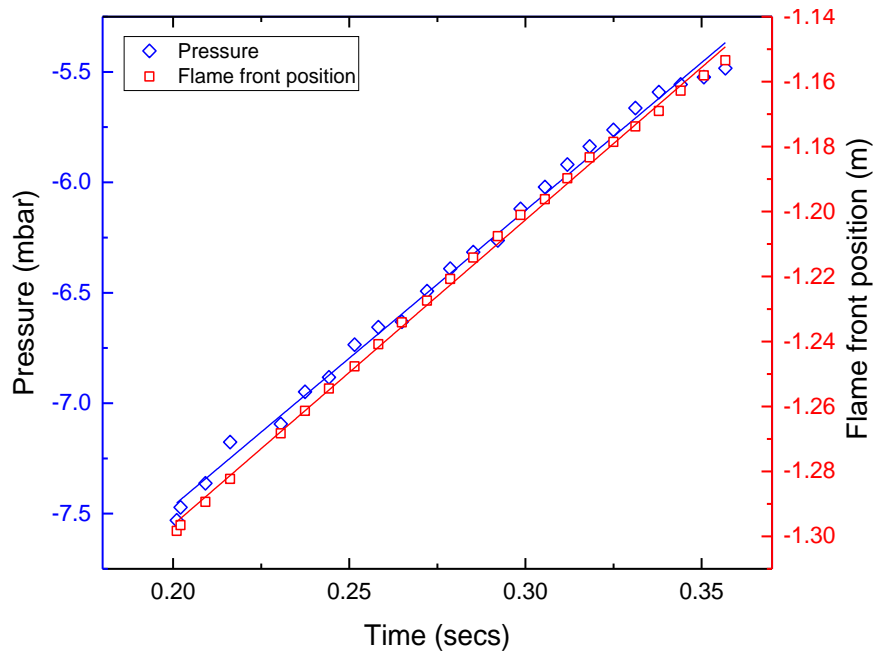


Figure 2.10: Log-log plot of the pressure amplitude of the flame as a function of time

In this work, the peak-to-peak amplitude of the pressure signal of the flame was used for the growth rate analysis. The pressure amplification of the flame can be seen as it is subjected to D-L instability and the corresponding flame front position, therefore representing both the pressure growth rate and the maximum flame front position growth rate as shown in Figure 2.9. The scatter in the data in the early stages arises from the low amplitude of the signal in the order of the apparently flame thickness and the nonlinearity at long times shows the onset of saturation of the instability [9]. The growth rate was computed by taking the gradient of the log-log data of the original graph as shown in Figure 2.10.

2.5.1 Flame Acoustic losses

Acoustic losses in flame tubes depend on the nature of the gaseous mixture, the geometry of the combustion chamber, and the location of the interface between cold and hot gases [45]. For our experimental set-up, the acoustic losses mainly occurred at the tube end opened to the atmosphere due to radiation, and, at the wall of the tube due to the presence of viscous and thermal boundary layer. Instability would be generated in the propagating flame if the flame produced a gain in the tube, larger than the acoustic losses generated. The acoustic losses characterised by the time are expressed as follows [45, 90]:

Radiative losses: The characteristic time for radiative loss $1/\tau_{rad} = \overline{\varepsilon_{rad}}/\bar{\varepsilon}$, can be expressed as

$$\frac{1}{\tau_{rad}} = \frac{(\omega r)^2}{8cL} \quad (2.5)$$

Where the tube radius is r , the tube length is L , the angular speed (V/r) is ω , the linear speed is V and the speed of sound is c , calculated using Gaseq software [91]. The radiative losses are proportional to ω^2 .

Wall losses: The characteristic time for diffusive processes is expressed as

$$\frac{1}{\tau_{wall}} = \sqrt{8} \frac{(\omega \alpha)^{0.5}}{r} [(\gamma - 1) + Pr^{0.5}] \quad (2.6)$$

Where the specific heat ratio is γ , the thermal diffusivity is α , the prandtl number (ν/α) is Pr and the kinematic viscosity is ν .

The total acoustic losses in the tube, $1/\tau_{loss}$, is expressed as

$$\frac{1}{\tau_{loss}} = \frac{1}{\tau_{rad}} + \frac{1}{\tau_{wall}} \quad (2.7)$$

2.6 Temperature Measurement Technique

Temperature measurements in the present day industrial environment cover a wide variety of applications and requirements. In meeting the broad range of necessities, the process control industries have developed scores of sensors and devices to handle these demands. More complex measurements like the temperature of power generating station smokestack gas, blast furnace, and a rocket exhaust gas, may require monitoring. More popular in temperature measurements are the temperature of the fluid in industrial processes and applications that support processes or solid objects temperatures like shafts in machinery, bearings and metal plates.

There is a broad range of systems used for measuring temperature. The particular system to use depends on what is to be measured, how accurate it is to be measured and if the reason for measuring is just for control or monitoring.

Temperature measurement systems are categorised into the following few general groups:

- Thermometers
- Probes (thermocouple)
- Non-contact method

Thermometers have proven to be oldest temperature measurement systems. The requisite to measure and quantify the temperature of matter is dated around 150 A.D. when Galen determined the ‘complexion’ of a human, based on quantities that are noticeable [92]. Following the progress in thermometer measurement, the next phase in the progress of temperature measuring systems was the development of the temperature probe (thermocouple). Becquerel in 1826 invent and used the first ever platinum-vs-palladium thermocouple. Before this time, the majority of temperature measurement was done with

thermometers filled with either gas or liquid. The creation of the thermocouple steered the new wave of development, leading to what is now known today as real thermometry.

The non-contact means of measuring temperature comprises of sensors that are principally optical in nature. They all function on the principle of heat transfer radiation and that generally, everything on the surface of the earth radiates heat. The heat radiated can be detected as either radiation from the device or light. By measuring the light/radiation, it is possible to determine the device temperature, not only from a distance of a small number of millimetres but also from millions of distant.

A typical example of a non-contact temperature sensor is the infrared thermometry. Applying the infrared thermometry technique in conjunction with the two-colour technique, the measurement of the temperature of flames is possible.

2.6.1 Pyrometer

The word pyrometer was initially used to describe instruments designed to measure the expansion of solids. As technology advances, pyrometers are now used to describe any device applied to measure temperatures above the upper limit of a mercury thermometer, and this limit, is the boiling point of mercury; $357^{\circ}C$ or $672^{\circ}F$ [93]. It can also be described as a device used for temperature determination of surfaces using the spectrum of the thermal radiation emitted by the surface from a distance. At present, pyrometers or simply put as infrared thermometers can measure the temperature of not just hot objects, but also cold objects by detecting their infrared radiation flux. The major advantage of a pyrometer is that, unlike a resistance temperature detector (RTD) and a thermocouple, there is no direct contact with the object whose temperature is being measured. Pyrometer measures the temperature of an object by comparing the brightness produce by the radiation from the object to a reference temperature. Further history, working principle and design of a pyrometer can be found in [93-95].

Pyrometers are commonly used for high-temperature measurements with particular application when a fast response time and less optical access are essential. However, pyrometer techniques for measuring these fast moving objects with less optical access are often limited by uncertainty in the object's surface emissivity. For applications where the size of the surface to be measured is known, monochromic pyrometer can be used because

of the easy setup required [96]. On the other hand, if the exact surface temperature is to be determined, it is essential that the emissivity of the surface at the wavelength the surface is being measured is known. If the emissivity of the surface is unknown and varies in the process of doing the measurement, then, it is unlikely the exact temperature of the surface would be determined accurately. Therefore, a temperature measurement technique that has a fast-responding feature, less-intrusive, can be set-up with ease and does not solely depend on the emissivity of the surface to be measured, is required. A thin filament pyrometer applying the two colour method is one of such device that meets some of these characteristics, especially for the measurement of the absolute surface temperature of object/surface without the prior knowledge of the emissivity of the object/surface, if the emissivities at the two wavelengths to be measured are equal and with less optical access. This method has been recognised to be a valuable tool for measuring the temperature of flames. The method offers a 1-D profile of temperature measurement laterally on the filament length.

Thin filament pyrometer (TFP) uses a 15 μm diameter β -SiC (beta-Silicon Carbide) fibre. The filament, when placed in an environment of high temperature glows and emits nearly blackbody radiation that is then filmed by a high-speed camera. Images from the high-speed camera are then processed further, applying the two-colour scheme and finally the flame temperature is determined, by correlating local gas temperature and the flame temperature through an energy balance of the fibre.

2.6.2 Two-Colour Method

Accurate and dependable measurements of furnace and flame temperatures including their profiles by non-contact approach are greatly required to comprehensively understand pollutant formation and combustion, carbon-in-ash levels, and several other combustion problems such as fouling and slagging [97]. In the past, different techniques have been developed to measure flame temperature, but currently, physical probes such as gas sampling probes or thermocouples have been in use. These techniques have palpable setbacks, such as degrading in a tough environment, single point measurement, and intrusive sensing. Resolving these setbacks, optical means such as laser scattering of molecules (LSM) and laser-induced fluorescence (LIF) have been established in recent

years. However, due to the complexity of these techniques and the structure of the system, they would not be suitable for repetitive measurements in industrial furnaces.

The two-colour method is a well-known optical technique for measuring the temperature of flames. It has the advantage of measuring the absolute temperature of a flame without knowing the surface emissivity. This technique was first used by Hottel and Broughton [98], where they applied it to determine the flame temperature in utility furnaces. Since then, this technique has been used, in combustion engines to determine the flame temperature and soot concentration [99-103], and in both diffusion and premixed flame in a burner [104, 105]. One of the downsides of all the different approaches was the inability of the sensing element to detect the temperature within a flame at multiple points. One and two charges coupled device (CCD) sensor was used by Zhou et al. [106] and Kawamura et al. [107], respectively in an attempt to measure flame temperature at multiple points but still encountered some setbacks. Huang and Yan [97] have also used a modified CCD sensor with little success.

The application of the Thin Filament Pyrometer for the measurement of flame temperature was first introduced by Vilimpoc [108], and he estimated that the transient response was around 1.5ms. Since then, many other researchers have also applied this technique in determining the flame temperature of both laminar and turbulent flame, be it diffusion or premixed flame. Pautin et al. [109], has applied the thin filament pyrometer technique to measure the flame temperature of up to 550 K for a weakly turbulent flame. Pitts [110], on the other hand, applying thin filament pyrometer showed there was generally good agreement between the temperature profile of the filament measured and an earlier radiation-corrected thermocouple result over a temperature range of 1200-2100K. Struk et al. [111] compared the thin filament pyrometer measured temperature with a thermocouple measured temperature and showed, that, the temperature difference is within 3.5% at temperatures above 1200K. Kuhn et al. [112] showed there was an overall good agreement between the gas temperature result using the thin-filament technique and that obtained using a computational approach. Ma et al. [113], recently, compared a laser-based technique using a thermocouple and the thin filament pyrometer technique; their results showed good agreement in the temperature measured, though there was also an uncertainty analysis done which provides insights on how to improve the TFP measuring accuracy.

CHAPTER THREE

RESEARCH METHODOLOGIES

3.1 Experimental Facilities

The major facility used for the present research is based on the work of Gerstein et al. [21] Although there are different robust methods for measuring the laminar burning velocity of fuels, there still exists a major setback of these methods not able to measure the velocity of lean fuel. The Sheffield flame tube rig was a creation of these major setbacks of other methods of determining the laminar burning velocity of fuels.

The experimental apparatus used for this study was originally designed and fabricated by Cook [114] in 2008 (Figure 3.1a), as part of the partial fulfillment for the award of a Masters of Engineering Degree, and was later adapted and improved by Mossa [3] to include a pressure indicator used to measure the vacuum pressure in the rig and a vacuum pump used to remove burnt gases from the rig after every firing (Figure 3.1b). As this research progressed, in addition to the high-speed image recordings, there was a need to simultaneously take transient pressure readings and the high-speed image recordings along the tube length, so that the experimental results can be compared more reliably with the acoustic analysis. To achieve this, a piezoelectric pressure transducer was attached to one end of the flame tube as a preliminary experiment showed that the pressure sensor at the tube end gave a more realistic result compared to when it was placed at the middle. **3.1.1**

Flames in Tube Test Rig

The test rig consisted of 20 mm bore copper tubes formed in a rectangular shape used for pre-mixing the fuel/air before being ignited. The central 700 mm length of one side of the tube is quartz to provide optical access, with two standard 50 mm computer cooling fans on adjacent sides of the rig for homogeneous mixing of the mixture. Compression fittings of 22mm bore were used for the ignition port, fuel injection port, the pressure indicator port, and the port used to connect the vacuum pump. The pressure indicator fitted to the rig was a PDCR 810 Druck digital pressure indicator and can read a maximum pressure of up to 1 bar, sufficient enough for checking the rig's pressure. The test rig is equipped with two three-way valves and a two-way valve, primarily used for letting air in or releasing air from the rig. The detailed design procedure of the rig can be found in [114].

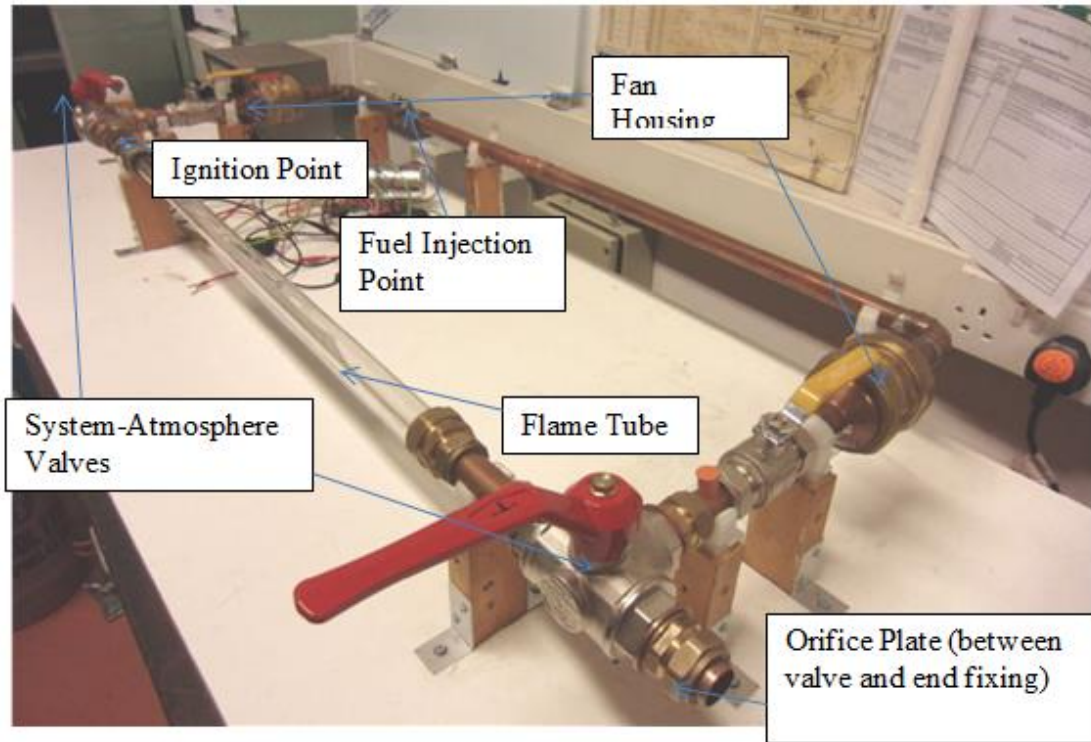


Figure 3.1a: First experimental test rig

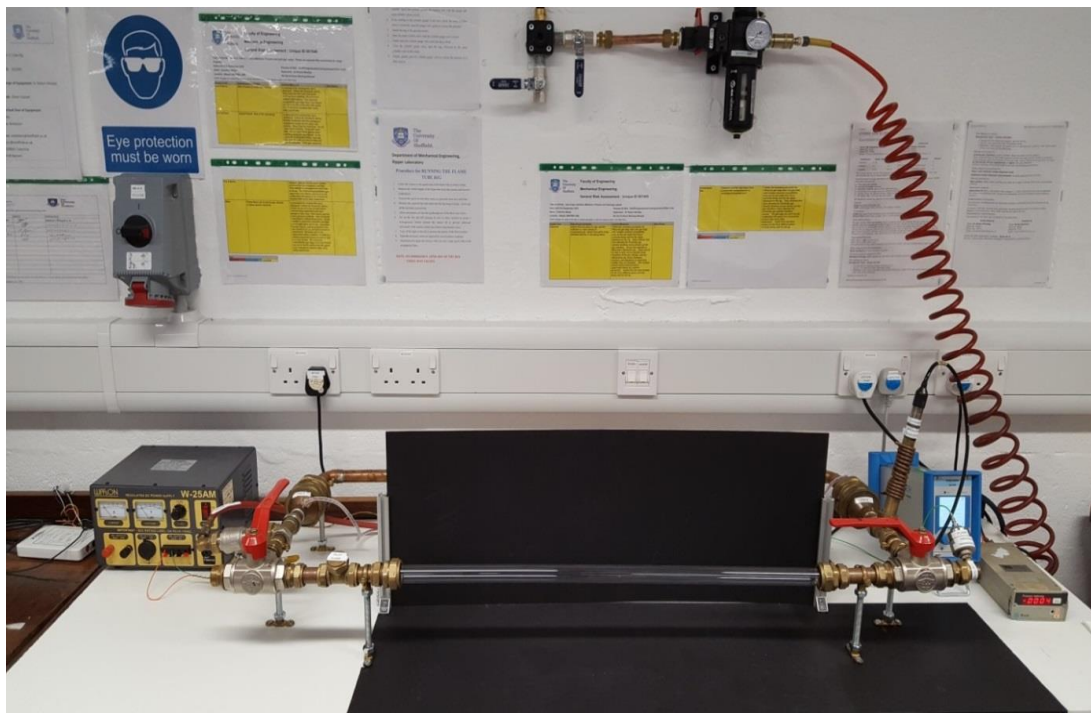


Figure 3.1b: Experimental test rig with pressure transducer and vacuum pump

To measure the speed of the flame, uniform and stable flame propagation are required. The tube length and diameter has been shown to affect the stability and uniformity of the propagating flame [8, 17, 18, 115], and ultimately has an impact on the flame speed. The same diameter and length of tube used by Mossa [3] were used for this work because he was able to achieve stable and uniform flames with this diameter and length of the tube.

For experiments where our focus was comparing the flammability limits of the horizontally and vertically propagating flame with both ends of the tube opened, the rig has orifice plates of 5mm (Figure 3.2) fitted to both ends of the tube allowing a uniform, stable and reproducible flame [4, 22] since the orifice plates suppress the pressure wave which may cause the flame to be distorted. The choice of 5mm orifice plate was from the results of Mallard [116] and Mossa and Woolley [117], where, in their experiment with orifice plates of different configurations (5mm/5mm, 3mm/5mm, 3mm/3mm and 1mm/5mm), found that, the highest flame speed was recorded with a 5mm orifice plate at both ends of the quartz tube.

The propagating flame was recorded using a coloured Casio EX-FH100 digital camera, with 224 x 168 pixels resolution operated at 400 fps and for further analysis/detailed observation of the flame oscillations, a Phantom V210 high-speed camera fitted with a Nikon AF NIKKOR 24-85mm f/2.8-4D IF lens, using 1280 x 128 pixels image resolution and operated at a framing rate ranging from 1000 to 3000 fps depending of the experimental configuration. The required volume of fuel needed at each equivalence ratio measured using a syringe was calculated with reference to the volume of the rig.

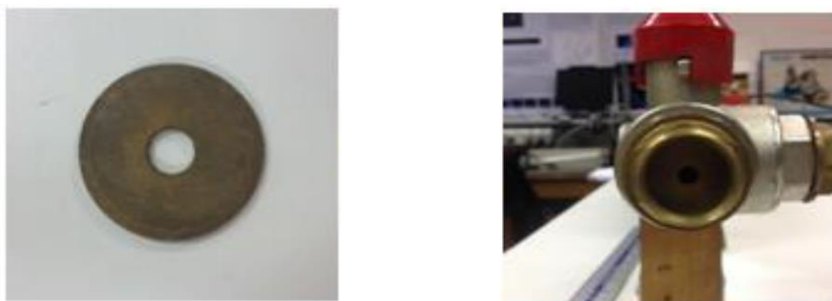


Figure 3.2: 5mm orifice plate fitted to the end of the rig

Ignition was performed using a pilot flame from a gas lighter by opening a port at one end of the tube. Flame propagation in tubes has been found to vary considerably with the

ignition source. According to Mossa and Woolley [117, 118] and Wu et al. [119], Spark ignition increases the flame speed of the propagating flame and also enhances the start of flame oscillations (Figure 3.2), hence, was not used for this research.

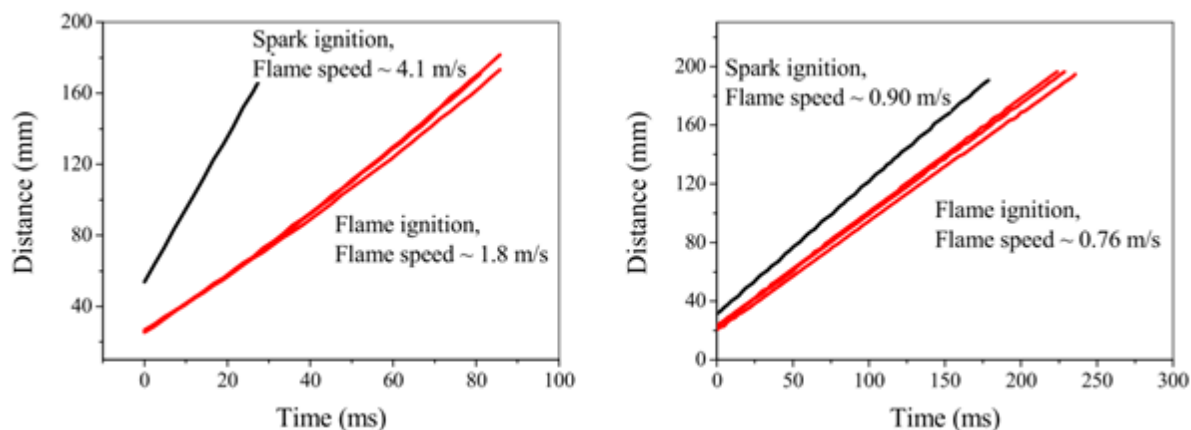


Figure 3.3: Effect of Ignition source on flame speed [117]

In the current research, the rig was positioned in two different configurations with different boundary conditions to achieve the aim. The first was the horizontal configuration as shown in figure 3.1b, where experiments were performed with orifice plates at both ends and at another time with both ends of the tube open to the atmosphere. Also in the horizontal configuration, SiC fibres were installed at the midsection and both ends of the quartz tube as shown in Figure 3.4a, to study the temperature profile in the tube. The second configuration was downward propagation first with orifice plates at both ends and consequently with the upper-end open to the atmosphere and the lower end closed with a metal cap carrying a flush mounted piezo-electric pressure sensor (Kisler type 7261) connected to a charge amplifier, then to a desktop computer (Figure 3.4b). The configuration with orifice plates at both ends and the flame propagating downwards was carried out to study the effect of gravity and to successfully determine the flammability limit of the fuels. Health and safety risk assessment and COSHH forms for the rig and the gas cylinders respectively are shown in Appendix G. This includes a detailed procedure for running the rig and also using the gas cylinders.

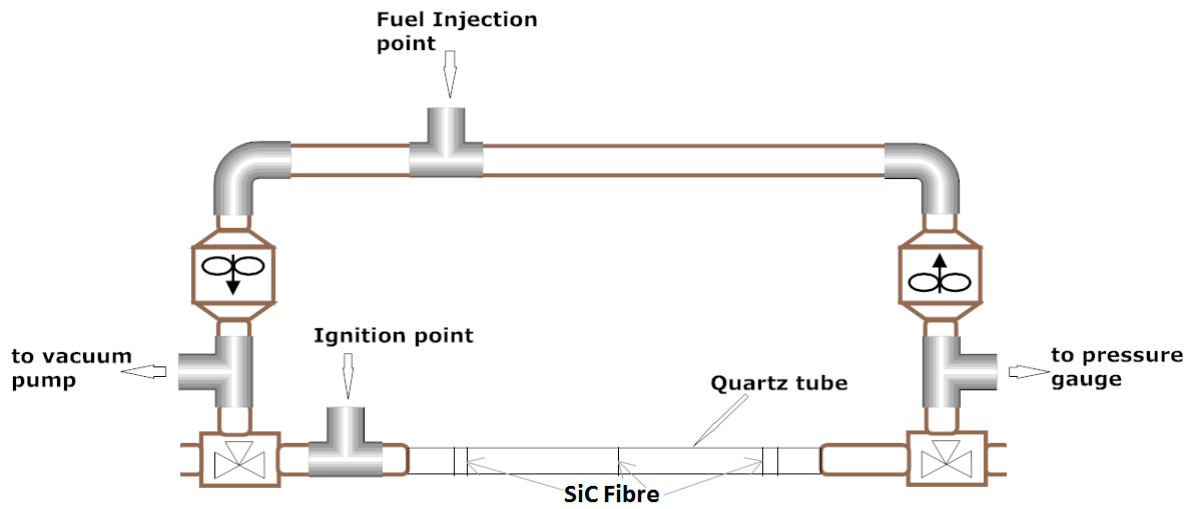


Figure 3.4a: Rig schematics for flame temperature measurement

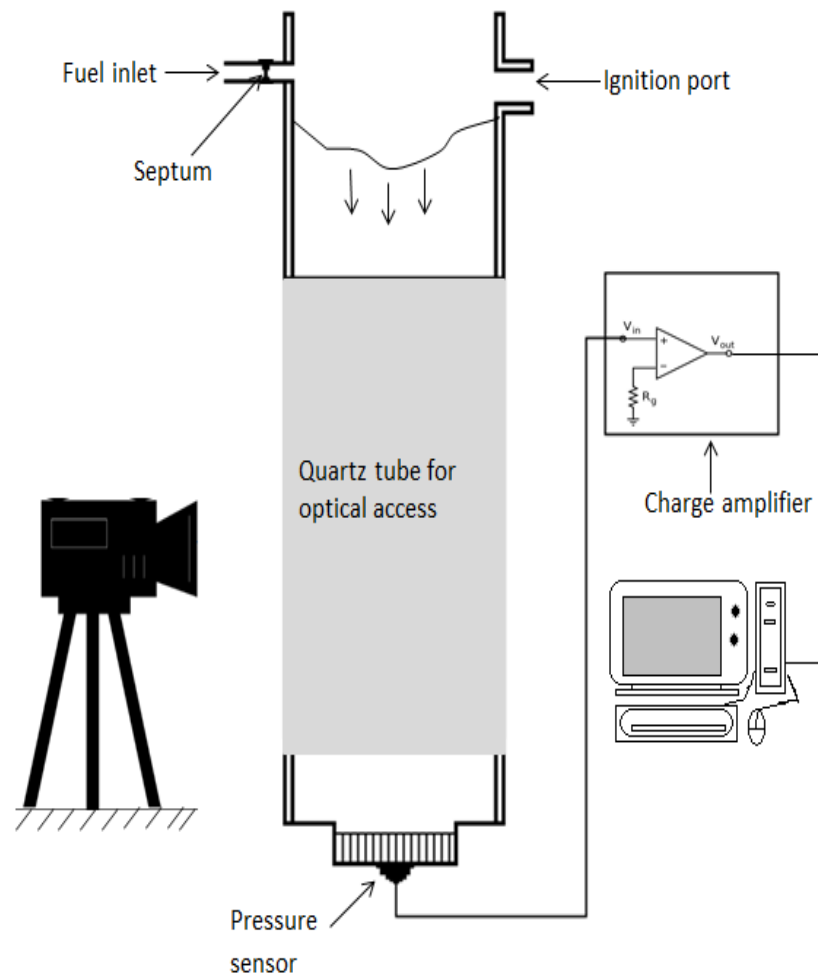


Figure 3.4b: Schematics of the downwardly propagating rig

3.1.2 High-Speed Cameras

High-speed image capturing is the art of taking pictures in a very fast motion. High-speed image capturing may also depict either one or both of the following. Firstly, is that, the image may be captured such that it appeared to halt the motion, especially to decrease the motion blur, which, requires sensors with a very good sensitivity or either a very fast strobe light or a very good shuttering system and secondly, is that a series of image could be captured at very high sampling frequency or framing rate with some ways of capturing sequential frames, either by rapidly moving data from electronic sensors or with a mechanical device.

Three different high-speed cameras were used for different cases of the experiment carried out in the current research. The first high-speed camera used was the Casio EX-FH100 camera, at a framing rate of 420 frames per second, and an image size of 224 x 168 pixels. This camera was used for the case where 5mm orifice plates were placed at both ends of the tube for both horizontal and downward propagating flame. The second high-speed camera used was the Phantom V210 high-speed camera, fitted with a Nikon AF NIKKOR 24-85mm f/2.8-4D IF lens. The camera framing rate was varied accordingly between 1000 to 3000 fps for the different configurations to capture the oscillating flames that were not possible to capture with the Casio camera. The camera image resolution was 1280 x 128 pixels. The third camera was a Photron fast cam SA4 high-speed camera, fitted with a SIGMA 17-50mm F2.8 EX DC (OS)* HSM lens. This camera was used for capturing images of glowing filaments placed in the tube for flame temperature measurement and at a framing rate of 2000 fps.

3.1.3 Pressure Sensor

The pressure sensor used for the current research is a Kistler type 7261 piezo-electric pressure sensor. It is a low-pressure quartz sensor for dynamic and short span static pressure measurements from vacuum to 10 bar with a high resonant frequency and flushes welded diaphragm. The charge signal of the sensor is transformed into a proportional output voltage in a charge amplifier. The propagating flame pressure variation signal was recorded at a sampling rate range of 1 to 3 kHz depending on the sampling rate of the high-speed camera as both pressure readings and the high speed must be in sync. The pressure sensor and the amplifier connected.

3.1.4 Gas, Syringe and Gas Bag

Propane, methane and hydrogen fuels were used for the research experiments and environmental air was used as the oxidizer. For health and safety reasons, the fuels in a BOC cylinder was kept outside the lab in a cage and gas bags with suitable chemical compatibility such as the one made from Kynar was used to transport the gas from the gas cylinders to the laboratory just before an experiment was to be conducted. The bags are emptied at the end of the days experiment for health and safety reasons and also as a precautionary measure because leaving the bags overnight may cause gas diffusion, leading to impurity in the gas. Syringes were used to measure the volume of fuel required at a particular equivalence ratio for the experiment. Different gas bag and syringes were used for the different fuel used for the experiment and they were all labelled according to the gases to prevent cross-contamination of gasses.

3.2 Experimental Procedure

The experimental procedures are as follows:

1. The camera was placed at the central point of the tube and levelled such that the quartz region test rig was clearly visible
2. The quartz tube length visible to the camera was measured and recorded (this is the calibration process)
3. The chamber was vacuumed three times for complete cleaning, each time to a pressure of about $\pm 0.9 \text{ bar}$
4. The fuel was then measured and injected into the rig through the fuel injection port
5. One of the three-way valves at the tube end(s) was opened to let atmospheric air into the chamber
6. The fans on adjacent ends of the test rig were turned on and were left running for about three to four minutes to form a homogeneous mixture before turning it off.
7. The lights in the Laboratory were turned off.
8. Depending on the experimental configuration, one or both three-way valve was opened
9. The homogeneous mixture was ignited simultaneously as a high-speed filming of the propagating flame was recorded.

3.2.1 Calibration

Before every experiment, there was always need to calibrate. This was done by first levelling the camera with the ground using the spirit level on the camera tripod stand. After levelling the camera to the balanced ground level, the camera was adjusted such that the horizontal gridlines displayed on the screen of the camera was parallel to the quartz tube and then a ruler was placed on the face of the tube visible to the camera to measure the length of the tube visible to the camera. The calibration process was repeated after every 6 runs. The flame recordings were later processed to get the flame speed with either the python code for the case of a tube with an orifice plate or PCC 2.5 (Phantom Camera Controller) Application for the case of a tube with open both ends and the data generated was analyzed with SciDAVis, Excel and OriginPro software.

3.2.2 Computing of required volume of fuel

To determine the volume of fuel required for each experiment at the different equivalence ratios, the total volume of the rig must first be determined. There are different techniques that could be used to determine the total volume of the rig such as doing numerical calculation and using the water test. The numerical calculation has been shown to have large errors because of the difficulties associated with determining the dimensions of some part of the rig while the water test has also been adjudged as inefficient because of the difficulty in cleaning the rig after the test and also the repeatability issues [3]. However, because of the shortcomings of these two methods, the method of injecting fluid (in this case gas) of a certain volume into the rig at vacuum was used. The method involves measuring the initial vacuum pressure, then after some time interval, the pressure before injecting the fluid was measured, pressure after injecting the liquid and the final pressure after some time interval was also recorded. Boyle's law for an ideal gas principle was applied to the four pressures taking into account the volume difference at points 2 and 3 as explained below.

Boyle's Law states that for a fixed mass of an ideal gas operating at a constant temperature, the pressure of the gas is inversely proportional to the volume. This understanding was applied to measure the rate of leakage in the rig and the volume. The measurement was achieved by first vacuuming the rig to approximately $\pm 0.9 \text{ bar}$, then the pressure readings

at four different times in interval of ± 20 secs was taken, at the same time injecting a fixed volume of air between points 2 and 3.

The assumptions made using this method were that:

1. The rig operates at a constant temperature throughout the test
2. Air has ideal gas characteristics
3. The mass of air is fixed

An example measurement taken and processed is as shown in Table 3.1 and plotted in Figure 3.5. The total volume of the rig was the difference between the final volume and the volume injected between points 2 and 3. This process was repeated for three times and the average of the three repeats was taken as the volume of the rig. The percentage leak in the rig was approximately 0.2 % of the total volume per minutes. This value is negligible as it does not pose any effect on the mixture composition including the experimental results.

Table 3.1: Rig Volume calculation

		v3-v2	50
S/N	Pressure (atm)	Time (secs)	Volume (mL)
1	0.959	0	1162.04
2	0.957	20	1164.47
3	0.918	35	1214.47
4	0.917	60	1215.66
Total Volume of Rig			1165.66

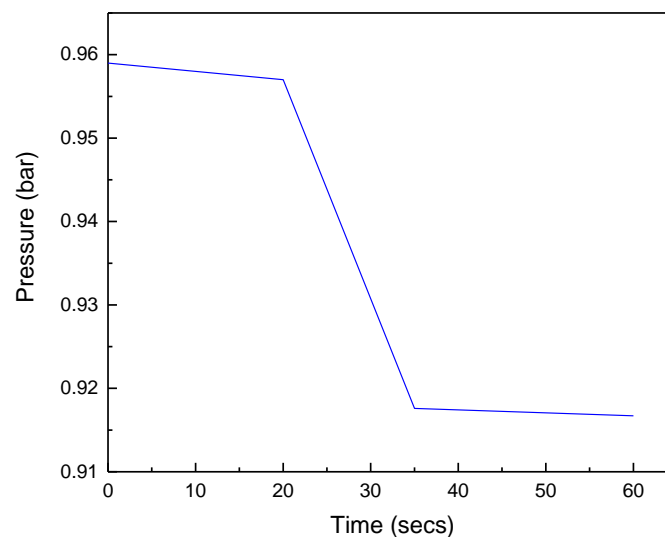


Figure 3.5: Pressure-Time graph for rig volume calculation

To calculate the volume of fuel required for the case of fuel-air mixture, there is one fuel and one oxidizer in the mixture. Equation 3.1 was used to determine the volume of fuel required for the experiment. For detailed derivation, see Appendix B

$$V_f = \left\{ \frac{V_T}{\left(\left(\frac{\bar{M}_f (A/F)_{stoic}}{\phi \bar{M}_a} \right) + 1 \right)} \right\} \quad (3.1)$$

Where V_T is the total volume of the rig, \bar{M}_a molecular weight of air, \bar{M}_f is the molecular weight of the fuel, ϕ is equivalence ratio, and $(A/F)_{stoic}$ is the stoichiometric air-fuel ratio. In the case of the fuel-air mixture with hydrogen addition, there are two fuels and one oxidizer in the mixture. While other researchers have used the mole fraction of hydrogen in the mixture and the overall equivalence ratio of the mixture as their governing parameters, the equation developed by Yu et al. [120] suggest that the core fuel and hydrogen have equal primacy to react with the mixture oxidizer. Since hydrogen is highly diffusive and reactive, therefore it is only rational to assume that hydrogen has a stronger propensity to react with oxygen. Thus, if the mole fraction of the core fuel, hydrogen and air are respectively as C_F , C_H and C_A , with $C_F + C_H + C_A = 1$, following the concept developed by Yu et al. [120], Equations 3.2 and 3.3 were used for determining the composition parameters for the mixture.

$$\phi_F = \frac{C_F / [C_A - (C_H / (C_H / C_A)_{st})]}{(C_F / C_A)_{st}} \quad (3.2)$$

$$RH = \frac{C_H + (C_H / (C_H / C_A)_{st})}{C_F + [C_A - (C_H / (C_H / C_A)_{st})]} \quad (3.3)$$

Where the subscript st represents the stoichiometric mixture mole concentration and RH is the amount of hydrogen added, which is the ratio of the total mole concentration of the hydrogen-air mixture to the total mole concentration of the core fuel-air mixture. The method assumes there is a complete oxidation of hydrogen but in practical term, complete oxidation of hydrogen cannot be justified, therefore this method should not be used for large amount of hydrogen addition [121]. The characteristic mixture properties of methane-air enriched with hydrogen in varying amount (RH) is shown in Table 3.2. The data table was generated using Gaseq [91] and Chemkin [122].

Table 3.2: Methane-Hydrogen-air mixture characteristics

RH	Mole Fraction (-)				Density (kg/m ³)		Speed of Sound (m/s)		Density Ratio	Speed Ratio	Adia. Temp. (K)	Burning Velocity (m/s)	Hydrogen Percentage (%)
	CH ₄	H ₂	O ₂	N ₂	Reactants	Products	Reactants	Products					
0	0.1119	0.0000	0.1865	0.7016	1.1138	0.1506	355.10	919.20	7.39	0.39	2136.80	0.3200	0.00
0.1	0.1017	0.0268	0.1830	0.6885	1.0899	0.1479	359.10	927.40	7.37	0.39	2165.20	0.3887	20.90
0.2	0.0933	0.0491	0.1801	0.6775	1.0699	0.1456	362.60	934.30	7.35	0.39	2188.70	0.4543	34.58
0.3	0.0861	0.0680	0.1776	0.6683	1.0531	0.1436	365.60	940.20	7.33	0.39	2208.60	0.5365	44.22
0.4	0.0799	0.0842	0.1755	0.6603	1.0386	0.1420	368.20	945.30	7.31	0.39	2225.40	0.599	51.39
0.5	0.0746	0.0983	0.1737	0.6534	1.0261	0.1406	370.60	949.70	7.30	0.39	2239.80	0.6601	56.92
0.6	0.0699	0.1105	0.1721	0.6474	1.0151	0.1395	372.60	953.60	7.28	0.39	2252.10	0.7198	61.33
0.7	0.0658	0.1214	0.1707	0.6421	1.0054	0.1384	374.50	957.00	7.26	0.39	2262.90	0.7783	64.91
0.8	0.0622	0.1310	0.1694	0.6374	0.9986	0.1375	376.20	960.00	7.26	0.39	2272.20	0.8352	67.89

3.3 Python code and PCC Application

The images of the propagating flames filmed were processed using a code written in Python programming language and the PCC software. For the images processed using the Python code, the recordings in form of a video were first cropped using VirtualDub software, leaving the only visible part as the flame propagates in the tube. The same software was then used to convert cropped video into images. These images were then processed using the python code. The code is only valid for the case of a tube with orifice plate at both ends where it is possible to calculate the surface area (See Appendix A).

The PCC software comes with the Phantom V210 high-speed digital camera for processing the videos. The PCC software was used to track the flame as it propagates from one end to the other end. The auto-tracking function of the PCC software was sometimes used where possible to track the flame propagation, applying a tracking sensitivity of greater than or equal 0.5. The result is the flame front position at a sampling rate of 1000fps, 1500 fps or 3000 fps depending on the sampling rate for the experiment at 1280 x 128 pixels resolution. The data generated was then saved as an Excel file for further processing using Excel, SciDavis, Origin and MATLAB.

3.3.1 Pressure data and high-speed image synchronisation

There was a need to synchronise the flame front position data from the high-speed images and the pressure data of the propagating flames. However, in practice, errors can be generated in determining the correct beginning or end point of these data since the mixture was manually ignited.

To resolve this difficulty of synchronising the two data, a post trigger was used to stop the camera from saving recorded data which in turn triggers the national instrument device to stop saving data. To successfully get the exact point of triggering since the instrument lags, a five volts circuit was connected to the trigger such that when the trigger is pressed, the five volts is read simultaneously with the pressure and image data and when the trigger is released, the 5 volts drops to zero. Finally, the data was extrapolated to find the start point of the data as shown in the 9 steps synchronising procedure using both the PCC software and Excel as presented in Appendix D.

3.4 Flame Oscillation Signal Processing and Analysis

In this research, there is a continuous measurement of the dynamic pressure signal generated by the propagating flame in the tube. After that, the signal recorded as voltage was multiplied by a conversion factor generated by the charged amplifier to obtain a physical value (Pascal) in the domain.

Finally, a Fast Fourier Transform (FFT) was performed on the data using Origin software. Hence, the resulting pressure spectrum is an average of the individual and independent spectra. This procedure has been previously applied to purely sinusoidal samples of known frequency and amplitude.

3.4.1 SciDAVis and Origin Software

SciDAVis is a free software for data analysis, which meets the quality of plotting for publication. It combines a low learning curve and an instinctive, easy-to-use graphical user interface with great features such as extensibility and scriptability. SciDAVis runs on Windows, MacOS and GNU/Linux; possibly also on other platforms like *BSD. Origin is a graphing and data analysis software with an easy-to-use user interface for engineers and scientist in academia, commercial industries and government laboratories globally.

SciDAVis and Origin were used for the frequency analysis and plotting the graphs in this work. They were applied to separate the oscillating part of the flame front position from the original flame front position and also used to determine the flame amplitude and the flame underlying speed. The flame area approximated by the number illuminated (white/grey) pixels was determined using the MATLAB code shown in Appendix A. The steps necessary to determine these parameters stated above are as shown below.

1. Plot the original data generated from your experiment.
2. Linearized the data or draw a linear fit to the data
3. With the equation of the linear fit, generate the linear plot/data.
4. Subtract the linear data from the original data
5. Do a low pass FFT filtering to the result in 4 above
6. Generate data for the low pass FFT filtering
7. Subtract 6 from 4
8. Plot 7 against time to generate the amplitude plot.

9. Differentiate the plot from 5 above
10. Generate data for the plot in 9 above
11. Add the slope/gradient of the linear fit in 2 to the data in 10 above
12. Plot your result from 11 against time to generate the speed graph/plot
13. To generate the image size plot, use the python code
14. First convert the video file to AVI file using the PCC software (setting the frame rate (fps) to 1), then use VirtualDub or PCC software to convert the AVI file to images (setting; filename to six digit letter, filename suffix to .bmp (i.e Windows BMP file), and minimum number of digit to 2).
15. Finally, use the Matlab code below to generate the flame pixels.

Two typical examples were solved as shown in Appendix E to show that this method works for determining the gradient of the line.

3.4.2 Data Filtering

In applying a filter to the data, three methods of filtering was applied to the data. The three methods are: (1) the FFT low pass filtering that works with the frequency of the data thereby you apply filtering with a frequency lesser than or equal the characteristic frequency of the data, (2) the Savitzky-Golay smoothing for polynomial; it works with the data points in a maximum range of points to the right and left of the number of data point minus one and (3) the smoothing FFT filtering which also works with data points ranging from zero to the total number of data points minus one that is correspondingly converted to frequency values. For the analysis in the current work, the FFT low pass filtering was used first because it works with the frequency of the data and secondly it gives the best results that minimise the loss of vital information about the data. The three methods used for a particular data analysis is shown in Figure 3.6. The Savitzky-Golay smoothing for polynomial was also used for smothering the final result of the analysis.

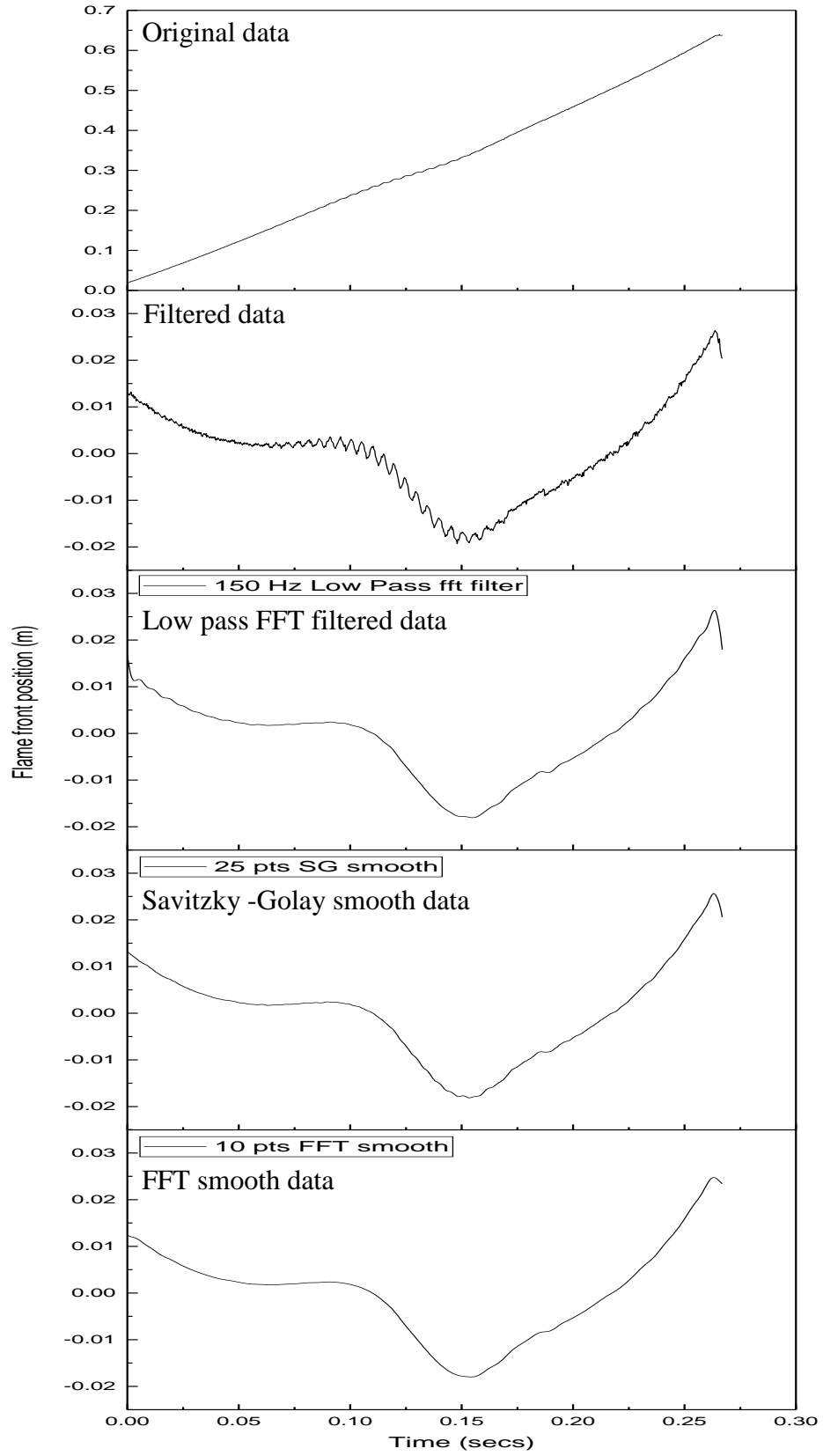


Figure 3.6: Filtering Methods

3.5 Laminar Flame Speed

The laminar burning velocity was determined using two different methods for the different cases studied. For the case where there were orifice plates at both ends, the method developed by Coward and Hartwell [18] that was later revised by Coward and Payman [115] to incorporate the gas velocity term was used. A CHEMKIN PREMIX GRI 3.0 mechanism [122] for steady laminar one-dimensional premixed flames was used to determine the laminar burning velocity for comparison. The data that was used for the implementation was generated from a chemical equilibrium program called GASEQ created by Morley [91]. Another analysis such as separating the oscillation part and determining the frequency of oscillation of the flame was done using SciDAVis and Origin software.

Coward and Payman correlated the laminar burning velocity S_l to the fundamental flame speed by Equation (3.4).

$$S_l = (S_f - S_{ug}) \left(\frac{\pi R^2}{A_f} \right) \quad (3.4)$$

The flame speed S_f was calculated by finding the flame front coordinates of each frame along the tube using a program originally developed in PYTHON programming language by Dr. Robert Woolley and now modified to include determining the flame speed, surface area and the laminar burning velocity of the flame (for details, see Appendix A).

The unburned gas velocity S_{ug} is known to affect the propagation speed of the flame in a tube where both ends are partially or completely closed. The unburned gas velocity for the rig used in this study was calculated by Mossa [3], and governed by Equation (3.5)

$$S_{ug} = 0.4107S_f - 0.0784 \quad (3.5)$$

For the experiments where both ends of the tube were opened without the orifice plate, there was no significant effect of the unburnt gas velocity because they escape.

3.5.1 Flame Surface Area

Accurately computing the surface area of a propagating flame in a tube has been a bone of contention for many researchers. This has been the major cause of error in determining the laminar burning velocity of fuels using the tube method until the introduction of the orifice

plate that gives the flame surface an approximate shape. Guenoche and Guoy [123] assumed the shape to be ellipsoidal but later conclude that the correct determination of the flame surface area was not possible with a true ellipsoid flame, even with three projections. The flame surface area has been determined to date by approximating the flame to known geometrical shapes such as spheroid and ellipsoid [17, 18, 21, 22, 124]. In this study, the methodology of Gerstein et al. [22] and Mossa [3] was adopted to calculate the surface area of the flame. The flame surface areas for the flames studied using the methodology of Gerstein et al. [22] are shown in Appendix C.

According to Mossa [3], the surface area was determined by assuming flame images were fragmented into many little cones with their tops chopped off as shown in Figure 3.7. These images were assumed to be a frustum, therefore the surface area is computed using equation for the surface area of a frustum as shown in Equation 3.6

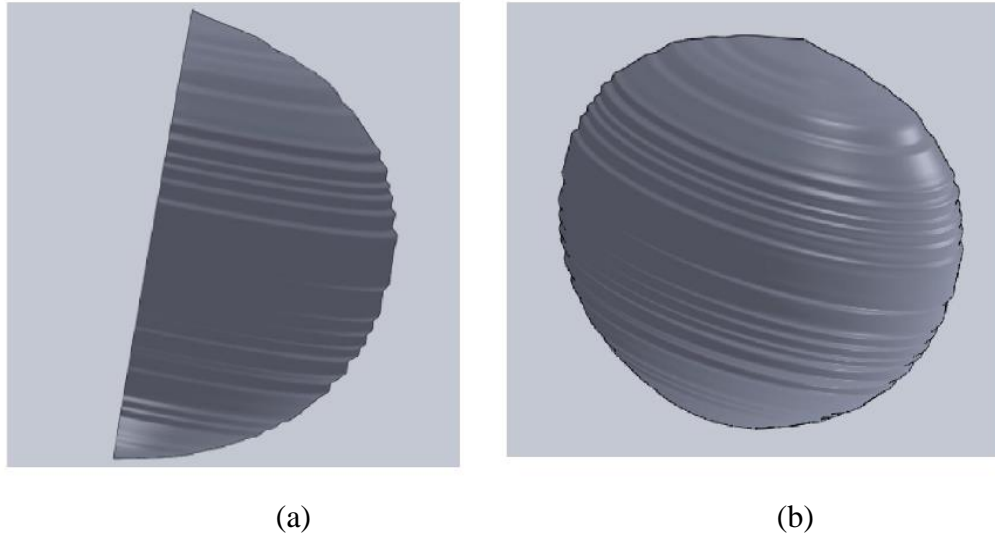


Figure 3.7: Flame Schematics (a) side view (b) front view (Mossa [3])

$$A_f = \pi(R_1 + R_2)^2 \sqrt{(R_1 - R_2)^2 + h^2} \quad (3.6)$$

Where, R_1 and R_2 are the top and bottom radius respectively and h is the height difference between the top and the bottom circles, as represented in the Figure 3.8. Frustum of right circular cone

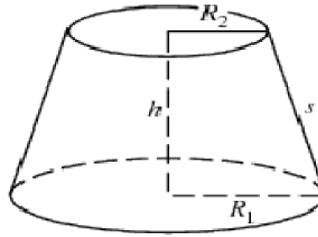


Figure 3.8: Frustum of a right circular cone

3.5.2 Rotational speed of the flame

The radius of the flame is determined from the curved flame using the necessary calibration data as represented in Figure 3.9.

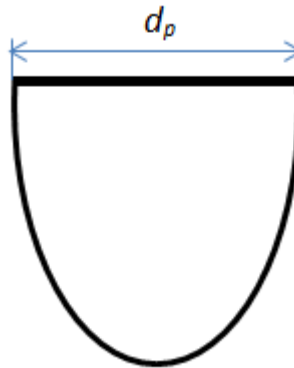


Figure 3.9: schematics of a curved flame

Distance in pixel = d_p pixels

Distance in meters = d_p meters

Therefore, Diameter of flame = d meters and

Radius of flame = $r = \frac{d}{2}$ meters

To determine the frequency of rotation of the flame, first, determine the period for one rotation from Figure 3.9 and then calculate the time taken for the flame to rotate from a particular point and back to that same point. The calculated time represents the period of rotation of the flame.

For the downward propagating flame,

The period of rotation = T secs

Frequency of rotational flame = $f = \frac{1}{T}$ Hz

For an object rotating either clockwise or anticlockwise about its orbit, one revolution is equal to 2π radians. Hence,

Angular frequency or angular speed (ω) = $2\pi f$

The tangential speed (v) = ωr

3.6 The two colour method technique

In this study, the fibre temperature was calculated by deriving the ratio of the colour-banded images that were recorded by the high-speed colour digital camera, instead of utilising the narrow bandpass filtering and beam-splitting approach in order to avoid the complex configuration and optical attenuation. Each image recorded by the RGB camera was separated into the three different channels conforming to the red, green and blue sub-images in the visible wavelength band. For this research, the R and G channel in the two colour technique were used in determining the fibre temperature because the radiation detected in the B channel was much weaker than that detected in the R and G channels (Equation. 3.7).

$$T_f = \frac{C_2 \left(\frac{1}{\lambda_G} - \frac{1}{\lambda_R} \right)}{\ln \frac{G(\lambda_R, T)}{G(\lambda_G, T)} + \ln \frac{S_{\lambda_G}}{S_{\lambda_R}} + \ln \left(\frac{\lambda_R}{\lambda_G} \right)^5} \quad (3.7)$$

3.6.1 Thermal Behaviour of Filaments

The actual local gas temperature and the fibre temperature are different and are related to the steady-state energy equation (Equation 3.8). It is a typical heat transfer problem as the fibre is heated by its surrounding hot gas and at the same time cooled by radiation loss. For the case of the thin filament, the conduction gain or loss axially is negligible since the ratio of the circumferential to cross-sectional area is large; meaning the heat transfer rate by convection and radiation is higher than the heat transfer by conduction in the axial direction. The hot gas temperature can be obtained from Equation (3.8).

$$T_g - T_f = \frac{\varepsilon \sigma (T_f^4 - T_a^4)}{h} \quad (3.8)$$

Where the emissivity of the silicon carbide fibre ε is 0.88, σ is the Stefan–Boltzmann constant ($5.6704 \times 10^{-8} Wm^{-2}K^{-4}$), T_a is the ambient temperature, T_f is the temperature of the fibre and h is the heat transfer coefficient for the tube.

It is obvious that the term on the left-hand side of the equation represents the difference between the hot gas temperature and the fibre temperature. To determine this difference, the heat transfer coefficient is required. This coefficient can be determined using the equations (3.9) to (3.11) below.

$$Re = \frac{\rho V D}{\mu} \quad (3.9)$$

$$Nu = (0.35 + 0.56 Re^{0.52}) Pr^{0.3} \quad (3.10)$$

$$h = \frac{Nu * k}{D_f} \quad (3.11)$$

Where the heat transfer coefficient comes from a Nusselt number correction for forced convection for a cylinder, this number is valid for $10^{-1} < Re < 10^5$ [125]. The fluid properties must be determined by the hot gas and ambient temperatures average, but because the temperature of the hot gas is unknown, to correct the temperature, an iterative method was applied.

The procedure applied to estimate the heat loss is outlined below. Firstly, the fibre temperature computed from Equation 3.7 was assumed to be the gas temperature. The characteristic properties of the major species concentration were calculated by the use of an adiabatic equilibrium chemical reaction at their respective equivalence ratio, from where the characteristic properties based on the transport properties can be found and used to calculate the Reynolds and the Nusselt number using Equations 3.9 and 3.10 respectively. Since the average heat transfer coefficient is the essential quantity, the Reynolds number was calculated using the average velocity of the flame going through the fibre. Once the Reynolds Number was established, the average heat transfer rate can be calculated and used to compute the corrected gas temperature, T_g , in Equation 3.7. The whole process was repeated two times.

3.7 Measurements, Processing and Data Analysing Errors

The Experiment, data processing and analysing were carried out with all precautionary measures adhere to minimise errors. The likely sources of errors and the precautionary measures applied to minimise these errors are as itemised in Table 3.3.

Table 3.3: Measurements, Processing and Data Analysing Errors

S/N	Error	Source	Precaution
1	Systematic Error	<ol style="list-style-type: none"> 1. Setting up of the camera 2. Measuring the length of the tube being recorded by the camera (calibration) 3. Choosing the best filtering method to apply to the data not to lose vital information about the flame. 	<ol style="list-style-type: none"> 1. Use of the spirit levels on the tripod stand, the grid lines on the screen of the camera and the top/bottom of the tube as a baseline. 2. The calibration was usually carried after few experimental runs and care usually taken to make sure the camera does not move in the cause of the experiment. 3. Three different methods were compared and the best one with minimal loss of data information was chosen
2	Random Error	<ol style="list-style-type: none"> 1. Gas leakage in the gas bags and the temporary joints of the rig. 2. Gas diffusion from gasbags. 	<ol style="list-style-type: none"> 1. The gasbags use a self-sealed septum which is intermittently replaced and the bags usually test for leakages before any experiment. Also before any experiment, the rig was always tested for leakage and if any, it was fixed. 2. Gasbags were usually emptied and a fresh gas filled in after being left for a long time say over 6 hours for a day or if left overnight.

		<ol style="list-style-type: none">3. Use of one storage bag/ syringe for more than one gas.4. Ignition source	<ol style="list-style-type: none">3. The storage bags/syringes were labelled for each of the gases that were for the research.4. Proper care was taken while igniting the flame, though this error could not be avoided as pilot flame with varying energy discharge at every ignition was used.
--	--	--	---

CHAPTER FOUR

FLAMES IN OPEN ENDED TUBE

4.1 Introduction

This chapter presents results and discussions from the experimental work conducted in an open-ended tube with and without orifice plates at both ends. Propane and methane flames were tested propagating both horizontally and vertically downwards. The aim was to study the effect of gravity, flammability limits and laminar burning speed in the two different configurations. Firstly the flame shapes are presented, followed by the flame position with respect to time, then the flame speed versus equivalence ratio flammable limits. Previous research has shown that with orifice plates at both ends of the tube produced relatively steady flame propagation in the entire length of the tube over a large range of equivalence ratio. Mossa [3] had reported the best orifice plate size for the rig was 5mm after doing a comparison using different orifice plates.

For the downwardly propagating flames, the images are presented horizontally with images presented from left to the right direction, represents flame propagation from top to bottom. Also presented results of flame propagation in the tube without orifice plate at both ends in the horizontal position, showing the effect of the position of a pressure sensor on the pressure signal produce followed by the flame shape and finally, the flame temperature analysis was presented.

4.2 Horizontal propagating flame

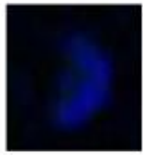
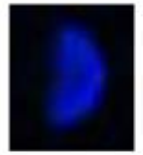
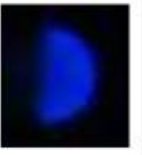
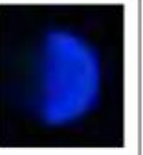
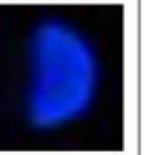
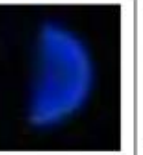
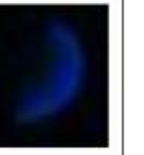
In this section, results for horizontally propagating methane and propane-air flame with orifice plates of 5mm diameter placed at both ends of the tube are presented.

4.2.1 Horizontal propagating methane/air mixture

Table 4.1 shows images of the propagating flame approximately halfway down the tube for the different equivalence ratios. These images were captured using the coloured Casio EX-FH100 high-speed digital camera at a framing rate of 420 fps. The flame, shaped like a hemisphere, propagated steadily down the tube at all equivalence ratios. Though as the flame become richer, the shape tended to slightly tip towards the unburned mixture. The tipping of the flame has been attributed to the influence of gravity on the hot gases causing the flame to tilt forward at the upper part of the tube [126]. The hemispherical shape is the

result of the effect of viscous force near the wall of the tube and heat transfer from the flame to the tube.

Table 4.1: Horizontal propagating methane flame shape at different equivalence ratio

Equivalence ratio						
0.8	0.9	1.0	1.1	1.2	1.3	1.4
						

Generally, the overall shape of the flame is highly influenced by the no-slip condition at the walls and the heat transfer from the reaction zone to the wall. Three repeat experiments were carried out for each equivalence ratio to check for the repeatability of the experiment and the representative result of the flame position against time for the range of equivalence ratio possible are shown in Figure 4.1.

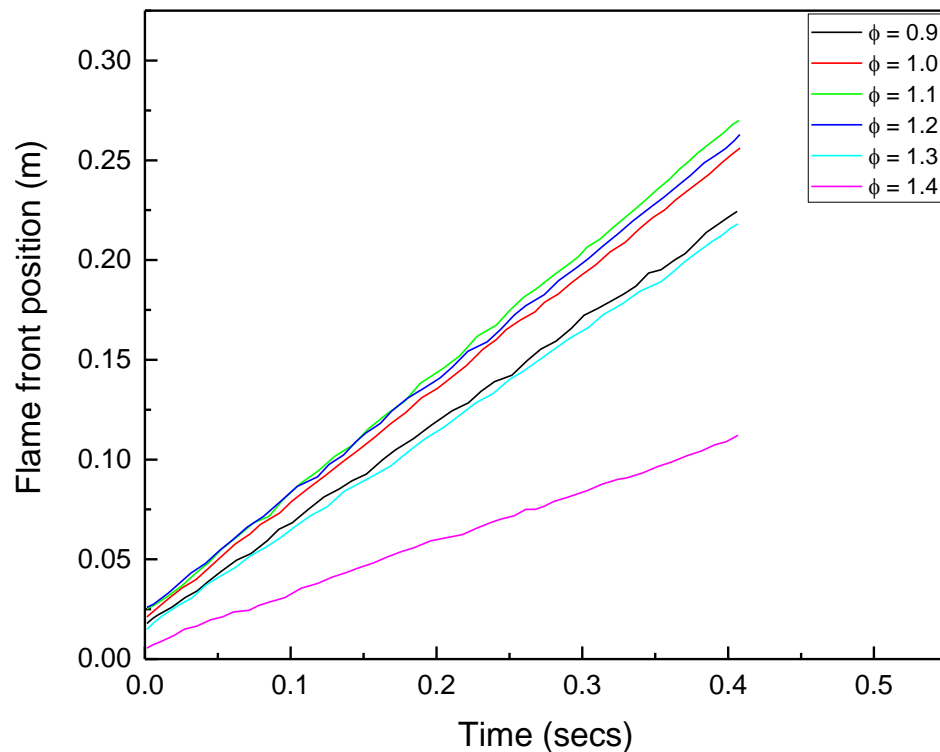


Figure 4.1: Flame front position against time for horizontally propagating methane flame. At lean and rich equivalence ratios, self-induced turbulence of the flame was observed to set in, making it difficult to accurately process the flame front. Similar observations were

made by Hamins et al. [127]; where they reported the presence of self-induced turbulence in the flame as a consequence of hydrodynamic instability.

The speed of the flame was calculated by taking the gradients of the position-time plot and the burning speed was also computed using equation (3.4) and the method described in 3.5, and the results are shown in Figure 4.2. The flame and burning speed peaked at 1.1 equivalence ratio with a flame speed of 0.76 m/s and burning speed was 0.58 m/s.

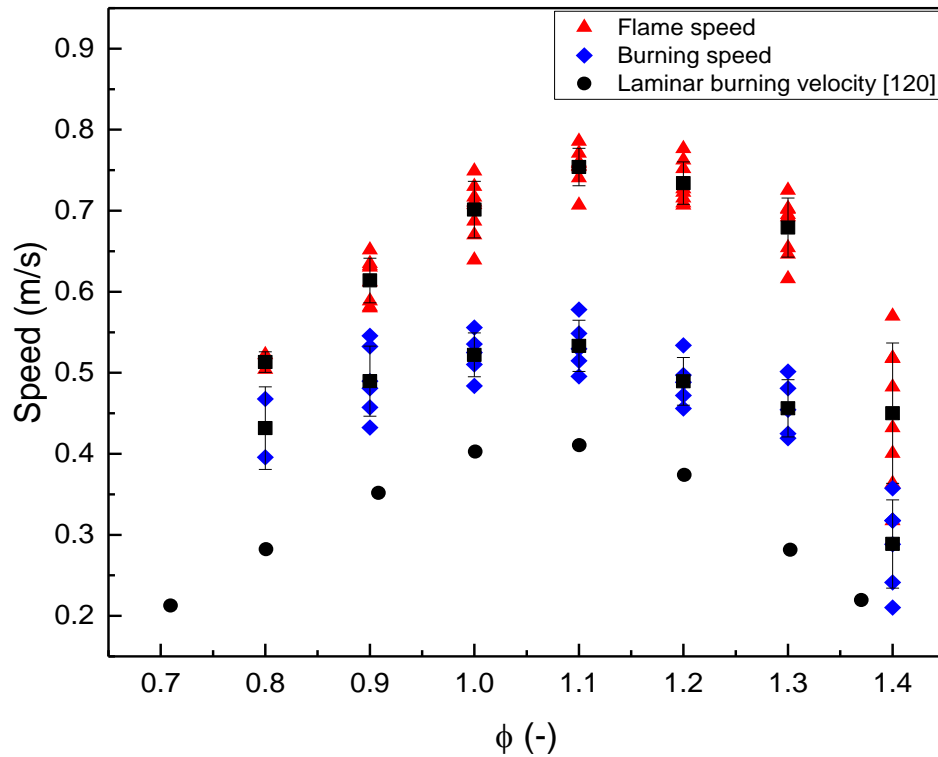


Figure 4.2: Speed against ϕ for horizontally propagating methane flame

The values of the burning speed are higher than the values of the laminar burning velocity obtained from spherically expanding flames of Yu et al. [120]. The main error was the calculation of the flame surface area which if not correctly calculated, influences the result of the laminar burning speed. Another source was also the wall quenching effect which retards the flame movement and because of the variability in the mixture formation as slight changes in the mixture formation can change the equivalence ratio and in turn changes the flame speed. A solution to this would be to use a complete premix mixture (i.e a premixing chamber).

4.2.2 Horizontal propagating propane/air mixture

Images from a horizontal propagating propane/air flame are shown in Table 4.2. The flame propagated with a hemispherical shape for all equivalence ratios within the flammable limits as was the case for methane flames. Figure 4.3 shows the flame front position as a function of time at each equivalence ratio. The flame speed was determined by finding the gradients of each line; this was plotted against the equivalence ratio (ϕ) as shown in Figure 4.4. There was a considerable variation in these data, though the flame speed tended to peak between $\phi = 1.1$ and $\phi = 1.3$ as against $\phi = 1.1$ for methane-air flame.

Table 4.2: Horizontal propagating propane flame shape at different equivalence ratio

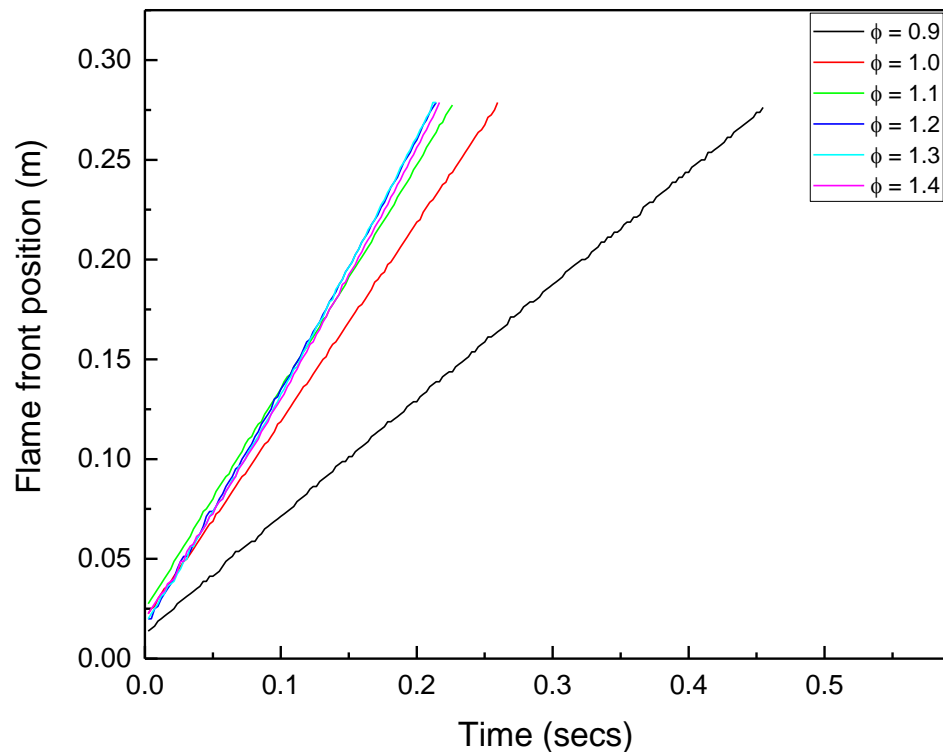
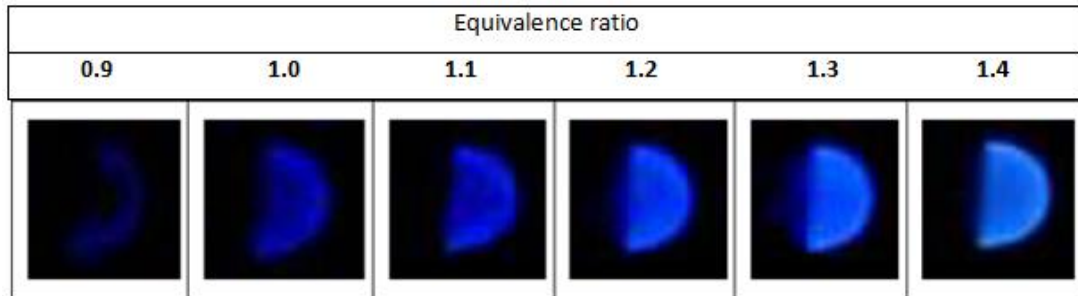


Figure 4.3: Flame front position against time for horizontally propagating propane flame

The laminar burning speed was also plotted against the equivalence ratio in Figure 4.4. The burning speed appears to be uniform from $\phi = 1$ to $\phi = 1.4$. This behaviour is very different from that of the measured laminar burning velocity also shown in Figure 4.4. This would seem to indicate that the flame stretch or the thermo diffusion effects are more significant in these flames.

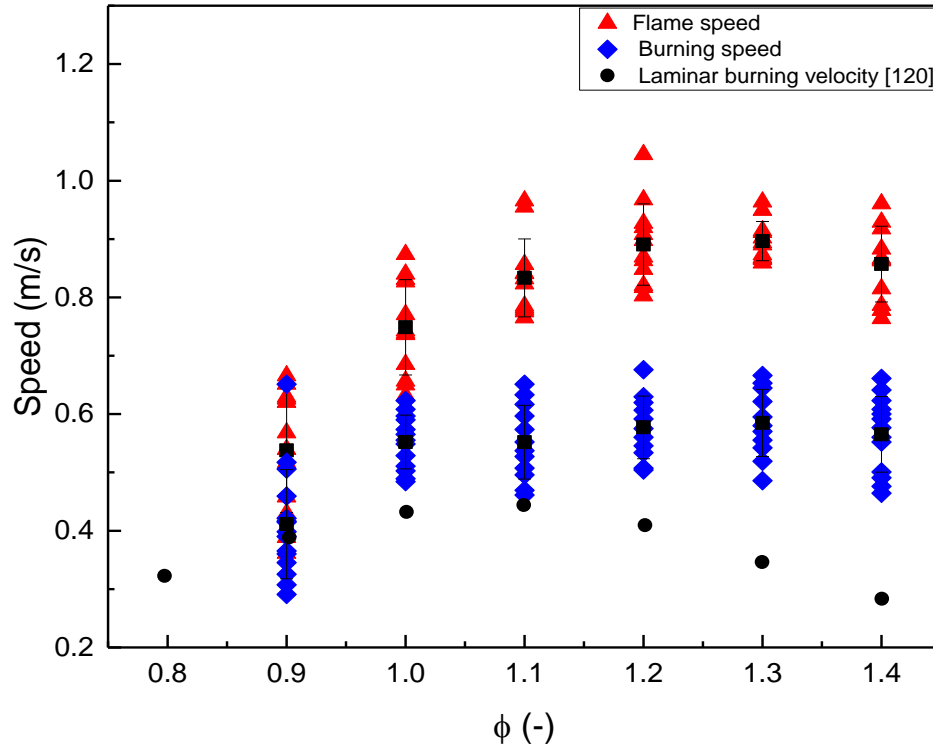


Figure 4.4: Speed against ϕ for horizontally propagating propane flame

4.3 Vertically downward propagating flame

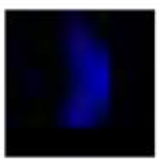
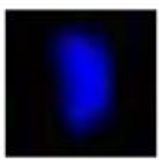
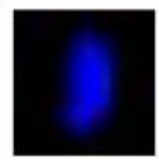
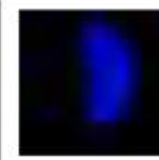
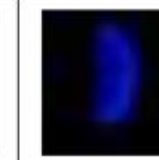
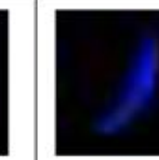
In this section, results and discussions of vertically downward propagating methane and propane-air mixtures are presented. Orifice plate of 5mm diameter was placed at both ends of the tube. In the downward propagation, the effect of gravity on the flame is evident.

4.3.1 Downward Propagating methane/air mixture

The flame images of downward propagating methane/air flame are shown in Table 4.3. There was a continuous change in the shape of the flame, though mostly hemispherical, at the different equivalent ratio within the flammable region. The flame front position at different equivalence ratio is plotted against time shown in Figure 4.5. The flame speed and

the burning speed are also plotted as functions of the equivalence ratios as shown in Figure 4.6. The flame speed peaked at $\phi = 1.1$ and decreased at richer and leaner ϕ up to the flammable limit, though with a very strong variation at $\phi = 1.5$, hence was not processed.

Table 4.3: Downward propagating methane flame shape at different equivalence ratio

Equivalence ratio					
0.9	1.0	1.1	1.2	1.3	1.4
					

There was strong variability in the burning speed calculated for $1.0 \geq \phi \geq 1.5$, which are higher than the flame speed at some equivalence ratios; this can be attributed to the uncertainty in the mixture composition as a slight change could change the equivalence ratio, hence, the flame speed. The flame speed peaked at $\phi = 1.1$ with a speed of 0.63 m/s, however the burning speed, peaked about $\phi = 1.0$ at a speed of 0.64 m/s.

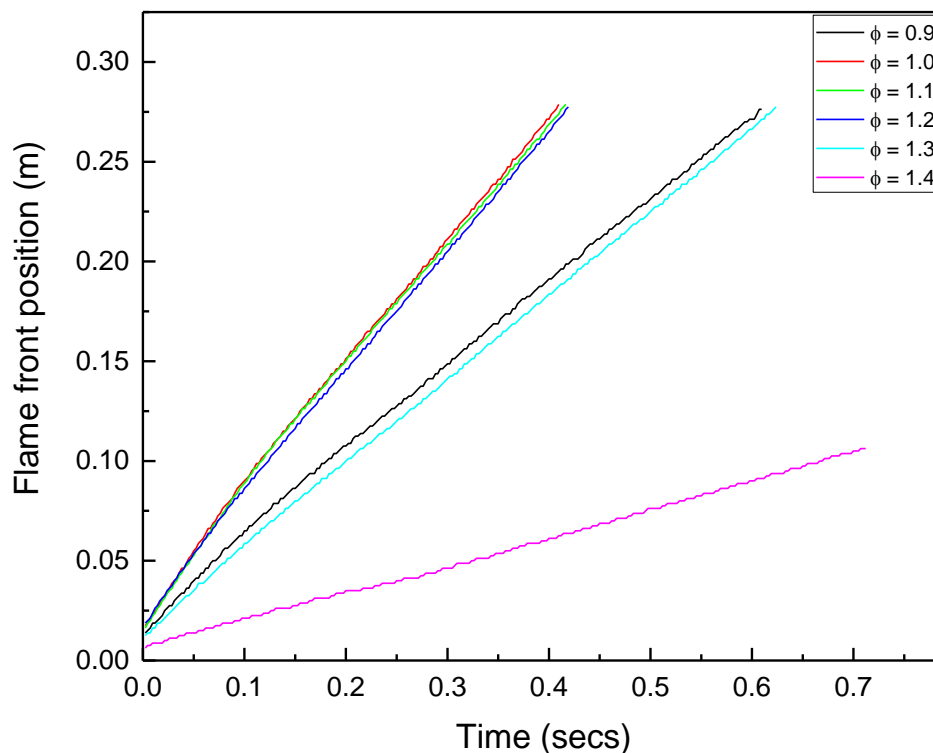


Figure 4.5: Flame front position against time for downwardly propagating methane flame

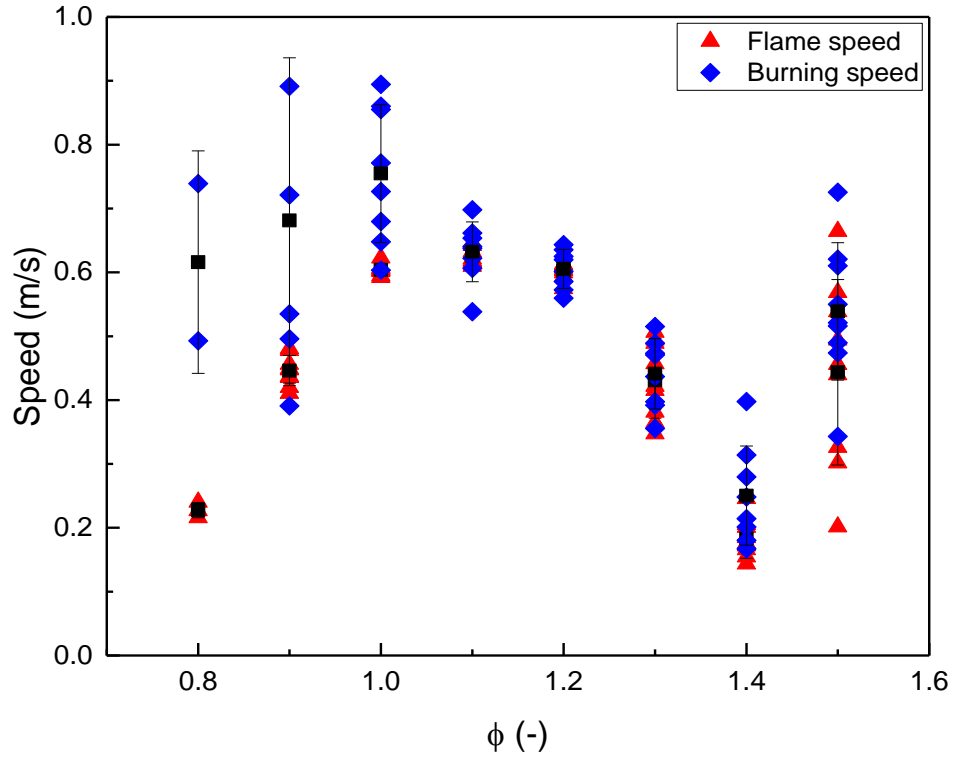


Figure 4.6: Speed versus ϕ for downwardly propagating methane flame

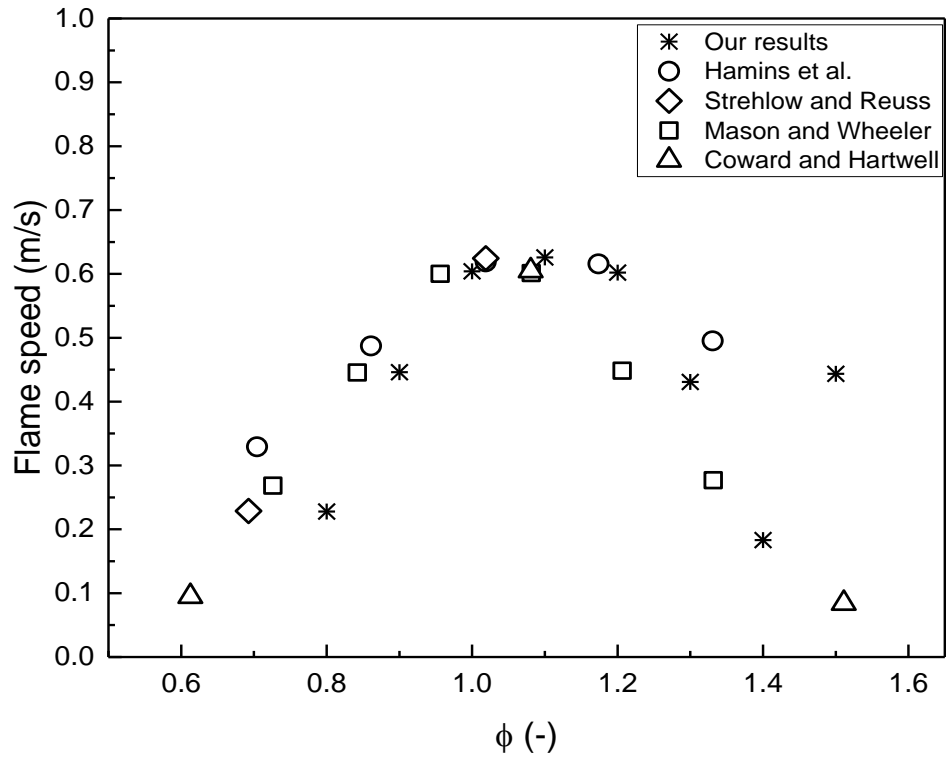


Figure 4.7: Comparison of speed versus ϕ for downwardly propagating methane flame


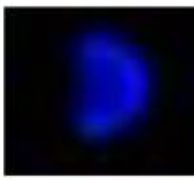
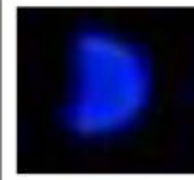
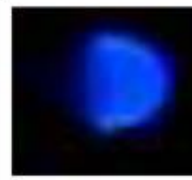





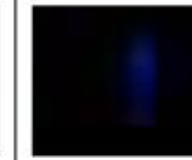
Comparing the flame speed results for few equivalence ratios with results from Coward and Hartwell [17], Hamins et al. [127], and Strehlow and Reuss [128], there was a general satisfactory agreement as shown in Figure 4.7. It is worthy to note that their results are in tubes of larger diameter compared to the tube used for the current research.

4.3.2 Downward propagating propane/air mixture

Pictures of the shape of a propane-air flame, propagating downwards in the tube, with 5mm orifice plates at both ends, are shown in Table 4.4. The flames of 0.8 to 1.5 equivalence ratios propagated steadily with a hemispherical shape, however, for $\phi > 1.5$, the flames initially propagated steadily with hemispherical shape until approximately 0.4 m from the point of ignition, before they became corrugated. The flame front position against time at the different equivalence ratio within the flammable region is shown in Figure 4.8. The flame speed and the burning speed are also plotted as functions of the equivalence ratios in Figure 4.9. The flame speed peaked at $\phi = 1.1$.

The burning speed data is scattered with the majority of the data within the error band and peaks at $\phi = 1.2$. The flame speed also have majority of its data within the error band and has a peak value at $\phi = 1.1$, of 0.84m/s whereas the maximum value of the burning speed is at $\phi = 1.0$ with a value of 0.65m/s.

Table 4.4: Downward propagating propane flame shape at different equivalence ratio

Equivalence ratio				
0.8	0.9	1.0	1.1	1.2
				
Equivalence ratio				
1.3	1.4	1.5	1.6	1.7
				

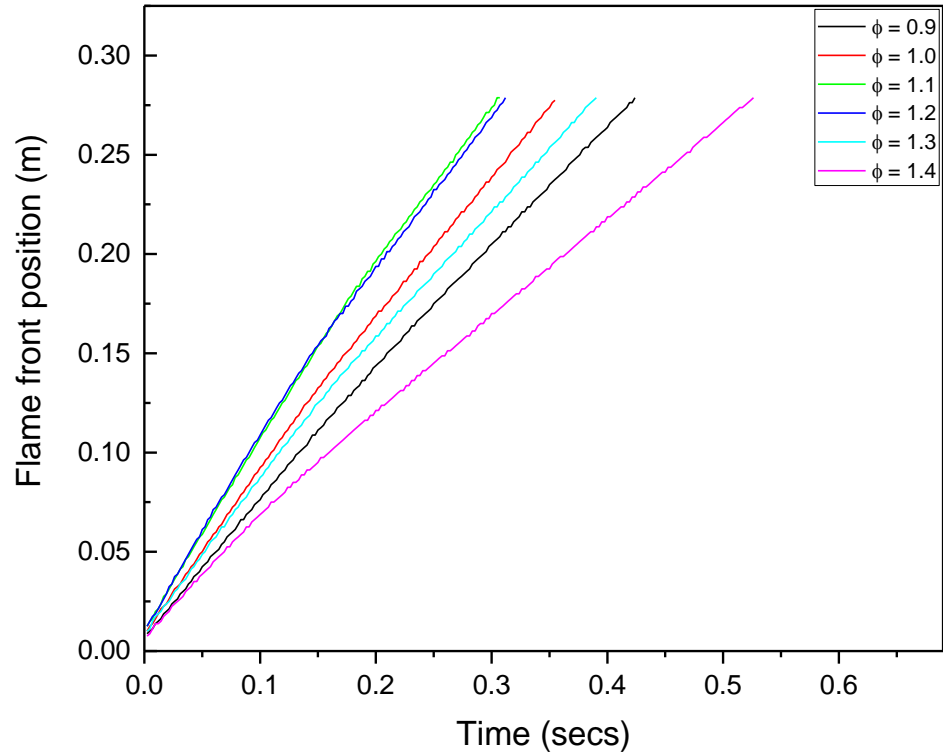


Figure 4.8: Flame front position against time of downwardly propagating propane flame

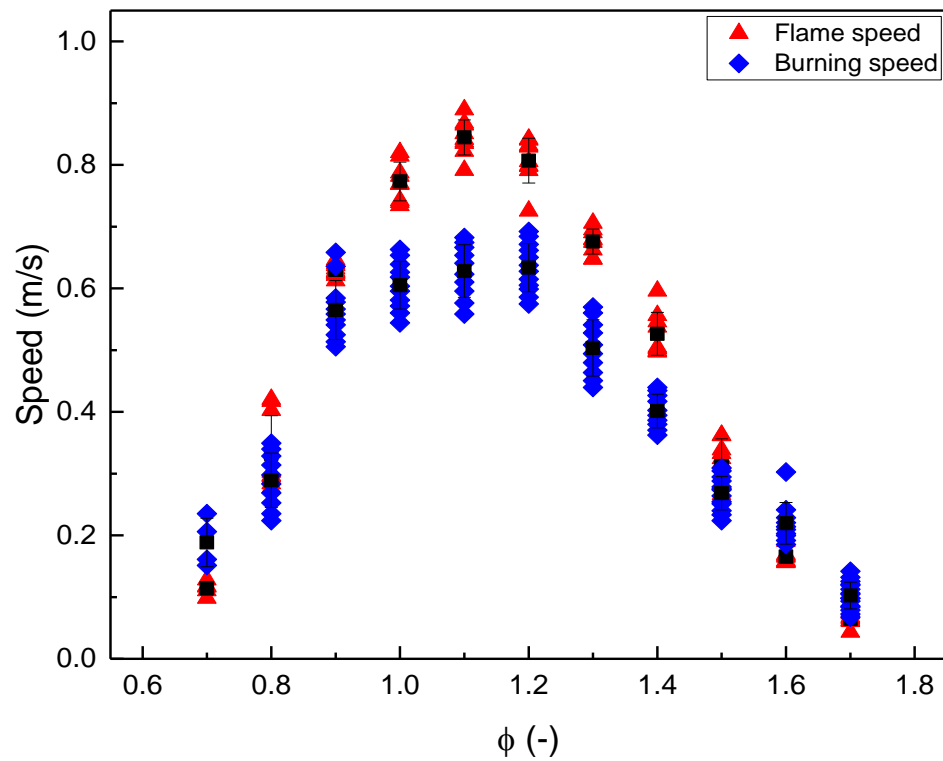


Figure 4.9: Speed versus ϕ of downwardly propagating propane flame

4.4 Flame comparison, flammability limits and gravity effect

The compared flame speeds of methane/air and propane/air flame in the horizontal and vertically downward propagation are shown in Figures 4.10 and 4.11. Though from literature, the maximum laminar burning velocity for both methane and propane lies around $\phi = 1.0$ and $\phi = 1.1$, but our result shows a shift in the peak flame speed into the rich region for horizontally propagating propane/air flame. The reason for the shift in the peak of the propane/air can be attributed to the variability in the mixture composition which changes the equivalence ratio, hence, the flame speed. For the downwardly propagating flame, the flame speed of methane/air and propane/air peaked at $\phi = 1.1$, decreasing on the right and left of the peak forming a bell shape. The flames also tend to change shape and extinguished when propagating in the downward configuration at some equivalence ratio, especially at the rich conditions of $\phi \geq 1.4$.

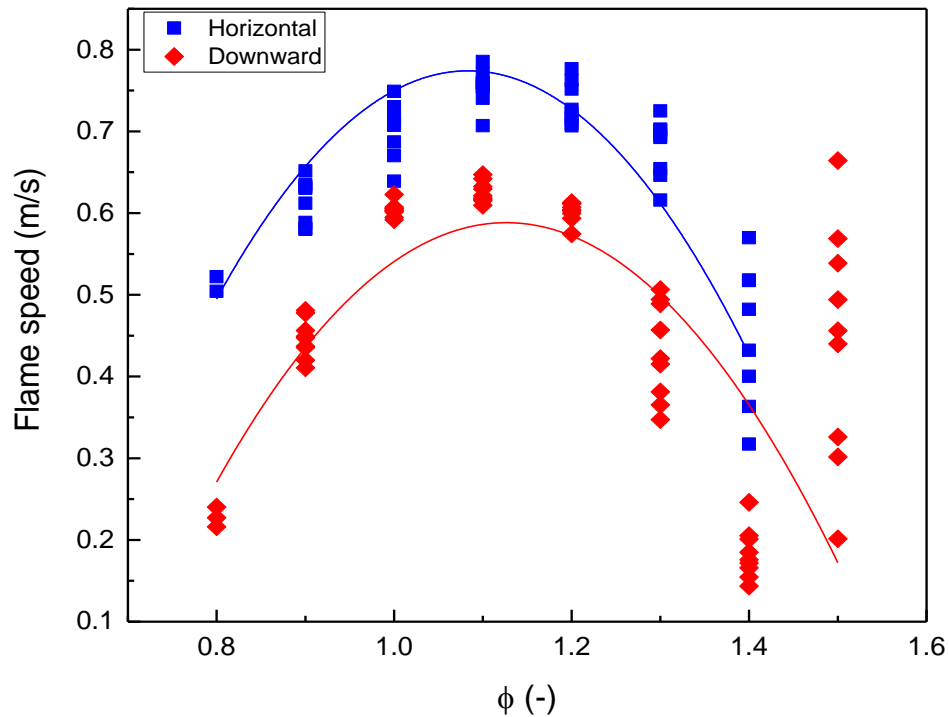


Figure 4.10: Comparison of horizontal and downward propagating flame for methane

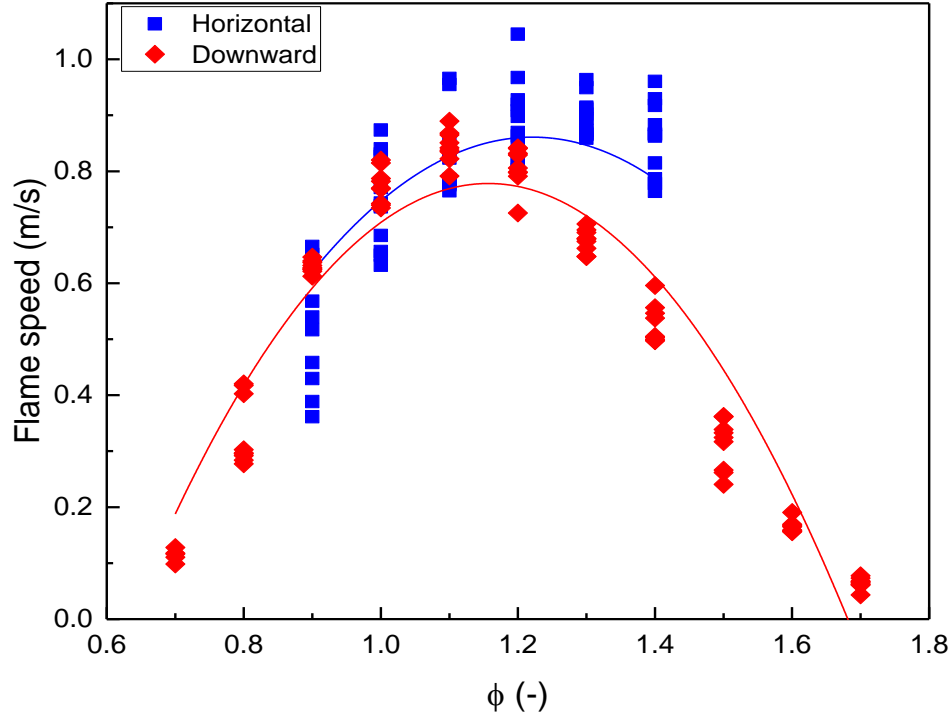


Figure 4.11: Comparison of horizontal and downward propagating flame for propane

For methane/air flame, flame extinguishing was observed at $\phi \leq 0.9$ and $\phi \geq 1.3$ and for propane/air flame, the flame extinguishing was observed at $\phi \leq 0.9$ and $\phi \geq 1.5$. therefore, the flame speed of the flames at $\phi \leq 0.9$ and $\phi \geq 1.4$ where processed using only the visible flames before it extinguish. For the downward propagating propane/air flame, the presence of cellular flames with rotating characteristics was first observe at $\phi \leq 1.7$.

The flame speed at each equivalence ratio for both fuel tested, tended to be lower for the downwardly propagating flame when compared to the horizontally propagating flame because of the influence of gravity which reduces the surface area of the flame, hence reducing the speed of the flame. This result is in agreement with Strehlow et al. [55], as they showed that flames propagating in the downward direction give lower flame speed when compared to flames propagating with zero gravity and flames propagating in the upward direction.

The effect of gravity was only observed as the flames get leaner and richer for the vertically downwardly propagating flames on both methane-air and propane-air. The effect resulted in a decrease in the propagating flame speed for the vertically downwardly propagating flames

compared to the horizontally propagating flames for both fuels tested. There was also a change in the shape of the flame which can be attributed to the gravity effect.

From the flammability limits results of the current experiment, as expected, it was observed that the flammability limits increased in the lean regime as well as the rich regime for both fuels when propagating downwards in the vertical configuration. The flammability range for methane/air and propane/air for the two configurations studied are shown in Table 4.5 and Table 4.6 respectively. These results have been compared to results in [129] and show reasonable agreement. The difference in the values can be attributed to the different apparatus used for the experiments as it has been shown in [130] that flammability limits of gases depend on the apparatus used for the experiment.

Table 4.5: Flammability limit data for downwardly propagating methane flame

Methane	Horizontal Propagation	Downward Propagation	Flammable limit from [128]
Lean Flammability Limit	0.8	0.7	0.6
Rich Flammability Limit	1.4	1.5	1.35
Max. Flame Speed	0.76 m/s @ $\phi=1.1$	0.63 m/s @ $\phi=1.1$	

Table 4.6: Flammability limit data for downwardly propagating propane flame

Propane	Horizontal Propagation	Downward Propagation	Flammable limit from (28)
Lean Flammability Limit	0.9	0.6	0.8
Rich Flammability Limit	1.4	1.8	1.8
Max. Flame Speed	1.05 m/s @ $\phi=1.2$	0.84 m/s @ $\phi=1.1$	

4.5 Flame acoustic pressure

Following from the discussion in Section 4.4, there seemed to be some form of flame shape changes at some equivalence ratio, especially for the rich flames. This change in the shape of the flame has been observed by Mossa [3] in a previous work with this rig. Mossa had reported some form of oscillation (rapid change in flame shape) which occurred in a horizontally propagating flame in a tube with both ends opened. However, Mossa only reported the flame position data without a pressure sensor. Therefore there was a need to also show the pressure signal for this flame behaviour.

Shown in Figure 4.12 are the effects of the position of the pressure sensor in the tube. The pressure sensor was placed in the middle of the tube and at the end of the tube to determine the effective pressure magnitude at these points. The pressure signal recorded when the pressure sensor was placed at the middle of the tube was approximately three to six times depending on the equivalence ratio, the signal recorded when the pressure sensor was placed at the end of the tube. When the sensor was placed in the middle of the tube, the signal generated is a combination of both the actual signal from the flame oscillation and the standing wave in the tube. It was also observed that the complete flame signal from the start of propagation to the end of propagation was not recorded when the pressure sensor was placed at the middle of the tube because of a sudden pressure rise after the flame had passed the midpoint of the tube. Also as observed from Figure 4.12, the pressure signal when the pressure sensor was at the end of the tube indicates the pressure tends to be higher in the middle of the tube. The pressure signal with a pressure sensor at the end of the tube was considered favourable for the later experiment because of the ease of visualising the flame propagation and recording the signal from the beginning to the end of the tube.

Figure 4.13 shows the picture of a flame propagating horizontally in a tube opened at both ends. Figure 4.13(a) is the early stage of the flame propagation immediately after ignition where the flame was curved and propagates steadily with a front that is convex towards the unburnt gas mixture. The convex shape has been attributed to the no-slip condition at the walls acting on the burnt gases and heat transfer from the reaction zone to the wall. In Figure 4.13(b) captured in the central length of the tube, the flame constantly changed shape and area forming a wave pattern and Figure 4.13(c) shows the final stage of the flame propagation before extinction.

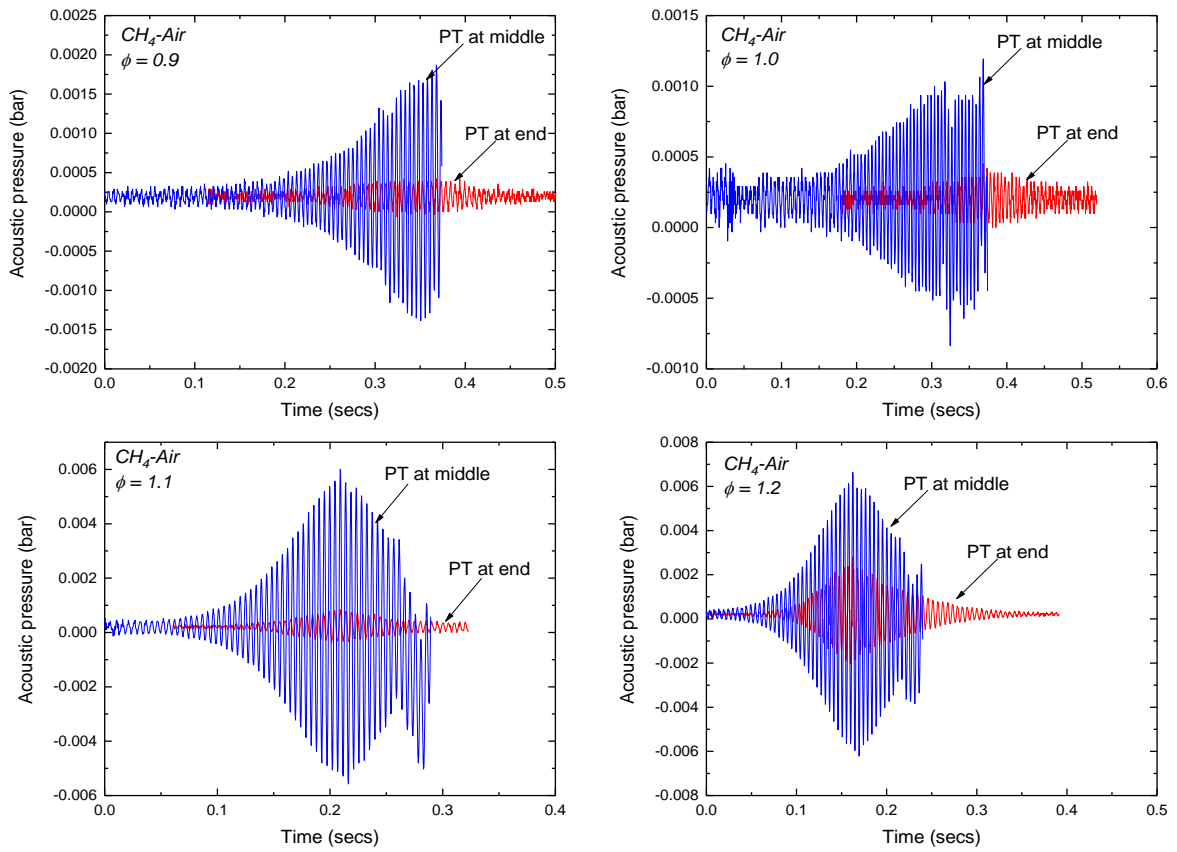


Figure 4.12: Comparison of flame pressure oscillation for pressure sensor at the middle and the end of the tube (Results from two experiments combined).

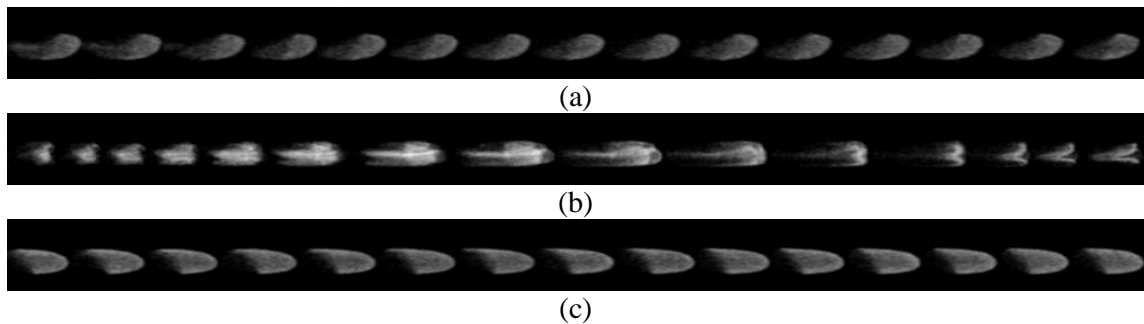


Figure 4.13: Horizontally propagating flames in open ends tube (a) early stage (b) Intermediate stage (c) final stage

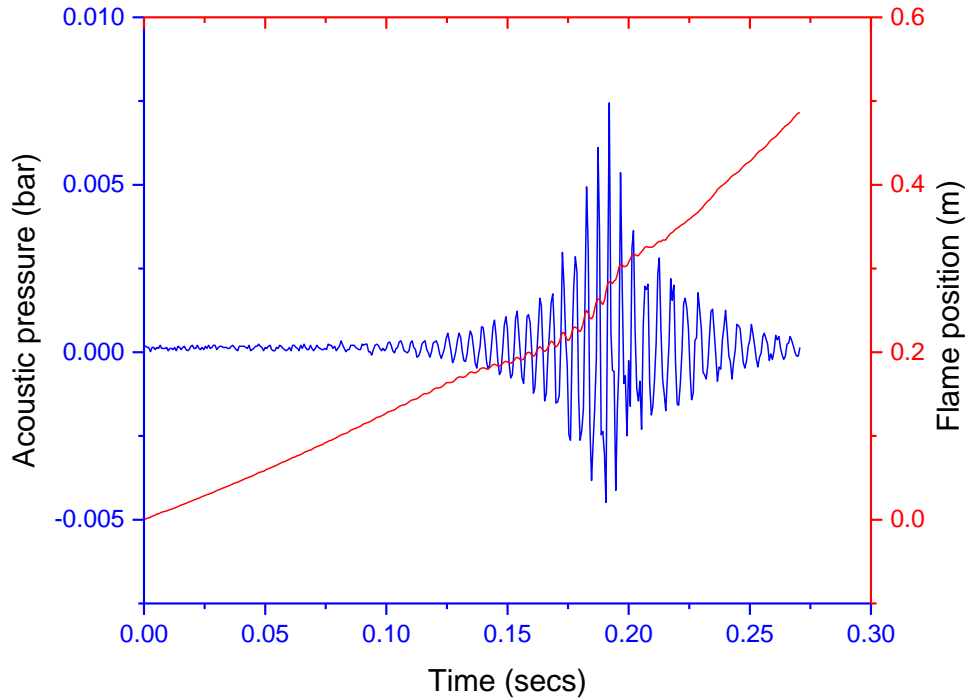


Figure 4.14: Pressure variation and relative flame position as a function of time

The flame regained its stability and appeared similar to its propagation in the early stages. Figure 4.14 shows the flame front position and the pressure signal on the y-axis and time on the x-axis. The pressure signal and flame position data show the presence of oscillations after an initial linear propagation which begins to die off as the flame propagates to the other end.

4.6 Flame intensity and temperature profile

High-speed image visualisation (Figure 4.13) has shown that flames propagating in a horizontal tube opened at both ends develop with relatively weak oscillation at the left side of the tube, then, at the middle, the flame oscillates and finally, the oscillation experienced a reduction towards the end of the tube. In Figure 4.15, the image shows the emission variation at the middle of the tube, captured by a mono-colour camera at 2000 frames per second (fps). It can be seen that the middle fibre emitted radiation at its centre first, and then it gradually increased towards each end of the fibre. This implies that higher temperature is observed at the mid-section of the glowing fibre compared to those nearer the tube walls.

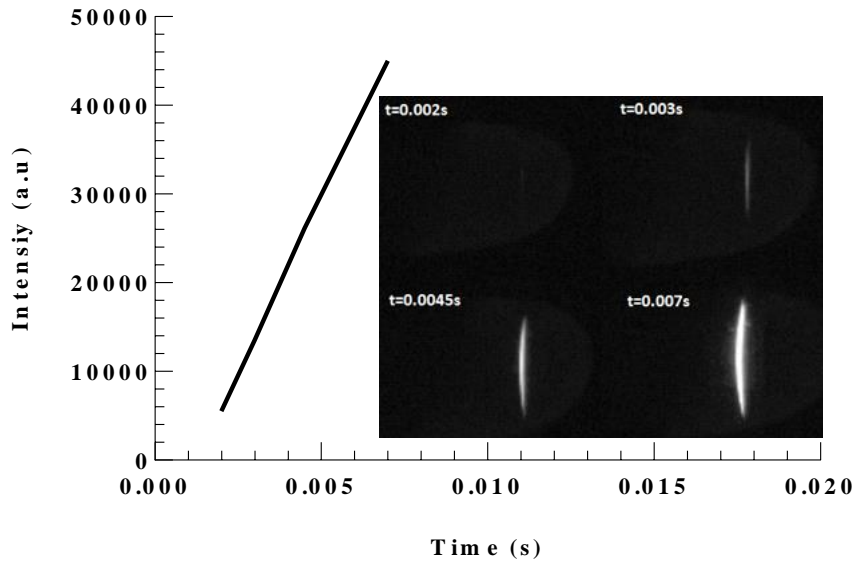


Figure 4.15: The glowing fibre as the flame crossed through tube middle section and time-dependent pixel brightness intensity response.

With reference to the gas temperature measurement, the imaging system of TFP pyrometer separately captured each glowing fibre placed in the middle and each end of the tube. At each location, the gas temperature was measured at three different equivalence ratio settings. It was not possible to image all fibres simultaneously because that would have caused a significant drop in spatial resolution. Figure 4.16 shows the locally derived gas temperature variation at the different fibre positions. Figure 4.14b illustrates a stronger oscillation in gas temperature than that shown in Figure 4.16(a,c). Figure 4.16a shows the gas temperature variation at the location near the ignition point, with two fibres placed 3mm apart, to check the variability in the thermal gradient.

It depicts a similar variation of the gas temperature, which indicates a small thermal gradient between these two fibres. Shown in Figure 4.14c is a moderate gas temperature variation at the far end of the tube. For all cases, obvious fibre deflection was not observed; the flame temperature variations were mainly due to flame instabilities which are stronger in the middle of the tube.

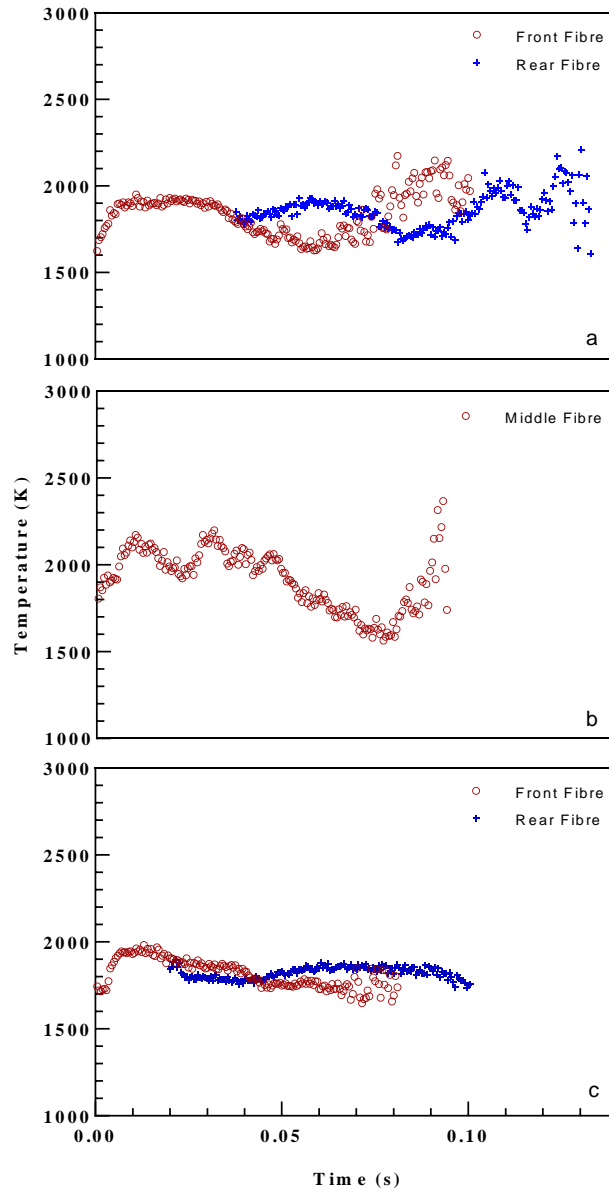


Figure 4.16: Time-dependent gas temperature variation at equivalence ratio = 1.1. (a) Temperature variation at the left end of the tube near ignition place, (b) Temperature variation at the middle of the tube, (c) Temperature variation at the right end of the tube.

In addition, the time-dependent pressure oscillation of the flame travelling through the tube from the left to the right end of the tube was also recorded. As can be seen in Figure 4.17, the amplitude of oscillation was relatively moderate before 0.1s, afterwards, the peak amplitude occurred around 0.2s which correspond to the position of the middle section of the tube, and finally, the amplitude was gradually tailed off by the tube right end. This

behaviour was similar to the time-varied variations of gas temperatures detected by the two-colour pyrometer as shown in Figure 4.16.

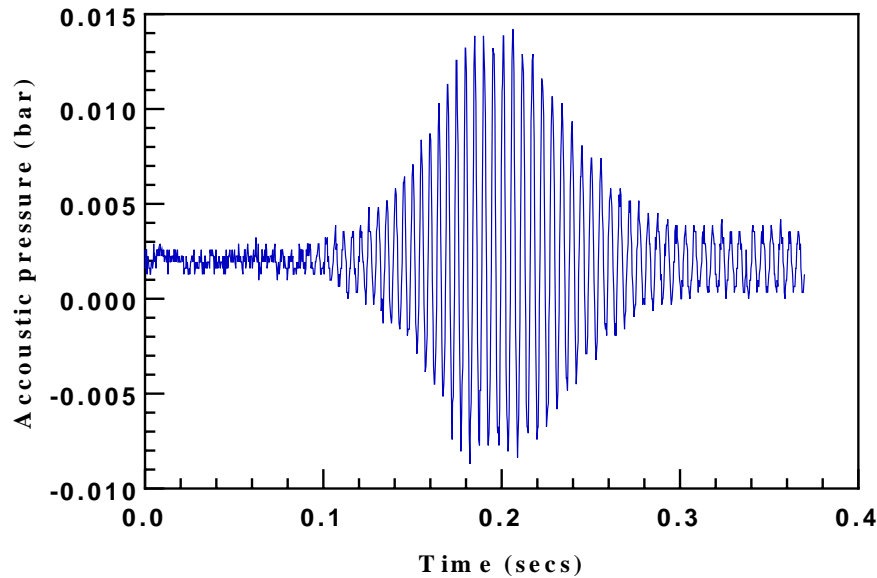


Figure 4.17: Pressure oscillation of the flame in the tube at equivalence ratio = 1.1

Furthermore, by using the illumination from each fibre the variation of the flame oscillation could also be observed. The captured RGB images of each glowing fibre were converted to grey images, and then only brightness intensity of pixels within the glowing fibre was summed up as the total intensity. Figure 4.18 (a,b and c) shows the cycle of heating up and cooling down as the flame passed each fibre at similar cycling time. The cooling rate increased from left to right of the tube. Figure 4.18 (d,e and f) shows the plots of the flame amplitude against the frequency, with the highest flame frequency occurring at the middle section of the tube.

The fibre and the corrected gas temperatures varying with equivalence ratio are shown in Figure 4.19, where each point averages 162 samples. The common trend shows that the temperatures increased from $\phi = 0.9$, peaked at $\phi = 1.1$, and then decreases until $\phi = 1.2$, which is similar in behaviour to the flame velocity variations shown in Figure 4.20. Both the highest flame velocity and gas temperature were found at $\phi = 1.1$.

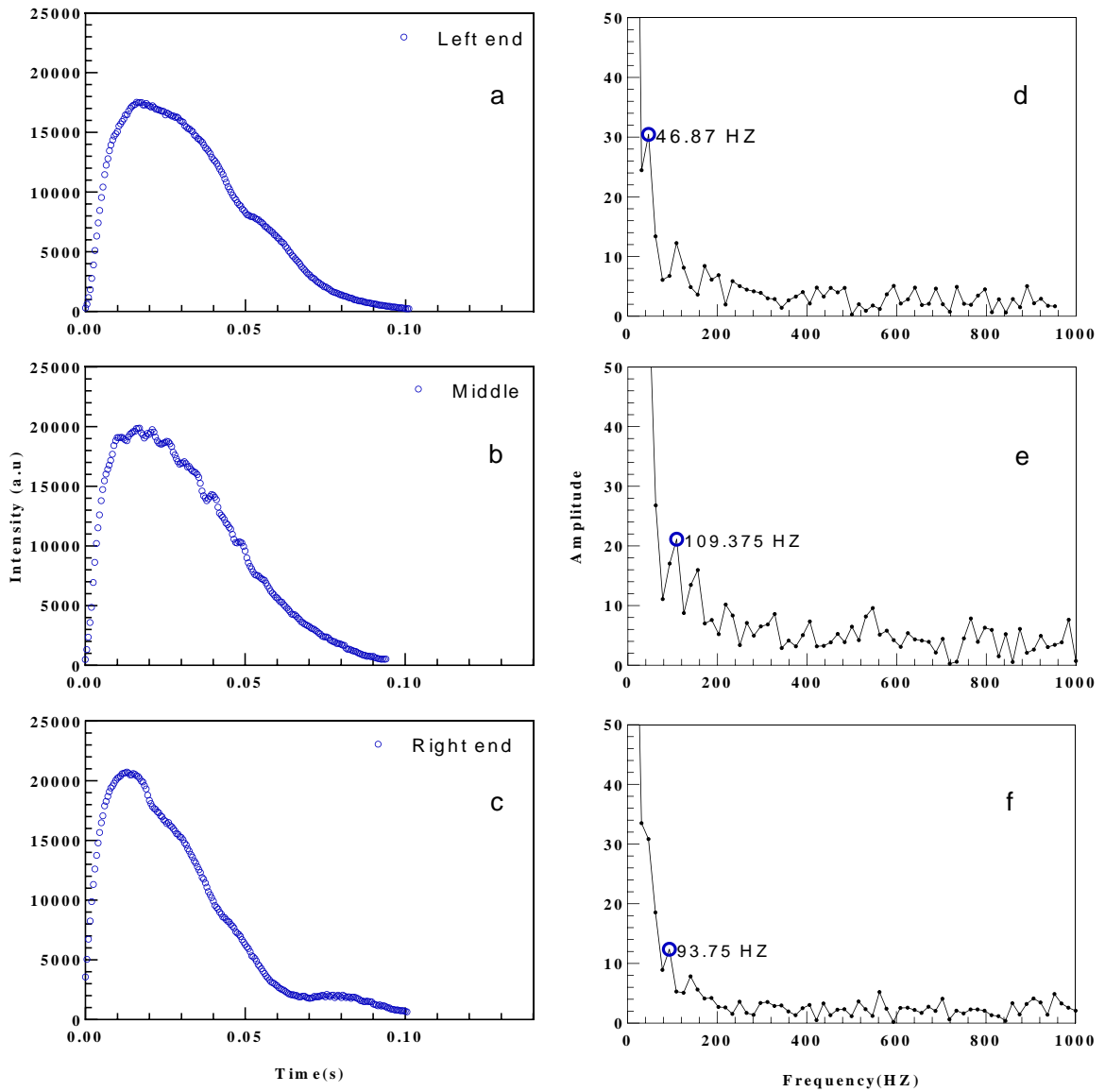


Figure 4.18: a,b and c Experimental heat-up and cool-down cycle at Left-end, Middle and Right end of the tube, d,e and d present the main frequency of intensity oscillation at the corresponding positions of the tube, using FFT.

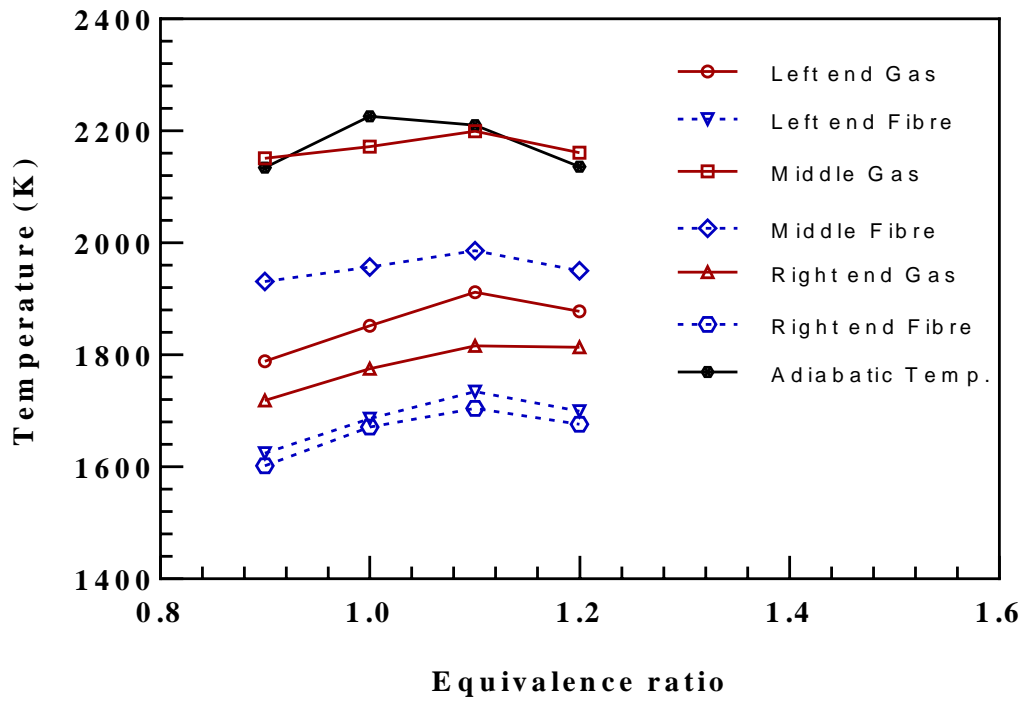


Figure 4.19: The average temperature of flame travelling through the fibre at different equivalence ratios

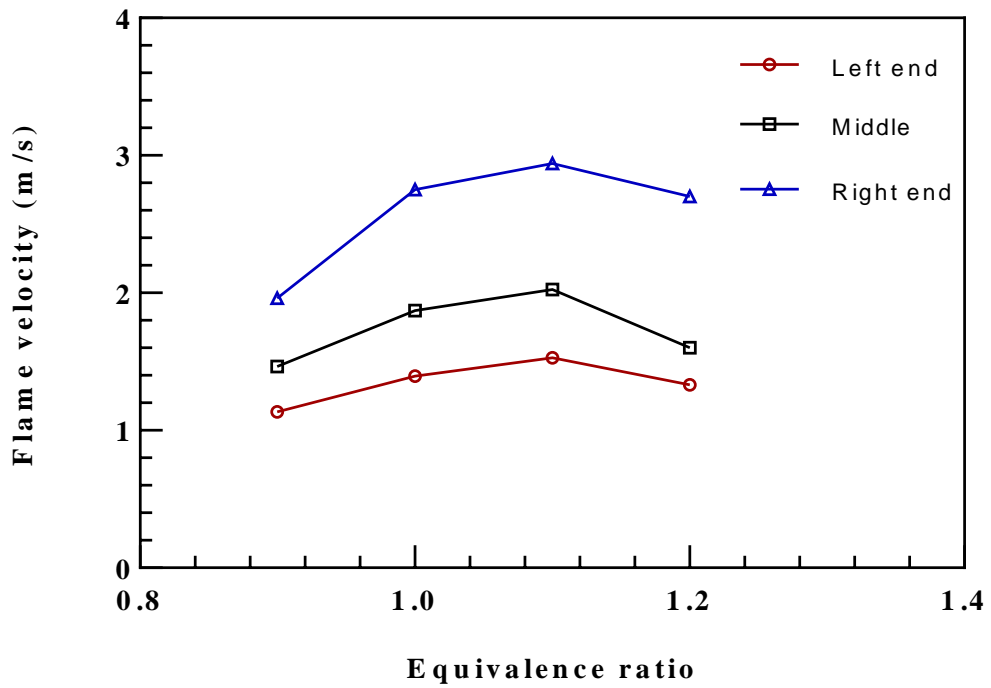


Figure 4.20: Flame velocity varying with equivalence ratio

To validate the sensitivity of the TFP method in determining the temperature of the flame even if the flame speed is increased, further experiments were carried out, but in this case, the focus was on the middle fibre as that is the point of interest. Results for the flame speed and the flame temperature plotted against the equivalence ratio are shown in Figure 4.21. The higher speed was achieved by closing one end of the tube (i.e. the end where the flame is ignited was closed giving the flame extra forward movement as the burnt gases could not escape, but rather get to a dead end and then push forward. As expected, the maximum propagation speed and the maximum temperature of the flame occurs at $\phi = 1.1$. Generally, the results so far are at a low flame speed and have shown to be in satisfactory agreement with the flame adiabatic temperature as shown in Figure 4.19. Figure 4.22 shows the temperature distribution at different equivalence ratios ranging from $\phi = 0.9$ to $\phi = 1.2$, at a faster flame speed. It was observed that the flame temperature distributions for all equivalence ratios are relatively the same.

The temperature correction between the surrounding temperature and fibre was derived from the energy balance. The energy balance involves the convective heat transfer from the hot gas to the fibre and heat loss by radiation from the fibre to ambient environment. The heat transfer by conduction along the fibre was not considered because it has a negligible effect on the heat transfer process [131]. Since the measurement of the gas temperature was not done by a direct process, it is important to consider the likely errors and their effect on the accuracy of the measured gas temperature.

The core uncertainties in the measurement of the gas temperature came from the computation of the fibre temperature, the determination of the emissivity of the fibre, and the computation of the convective heat transfer coefficient. Additionally, there are several other sources of uncertainty in the determination of the Nusselt number; such as the correlation not completely fitting the flow conditions used in the experiment and since the Reynolds number (Re) is essential to calculate the Nusselt number, therefore determining the gas velocity perpendicular to the fibre. In this study, only the averaged velocity traversing the fibre was predictable by the imaging-based method.

Furthermore, the tolerance of the diameter of the fibre and its emissivity depends on the roughness of the fibre and the oxidation resistance which may vary in environments at high-temperature.

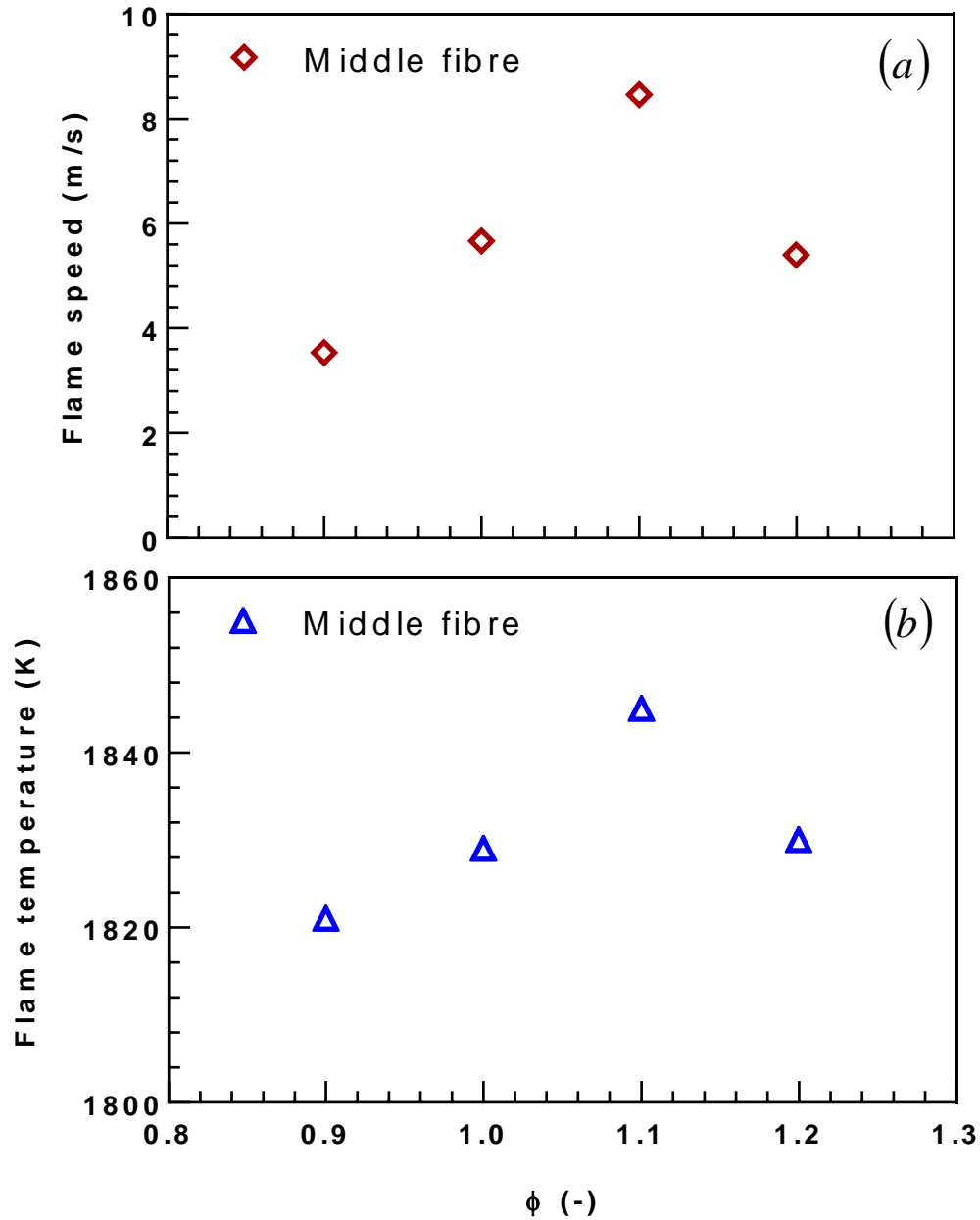


Figure 4.21: Flame speed and temperature for faster methane flames versus equivalence ratio

The obvious uncertainty exists in the determination of the fibre temperature. The measured temperature difference between using the two-colour and Infra pyrometers has been discussed in [132]. This difference could arise from misalignment of the measured spot area using the two techniques, and the fibre emissivity may not be consistent along the length of the fibre.

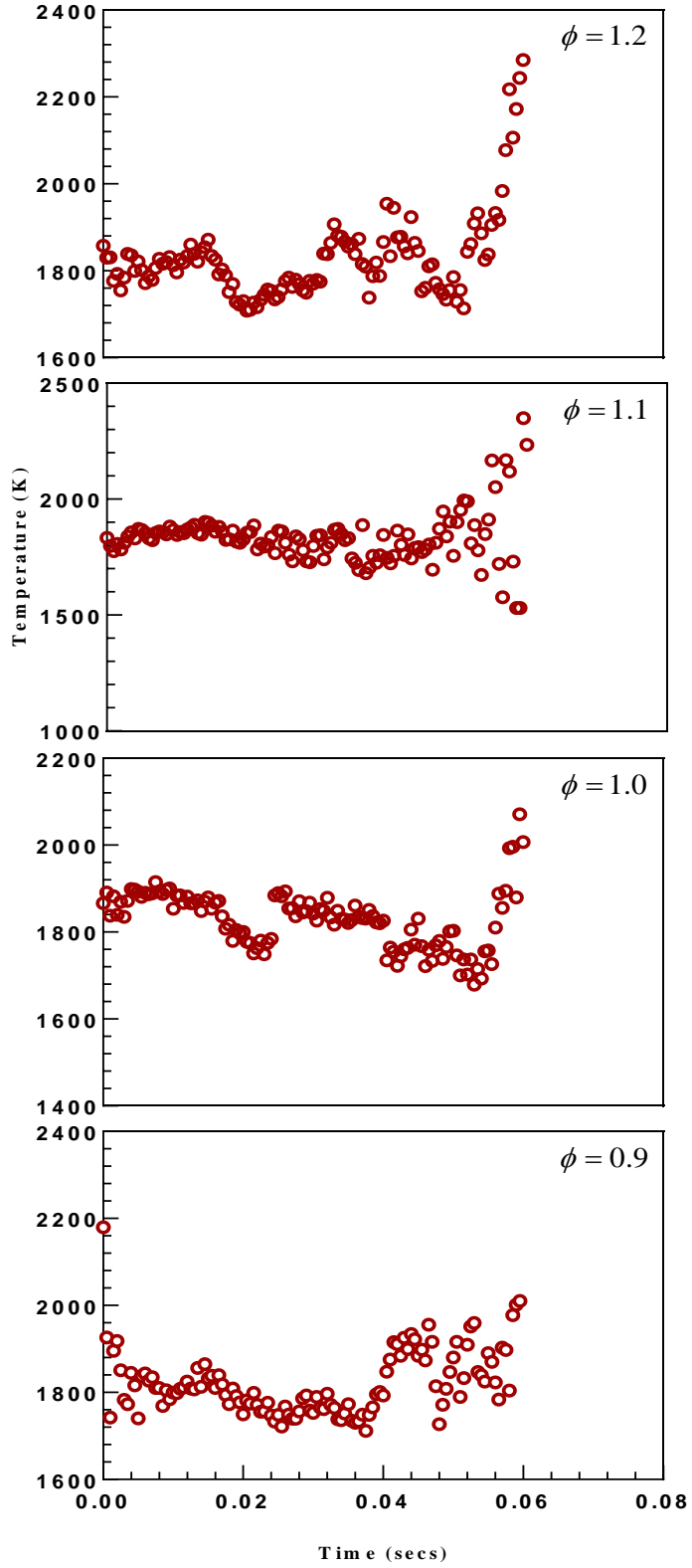


Figure 4.22: Middle of tube time-dependent gas temperature variation at different equivalence

CHAPTER FIVE

HYDROGEN ENRICHED FLAME IN OPEN ENDED TUBE

5.1 Introduction

In this chapter, experimental results of flames propagating in a horizontal tube opened at both ends are reported and discussed. In chapter four, the presence of oscillation at the middle of the tube for a flame propagating horizontally in a tube opened at both ends was discussed and it was found that there was a correlation between the flame temperature and the flame acoustic pressure. The speed of the flame was increase by closing one end of the tube to observe this relation and a reasonable agreement was achieved. This chapter further examined flames at a higher speed in a horizontal tube opened at both ends configuration, where in this case, the speed of the flame was increased by enriching the flame with hydrogen of varying amounts. Because of the close relationship in the behaviour of propane/air and methane/air fuel, in this chapter, methane fuel was used.

5.2 Flame speed of methane/hydrogen/air mixture

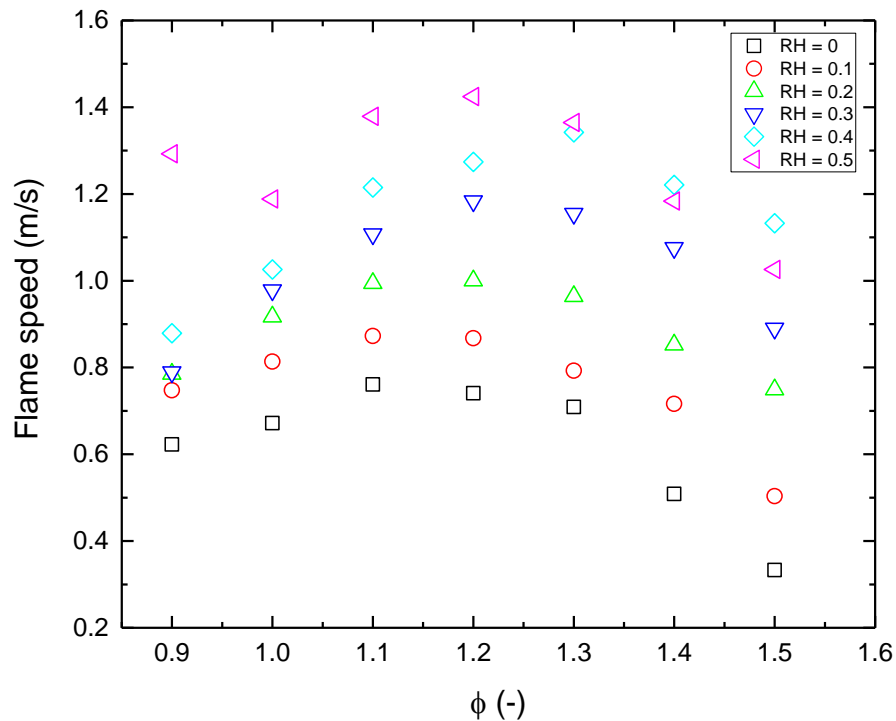


Figure 5.1: Flame speed of Methane/Hydrogen/Air mixture against equivalence at different *RH*

Shown in Figure 5.1 are plots of the experimental fundamental flame speed against equivalence ratio at varying hydrogen addition. The flame speed increases for $\phi \leq 1.3$ as the hydrogen addition (RH) increases up to the amount tested. This behaviour tend to change as ≥ 1.4 ; the flame speed increase as the RH increase up to $RH = 0.3$. For $RH > 0.3$, the flame underlying speed decreased.

5.3 Methane Hydrogen/Air Flame Analysis for open-ended tube

Shown in Figures 5.2 to 5.4 are the flame propagation in the tube for Methane and Methane with $RH = 0.1$ to 0.5 at time between frames of 0.0003 seconds. The photographs illustrate the shape variations of the travelling flames. Comparing the shapes of the flames visually, pure methane flames seemed stable for some flame, though analysis showed the presence of unstable behaviour. For $RH = 0.1$ to 0.3 , the flames looked stretched and unstable compared to the $R_H = 0.4$ and 0.5 flames, which seemed less affected by the oscillations, showing that the addition of hydrogen subjects the flame to oscillation.

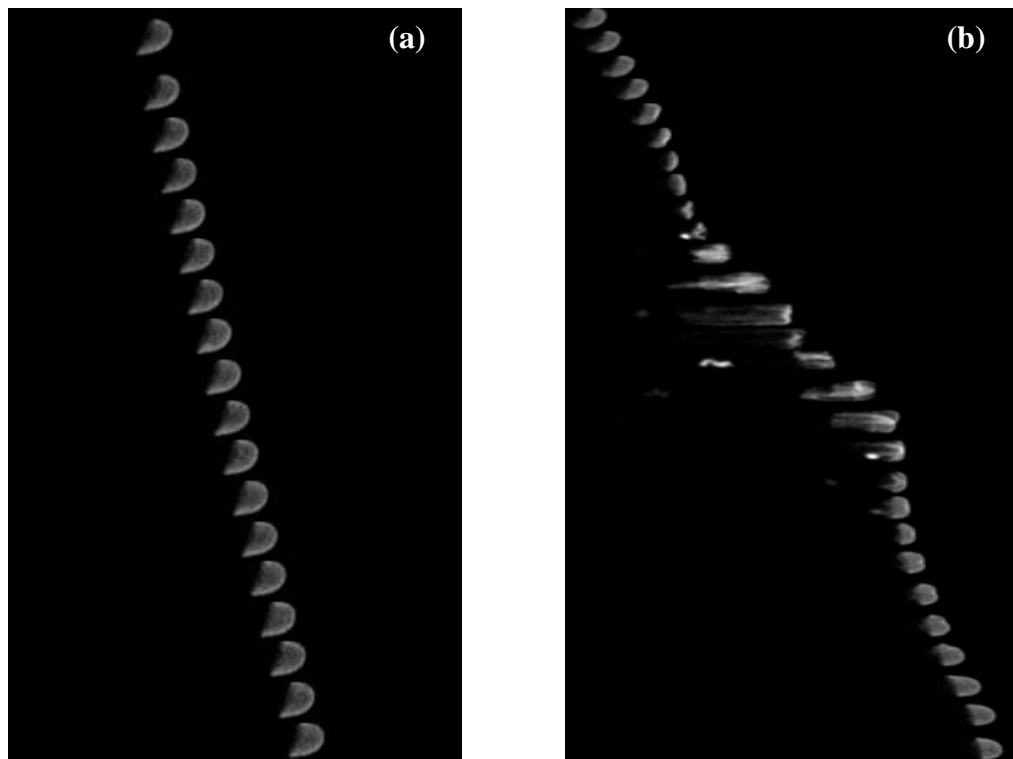


Figure 5.2: Methane flame propagation at 1.2 equivalence ratio (a) $RH = 0$ (b) $RH = 0.1$

It was also observed that the $RH = 0.1$ flame was most affected by the acoustic oscillations; this contravenes our expectations since due to the high reactivity and diffusivity of Hydrogen, one would have expected the $RH = 0.5$ flame to be subjected to more oscillations. Shown in Figure 5.2(b), at the early stage of the flame propagation immediately after ignition, the flame front was convex in the direction of the unburnt gas mixture and tipped forward. The convex shape has been attributed to the non-slip condition at the walls acting on the burnt gases and heat transfer from the reaction zone to the wall. The tipping is thought to occur due to the hot and less dense combustion gases behind the flame rising relative to the cooler unburnt gases [118]. At the central length of the tube, as represented in the same figure, the flame constantly changed shape and area forming a wave pattern. Finally, the flame regained its stability and appeared similar to its propagation in the early stages before the end of the tube length. However, the flame tipping at the initial stage can be seen to have reversed with the top of the flame longer than the bottom. Thus, alternative (non-gravitational) mechanisms may have imposed the non-symmetrical behaviour on the flame. These three stages of propagation were also observed for all the other methane/hydrogen flames studied in this research.

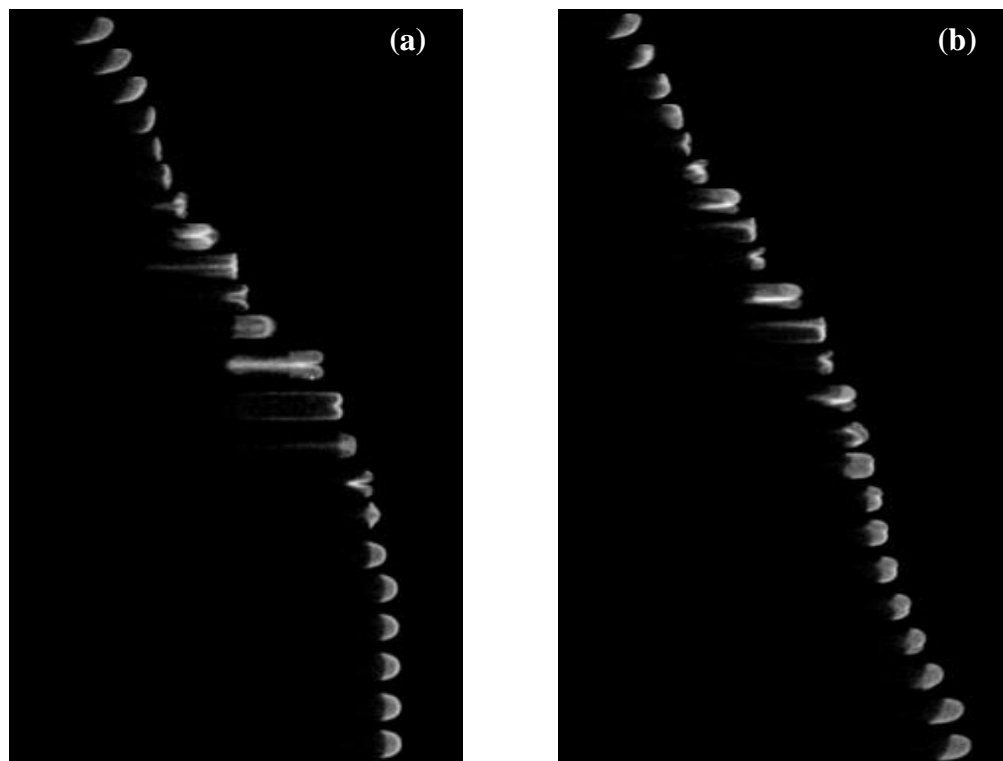


Figure 5.3: Methane flame propagation at 1.2 equivalence ratio (a) $RH = 0.2$ (b) $RH = 0.3$

Figure 5.3 (a and b) has similar flame behaviour as discussed above though there was no flame tipping reversal as was seen in Figure 5.2(b) and as stated before, an alternative mechanism might have caused the reversal of the tipping direction.

In Figure 5.4 (a and b), despite the high burn rate resulting from the increased hydrogen concentration, the flame immediately following ignition is strongly tipped with a long tail following the flame at the bottom of the tube. In the central length of the tube, the flame was again subjected to oscillations resulting in an alternate lengthening and shortening of the flame. Following the oscillatory period in the central length of the tube, the flame again stabilised becoming convex towards the unburned mixture and propagating steadily down the tube. Reversal in the flame tipping direction was observed for $RH = 0.4$, and as afore stated, there may be a different mechanism responsible for this phenomenon as it is not a function of the flame or tube properties.

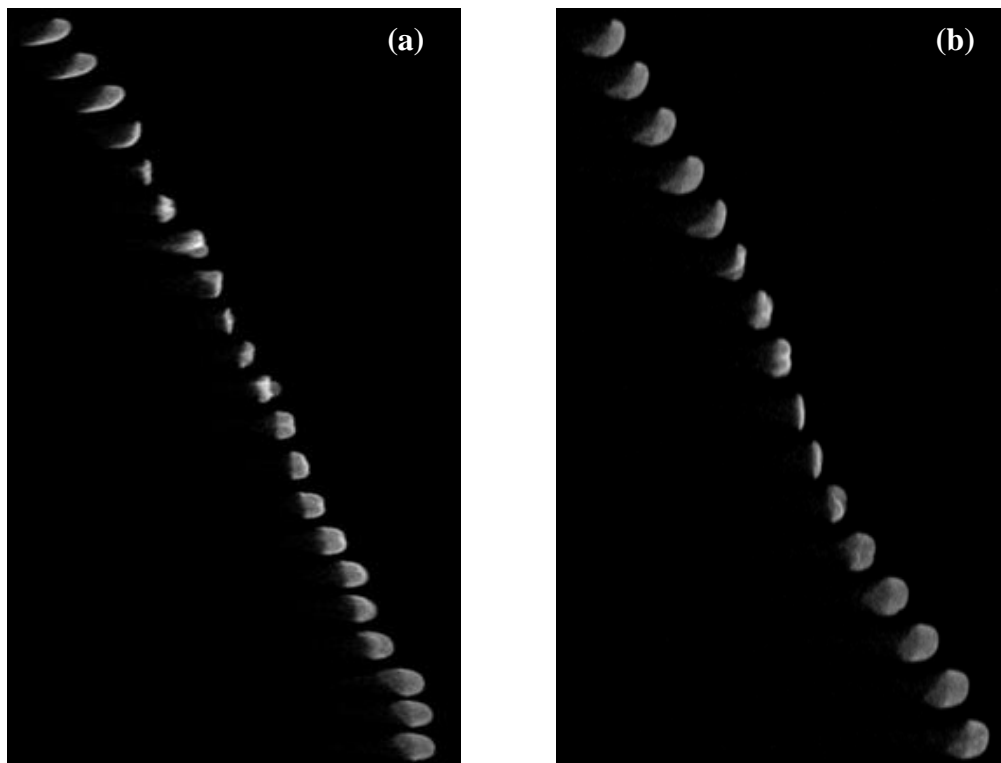


Figure 5.4: Methane flame propagation at 1.2 equivalence ratio (a) $RH = 0.4$ (b) $RH = 0.5$

Shown in Figure 5.5 are plots of maximum flame front position against time for increasing Hydrogen concentration at $\phi = 1.2$. Pure methane flames were observed to propagate relatively steady along the entire length of the tube with a slight increase in velocity as they

progressed. Some of the pure methane flames were subjected to small oscillations, but no changes in the flame shape were seen as shown in the photograph of Figure 5.2(a). For methane/air flame mixtures of $RH = 0.1$ to 0.3 , strong oscillations were observed, and these flames are grouped together as shown on the plot. As the hydrogen concentration was increased to $RH = 0.4$ and 0.5 , the initial flame propagation was noticeably higher than for the flames with small values of RH as evidenced by the distance achieved by these flames at 0.05 s. When the oscillation occurred in the central length of the tube, the flame slowed and then started to accelerate once the flame had passed through the acoustic field. To summarise, three types of behaviour were observed for premixed methane/air flames propagating down an open-ended tube: I, the flame propagated down the tube steadily with a no significant oscillations at the central length of the tube ($RH = 0$); II, the flame propagated down the tube steadily and was then subjected to violent acoustic oscillations resulting in an increase in the burn rate ($RH = 0.1$ to 0.3); and III, the flame propagated down the tube steadily and was then subjected to acoustic oscillations that resulted in a decrease in the burn rate ($RH = 0.1= 0.4$ to 0.5).

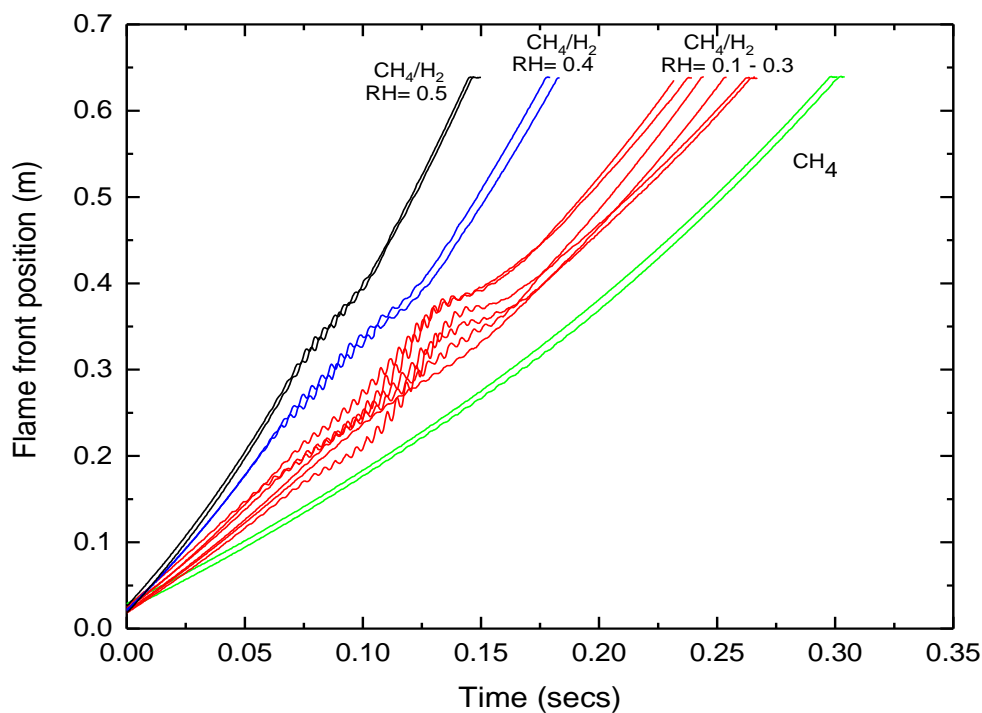


Figure 5.5: Methane/Hydrogen flame propagation at $\phi=1.2$ and different RH

5.4 Flame oscillation analysis

Further analysis has been performed on the flame front images and this is shown in Figures 5.6 to 5.9 for flames at $RH = 0$ to $RH = 0.7$. The flame front position and pressure amplitude plotted against time is labelled as (a) and (b) respectively on each Figure. A low pass FFT filter was applied to the flame position and the result subtracted from the original data to get the amplitude of the high frequency oscillations of the flame front, a , labelled as (c) on each Figure. For all RH cases, the oscillations appear part way along the tube apart from $RH = 0$ flame where there was small though insignificant oscillation as it was not noticed on the flame by visual inspection. The maximum amplitude fluctuations in the flame front position of the $RH = 0.1$, $RH = 0.2$ and $RH = 0.3$ flame was ± 10 mm compared to ± 5 mm for the $RH = 0.4$ and $RH = 0.5$ flame. For all $RH > 0$ cases, the reacting flame front was being dragged back towards the burned mixture some of the time, although this seems to be more so for the $RH = 0.1$ flame. Yang et al. [118] have measured CH^*/C_2^* emission from propane-air flames subjected to acoustic oscillations in the same rig and demonstrated significant variation in this ratio as the flame oscillates. This might be a result of changes in the flame front chemical mechanism as the flame traverse the acoustic field. The underlying burn speed derived from the low pass FFT filtered flame position, u_{fft} , is labelled as (d) as shown in Figures 5.6, 5.7, and 5.8, where the different behaviour of the flames was evident. In the case of the $RH = 0.1 - 0.3$ flame, it initially slightly slowed as it reached the acoustic field but then rapidly accelerated reaching a maximum speed of 4.59 m/s, followed by a slowing down to a minimum speed of 0.76 m/s, then a steady increase in the flame speed before extinction. For $RH = 0.2$ flame, it also initially slowed as it reached the acoustic field, then accelerates rapidly reaching a maximum speed of 4.24 m/s, followed by another rapid slowing down to a minimum speed of 1.08 m/s, then a steady increase in the speed before extinction of the flame. $RH = 0.3$ flame also have the same characteristic behaviour as the $RH = 0.1$ and $RH = 0.2$ flame but with a maximum speed of 3.37 m/s, and minimum speed of 1.10 m/s, as the flame slowed after the acoustic field. For these flames, the maximum underlying flame speed occurs with the maximum amplitude in the oscillations as seen in the figures. For the $RH = 0.4$ and $RH = 0.5$ flame, however, the flame slows as it passes through the acoustic field and has a speed of 2.38 m/s and 3.24 m/s respectively, which is lower than the peak speed seen for the $RH = 0.1, 0.2$ and 0.3 flame.

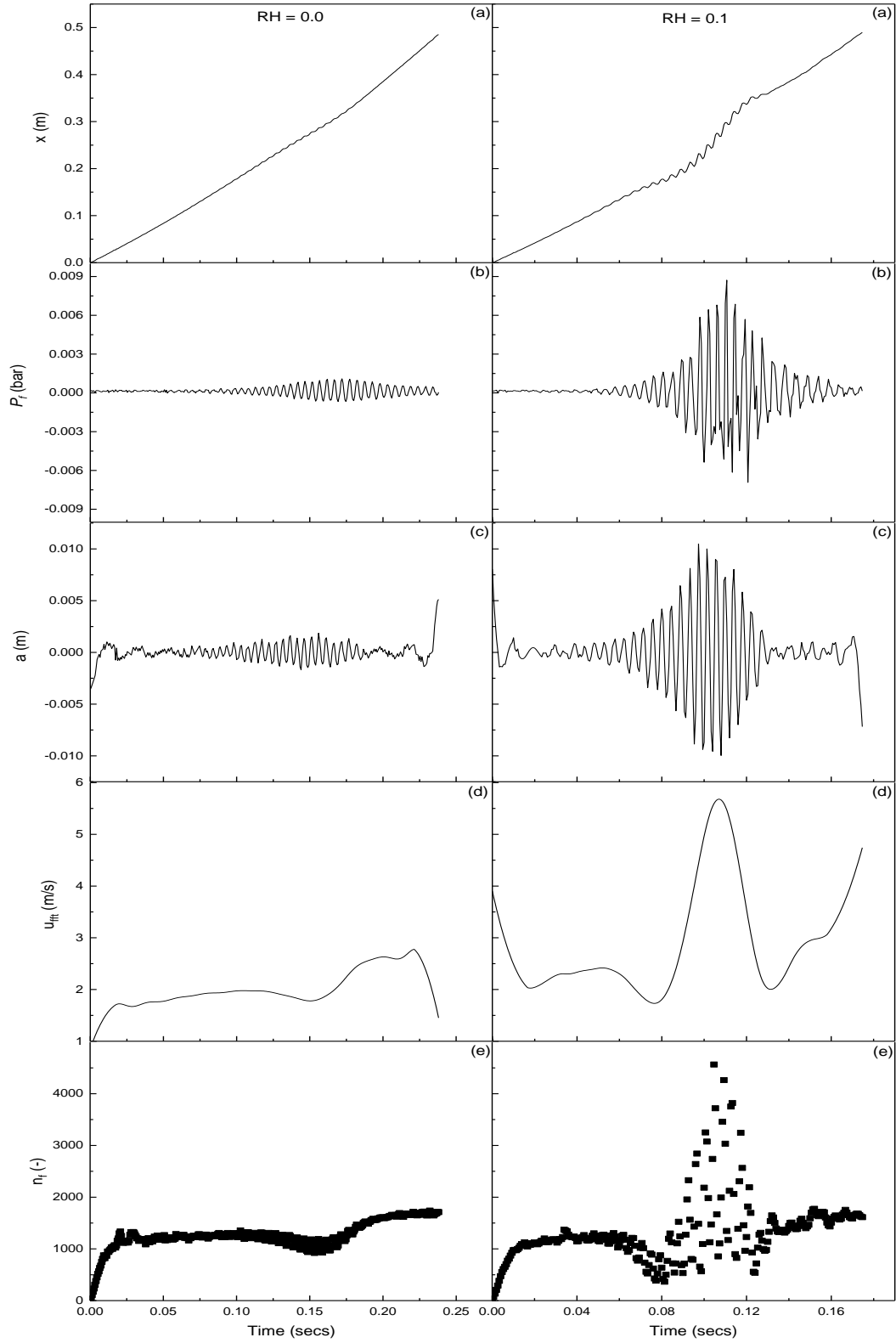


Figure 5.6: CH_4-H_2 - air flame at $\phi = 1.2$ for $RH = 0$ and $RH = 0.1$: (a) x in the flame front position (b) P_f is the flame pressure amplitude (c) a is the flame amplitude (d) u_{fft} is the FFT filtered flame speed (e) n_f is the flame size approximated by the number of pixels

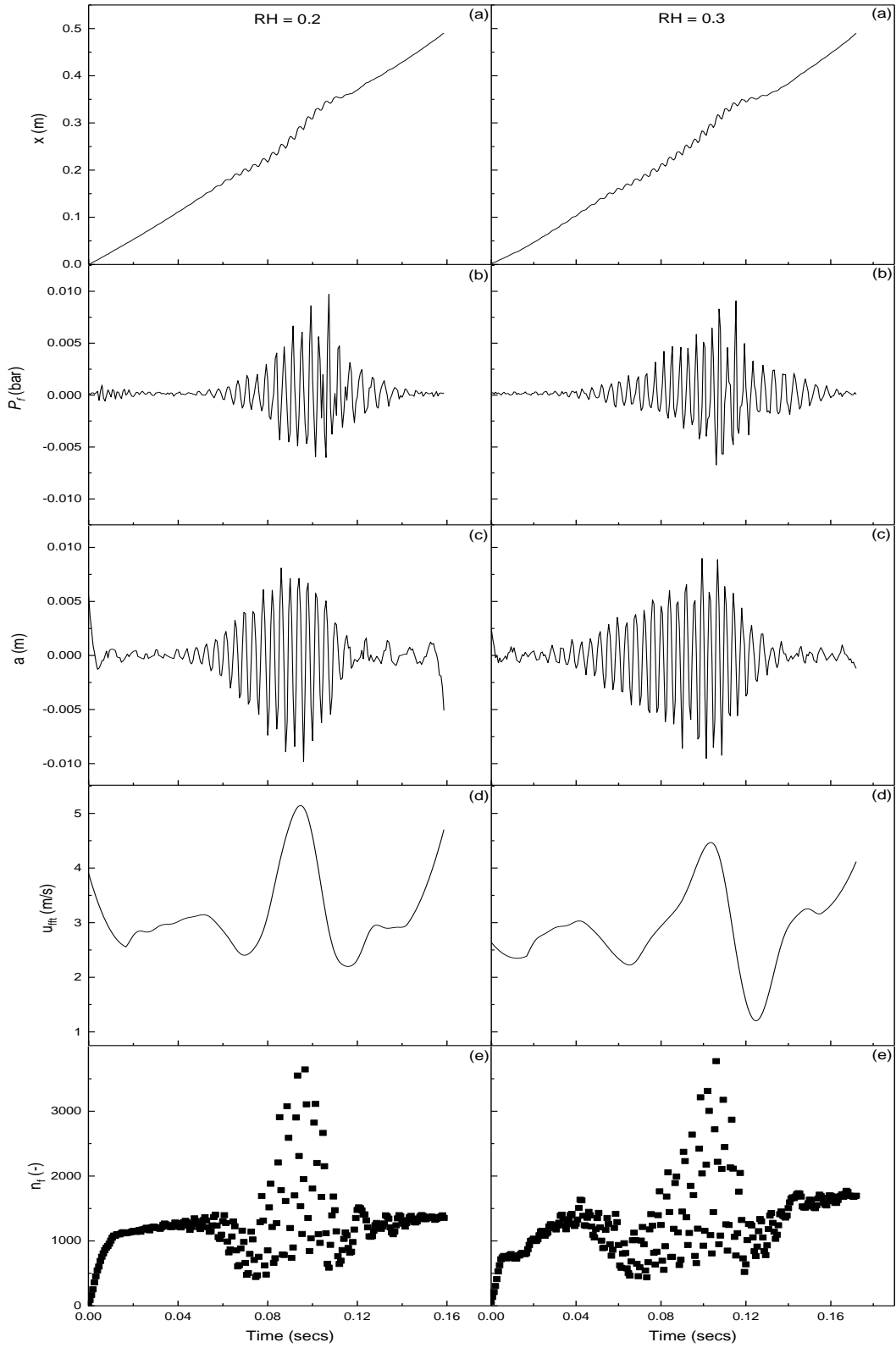


Figure 5.7: $CH_4 - H_2$ - air flame at $\phi = 1.2$ for $RH = 0.2$ and $RH = 0.3$: (a) x in the flame front position (b) P_f is the flame pressure amplitude (c) a is the flame amplitude (d) u_{fft} is the FFT filtered flame speed (e) n_f is the flame size approximated by the number of pixels

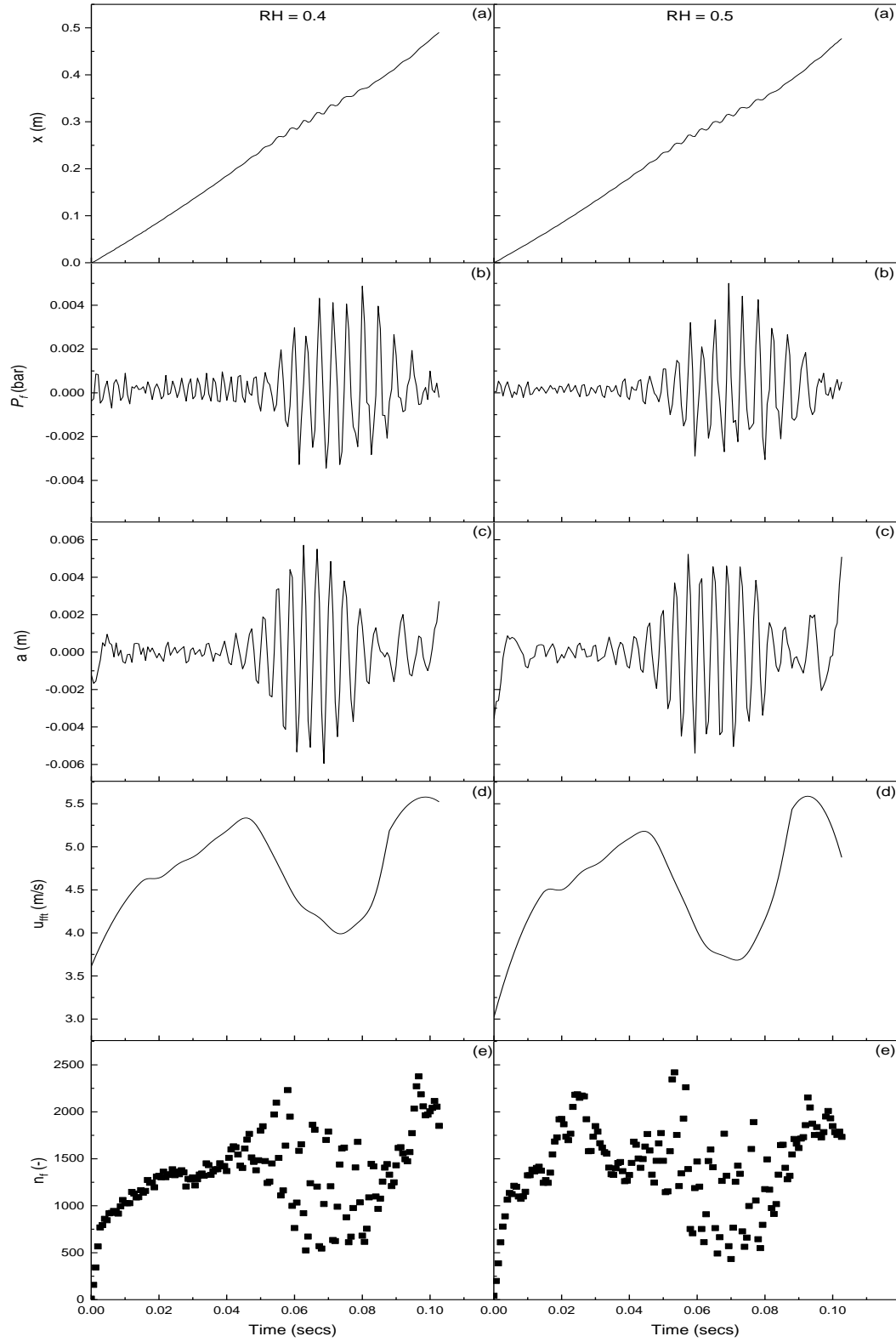


Figure 5.8: $CH_4 - H_2$ - air flame at $\phi = 1.2$ for $RH = 0.4$ and $RH = 0.5$: (a) x in the flame front position (b) P_f is the flame pressure amplitude (c) a is the flame amplitude (d) u_{fft} is the FFT filtered flame speed (e) n_f is the flame size approximated by the number of pixels

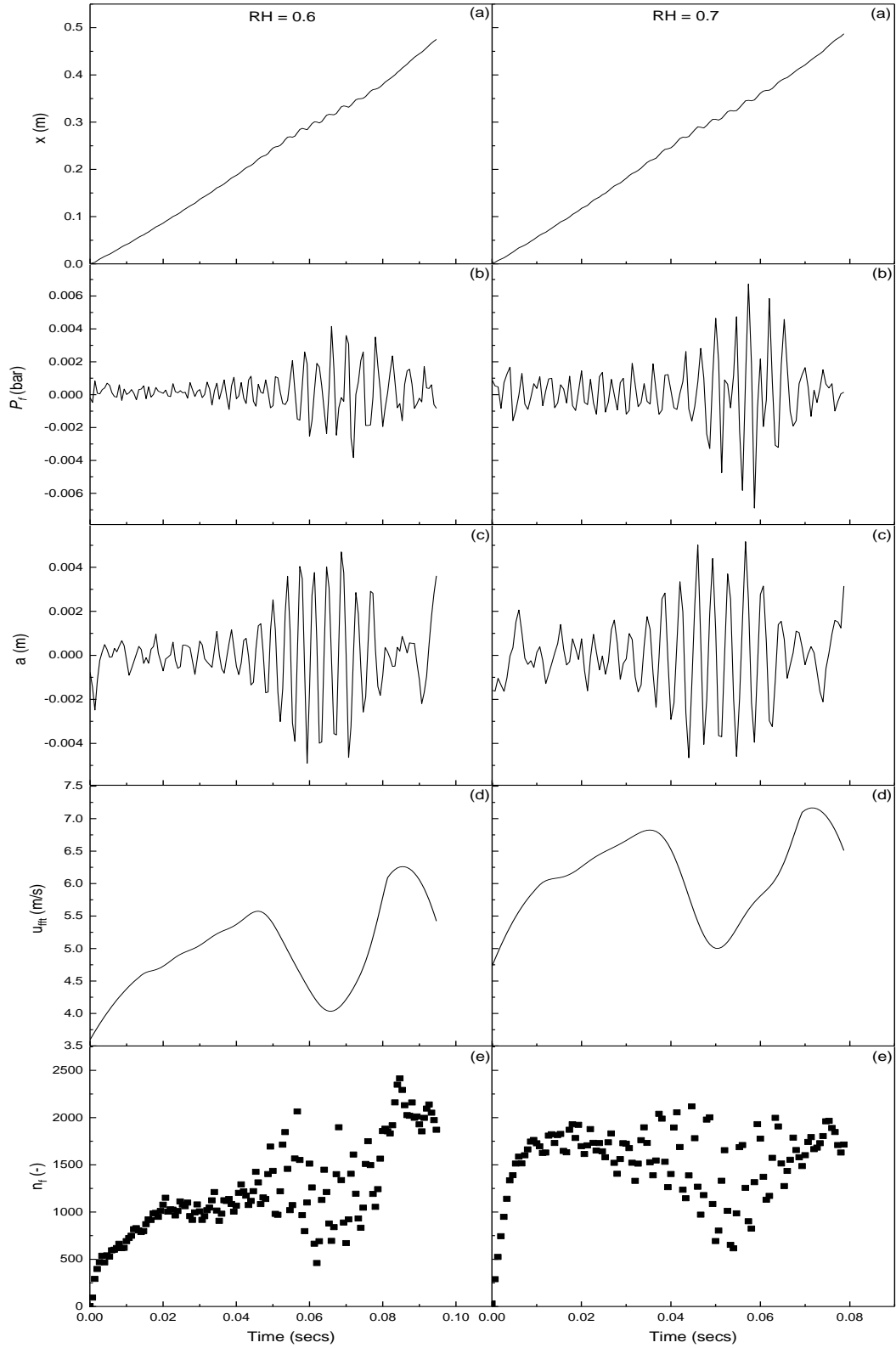


Figure 5.9: $CH_4 - H_2$ - air flame at $\phi=1.2$ $RH = 0.6$ and $RH = 0.7$: (a) x in the flame front position (b) P_f is the flame pressure amplitude (c) a is the flame amplitude (d) u_{fft} is the FFT filtered flame speed (e) n_f is the flame size approximated by the number of pixels

In order to obtain an approximate flame area, the numbers of illuminated (white/grey) pixels, n_f , were counted in each image. These are labelled as (e) as shown in Figures 5.6, 5.7, and 5.8. Similarly, with the flame amplitude and underlying speed discussed above, different behaviour can be seen for all the flames. In the case of the $RH = 0.1$, $RH = 0.2$ and $RH = 0.3$, n_f was seen to reach much higher values when subjected to acoustic oscillations whilst the flame area for $RH = 0.4$ and $RH = 0.5$ decreased when subjected to the acoustic oscillation. These results compliment the measurements of flame speed, u_{ff} . There does appear to be a correlation of n_f with u_{ff} , both when the flame is subjected to acoustic oscillation and when it is not. For example, for the $RH = 0.1$ both the flame speed and n_f can be seen to increase between 0.2 and 0.25 s.

Out of curiosity on the behaviour of the flame when the amount of hydrogen, RH , was increased, the RH was further increased to 0.6 and 0.7. The result is shown in Figure 5.9. The maximum amplitude fluctuations in the flame front position was ± 4 mm, the flame slows as it passed through the acoustic field and the flame area approximated by the numbers of illuminated (white/grey) pixels also shows a drop as the flame traverse the acoustic field. Hence, increasing the RH value beyond 0.7 could further reduce the magnitude of the flame acoustic oscillation; though there is need for future work requiring increasing the RH value above 0.7 and also at different equivalence ratios to further support these results.

Shown in Figure 5.10 is the frequency of the flames for $RH = 0$ to $RH = 0.5$, the frequency of the oscillations was found to be approximately 200 Hz for $RH = 0$, where there was little or insignificant oscillation on the flame, however, for $RH > 0$, where there was significant oscillations on the flame, the frequency ranged approximately 240 Hz to 260Hz (239 Hz for $RH = 0.1$, 244 Hz for $RH = 0.2$, 260 Hz for $RH = 0.3$, 251 Hz for $RH = 0.4$, 251 Hz for $RH = 0.5$, 262 Hz for $RH = 0.6$ and 264 Hz for $RH = 0.7$), and this is thought to be a combine effect of the tube characteristic acoustics ($\cong 243$) and the flame chemical reaction, hence the slight difference in the frequencies. The reduced amplitude of the oscillations of the $RH \geq 0.4$ flames compared to the $RH = 0.1$, $RH = 0.2$ and $RH = 0.3$ flame might be the result of the changes in the acoustic field or the higher burn rate of the hydrogen rich flames traversing the acoustic field with relative ease. An alternative viewpoint may be that the Rayleigh criterion was only fulfilled for the $RH = 0.1$, $RH = 0.2$ and $RH = 0.3$.

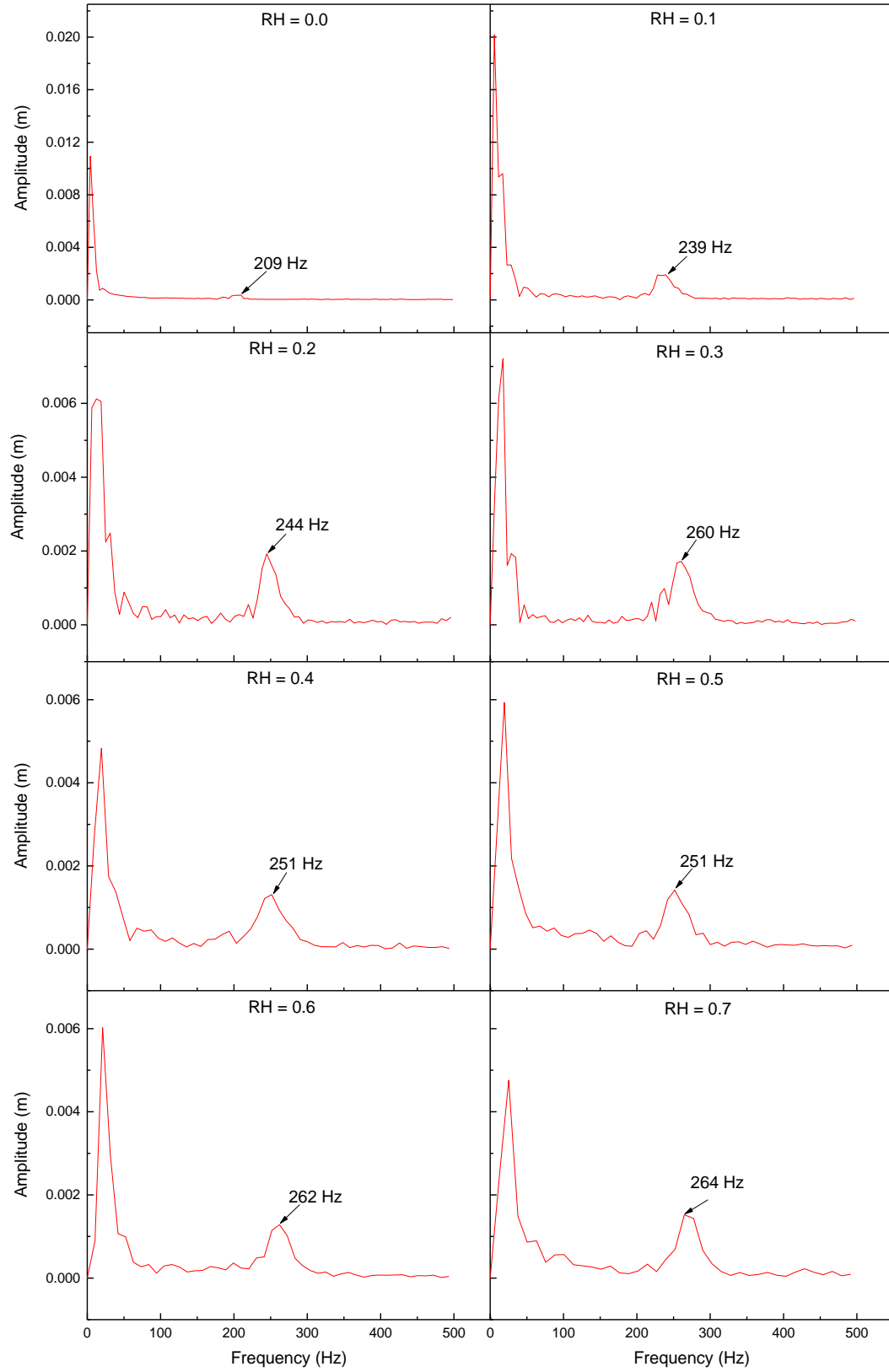


Figure 5.10: Frequency of the flames at the different hydrogen addition (*RH*)

5.4.1 Rayleigh Taylor impact on the Flame oscillation

The increase or decrease of the underlying speed of an horizontally propagating flame in the open ends tube as it traverses the acoustic field when there is an increase in the speed of the flame (in this case by increasing the amount of hydrogen addition) is further analyse by studying the flame propagation at different points on the tube. The results are shown in Figure 5.11(a-c) for $RH = 0.2$ and $RH = 0.4$ to indicate two different flame with high and low impact of Rayleigh Taylor respectively. Due to the difference in densities of the unburned and the burned gases in front and behind the propagating flame respectively, there is apart from hydrodynamic instability due to the jump in density across the flame front, there also exists the presence of the Rayleigh Taylor instabilities.

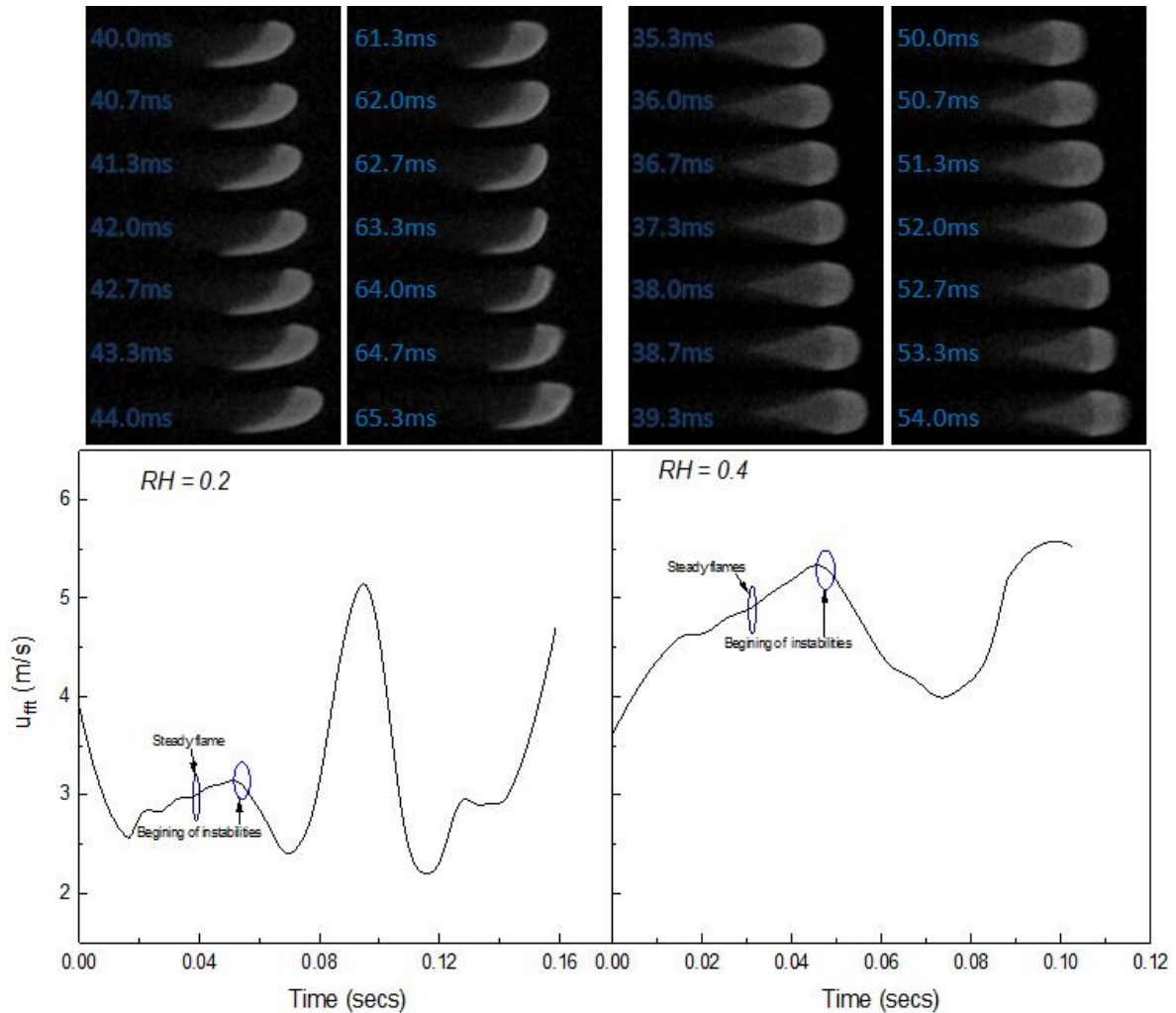


Figure 5.11a: An example flame characteristic behaviours with and without RT instabilities

The presence of the Rayleigh Taylor instabilities reduces; as the flame speed was increased hence the impact on the flame also reduces. Also, there was a decrease in the density difference between the burned and unburned gases as the speed of the flame was increased. It has been shown in the previous section that as hydrogen was added to the methane-air flame, the flame underlying speed increases when the flame traverses the acoustic field up to $RH = 0.3$. When the amount of RH is increased above $RH = 0.3$, there was rather a decrease in the underlying speed as the flame passes through the acoustic field. This behaviour of the flame is attributed to the impact of the presence of the Rayleigh Taylor instabilities, though McIntosh [133] had reported that faster, stronger flames have a greater tendency to recover from instabilities.

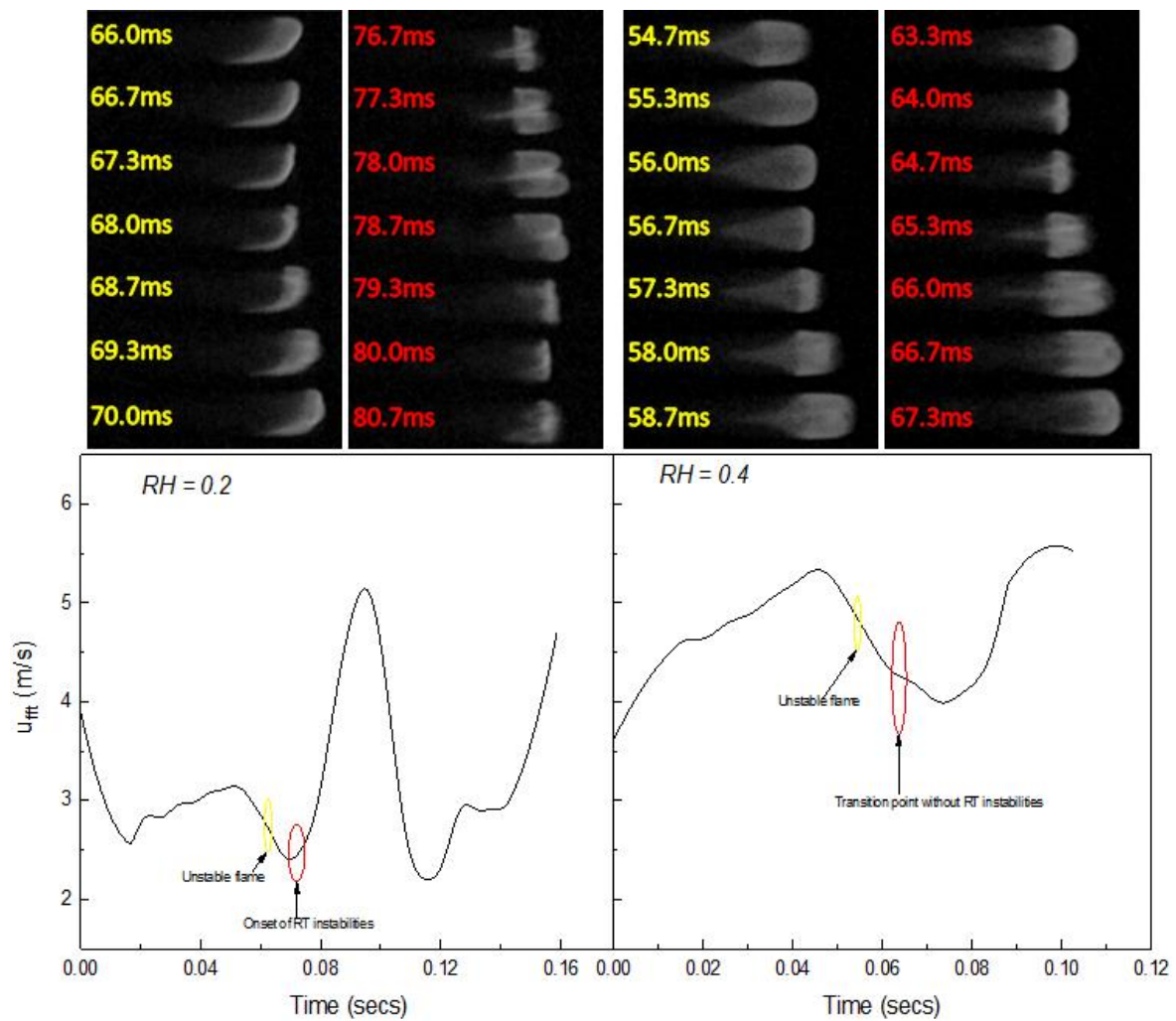


Figure 5.11b: An example flame characteristic behaviours with and without RT instabilities

Shown in Figure 5.11a is the flame propagation almost immediately after ignition (navy blue circle) and at the point where oscillations begin (blue circle). The flame propagated steadily at the beginning with relatively the same flame front shape that is convex to the unburned gas for both RH value, until about 0.05ms where the flames starts being unstable. The flame instability continues with changes in its shape as the front starts showing signs of wrinkle and the flame shape changing rapidly (Figure 5.11b) with a steady decrease in the underlining speed for both flame. Though this is more evident on the $RH = 0.2$ flame (yellow circle). The flame got to a transition point as indicated by the red circle but at different times for the two flames as $RH = 0.2$ is faster than $RH = 0.4$ flame.

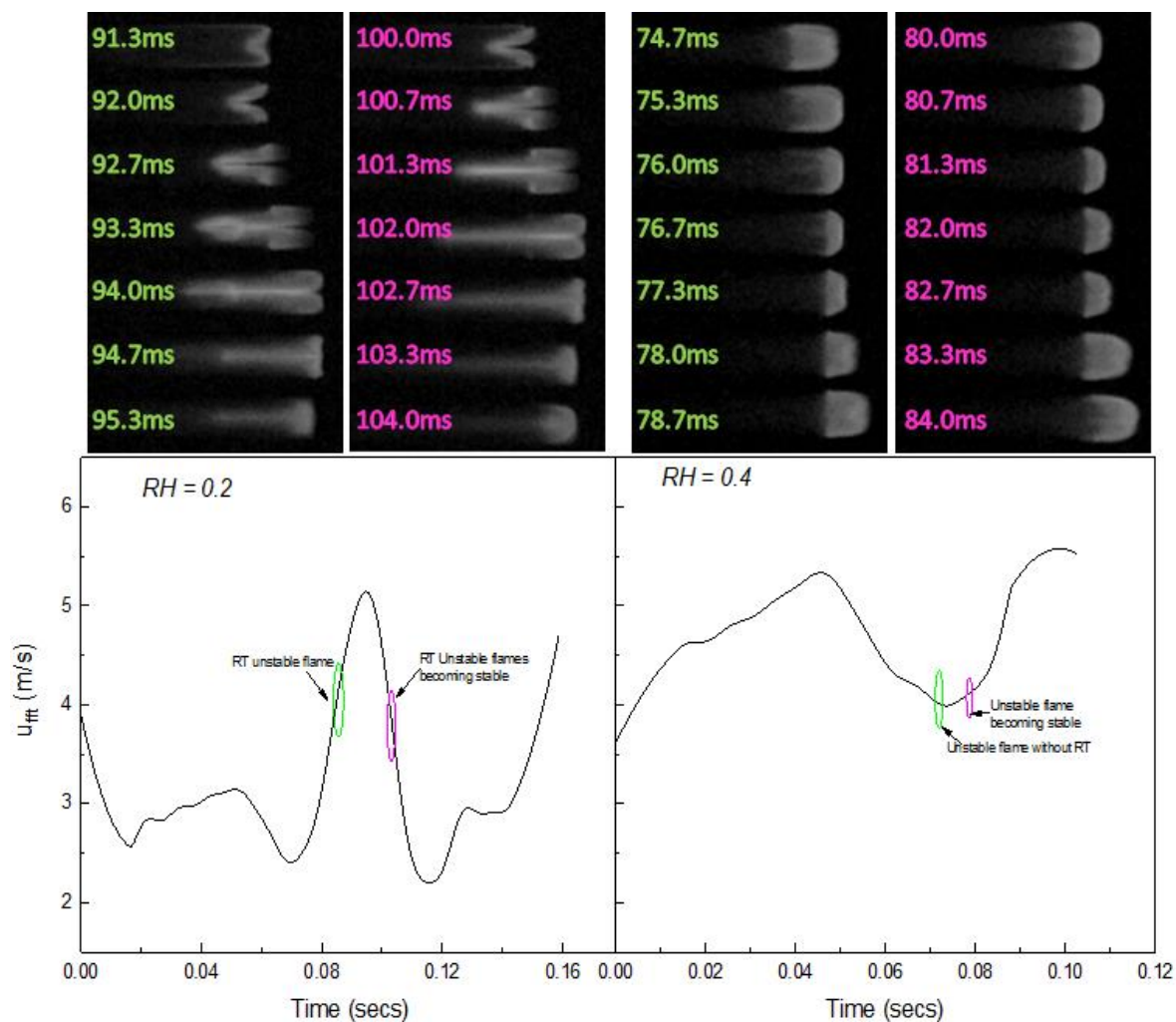


Figure 5.11c: An example flame characteristic behaviours with and without RT instabilities

Indicative of this point is the onset of the Rayleigh Taylor instabilities on the $RH = 0.2$ flame and a resultant impact of a rapid increase in the underlying speed while the $RH = 0.4$ flame showed little or no sign of the Rayleigh Taylor instabilities and the resultant impact was a decrease in the underlying speed of the flame. The flame propagation continues with Rayleigh Taylor instabilities still present on the $RH = 0.2$ flame until it got to a maximum point, then starts decreasing (green circle) while the $RH = 0.4$ flame also decrease in speed until it got to a minimum point then starts increasing (Figure 5.11c). The control measure for the maximum or minimum underlying flame speed is not clear yet, but it is thought to be a function of the tube length as it has been observed in a similar experiment with a longer tube the existence of a second instability after the first stability was regained. The Rayleigh Taylor instabilities continues on the $RH = 0.2$ flame while the $RH = 0.4$ flame showed no sign of the Rayleigh Taylor instabilities, after the maximum and minimum underlying flame speed respectively (pink circle). Both flames consequently regain their stability before the end of the tube. The formation of the Rayleigh Taylor instabilities has been attributed to the reflected pressure wave from the closed end of the tube producing a vorticity on the flame which distort the flame [8, 133-135]. The strength of the vorticity produce depends on the initial flame speed and the chemical reactions of the flame. Therefore, for faster flame, there is a higher tendency of recovering from the shock hence the little or no sign of the Rayleigh Taylor instabilities on the $RH > 0.4$ flames. Figure 5.12 shows the pressure and flame position growth rate of the flame at different RH . Though there is a scatter in the pressure growth rate, the flame position growth showed no changes with a value of approximately 1 s^{-1} . Hence the growth rate of the flame does not impact strongly on the flame behaviour, rather the strong presence of the Rayleigh Taylor instabilities on the $RH \leq 0.3$ had impacted on the flame as it traverse the acoustic field already set up causing the sudden increase in the underlying speed and the little or non-presence of the Rayleigh Taylor instabilities on the $RH \geq 0.4$ caused the decrease in the speed as the flame goes through the acoustic field.

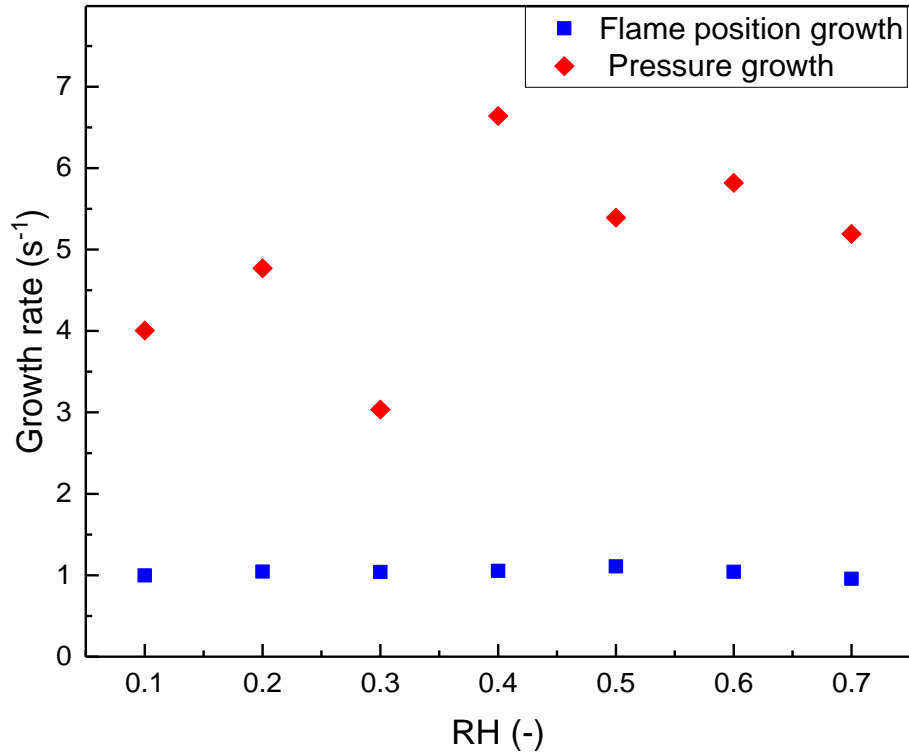


Figure 5.12: Flame growth rate at the different hydrogen addition (RH)

5.5 Flame propagation in longer tube

To further clarify the observation of the flame characteristics being a function of the tube as discussed above, the length of the tube was increased to twice the original length. For this experiment, propane fuel enriched with hydrogen at $\phi=1.2$ and $RH = 0.1$, was used because the pictures are brighter. The result for the flame position against time is shown in Figure 5.13. The two flames showed the same behaviour as the flame immediately after ignition propagates steadily, then become oscillated and finally, the flame became steady. Though, for the flame with the longer tube, there seemed to be the presence of a second oscillation almost at the far end of the tube. This second oscillation would happen if the length of the tube was increased beyond 130cm as indicated by the green circle in the figure.

The frequency plot of the flame is shown in Figure 5.14. As the length of the tube was increased, the frequency of oscillation reduces by approximately 40% of the frequency of the original tube length. Also worthy to note is that the frequency of the oscillating flame is approximately equal to the frequency of the standing wave in the tube ($\cong 245$ Hz for the tube of length equal to 130 cm and 132 Hz for the tube of length equal to 70 cm).

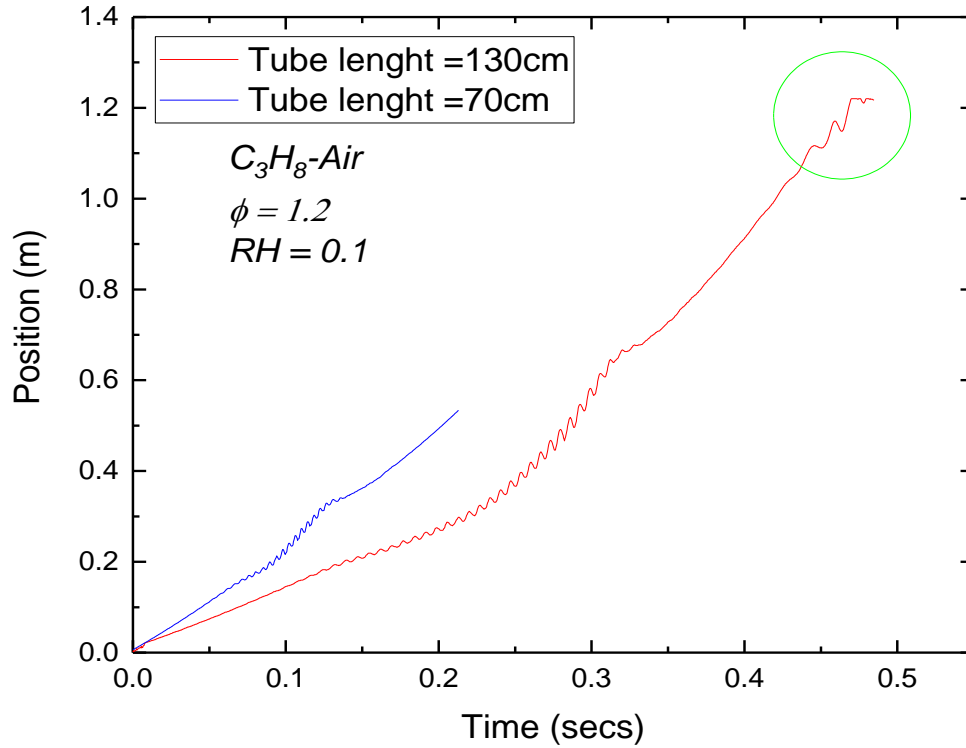


Figure 5.13: Propane/Hydrogen flame propagation at $\phi=1.2$ and $RH = 0.1$

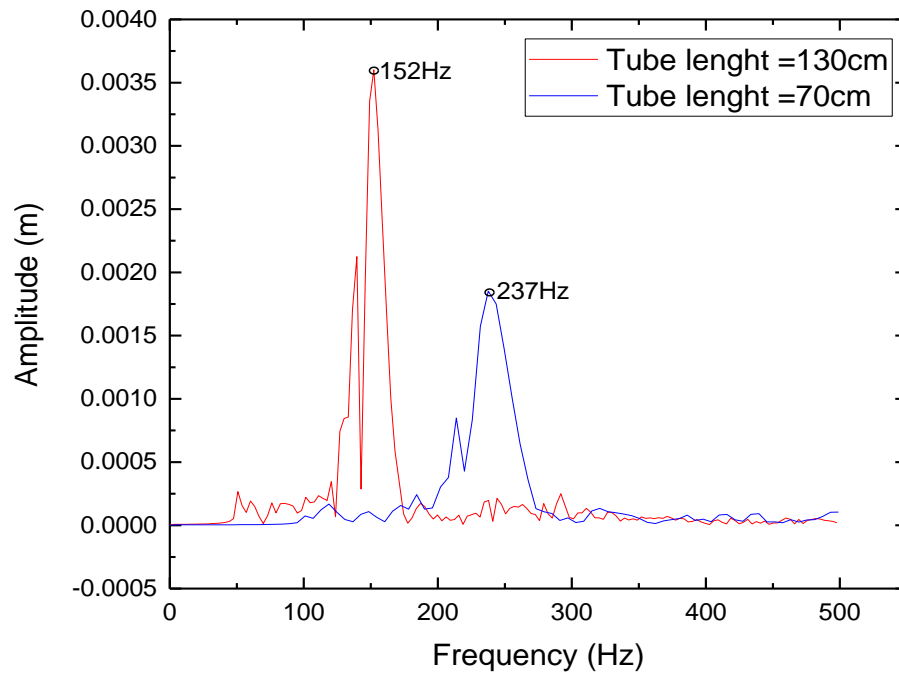


Figure 5.14: Propane/Hydrogen flame propagation frequency at $\phi=1.2$ and $RH = 0.1$

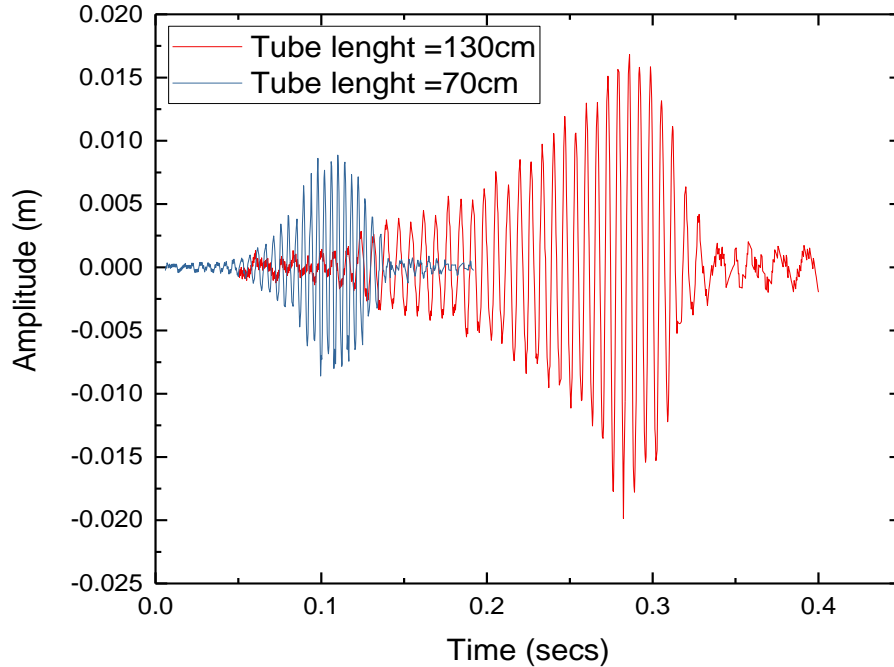


Figure 5.15: Propane/Hydrogen flame propagation oscillation amplitude at $\phi=1.2$ and $RH = 0.1$

This shows the evidence of the influence of the tube length and diameter on the characteristic of the oscillating flame. The frequency does not also depend completely on the fuel type used as the oscillating frequency for both methane/hydrogen-air flame and propane/hydrogen-air flame at $RH = 0.1$ are approximately the same. The amplitude against time plot of the oscillating flame for the two fuels is shown in Figure 5.15. The flame in the longer tube tends to have higher oscillation amplitude than the flame in the original tube as expected.

CHAPTER SIX

DOWNWARDLY PROPAGATING FLAME TOWARDS A CLOSED END

6.1 Introduction

In recent years, significant progress has been made in understanding the nature and characteristics of combustion/acoustic instability in premixed flames. One of the difficulty generally encountered, has been to interpret the interactions between the heat release fluctuation and the disturbances that initiate them (i.e. the boundary conditions). The heat release processes may be due to the fluctuation of the pressure, temperature, velocity, and reactants composition that is present simultaneously in the combustion system. In the previous chapters, horizontally propagating flames subjected to combustion/acoustic instability was presented. Results and discussions on how the temperature, pressure, and flame area effectively interact/react to the instabilities on the propagating flame. Referring to Figure 2.2, it can be generally said that the form of instabilities studies so far has been the secondary form of instabilities which is often more predominant in flames propagating in a horizontal channel. To effectively study both the primary and secondary form of instabilities, the flame was made to propagate downwards towards a closed end.

Downward propagating methane-air and propane-air flame towards a closed end over the ignitable range of equivalence ratio was studied in a 20mm tube. These flames have varying propagation behaviours at different point in the tube and at the different equivalence ratio. Synchronised data of the flame front position and the pressure signal were recorded. These data were plotted against time as a reference to a particular frame in the image sequence since it was not possible to define a consistent time zero, rather, the time the camera and the pressure signal were triggered was used.

6.2 Flame behaviour and Characteristics

Shown in Figure 6.1 are four distinct behaviours of all the flames studied propagating downwards from the top of a vertical tube towards a closed end. The corresponding pressure signal and flame front position recorded as a function of time for methane and propane over the ignitable range of equivalence ratios are shown in Figure 6.2(a to d).

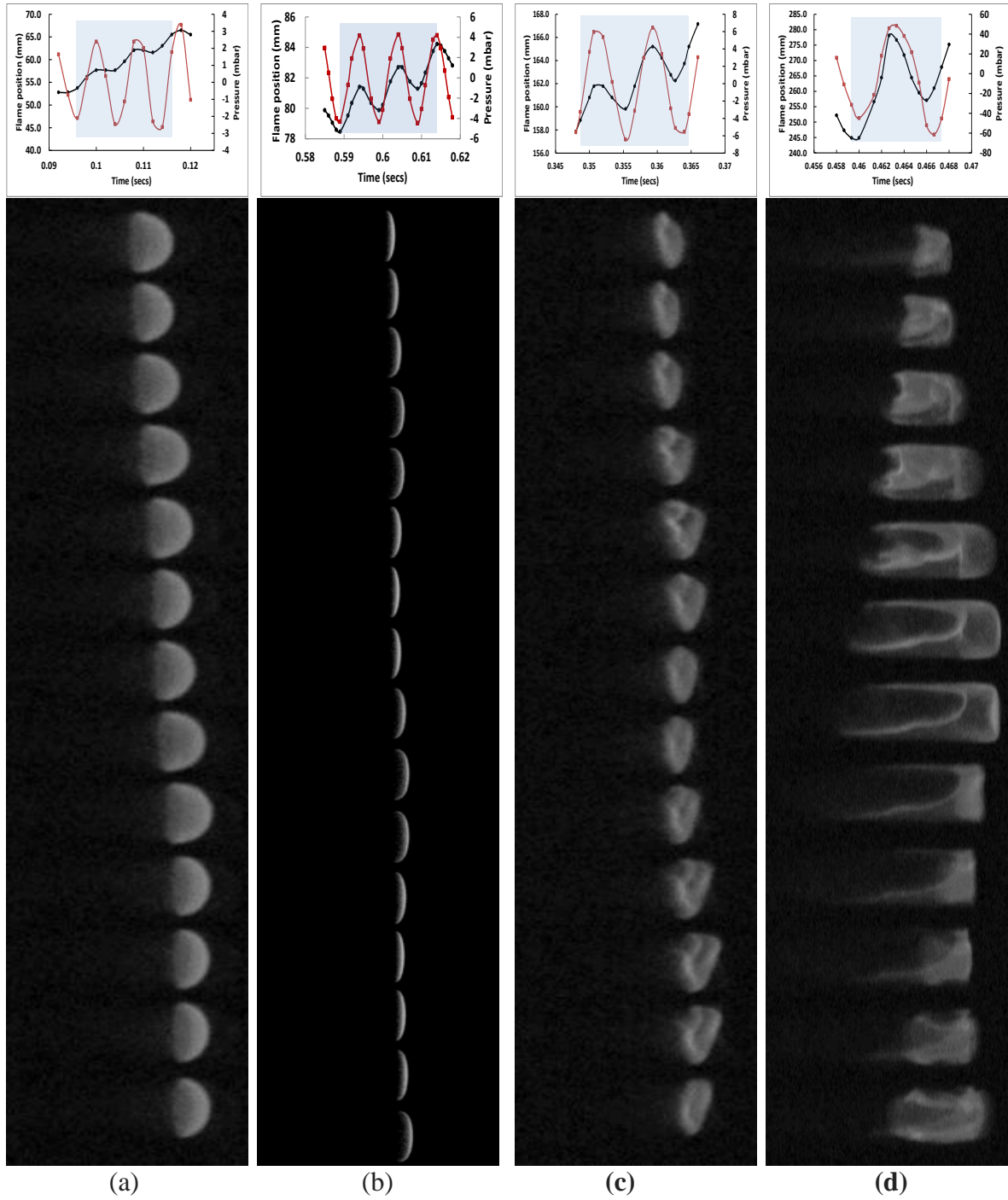


Figure 6.1: Propagating flame behaviour in the different regime at $\phi = 0.8$. (a) Curved flame (b) Flat flame during the low-level acoustical instability (c) cellular flame (d) shaken flame

Shown in Figure 6.1 (a) are flames that are curved and convex towards the unburned gas. These flames are indicative of the type 1 flames from Searby [7]; the flame propagated

steadily. This form of flame front was also observed in the upper portions of the tube before the onset of the acoustic instabilities for the entire equivalence ratio covered.

Shown in Figure 6.1(b) are typical flat flames close to the mid-point of the tube after the initial curved flame following the primary acoustic instability. This behaviour corresponds to the situation (2) in Searby's work. Shown in Figure 6.1(c) are faster flames with a short period of pulsating cellular flame that grew from a single cell to multiple cells ranging between 2 to 6 as the case may be which rotates over 4 to 6 cycles. The cellular flame then increased very rapidly in amplitude and pressure into a shaken flame as shown in Figure 6.1(d), before reaching the closed end of the tube.

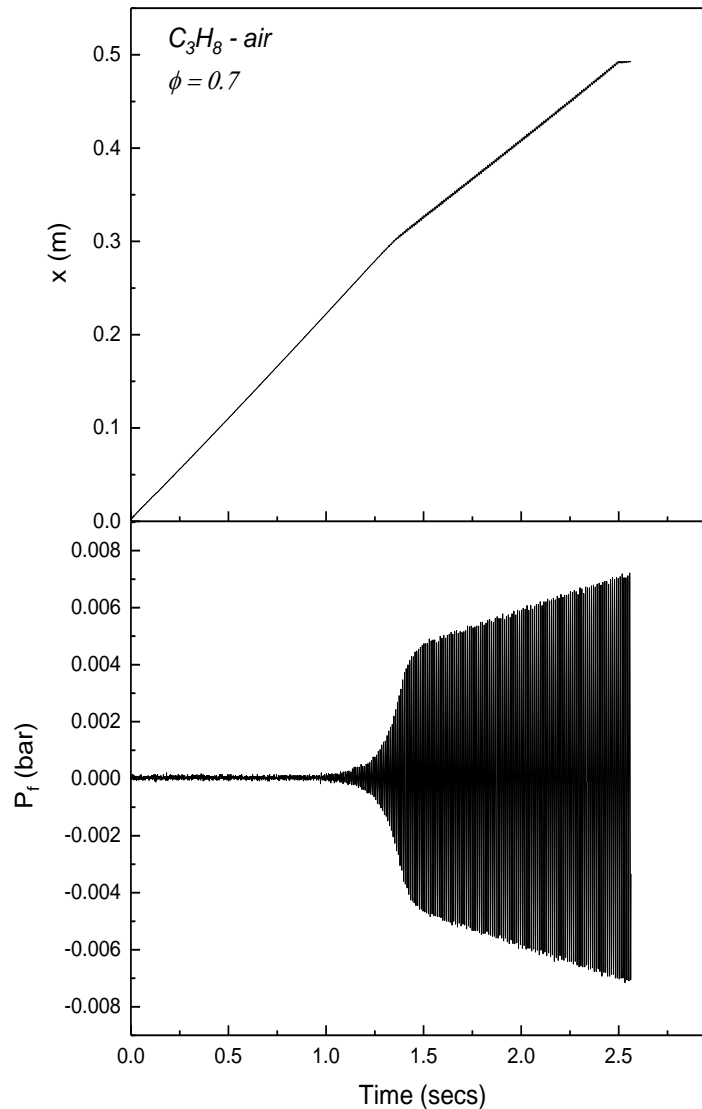


Figure 6.2(a): Relative flame position (x) and pressure variation (P_f) as a function of time

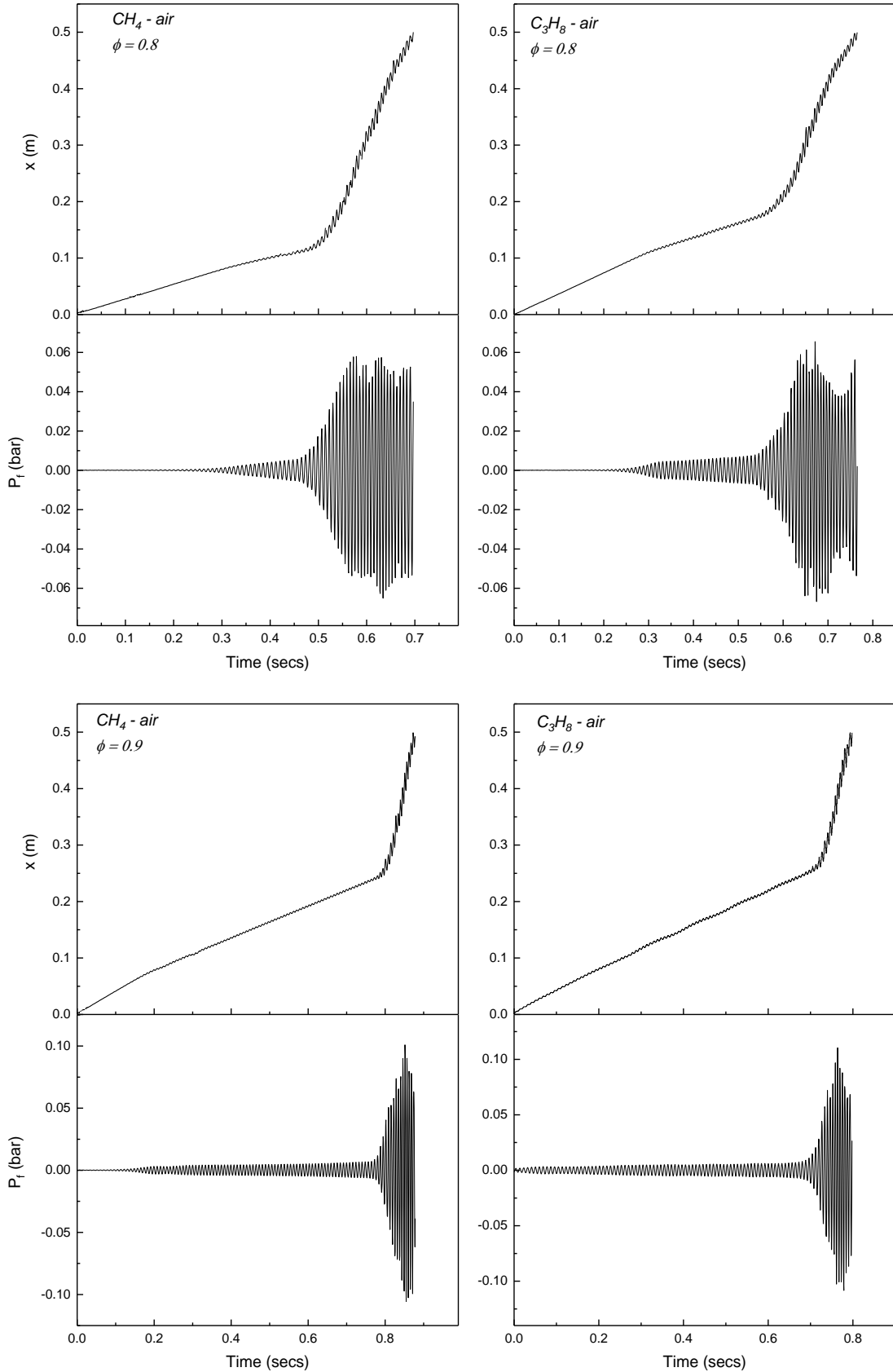


Figure 6.2(b): Relative flame position (x) and pressure variation (P_f) as a function of time

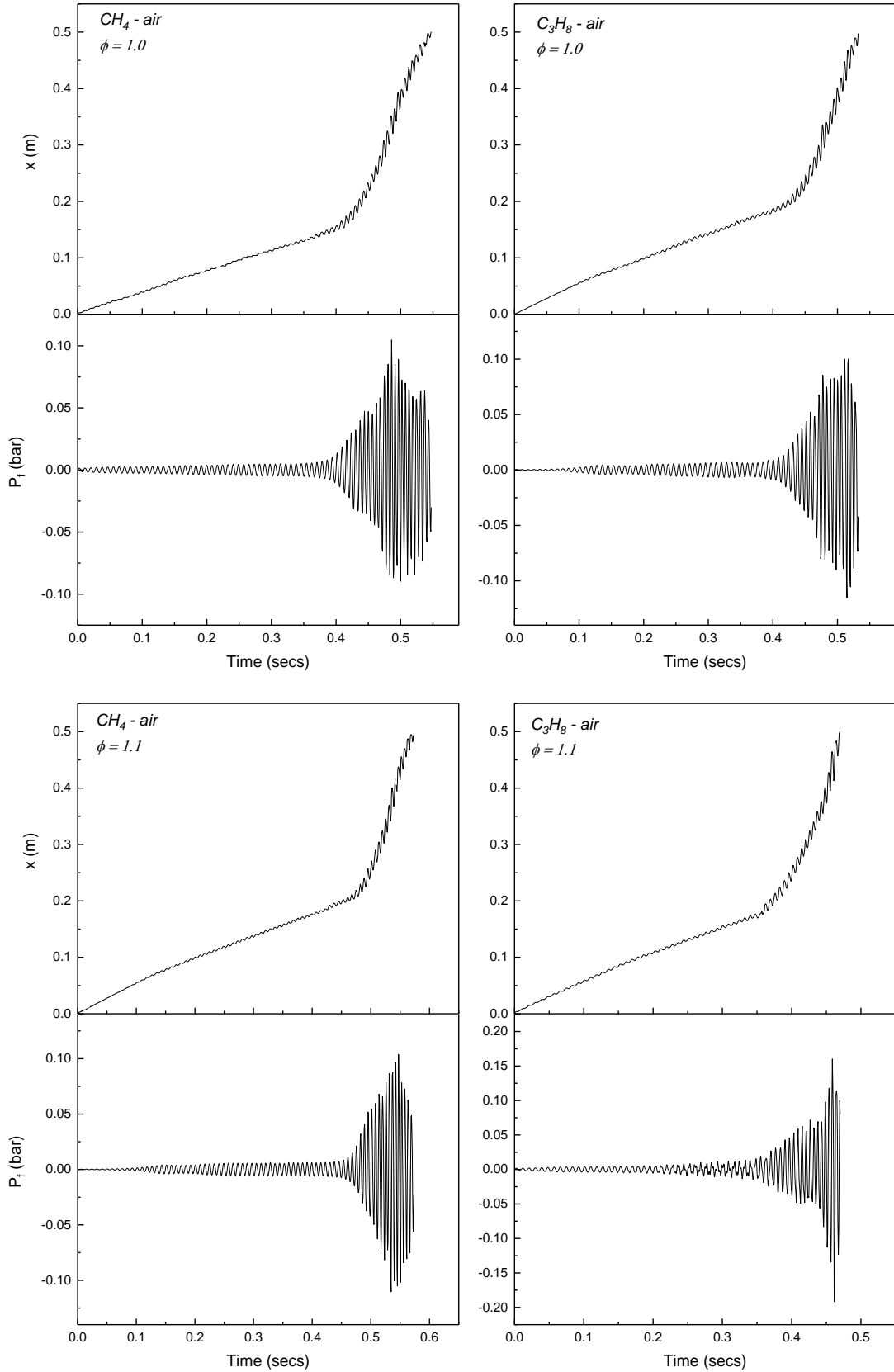


Figure 6.2(c): Relative flame position (x) and pressure variation (P_f) as a function of time

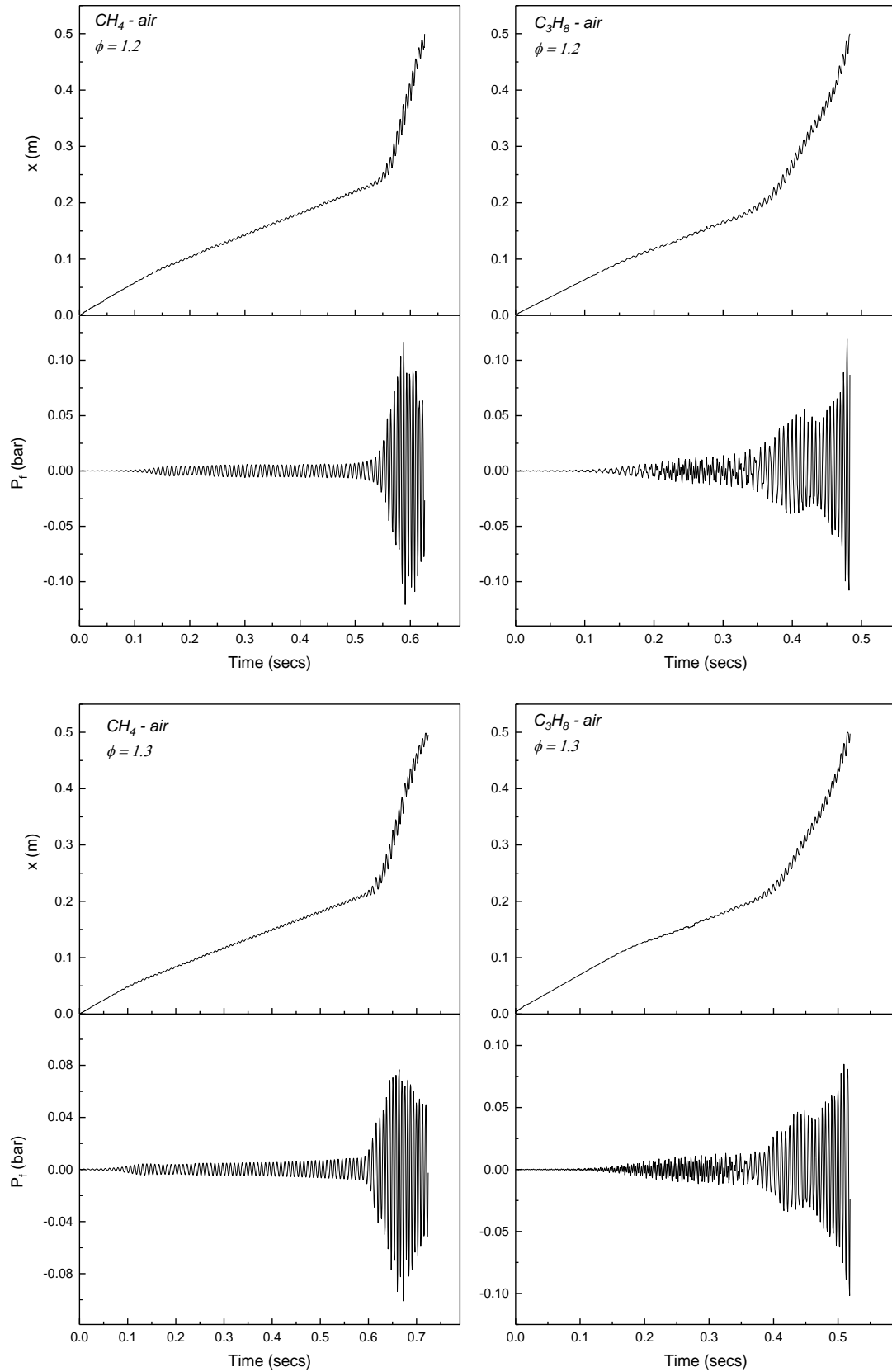


Figure 6.2(d): Relative flame position (x) and pressure variation (P_f) as a function of time

The complete summary of the flame characteristics for methane-air and propane-air flame is shown in Table 6.1. Both flames showed almost similar characteristics at both fuel lean and fuel rich conditions. It was not possible to show results for methane at $\phi = 0.7$, because it was difficult to ignite and when it did ignite, it was not possible to process the flame as it was not visible. All the flames from $\phi = 0.7$ to $\phi = 1.3$ starts propagating with a curved and steady flame and ends with a shaken flame except for $\phi = 0.7$, when the flame remained flat until the exit point. The flames from $\phi = 0.8$ to $\phi = 1.3$ for both fuels has cellular flames which rotates at some equivalence ratios and showed some form of tulips flames at some equivalence ratios.

Table 6.1: Characteristic behaviour of propane and methane at both lean and rich conditions

ϕ (-)	Flame characteristics	
	Methane	Propane
0.7		Curved flame and Flat flame
0.8	Curved flame, Flat flame, Cellular flame and Shaken flame	Curved flame, Flat flame, Cellular flame and Shaken flame
0.9	Curved flame, Flat flame Cellular flame with rotation and Shaken flame	Curved flame, Flat flame Cellular flame with rotation and Shaken flame
1.0	Curved flame, Cellular flame with rotation and Shaken flame	Curved flame, Cellular flame with rotation and Shaken flame
1.1	Curved flame, Cellular flame with rotation and Shaken flame	Curved flame, Cellular flame with rotation and Shaken flame
1.2	Curved flame, Cellular flame and Shaken flame	Curved flame, Cellular flame and Shaken flame
1.3	Curved flame, Cellular flame and Shaken flame	Curved flame, Cellular flame and Shaken flame

It was only the $\phi = 0.8$ and $\phi = 0.9$ flames that exhibits the characteristics of curved flame, flat flame, cellular flame and shaken flame. All the other equivalence ratios are characterised by curved flame, cellular flame with or without rotations/tulips and shaken flame, except $\phi = 0.7$ which has only curved and flat flame.

For further detailing of the flame behaviours, three different equivalence ratios with the four distinct flame behaviours are presented. Shown in Figure 6.3 are the flame acoustic pressure variation and relative flame position as a function of time for propane-air at $\phi = 0.7$. For this equivalence ratio, the flame has two behaviours; first the curve flame with a primary acoustic oscillation which occurs close to the middle of the tube, then a regime of flat vibrating flame during a low-level acoustic oscillation that remains flat until the end of the tube. The flame has an acoustic frequency of $\cong 100\text{Hz}$. The peak pressures were relatively constant over the time of filming the images. The transition from a curved flame to a flat flame occurred within a number of acoustic cycles during the primary acoustic instability, after which, the flame remains flat until close to the end of the tube.

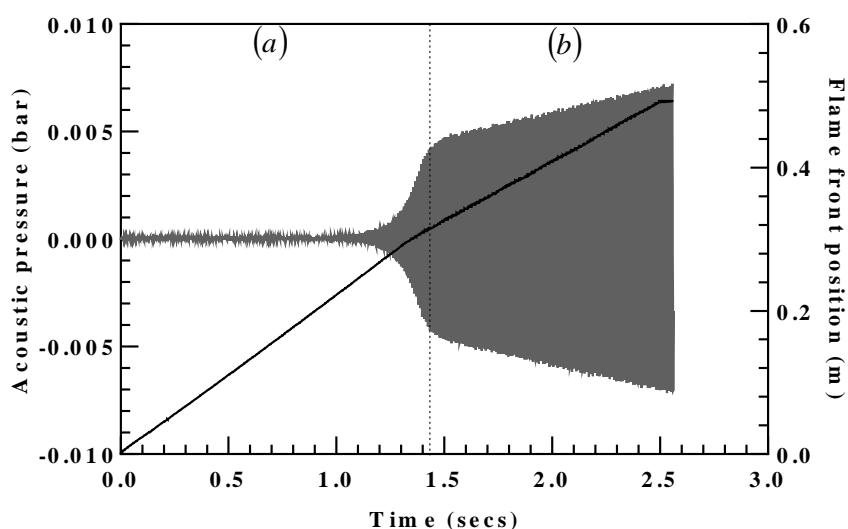


Figure 6.3: Pressure variation and relative flame position as a function of time for primary acoustically unstable flames at equivalence ratio of 0.7 and flame speed = 0.221 ms^{-1} . (a) Curved flame (b) Flat flame

The flame acoustic pressure signal and flame front position recorded as a function of time for propane-air flame at $\phi = 0.8$ is shown in Figure 6.4. It represents faster flames with the four different behaviours as it propagates down the tube. The flame propagation starts with

a curved flame up to one fourth the length of the tube usher in the primary acoustic oscillation close to the middle of the tube, then a regime of flat vibrating flame during a low-level acoustic oscillation, thereafter, a short period of pulsating cellular flame that grew from a single cell to multiple cells ranging between 2 to 6 as the case may be which rotates over 4 to 6 cycles leading to the secondary oscillation stage of high level acoustic oscillations and finally the speed of the cellular flame increased very rapidly in amplitude and pressure transforming into a shaken flame before reaching the closed end of the tube. The speed of the flame varies at the different regime of propagation and the flame oscillates at an acoustic frequency of $\cong 130\text{Hz}$.

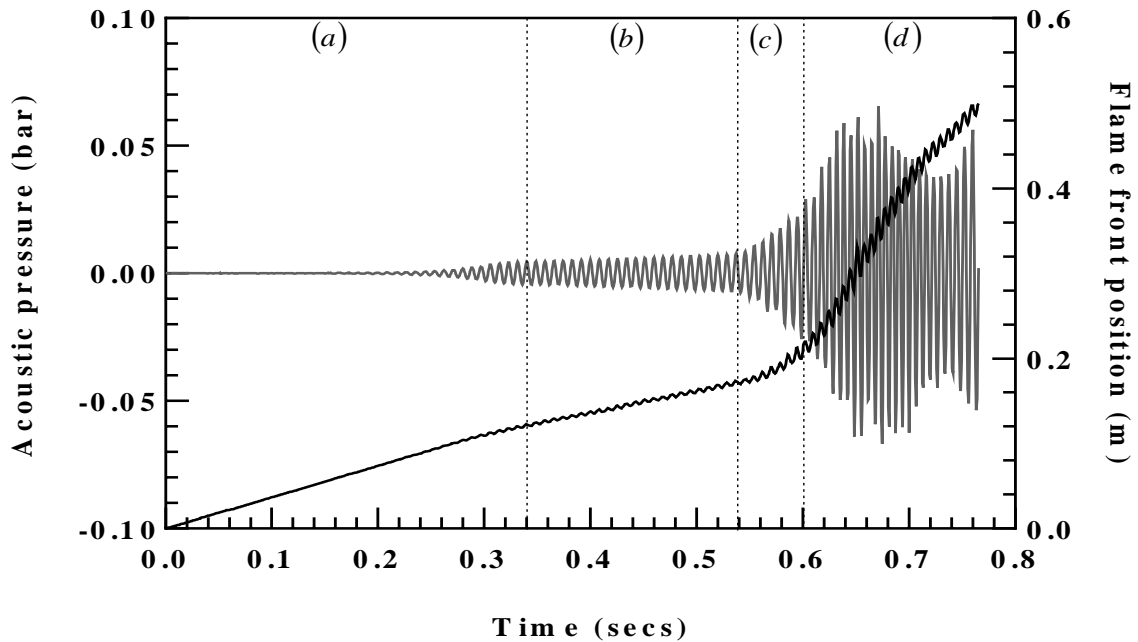


Figure 6.4: Pressure variation and relative flame position as a function of time for secondary acoustically unstable flames at equivalence ratio of 0.8 and flame speed = 0.318 m s^{-1} . (a) Curved flame (b) Flat flame (c) Cellular flame (d) Shaken flame

Shown in Figure 6.5 are the pressure variation and the relative flame front position as a function of time of flame with a continuous transition from primary to secondary acoustically unstable flames for a faster-propagating propane-air flame at $\phi = 1.0$ and flame speed of 0.434 m/s . These flames have only three regimes of propagation, first was the curved flame which sets in the primary acoustic oscillation before the middle of the tube and then a cellular structure that rotates about the centre of the tube for about 4 to 6

acoustic cycle with varying number of cells being formed and destroyed continuously, and immediately followed by a secondary acoustic oscillations. The speed of the flame at this different regime also varies and the flame oscillates at an acoustic frequency of $\cong 170\text{Hz}$.

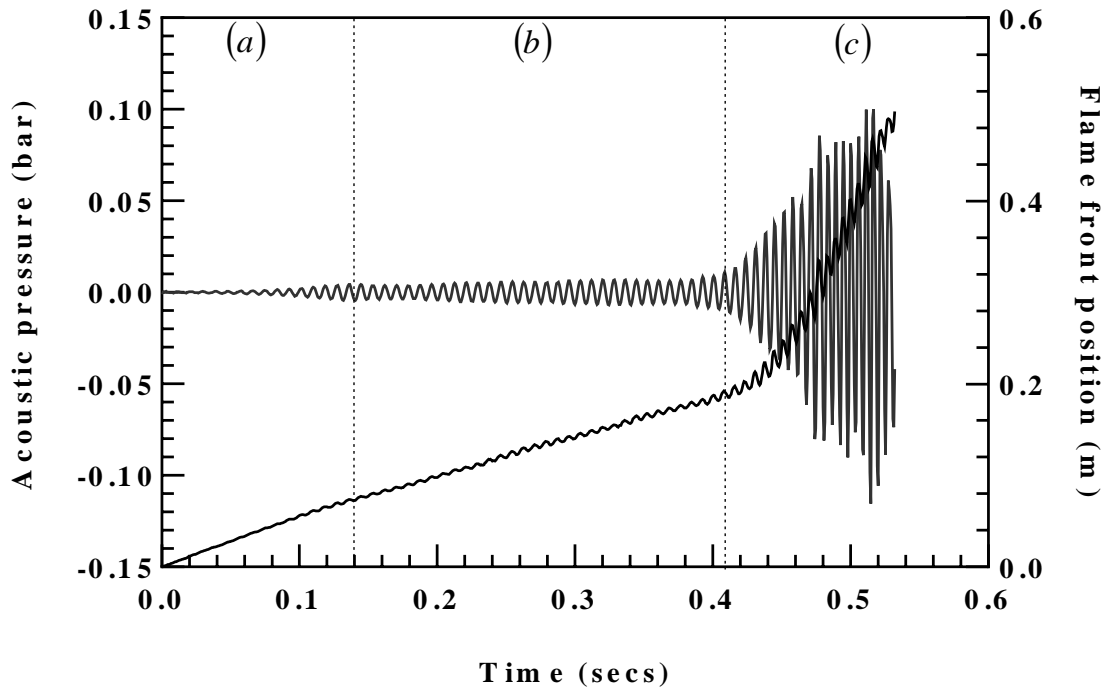


Figure 6.5: Pressure variation and relative flame position as a function of time for flame with continuous transition from primary to secondary acoustically unstable flames at equivalence ratio of 1.0 and flame speed = 0.429 ms^{-1} . (a) Curved flame (b) Cellular flame (c) Shaken flame

6.2.1 Flame rotational behaviour

Some of the flames with cellular structures were observed to rotate with some of them forming a tulip structure. Shown in Figure 6.6 and Figure 6.7 are selected frames from a high-speed recording of the flame front during the cellular structure formation of the flames. The cellular structure was seen rotating along the central axis of the tube. The direction of the rotation is not fixed as at some equivalence ratios the flame rotates clockwise as shown in Figure 6.6 and at some other equivalence ratios, the flames rotate in the anti-clockwise direction as shown in Figure 6.7.

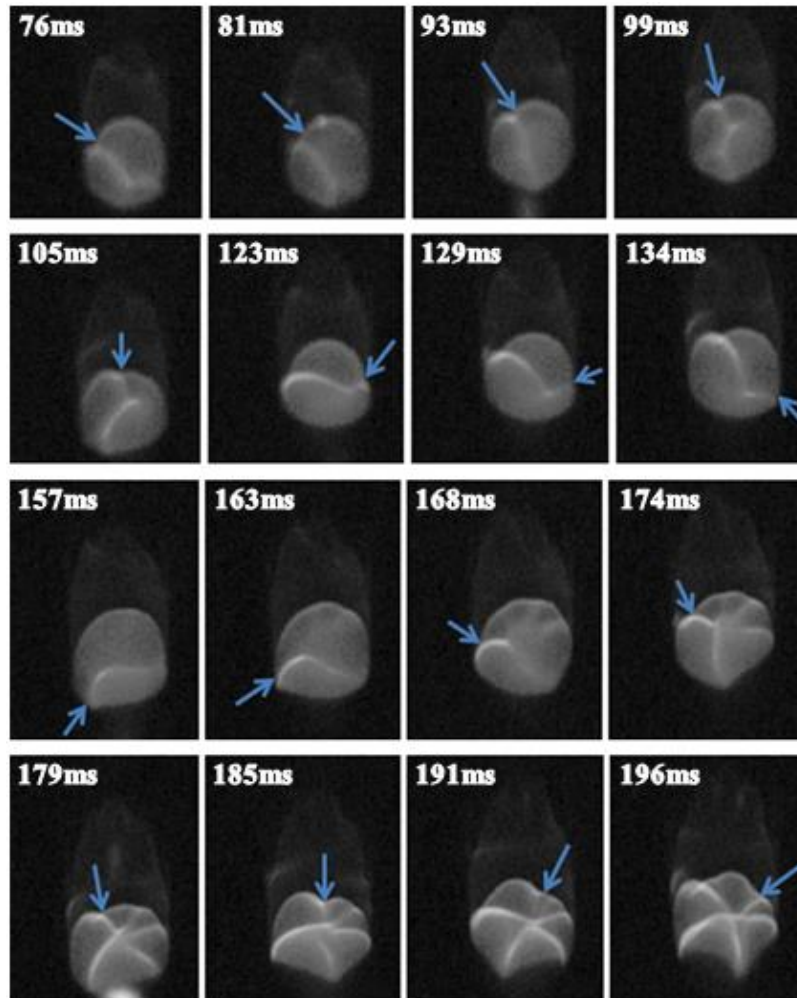


Figure 6.6: Downwardly propagating cellular flame rotating clockwise

The period of rotation is usually short as the pulsating cellular flame grows from a single cell to multiple cells ranging between 2 to 6 and rotates over 4 to 6 cycles at an average angular speed of approximately 68 radians/sec, leading to the secondary oscillation stage of high-level acoustic oscillations which rapidly increase in amplitude and pressure transforming into a shaken flame before reaching the closed end of the tube.

The flame rotation was observed for both methane-air and propane-air flame. Kadowaki and Hasegawa [136] had observed the cellular front is formed if the inlet velocity of the flame is equal to the velocity of the cellular flame and that the cellular flames are generated by the interactions of the hydrodynamic, body-force and diffusive-thermal effects, hence, the characteristics cell size, flame-surface area, cell depth, and flame velocity of the cellular flames depend on the adiabatic flame temperature, acceleration, and Lewis number. This is

in agreement with the results of this work as the maximum number of cells were observed when the flame area increased. Therefore, the breaking and forming of the cells could be related to the diffusive thermal effect which causes the lateral movement of the flame thereby breaking the cell line of symmetry. However, Deshpande and Kumar [88] who also observe the presence of the spinning/rotating flame in a tube have stated that the spinning was a result of the escaping unburned mixture from the dead space near the tube wall.

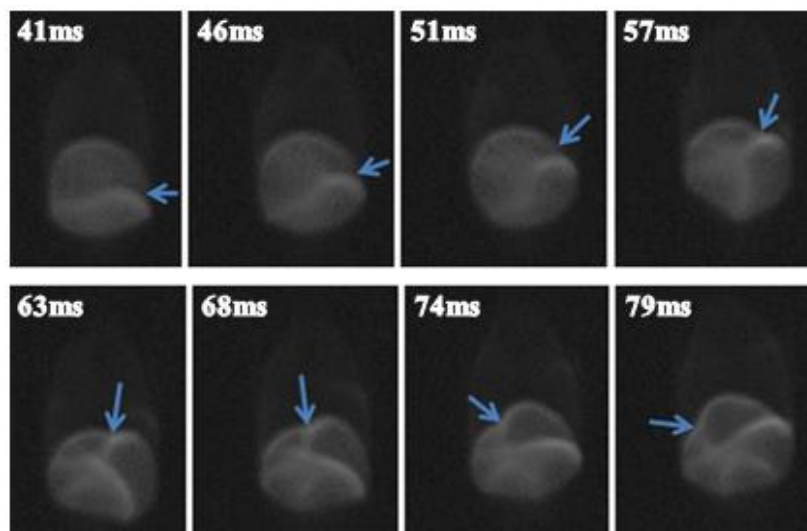


Figure 6.7: Downwardly propagating cellular flame rotating anti-clockwise

6.2.2 Flame Rayleigh Taylor analysis

Shown in Figure 6.8 are images from the high-speed video of the flame subjected to Rayleigh-Taylor instability. As the flame propagates, there are two incompressible fluids (fluids at the burnt side of the tube and fluids at the unburnt/fresh gas side of the tube) of different densities separated by an interface (flame front) which is subjected to oscillation. The evolution of the Rayleigh–Taylor instability starts with the formation of a U shape flame where the perturbation amplitudes are small compared to their wavelengths. However, after the end of the first stage of U-shaped flames, as nonlinear effects start to set in, the beginning of the formation of the tulip flame where the heavy fluid starts growing into the lighter fluid was observed. This movement of the heavier fluid into the lighter fluid continues, resulting in a growth and the heavier fluid begin to interact with the lighter fluid which eventually develops into a region of turbulent mixing that leads to the

secondary oscillation. The formation of the U-shape which then transform to a tulip flame occurred in about 2 to 6 cycle depending on the equivalence ratio of the flame before eventually developing into a turbulent/shaken flame (Figure 6.8a).

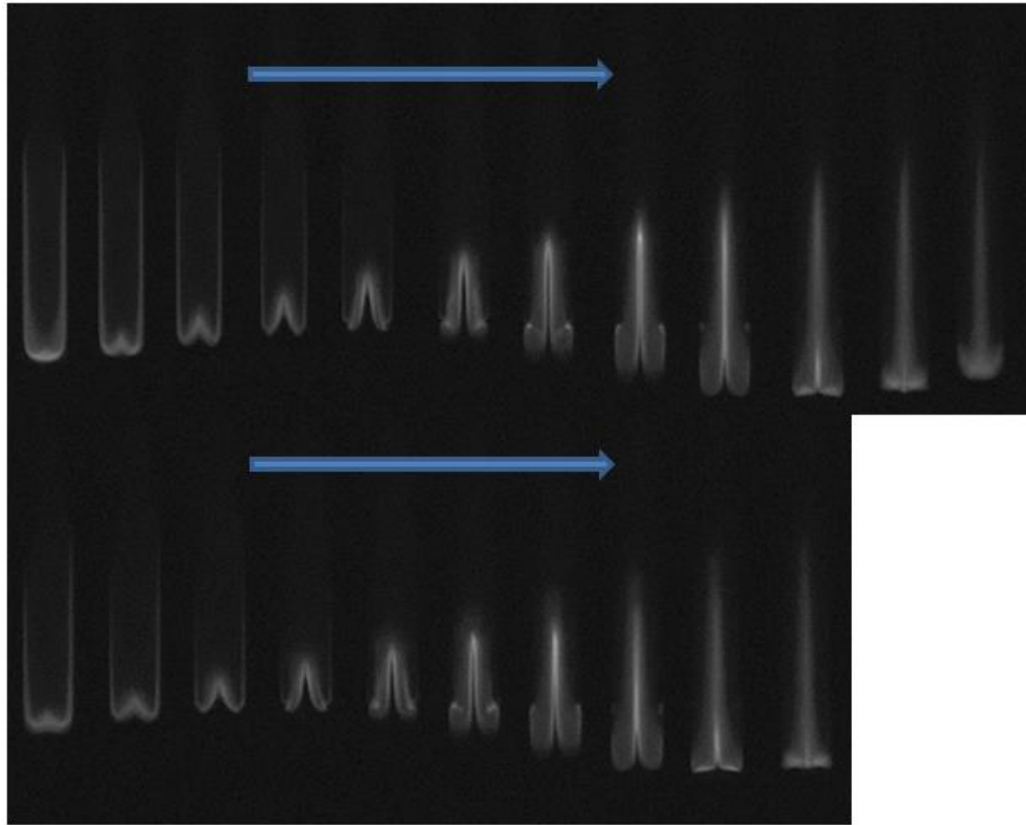


Figure 6.8a: Downwardly propagating cellular flame subjected to R-T instability

Violent folding of the flame front has been observed in a flame acoustic resonance for a flame propagating in a tube from an open end to a closed end [73]. The presence of Rayleigh–Taylor instability was strongly detected and the formation of ‘blobs’ of the burnt matter being pushed into the fuel-air mixture was also observed. When the flame propagated forward, there was also a proportionate expansion and contraction of the flame and vice versa as shown in Figure 6.8b. This is such that, the flame forward movement was the combination of the flame simultaneously expanding from the front and the back and the flame backward movement was also the result of the flame simultaneously contracting from both the flame front and back.

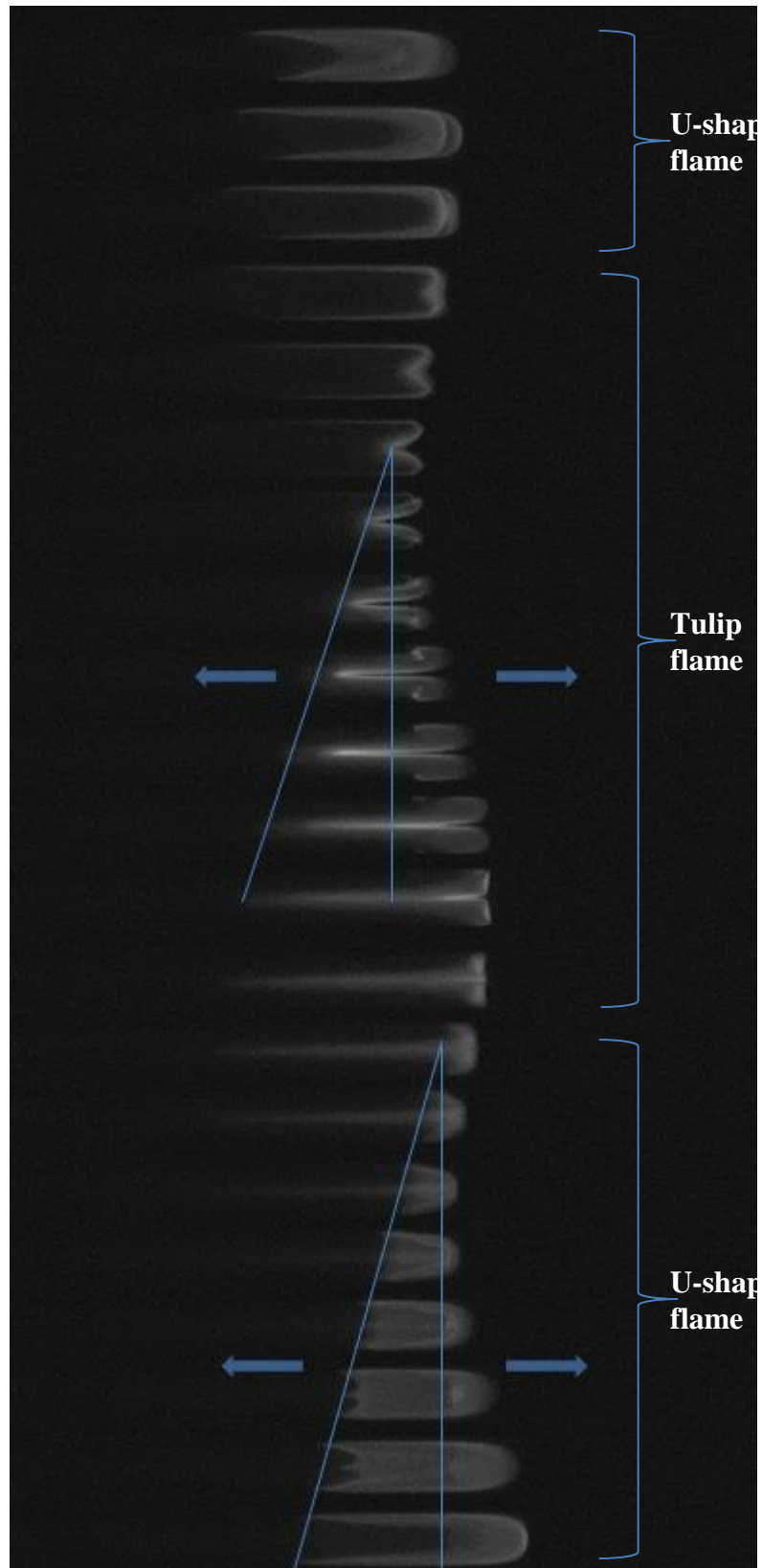


Figure 6.8b: Downwardly propagating cellular flame subjected to R-T instability

The speed with which the flame moves backwards when subjected to the Rayleigh–Taylor instability was determined for some of the flames as shown in Figure 6.9. The instability as seen in the flame tends to occur at a constant speed for a certain time period and dies off before the next wave comes in. The period at which the flame was subjected to the instability was always constant at every instant tested. It is thought to be some sort of wave which pushes the unburnt gas mixture into the burnt gas mixture constantly without a stop. On average, the speed of propagation of the flame into the burnt gases was approximately 14 m/s. This speed is larger than the laminar burning speed of the flame.

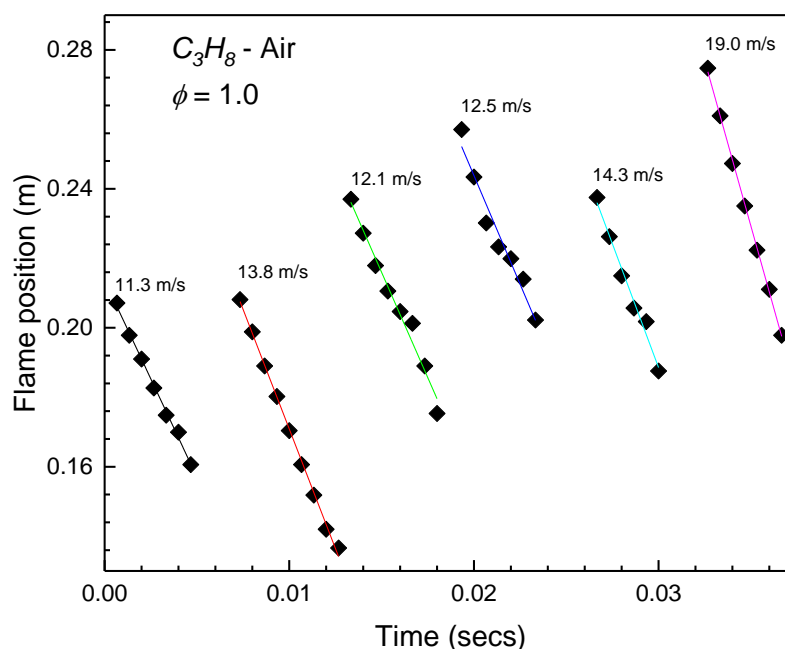


Figure 6.9: Downwardly propagating cellular flame subjected to R-T instability

Further analysis to investigate the underlying mechanism driving the flame propagation speed showed that the change in the flame acoustic pressure drives the measured flame speed and this is the same through the beginning of the flame propagation to the end. There is no effective flame damping going on at the point where the flame is subjected to secondary oscillation. A plot of selected points of the flame acoustic pressure and its corresponding velocity at constant time as shown in Figure 6.10 indicates the characteristic behaviour between the flame position hence the flame velocity and the flame acoustic pressure is governed by the Bernoulli's equation. There seemed to be a linear relationship

between the flame acoustic pressure and the square of the flame speed, showing no effective damping in the flame propagation due to the oscillation.

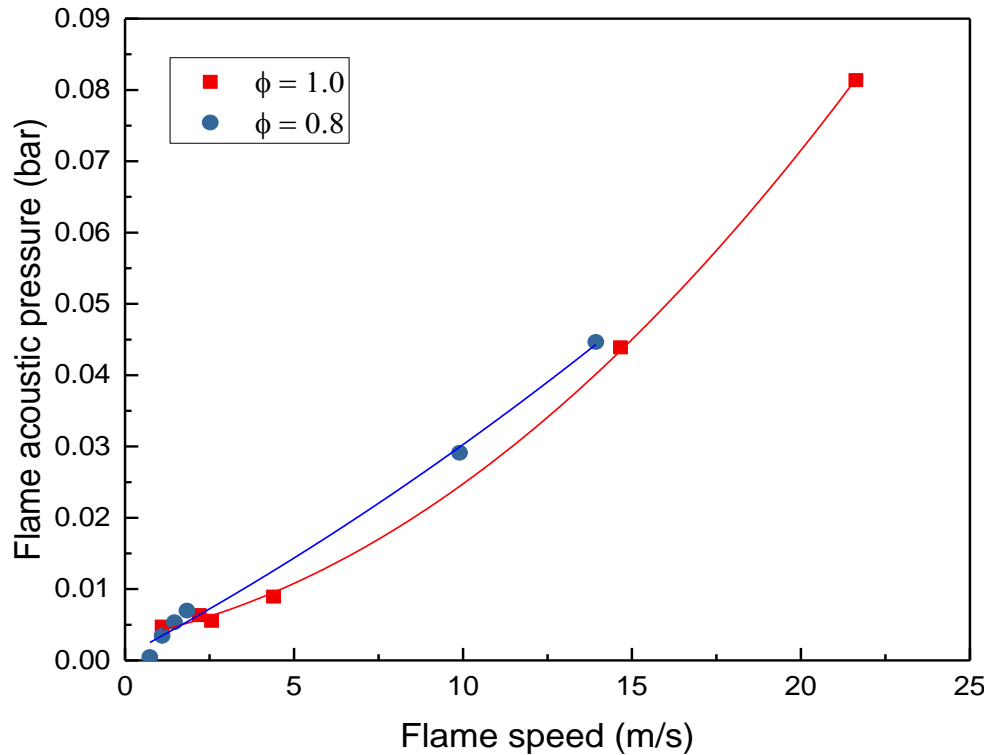


Figure 6.10: Downwardly propagating cellular flame subjected to R-T instability

6.2.3 Flame pressure and frequency characterisation

The maximum pressure attained by the propagating flame at each regime (the primary acoustic oscillation regime, secondary acoustic oscillation regime and the peak pressure oscillation attained after the secondary acoustic oscillation regime) and for all equivalence ration covered is shown in Figure 6.11 for both methane-air and propane-air. Figure 6.11a shows the ratio of the maximum attained pressure of the flame to the maximum pressure attained at the primary acoustic oscillation regime against equivalence ratio. The maximum pressure attained by the flame increased as the equivalence ratio increased and peaked between $\phi = 1.0$ and $\phi = 1.1$ for both methane-air and propane-air and as the flame get richer, the pressure starts dropping. Though both flame has the same trend, the maximum pressure attained by propane tend to be higher around stoichiometric but when the flame became richer or leaner, the maximum pressure attained by methane became higher.

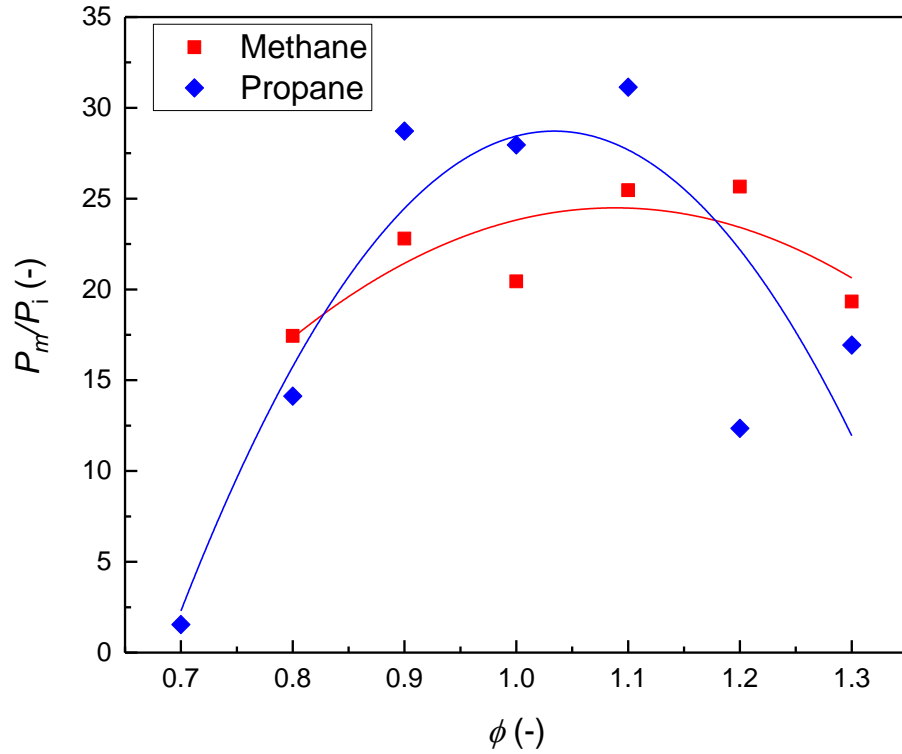


Figure 6.11a: Maximum pressure of flame primary acoustic oscillation against ϕ .

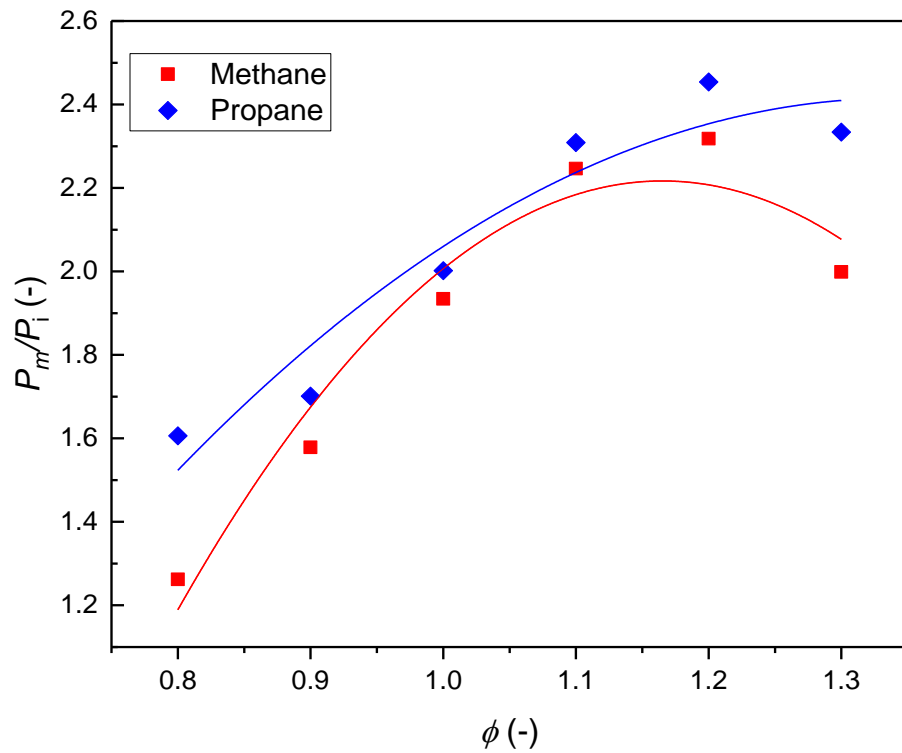


Figure 6.11b: Maximum pressure of flame secondary acoustic oscillation against ϕ .

The same trend of the maximum flame acoustic pressure attained for the primary acoustic oscillation regime was also seen in the secondary acoustic oscillation regime (Figure 6.11b). The pressure increased as the equivalence move from the lean region into the rich region then peaks before a decrease as the flame became richer.

The frequency of the propagating flame for methane-air and propane-air is also shown in Figure 6.12. The frequency increased slightly as the equivalence ratio of the flame increased, hence, though the frequency might be a characteristic of the tube, a change in the chemistry of the propagating flame slightly changes the frequency of the flame.

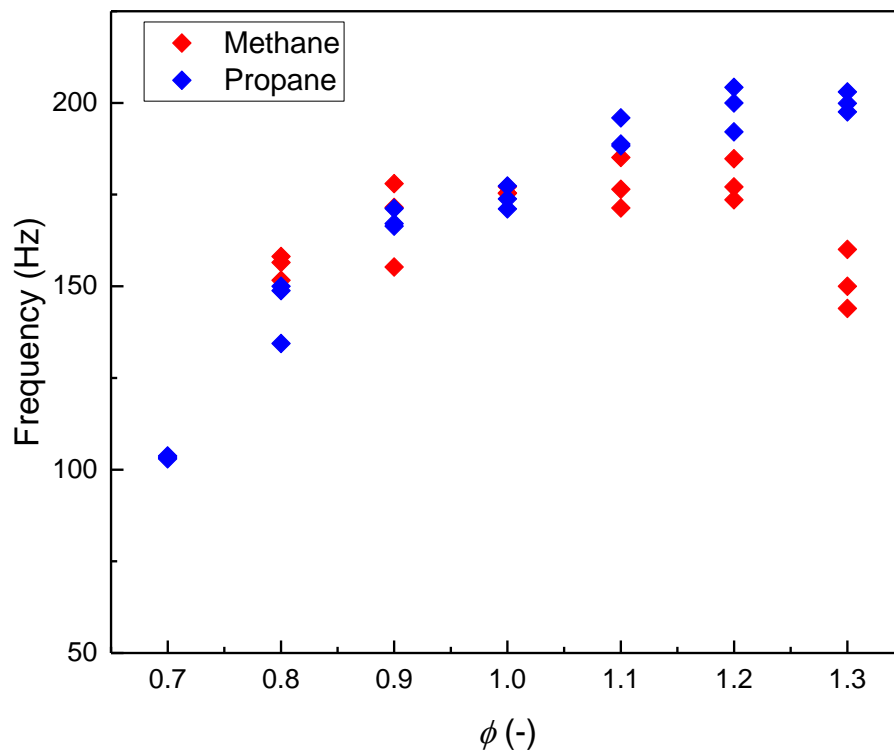


Figure 6.12: Oscillating frequency against ϕ for propane and methane.

6.3 Flame growth rate and acoustic loss

The experimentally measured growth rates for both the pressure and the flame front position are plotted as a function of the equivalence ratio for methane-air and propane-air flame at the primary oscillation regime and the secondary oscillation regime as shown in Figure 6.13 (a,b,c and d). The pressure growth rate for both the primary and secondary oscillations was compared for both fuel and found to be averagely similar in the lean regime. As the fuel becomes rich ($\phi = 1.1$ to $\phi = 1.3$), while the primary and secondary

growth rate of propane remain relatively constant for all ϕ , that of methane was only relatively constant for the primary growth rate and changes in a non-uniform order for the secondary growth rate. The reason for the discrepancy in the growth rate as the flames reaches the secondary oscillation regime is not clear, however, a possible explanation could be the increase in the flame surface area that could lead to an increase in the total gas consumed, hence a sudden acceleration of the unburned gas that invariably increase the growth rate of the instability. This result is in agreement with Searby's [7] growth rate using similar approach for its computation. The flame front position growth rate is constant with an approximate value of 1 s^{-1} for both methane-air and propane-air flame at all equivalence ratios tested. This result is in agreement with the computational result for the adiabatic pressure coupling mechanism of Clavin et al. [44], which is of the order of 1 s^{-1} , if all acoustic losses are neglected. The secondary flame front position growth rate showed some form of scatter but still within an acceptable range; hence it is also thought to be similar.

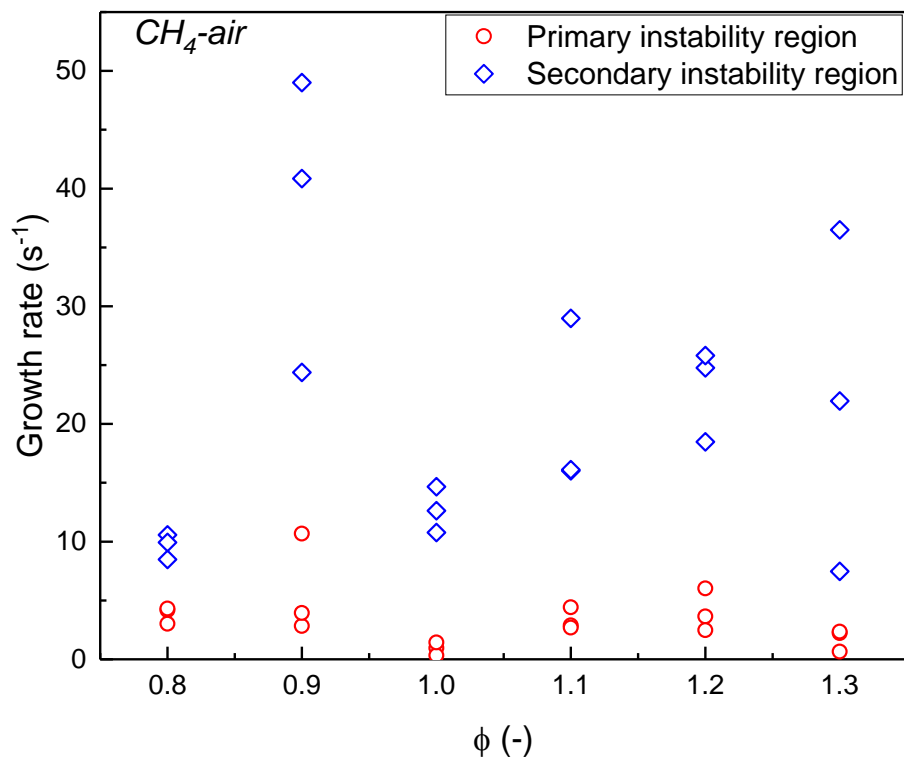


Figure 6.13a: Pressure growth rate for methane-air flame against equivalence ratio

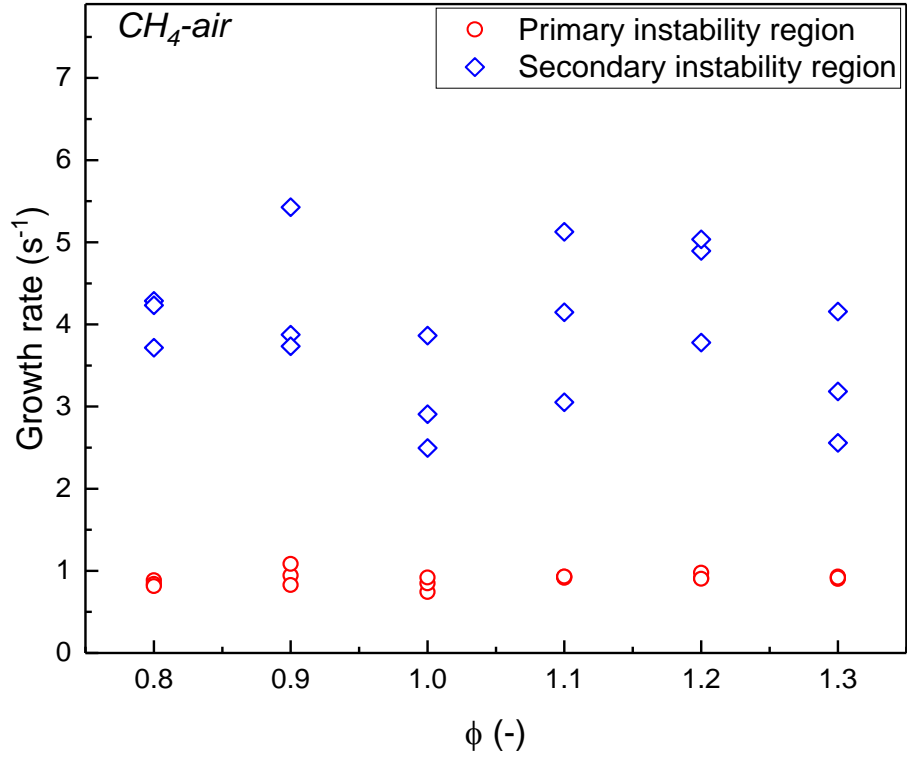


Figure 6.13b: Flame front position growth rate for methane-air flame against equivalence ratio

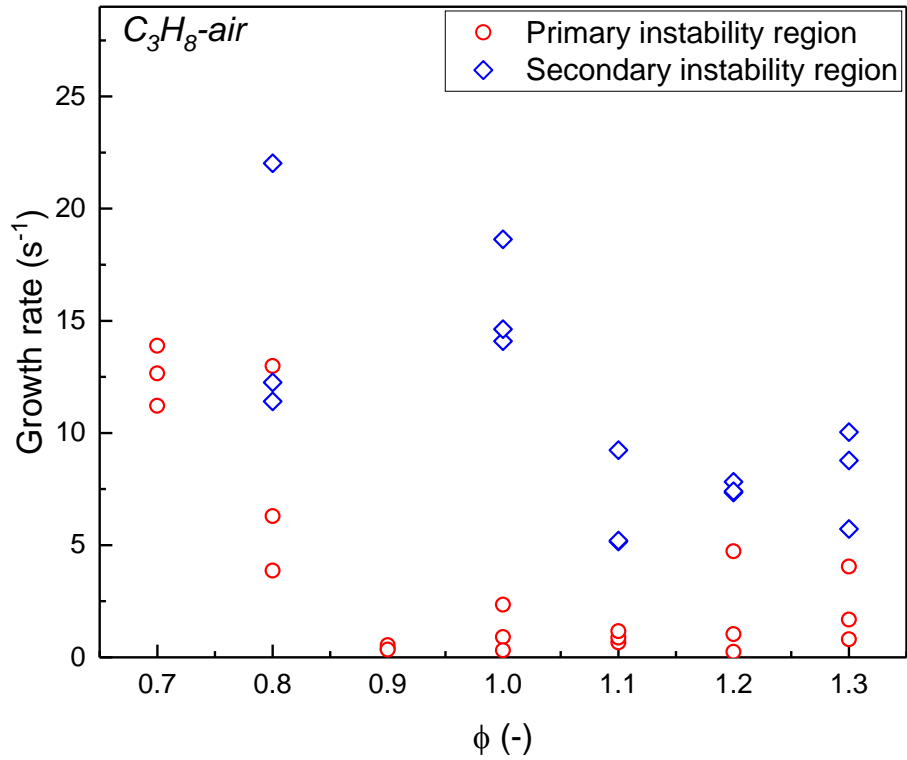


Figure 6.13c: Pressure growth rate for propane-air flame against equivalence ratio

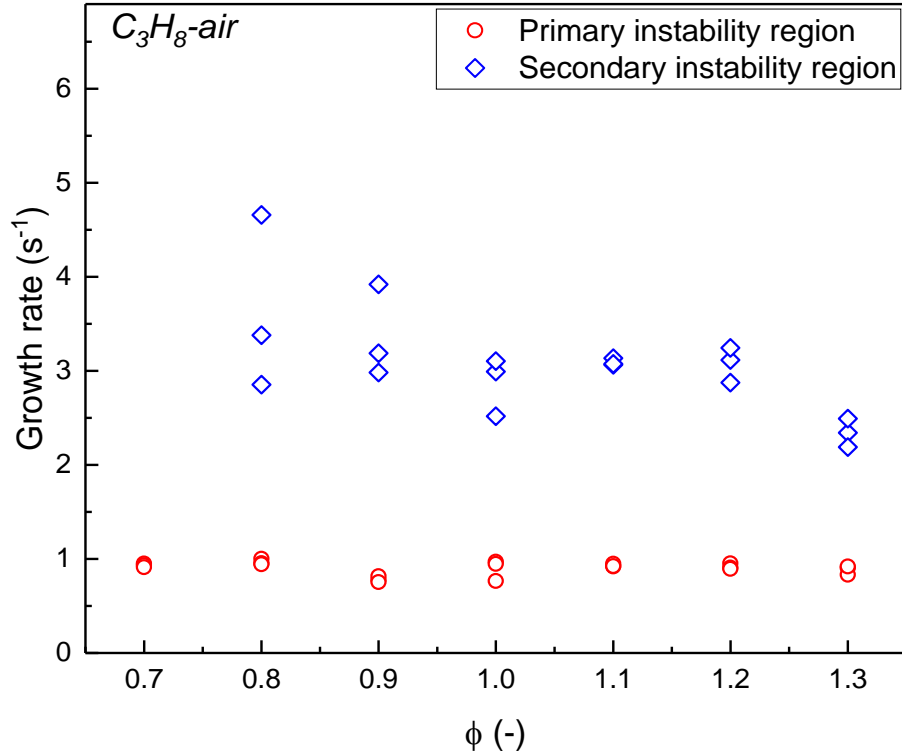


Figure 6.13d: Flame front position growth rate for propane-air flame against equivalence ratio

It is generally impossible to avoid natural acoustic process in flame propagation in tubes where one end or both ends are closed. The acoustic process, in this case, consists of radiative losses at the open end and wall losses. For the radiative losses, there is a lesser radiation losses time on the lean and rich region which peaks at $\phi = 1.1$ for both propane and methane with propane having higher losses time compared to methane (Figure 6.14a).

For the wall losses (Figure 6.14b), as the flame became rich, the kinematic viscosity and the thermal diffusivity continue to increase. Similarly, there was an increase in the angular speed with a corresponding increase in the wall losses time for lean mixture which peaks at $\phi = 1.1$ and then decreased as it get richer for both propane and methane mixtures. Figure 6.15, shows the total acoustic losses time versus the equivalence ratio. The total acoustic loss time decreased for both leaner and richer mixtures which peak at $\phi = 1.1$.

Shown in Figure 6.16 are the comparison between the characteristics times for total acoustic losses measured for propane and methane versus acoustic angular speed. The total acoustic losses time increased as the angular speed of the flame was increased for both methane and propane fuel. Therefore the generation of acoustic energy for propane was

smaller than that of methane in comparison with the natural damping effect produced by the flames.

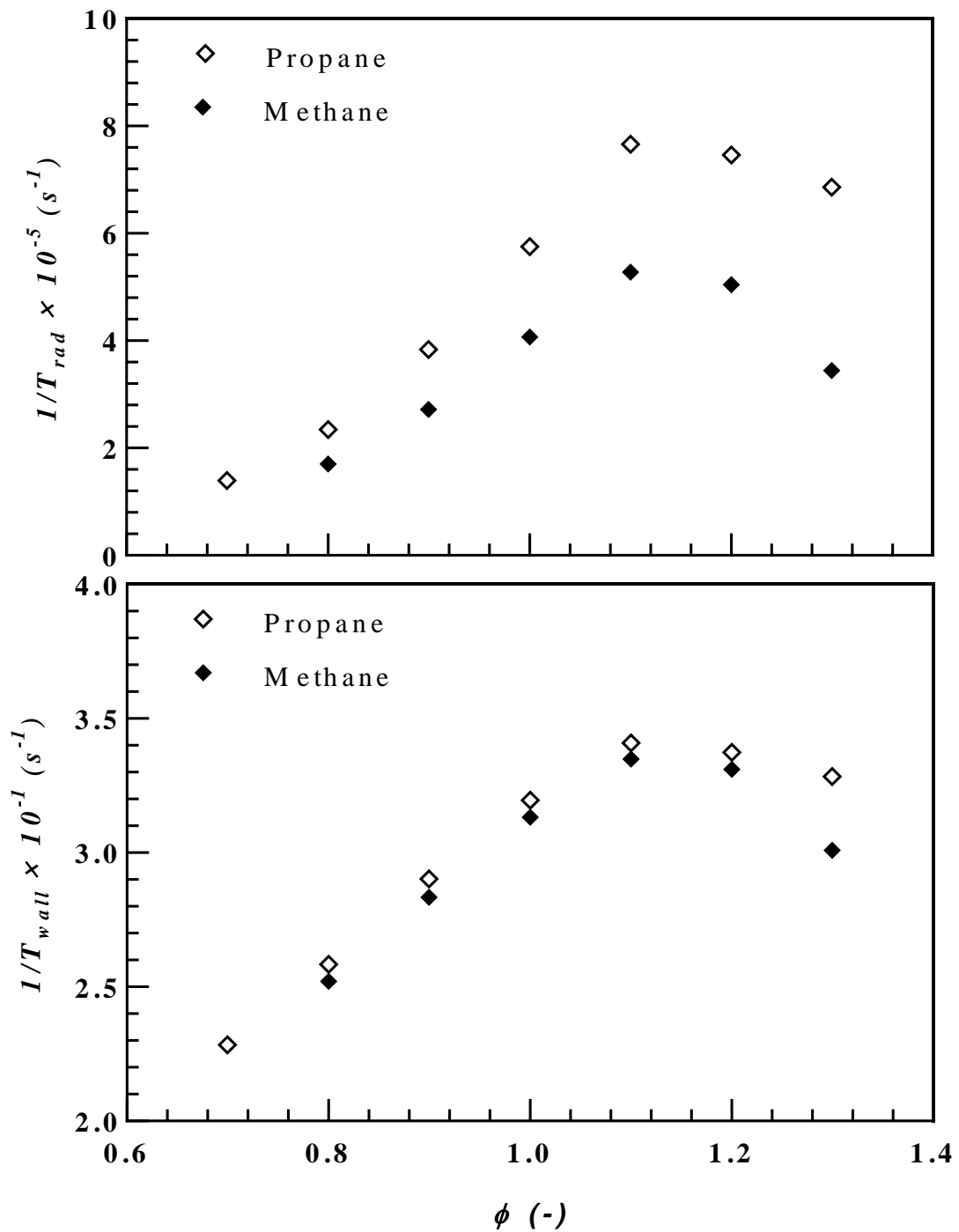


Figure 6.14: Comparison between the characteristic times for acoustic losses measured for propane and methane versus equivalence ratio (a) radiative losses and (b) wall losses.

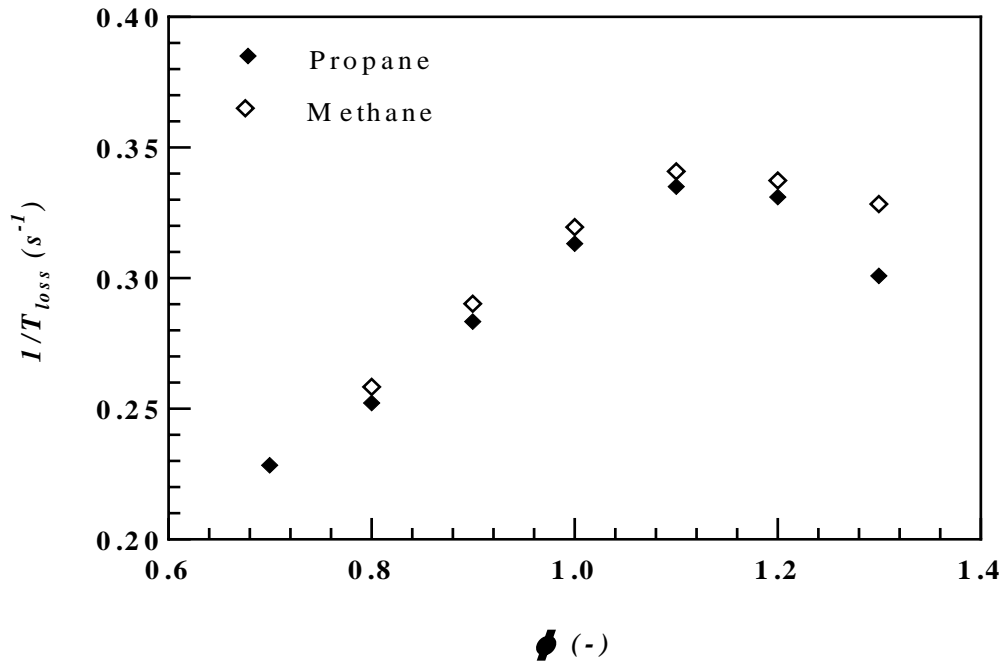


Figure 6.15: Comparison between the characteristic times for total acoustic losses measured for propane and methane versus equivalence ratio.

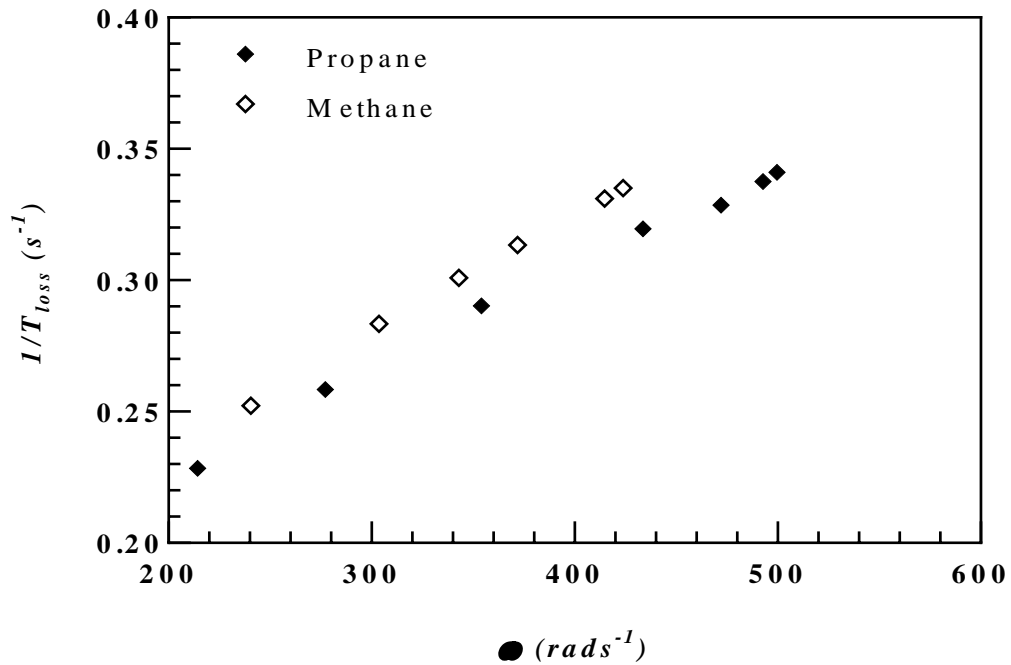


Figure 6.16: Comparison between the characteristic times for total acoustic losses measured for propane and methane versus acoustic angular speed.

6.4 Flame oscillation analysis

A further analysis has been performed on the flame front position of the flames with $\phi = 0.7$, $\phi = 0.8$ and $\phi = 1.0$, as these three flames showed the four characteristic behaviours of the flames in [7] and this is shown in Figure 6.17. The flame front position plotted against time is shown in Figure 6.17(a). The flame front positions for all three flames are approximately the same as the flames propagate throughout the entire tube length. The flame acoustic pressure oscillation is shown in Figure 6.17(b) with the primary acoustic oscillation and the secondary acoustic oscillation where applicable, clearly shown. To check the synchronisation of the flame front position and the flame acoustic pressure signal, a phase difference analysis was carried out as shown in Figure 6.17(c). Both signals seemed to be slightly out of phase as the flame traverses the acoustic field, though because of the noise level and the quality of the flame signal at the beginning of propagation, it was not clearly what was happening at that point. A low pass FFT filter was applied to the flame position and the result subtracted from the original data to give Figure 6.17(d), which is the amplitude of the high frequency oscillations of the flame front, a . In the three cases, the presence of the primary acoustic oscillation and the secondary acoustic oscillation are evident. The frequency of the oscillations were found to be approximately 100 Hz for $\phi = 0.7$, 130 Hz for $\phi = 0.8$ and 170 Hz for $\phi = 1.0$, therefore it is suspected the flame chemical composition modulates the flame behaviour and depend on the boundary condition the flame is subjected since these values are different from the frequency of the standing waves in the tube. This would be discussed in the next sub section.

The maximum amplitude fluctuation in the flame front position increases as the flame equivalence ratio was increased and the reacting flame front was being dragged back towards the burned mixture some of the time, although this seems to be more so for flames at higher equivalence ratio. This might be a result of changes in the flame front chemical mechanism as the flame traverse the acoustic field. The underlying burn speed derived from the low pass FFT filtered flame position, u_{fft} , is shown in Figure 6.17(e) where the different behaviour of the two flames is evident.

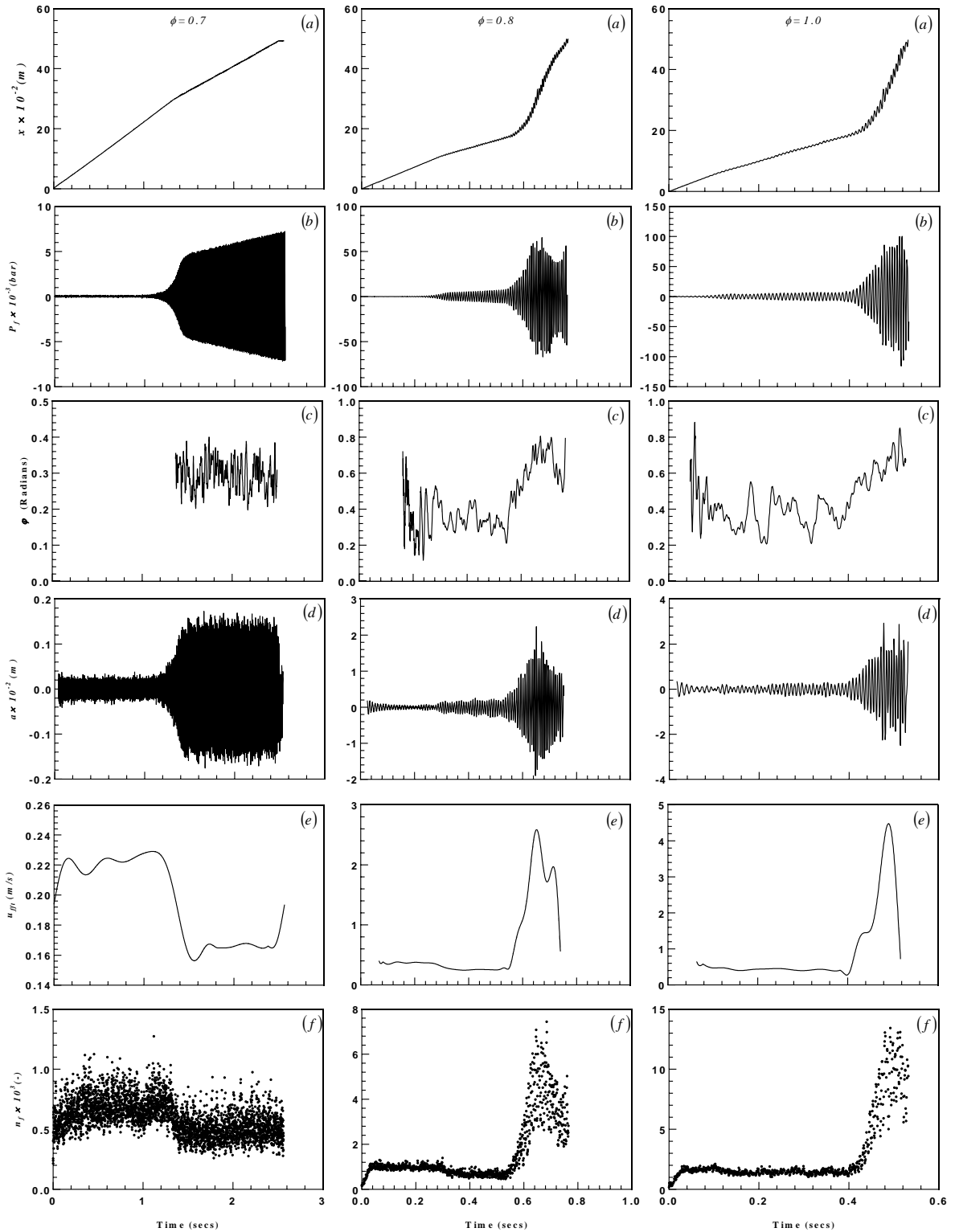


Figure 6.17: Propane-air flame at $\phi=0.7, 0.8$ and 1.0 (a) x in the flame front position (b) P_f is the flame pressure amplitude (c) ϕ is the flame position and pressure amplitude phase difference (d) a is the flame amplitude (e) u_{ff} is the FFT filtered flame speed (f) n_f is the flame size approximated by the number of pixels

In the case of the $\phi = 0.7$ flame, it initially propagate with relatively constant speed until the point of the primary acoustic oscillation where the speed of the flame slowed to a minimum of 0.15 m/s at the end of the oscillation, then, a small speed increase to a value significantly lower than the initial propagating speed of the flame that remained steady for the rest of the propagation. The drop in the flame speed occurs with the primary acoustic oscillation.

For the $\phi = 0.8$ flame, started propagating steadily immediately after ignition, it slows as it passes through the primary acoustic field to a speed of approximately 0.2 m/s and then continue in that speed until the secondary acoustic field where the flame rapidly increase in speed to a maximum speed of 2.6 m/s (approximately 4 times the laminar burning velocity). The $\phi = 0.8$ flame, also started propagating steadily immediately after ignition, then slows as it passes through the primary acoustic field to a speed of approximately 0.4 m/s and then continue in that speed until the secondary acoustic field where the flame rapidly increase in speed to a maximum speed of 4.4 m/s (approximately 8 times the laminar burning velocity).

The influence of the surface area on the flame propagation of the horizontal tube was examined. In order to obtain an approximate flame surface area, the numbers of illuminated (white/grey) pixels, nf , were counted in each image. The results are shown in Figure 6.17(f) for the three equivalence ratios. Similarly, with the flame oscillation amplitude and the underlying speed, different behaviour can be seen in the three flames. The flame surface area was seen to decrease at the point it was to go through the primary acoustic field for all three flames shown. However, when the flame reached the secondary acoustic field (in this case for $\phi = 0.8$ and above), the immediately increased in area. These results compliment the measurements of flame speed, $ufft$. There does appear to be a correlation between the underlying flame speed and the flame surface area, both when the flame is subjected to primary acoustic oscillation, secondary acoustic oscillation and when it was not, since both the underlying flame speed and flame surface area can be seen to increase and decrease at specific time intervals. It therefore means that the surface area of the flame has some major of influence on the coupling mechanism of the primary and secondary acoustic oscillation. Though this result is not in agreement with the result of [46], where they reported that the variation in flame surface area does not always influence the coupling mechanism of the

primary acoustic instability. The reduced underlying flame speed as the flames traverse the primary acoustic field compared to the increased underlying flame speed as the flames go through the secondary acoustic field might be the result of the changes in the acoustic field or a damping effect generated by the end boundary condition creating a friendly environment for the flame to go through with relative ease.

6.5 Flame chemiluminescence

When a chemical reaction leads to the formation of atoms or molecules in an electronically excited state, radiation occurs, which leads to the emission of light in the same proportion as that expected from a thermal emission. The chemical process is termed chemiluminescence. This process emits different species, but the species that are of importance are the radicals of CH and C₂, formed from the strongly exothermic reaction. The C₂ species emission occurs primarily in the fuel rich regime and this is due to the decrease in the oxygen concentration which leads to the change in flame colour from the violet-blue characteristic of CH radiation to green.

High-speed colour images of a downwardly propagating propane/air flame were captured for $\phi=0.8$ and $\phi=1.0$ at a framing rate of 1000 fps. The propane data is presented as it gave better quality images than the methane-air mixtures. The CH* and C₂* luminescence were processed. With the assumption that the unburned gases were fully mixed, the value of CH* and C₂* would be expected to remain constant throughout the flame propagation.

Images at the point where the flame was not oscillating and when the flame was oscillating are shown in Figure 6.18 at image interval of five. As the flame propagates, obvious changes in CH* and C₂* can be observed in both figures. The CH* and C₂* reduces as the flame was drawn back towards the burned gases and increased as the flame push forward, theoretically indicating an alteration of the flame front reaction mechanism.

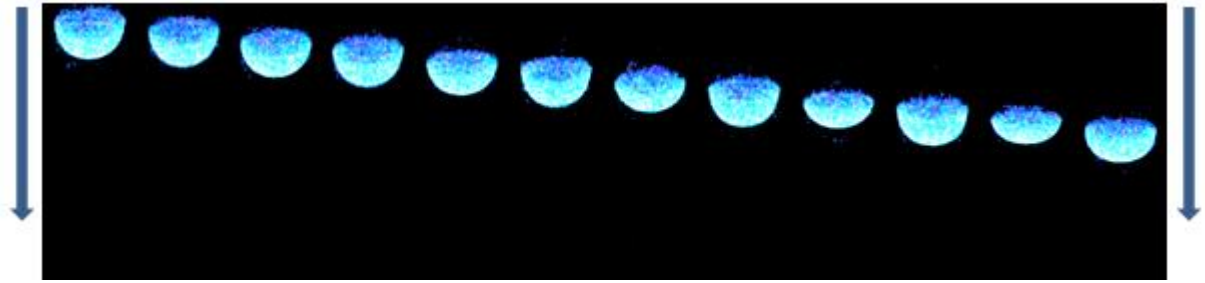


Figure 6.18a: Coloured image sequences without oscillation of propane-air flame recorded at 1000 fps

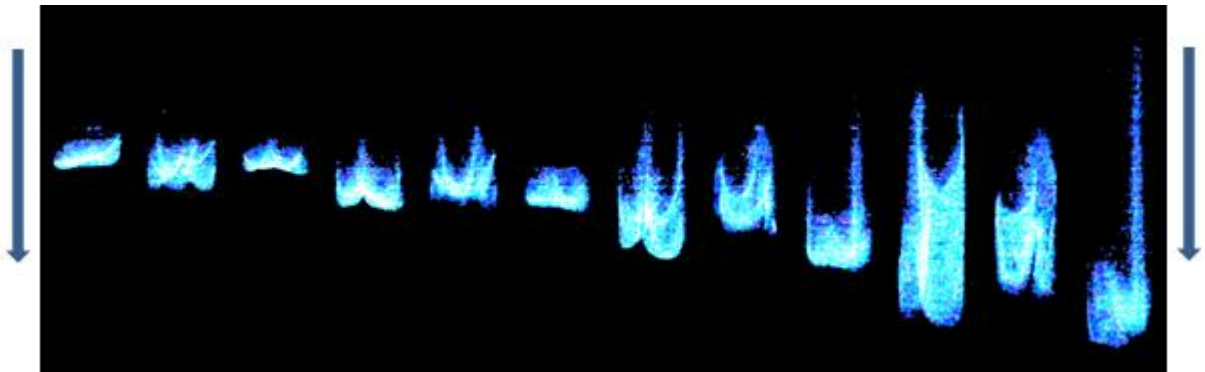


Figure 6.18b: Coloured image sequences with oscillation of propane-air flame recorded at 1000 fps

Results for the CH* and C2* and flame acoustic pressure are plotted against time as shown in Figure 6.19a for propane-air at $\phi=0.8$ and Figure 6.19b for same propane-air at $\phi=1.0$. From the flame acoustic pressure plot, the presence of the primary acoustic oscillation regime and the secondary acoustic oscillation regime is evident. Changes in the CH* and C2* ratio can be seen in the entire time of the flame propagation for both flames. The amplitude of the fluctuations in CH* and C2* increased only slightly in the region of primary acoustic oscillation up to the plateau region while on the secondary acoustic oscillation regime, there seemed a dramatic increase in the amplitude of the fluctuations in CH* and C2*, hence a weak flame at low CH* and C2* and strong flame burning fast at high CH* and C2*.

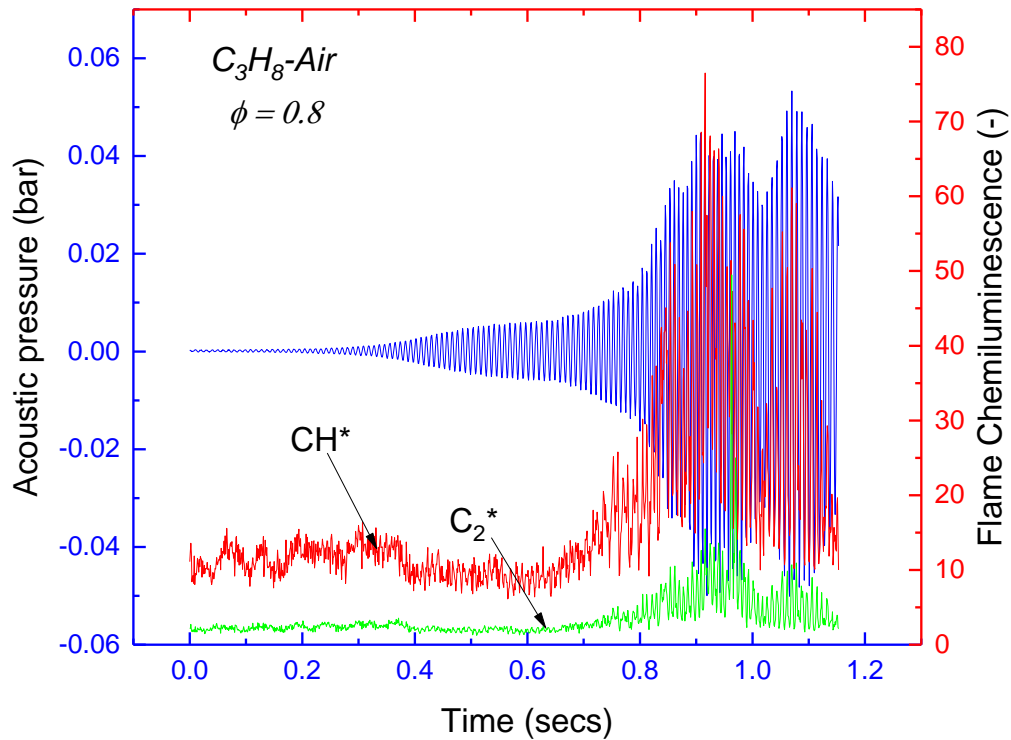


Figure 6.19a: Acoustic pressure and CH*/C2* against time for propane-air flame at $\phi = 0.8$

The flame acoustic pressure seemed to be slightly out of phase with CH* and C2*, as the flame traversed the acoustic field. Nevertheless, since the CH* and C2* and acoustic pressure fluctuate as the flame propagates, at low CH* and C2*, the flame propagation direction was always backward. At high CH* and C2*, the flame propagation direction was always forward. This could be a result of the quenching of the CH* and C2* which is likely to significantly alter with the acoustic pressure [137], although measurements of the ratio CH*/OH* demonstrate little difference as the pressure increased up to 3 bar [138].

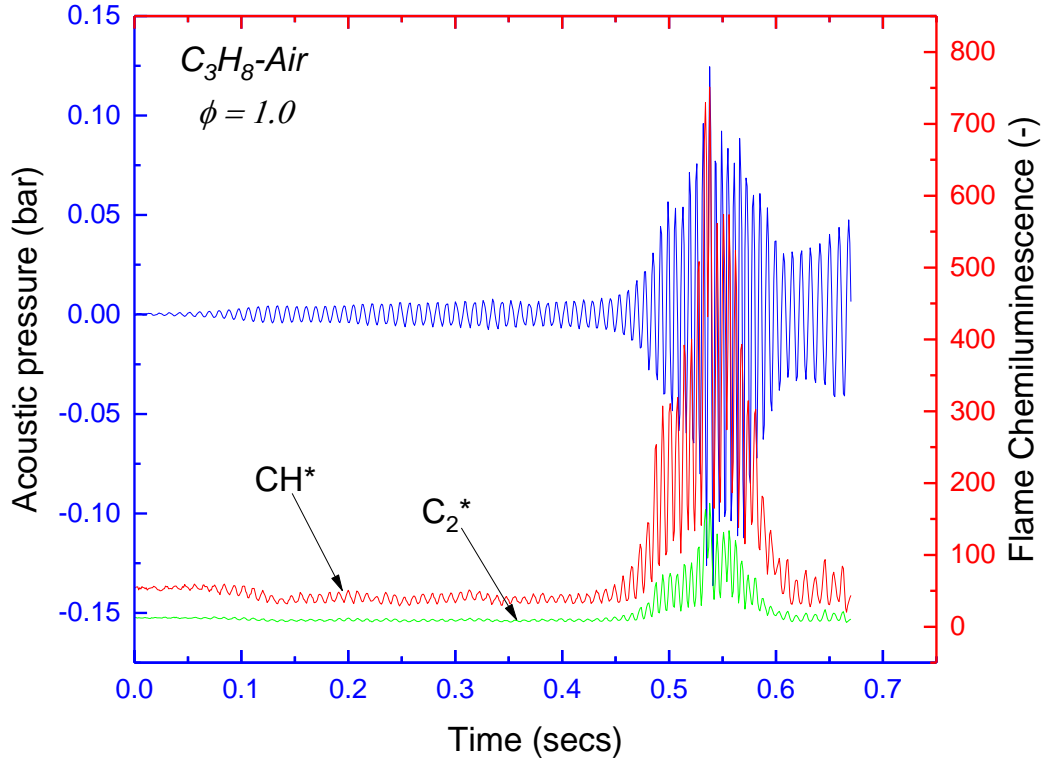


Figure 6.19b: Acoustic pressure and CH*/C2* against time for propane-air flame at $\phi = 1.0$

To check the coincidence of the CH* and C2* signal and the pressure signal, Fast Fourier Transforms (FFT) were used to find the primary excitation frequencies in the signals. Shown in Figure 6.20a and Figure 6.20b are the frequencies of the pressure oscillations and the CH* oscillations respectively, for both primary and secondary oscillation. The results showed the two signals oscillate at the same frequency both on the regime of primary acoustic oscillation and the regime of secondary acoustic oscillation, displaying the two signals are well in unison.

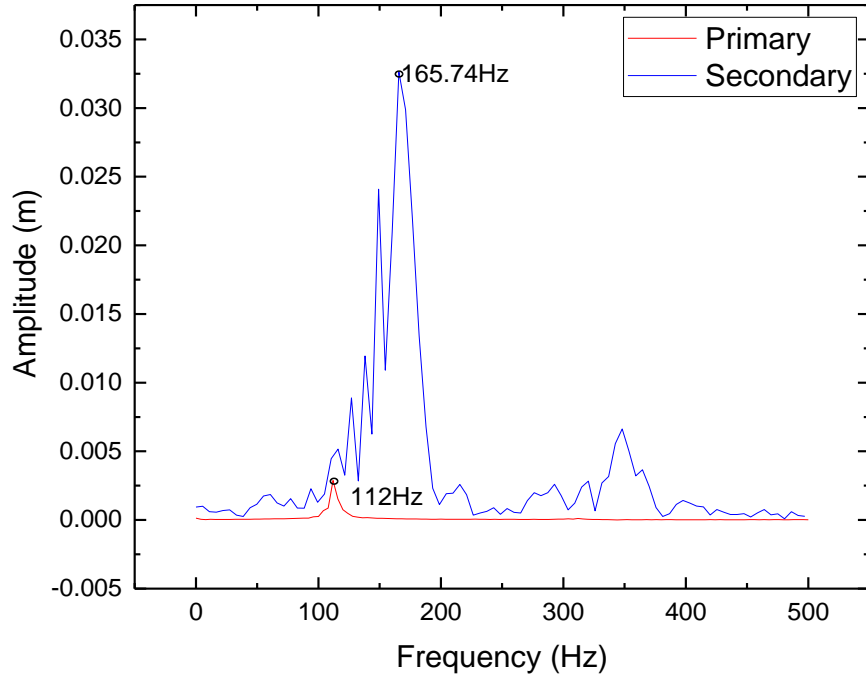


Figure 6.20a: Frequency of the pressure oscillation for downwardly propagating flame

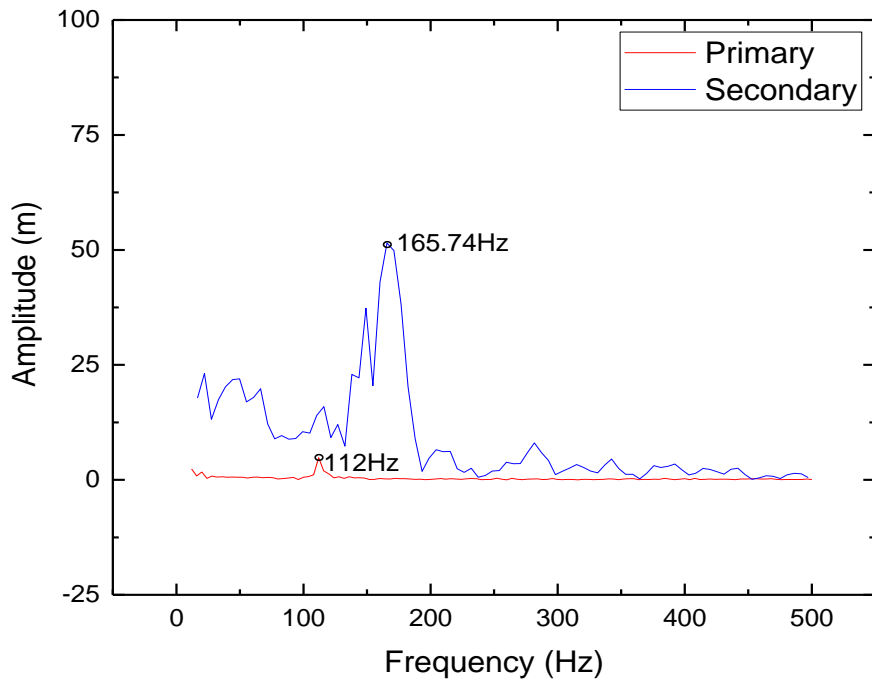


Figure 6.20b: Frequency of the CH* for downwardly propagating flame

CHAPTER SEVEN

CONCLUSIONS AND RECOMMENDATIONS

7.1 Conclusions

In this research, the dynamic behaviour of premixed methane-air, propane-air and methane-air enriched with hydrogen flames propagating in a 20mm internal diameter quartz tubes was experimentally investigated at room temperature and pressure. Experiments were done both in the vertical and horizontal position with the ends of the tubes subjected to different boundary conditions such as open both ends with and without orifice plates and downward propagation to a closed end. The purpose of the research was to characterise experimentally the phenomena, flame speed and modes of propagation, and the resulting effect of oscillation on these flames. The flame propagation was highly affected by coupled interactions between the hydrodynamic, thermal, and chemical process resulting in oscillations. Hence, the major concentration of this work was to check the effect of the flame surface area, the flame temperature, and the flame chemiluminescence (CH^* and C_2^* emission) on the flame.

- The effect of gravity, flammability limits and laminar burning speed for a propagating flame was studied with orifice plate placed at the tube ends. Methane and propane-air mixtures were tested for horizontal and downward propagating flame with a 5mm orifice plate on both ends and the results are compared. For the horizontal propagation, the flame propagated steadily with a relatively constant hemispherical or semi-ellipsoidal shape at all equivalence ratios studied. Methane gives a flame speed graph comparable to data in the literature. The laminar flame speed of methane peaked at equivalence ratio of 1.1 and fell off for both rich and lean mixtures while that for propane shifted from the literature value of $\phi = 1.1$ to $\phi = 1.3$. For the downward propagation, there was a variation in the flame shape for the different equivalence ratios studied. There was a change in shape for methane-air flames at $\phi < 0.9$ and $\phi > 1.3$, accompanied by flame quenching. For propane, similar behaviour as that of methane-air flame except for $\phi > 1.5$, where there was a continuous change in the shape of the flame throughout the propagation was observed. The flammability limits of both fuels tend to increase. The results showed that the effects of gravity became more important as the lean flammability limit was approached.

- With both ends of the tube opened and with the tube in the horizontal position, the shape of the flame was stable at lean conditions and became subject to oscillations at $\phi = 1.1$ to $\phi = 1.3$ becomes steady for $\phi \geq 1.4$ again. The temperature of the flame was measured using the TFP (Thin Filament Pyrometer) method applying the two colour approach. The flame temperature distribution along the tube diameter was higher at the mid-section of the glowing fibre compared to those nearer the tube walls. Both the time-dependent flame temperature and the pressure oscillations reached their peaks at the middle section of the tube, showing the temperature have some influence on the flame oscillation.
- When methane-air flame was enriched with hydrogen at different percentage ($RH = 0.1$ to 0.7), the flame speed increased as the amount of hydrogen increased and three types of flame behaviour were observed: I, the flame propagated down the tube steadily ($RH = 0$); II, the flame propagated down the tube steadily and was then subjected to violent acoustic oscillations resulting in an increase in the burn rate ($RH = 0.1$ to 0.3); III, the flame propagated down the tube steadily and was then subjected to acoustic oscillations that result in a decrease in the burn rate ($RH = 0.4$ to 0.7). As the percentage hydrogen addition increase above $RH = 0.3$, the flame acoustic oscillation was suppressed. The frequency of the acoustic oscillations ranged from 240 Hz to 260 Hz and was attributed to the characteristic mode of the tube and the flame chemical reaction, hence the slight difference in the frequencies. The flame area (here approximated by the number of grey/white pixels) appeared to influence the underlying flame speed and oscillation. The larger area flames tended to travel faster. Further analysis showed that the presence of Rayleigh Taylor instabilities on the $RH \leq 0.3$ flames caused the sudden increase in the underlying flame speed while the little or non-presence of the Rayleigh Taylor instabilities on the $RH \geq 0.4$ caused the decrease in the underlying flame speed as the flame traverse the acoustic field.
- For the downward-propagating premixed flames in a tube, closed at the lower end, flames initially propagated steadily. At approximately a third of the way down the tube, the primary acoustic oscillation occurred which resulted in changes to the flame shape. This was then followed by a plateau of variable length before a more

violent secondary acoustic oscillation. Under fuel lean conditions ($\phi < 0.8$), the behaviour of methane and propane was similar; they both demonstrated similar primary acoustic growth and similar flame speeds. No secondary acoustic growth was observed. For flames where, $\phi \geq 0.8$, cellular flames were observed following the primary acoustic growth. In the case of methane the flames were observed to rotate about 4 to 6 acoustic circles before the cells were destroyed followed by the onset of the secondary acoustic oscillation. Some of the flames were subjected to Rayleigh Taylor instabilities which pushed the flame front inward at a uniform speed significantly larger than the laminar burning speed of the flame. The flame front position and pressure growth rate for both the primary and secondary oscillations were calculated, compared and found to be similar at lean ϕ . As the mixture became rich ($\phi = 1.1$ to $\phi = 1.3$), while the primary and secondary growth rate of propane remain relatively constant for all ϕ , that of methane was only relative constant for the primary growth rate and changes in a non-uniform order for the secondary pressure growth rate. When the amplitude of oscillation (both flame front position and pressure) was low, the pressure signal and the flame front position were observed to be in phase. As the amplitude increased the flame front position lagged that of the pressure signal probably due to the fluctuation in the inertial force of the flame as it became more violent. The effects of acoustic losses were also determined. The total acoustic loss time for propane and methane decreased at both lean and rich mixtures peaking at $\phi = 1.1$. There was also an increase in the total acoustic loss time as the angular speed of the flame increased. The generation of acoustic energy for propane was smaller than that of methane compared to their natural damping effect.

- The influence of the flame oscillations on the flame chemistry was examined by capturing the CH^* and C_2^* chemiluminescence using a high-speed coloured camera, to observe changes in the flame chemistry as the flame pass through the acoustic field. The CH^* and C_2^* were observed to decrease as the flame was dragged backwards towards the burned mixture and increased as the flame progressed forward. This behaviour was observed throughout the flame propagation even when oscillations in the flame position were small. Therefore, there is a strong

correlation between the flame surface area and the flame oscillations as well as between the flame chemistry and the flame oscillation.

On the basis of these observations, it is concluded that the flame oscillation tends to be influenced by the flame temperature, flame surface area and the flame chemistry. While the flame temperature is independent of the flame oscillation type (whether primary or secondary oscillation), the primary oscillation is predominantly influenced by the flame surface area, while the secondary oscillation is influenced by both the flame surface area and the flame chemistry.

7.2 Recommended future work

If the flow fields produced from the propagation of flames in combustors and channels are to be controlled or exploited by modern technology, more comprehensive studies should be done for the flame propagation behaviour and the mechanisms driving them, in order to predict correctly the conditions under which the flame propagation behaviour is suitable for the applications. For example, it has been established in this research that there is limit of addition of hydrogen to conventional fuels that leads to either an increase or decrease in the underlying speed of the flame, hence more thorough studies of the effect of boundary conditions would feasibly yield different propagation conditions since it has been reported that boundary conditions play a very significant role in determining the types of flame propagation. Some of the recommended future works are:

- There is need to check how the flame temperature is affected if the flame propagates downwards either towards a closed end or for open both ends.
- Further alternative analysis of the horizontally propagating flame in the tube with both ends opened and a possible experiment with other fuel like propane.
- The effect of hydrogen addition on a downwardly propagating flame for both the open both ends and the propagation towards a closed end.
- To further validate these results, a model and simulation of the flame characteristics would be a welcome future work.

REFERENCE

1. British P (2014) Statistical Review of World Energy 2014.
2. Mishra DP (2007) Fundamentals of combustion PHI Learning Pvt. Ltd.
3. Mossa F (2014) Flames in Tubes Mechanical Engineering University of Sheffield, Sheffield.
4. Rallis CJ, Garforth AM (1980) The determination of laminar burning velocity. Progress in Energy and Combustion Science 6: 303-329
5. Mallard EF, Le Chatelier H (1883) Combustion of explosive gas mixtures. Ann Mine
6. Searby G, Rochwerger D (1991) A parametric acoustic instability in premixed flames. Journal of Fluid Mechanics 231: 529-543
7. Searby G (1992) Acoustic instability in premixed flames. Combustion Science and Technology 81: 221-231
8. Guenoche H (1964) Nonsteady flame propagation, Ed. G.H. Markstein. Pergamon Press, New York: 107-181
9. Clanet C, Searby G (1998) First experimental study of the Darrieus-Landau instability. Physical review letters 80: 3867
10. Law CK (2006) Combustion physics Cambridge University Press
11. Kadowaki S (2001) Flame velocity of cellular flames at low Lewis numbers. Combustion Science and Technology 162: 223-234
12. Lewis DJ (1950) The Instability of Liquid Surfaces when Accelerated in a Direction Perpendicular to their Planes. II. Proceedings of the Royal Society of London Series A, Mathematical and Physical Sciences 202: 81-96 DOI 10.2307/98515
13. Taylor G (1950) The Instability of Liquid Surfaces when Accelerated in a Direction Perpendicular to their Planes. I. Proceedings of the Royal Society of London Series A, Mathematical and Physical Sciences 201: 192-196 DOI 10.2307/98398
14. Rayleigh L (1879) On the stability, or instability, of certain fluid motions. Proceedings of the London Mathematical Society 1: 57-72
15. Rayleigh JWSB (1896) The theory of sound Macmillan

16. Wheeler RV (1914) CCXLIII.—The propagation of flame in mixtures of methane and air. The “uniform movement.”. *Journal of the Chemical Society, Transactions* 105: 2606-2613
17. Coward HF, Hartwell FJ (1932) 277. Studies in the mechanism of flame movement. Part I. The uniform movement of flame in mixtures of methane and air, in relation to tube diameter. *Journal of the Chemical Society (Resumed)*: 1996-2004
18. Coward HF, Hartwell FJ (1932) 401. Studies in the mechanism of flame movement. Part II. The fundamental speed of flame in mixtures of methane and air. *Journal of the Chemical Society (Resumed)*: 2676-2684
19. Lefebvre AH (1998) *Gas turbine combustion* CRC Press
20. Fiock EF, Marvin CF (1937) The Measurement of Flame Speeds. *Chemical Reviews* 21: 367-387 DOI 10.1021/cr60070a002
21. Gerstein M, Levine O, Wong EL (1950) Fundamental Flame Velocities of Pure Hydrocarbons: I. Alkanes, Alkenes, Alkynes, Benzene and Cyclohexane National Advisory Committee for Aeronautics
22. Gerstein M, Levine O, Wong EL (1951) Flame propagation. II. The determination of fundamental burning velocities of hydrocarbons by a revised tube method. *Journal of the American Chemical Society* 73: 418-422
23. Fuller LE, Parks DJ, Fletcher EA (1969) Flat flames in tubes—easy fundamental flame speed measurements. *Combustion and Flame* 13: 455-460
24. Lieuwen T, Neumeier Y, Zinn BT (1998) The Role of Unmixedness and Chemical Kinetics in Driving Combustion Instabilities in Lean Premixed Combustors. *Combustion Science and Technology* 135: 193-211 DOI 10.1080/00102209808924157
25. Zinn B (1986) Pulsating combustion. *Advanced combustion methods*(A 87-50643 22-25) London and Orlando, FL, Academic Press, 1986: 113-181
26. Ellis OdC (1928) Flame movement in gaseous explosive mixtures. *Fuel Sci* 7: 502-508
27. Clanet C, Searby G (1996) On the “tulip flame” phenomenon. *Combustion and Flame* 105: 225-238

28. Mason W, Wheeler RV (1920) V.—The propagation of flame in mixtures of methane and air. Part I. Horizontal propagation. *Journal of the Chemical Society, Transactions* 117: 36-47
29. Manson N Contribution to the hydrodynamical theory of flame vibration, pp. 187-199.
30. Chu B-T (1953) On the generation of pressure waves at a plane flame front. *Symposium (International) on Combustion* 4: 603-612 DOI [http://dx.doi.org/10.1016/S0082-0784\(53\)80081-0](http://dx.doi.org/10.1016/S0082-0784(53)80081-0)
31. Chu B-T (1956) Mechanism of generation of pressure waves at flame fronts
32. Coward HF, Hartwell FJ (1926) CXCXVII.—Extinction of methane flames by diluent gases. *Journal of the Chemical Society (Resumed)* 129: 1522-1532
33. Guénoche H, Jouy M (1953) Sur des flammes cellulaires stabilisees *Comptes rendus hebdomadaires des seances de l'academie des sciences* 236: 2295-2297
34. Kurdyumov VN, Matalon M (2013) Flame acceleration in long narrow open channels. *Proceedings of the Combustion Institute* 34: 865-872 DOI <http://dx.doi.org/10.1016/j.proci.2012.07.045>
35. Kurdyumov VN, Matalon M (2015) Self-accelerating flames in long narrow open channels. *Proceedings of the Combustion Institute* 35: 921-928 DOI <http://dx.doi.org/10.1016/j.proci.2014.05.082>
36. Mallard. E. and Le Chatelier H (1883) *Recherches experimentelles et théoriques sur la combustion des mélanges gazeux explosifs*. *Ann Mines* 8
37. Markstein GH (1970) Flames as amplifiers of fluid mechanical disturbances *Proceedings of the Sixth US National Congress for Applied Mechanics*, Harvard University, Cambridge, MA pp. 11-33.
38. Markstein GH (1953) Instability phenomena in combustion waves *Symposium (international) on Combustion*, 1 edn Elsevier, pp. 44-59.
39. Kaskan WE (1953) An investigation of vibrating flames *Symposium (international) on Combustion*, , 1 edn Elsevier, pp. 575-591.
40. Leyer J-C, Manson N (1971) Development of vibratory flame propagation in short closed tubes and vessels. *Symposium (International) on Combustion* 13: 551-558 DOI [http://dx.doi.org/10.1016/S0082-0784\(71\)80056-5](http://dx.doi.org/10.1016/S0082-0784(71)80056-5)

41. Leyer JC (1969) Interaction between combustion and gas motion in case of flames propagating in tubes. *Astronautica Acta* 14: 445
42. Clavin P (1994) Premixed combustion and gasdynamics. *Annual Review of Fluid Mechanics* 26: 321-352
43. Dunlap RA (1950) Resonance of a flame in a parallel-walled combustion chamber Aeronautical Research Centre, University of Michigan.
44. Clavin P, Pelcé P, He L (1990) One-dimensional vibratory instability of planar flames propagating in tubes. *Journal of Fluid Mechanics* 216: 299-322
45. C. Clanet, G. Searby, P. Clavin (1999) Primary acoustic instability of flames propagating in tubes: cases of spray and premixed gas combustion. *J Fluid Mech* vol. 385: 157-197
46. Yoon SH, Noh TJ, Fujita O (2016) Onset mechanism of primary acoustic instability in downward-propagating flames. *Combustion and Flame* 170: 1-11
47. Bosschaart KJ, de Goey LPH (2003) Detailed analysis of the heat flux method for measuring burning velocities. *Combustion and Flame* 132: 170-180 DOI [http://dx.doi.org/10.1016/S0010-2180\(02\)00433-9](http://dx.doi.org/10.1016/S0010-2180(02)00433-9)
48. Strehlow RA (1984) *Combustion fundamentals* McGraw-Hill College
49. Heywood JB (1988) *Internal combustion engine fundamentals* McGraw-Hill New York
50. Metghalchi M, Keck JC (1982) Burning velocities of mixtures of air with methanol, iso-octane, and indolene at high pressure and temperature. *Combustion and flame* 48: 191-210
51. Milton BE, Keck JC (1984) Laminar burning velocities in stoichiometric hydrogen and hydrogen-hydrocarbon gas mixtures. *Combustion and Flame* 58: 13-22 DOI [http://dx.doi.org/10.1016/0010-2180\(84\)90074-9](http://dx.doi.org/10.1016/0010-2180(84)90074-9)
52. Rhodes DB, Keck JC (1985) Laminar burning speed measurements of indolene-air-diluent mixtures at high pressures and temperatures SAE Technical Paper.
53. Lewis B, von Elbe G (1987) *Combustion, flames & explosions of gases*, 3rd edn Academic Press Inc. (London) LTD, London
54. Jarosiński J (1983) Flame quenching by a cold wall. *Combustion and Flame* 50: 167-175 DOI [http://dx.doi.org/10.1016/0010-2180\(83\)90059-7](http://dx.doi.org/10.1016/0010-2180(83)90059-7)

55. Strehlow RA, Noe KA, Wherley BL (1988) The effect of gravity on premixed flame propagation and extinction in a vertical standard flammability tube. Symposium (International) on Combustion 21: 1899-1908 DOI [http://dx.doi.org/10.1016/S0082-0784\(88\)80426-0](http://dx.doi.org/10.1016/S0082-0784(88)80426-0)
56. Barrere M, Williams FA (1969) Comparison of combustion instabilities found in various types of combustion chambers Symposium (International) on Combustion, 1 edn Elsevier, pp. 169-181.
57. Bychkov VV, Liberman MA (2000) Dynamics and stability of premixed flames. Physics Reports 325: 115-237
58. Clavin P (1985) Dynamic behavior of premixed flame fronts in laminar and turbulent flows. Progress in Energy and Combustion Science 11: 1-59 DOI [http://dx.doi.org/10.1016/0360-1285\(85\)90012-7](http://dx.doi.org/10.1016/0360-1285(85)90012-7)
59. Kaiser C, Liu J-B, Ronney P (2000) Diffusive-thermal instability of counterflow flames at low Lewis number 38th Aerospace Sciences Meeting and Exhibition, pp. 576.
60. Okafor EC, Hayakawa A, Nagano Y, Kitagawa T (2014) Effects of hydrogen concentration on premixed laminar flames of hydrogen–methane–air. International Journal of Hydrogen Energy 39: 2409-2417 DOI 10.1016/j.ijhydene.2013.11.128
61. Sivashinsky GI (1977) Diffusional-Thermal Theory of Cellular Flames. Combustion Science and Technology 15: 137-145 DOI 10.1080/00102207708946779
62. Kailasanath K, Oran E, Boris J (1989) Numerical simulations of flames and detonations Numerical Combustion Springer, pp. 82-97.
63. Denet B, Haldenwang P (1992) Numerical study of thermal-diffusive instability of premixed flames. Combustion Science and Technology 86: 199-221
64. Wang Y, Hu S, Pitz RW (2009) Extinction and cellular instability of premixed tubular flames. Proceedings of the Combustion Institute 32: 1141-1147
65. Roberts MS, Jacobs JW (2016) The effects of forced small-wavelength, finite-bandwidth initial perturbations and miscibility on the turbulent Rayleigh–Taylor instability. Journal of Fluid Mechanics 787: 50-83

66. Roberts MS (2012) Experiments and simulations on the incompressible, Rayleigh-Taylor instability with small wavelength initial perturbations The University of Arizona
67. Richtmyer RD (1960) Taylor instability in shock acceleration of compressible fluids. *Communications on Pure and Applied Mathematics* 13: 297-319
68. Meshkov EE (1969) Instability of the interface of two gases accelerated by a shock wave. *Fluid Dynamics* 4: 101-104 DOI 10.1007/bf01015969
69. Abarzhi SI, Nishihara K, Glimm J (2003) Rayleigh–Taylor and Richtmyer–Meshkov instabilities for fluids with a finite density ratio. *Physics Letters A* 317: 470-476
70. Rayleigh JWS (1878) The explanation of certain acoustical phenomena. *Nature* 18: 319-321
71. Markstein GH (1950) Experimental and theoretical studies of flame-front stability. *Journal of the Aeronautical Sciences (Institute of the Aeronautical Sciences)* 18
72. Akkerman V, Bychkov V, Petchenko A, Eriksson L-E (2006) Flame oscillations in tubes with nonslip at the walls. *Combustion and Flame* 145: 675-687
73. Petchenko A, Bychkov V, Akkerman Vy, Eriksson L-E (2006) Violent folding of a flame front in a flame-acoustic resonance. *Physical review letters* 97: 164501
74. Petchenko A, Bychkov V, Eriksson L-E (2007) Flame–sound interaction in tubes with nonslip walls. *Combustion and Flame* 149: 418-434
75. Shalaby H, Luo KH, Thévenin D (2014) Response of curved premixed flames to single-frequency and wideband acoustic waves. *Combustion and Flame* DOI 10.1016/j.combustflame.2014.05.002
76. Xiao H, An W, Duan Q, Sun J (2013) Dynamics of premixed hydrogen/air flame in a closed combustion vessel. *International Journal of Hydrogen Energy* 38: 12856-12864
77. Teerling OJ, McIntosh AC, Brindley J, Tam VHY (2005) Premixed flame response to oscillatory pressure waves. *Proceedings of the Combustion Institute* 30: 1733-1740
78. Matkowsky BJ, Putnick LJ, Sivashinsky GI (1980) A Nonlinear Theory of Cellular Flames. *SIAM Journal on Applied Mathematics* 38: 489-504

79. Gaydon AG, Wolfhard HG (1979) *Flames: their structure, radiation and temperature* Chapman & Hall London
80. Bayliss A, Matkowsky BJ (1992) NONLINEAR DYNAMICS OF CELLULAR FLAMES. *SIAM Journal on Applied Mathematics* 52: 396-415 DOI 10.1137/0152022
81. Sohrab SH, Law CK (1985) Influence of burner rim aerodynamics on polyhedral flames and flame stabilization. *Combustion and Flame* 62: 243-254
82. Kwon MJ, Lee BJ, Chung SH (1996) An observation of near-planar spinning premixed flames in a sudden expansion tube. *Combustion and Flame* 105: 180-188 DOI [http://dx.doi.org/10.1016/0010-2180\(95\)00188-3](http://dx.doi.org/10.1016/0010-2180(95)00188-3)
83. El-Hamdi M, Gorman M, Robbins KA (1993) Deterministic chaos in laminar premixed flames: Experimental classification of chaotic dynamics. *Combustion Science and Technology* 94: 87-101
84. Gololobov IM, Granovskii EA, Gostintsev YA (1981) Two combustion modes at the limit of luminous flame propagation. *Combustion, Explosion and Shock Waves* 17: 22-26
85. Pearlman HG, Ronney PD (1994) Near-limit behavior of high-Lewis number premixed flames in tubes at normal and low gravity. *Phys Fluids* 6: 4009-4018
86. Xu B, Ju Y (2007) Experimental study of spinning combustion in a mesoscale divergent channel. *Proceedings of the Combustion Institute* 31: 3285-3292 DOI <http://dx.doi.org/10.1016/j.proci.2006.07.241>
87. Kurata O (2008) X-shaped flames consisting of rotating slant flamelets. *Combustion and Flame* 152: 206-217 DOI <http://dx.doi.org/10.1016/j.combustflame.2007.06.023>
88. Deshpande AA, Kumar S (2013) On the formation of spinning flames and combustion completeness for premixed fuel-air mixtures in stepped tube microcombustors. *Applied Thermal Engineering* 51: 91-101
89. Pelce P, Rochwerger D (1992) Vibratory instability of cellular flames propagating in tubes. *Journal of Fluid Mechanics* Vol. 239: 293-307
90. Landau LD, Lifshitz EM (1987) *Mechanics "Course of Theoretical Physics", 2nd edn* Pergamon Press, Oxford, Oxford

91. Morley C (2005) Gaseq: a chemical equilibrium program for Windows. [http:// www gaseq co uk](http://www.gaseq.co.uk)
92. (Retrieve: 10/02/2016) Temperature Missouri University of Science and Technology, <http://web.mst.edu/~cottrell/ME240/Resources/Temperature/Temperature.pdf>
93. Darling CR (1911) Pyrometry: a practical treatise on the measurement of high temperatures E. & FN Spon, Limited
94. GünniX (2017) Pyrometer Wikipedia.
95. Johnson C (2011) Optical Pyrometer Transducers.
96. Müller B, Renz U (2001) Development of a fast fiber-optic two-color pyrometer for the temperature measurement of surfaces with varying emissivities. Review of scientific instruments 72: 3366-3374
97. Huang Y, Yan Y (2000) Transient two-dimensional temperature measurement of open flames by dual-spectral image analysis. Transactions of the Institute of Measurement and Control 22: 371-384
98. Hottel HC, Broughton FP (1932) Determination of true temperature and total radiation from luminous gas flames. Industrial & Engineering Chemistry Analytical Edition 4: 166-175
99. Li X, Wallace JS (1995) In-cylinder measurement of temperature and soot concentration using the two-color method SAE Technical Paper.
100. Takagi H, Ohno T, Asanuma T (1990) Temperature Measurements of Combustion Gas in a Spark Ignition Engine by Infrared Monochromatic Pyrometry SAE Technical Paper.
101. Quoc HX, Vignon J-M, Brun M (1991) A new approach of the two-color method for determining local instantaneous soot concentration and temperature in a DI diesel combustion chamber SAE Technical Paper.
102. Matsui Y, Kamimoto T, Matsuoka S (1979) A study on the time and space resolved measurement of flame temperature and soot concentration in a DI diesel engine by the two-color method SAE Technical Paper.

103. Matsui Y, Kamimoto T, Matsuoka S (1980) A study on the application of the two-color method to the measurement of flame temperature and soot concentration in diesel engines SAE Technical Paper.
104. Flower WL (1983) Optical measurements of soot formation in premixed flames. *Combustion Science and Technology* 33: 17-33
105. Flower WL (1989) Soot particle temperatures in axisymmetric laminar ethylene-air diffusion flames at pressures up to 0.7 MPa. *Combustion and Flame* 77: 279-293
106. Zhou H, Lou X-s, Xiao J (1995) Experimental study on image processing of flame temperature distribution in a pilot scale furnace. *Proceedings-chinese society of electrical engineering* 15: 295-300
107. Kawamura K, Saito A, Yaegashi T, Iwashita Y (1989) Measurement of flame temperature distribution in engines by using a two-color high speed shutter TV camera system SAE Technical Paper.
108. Vilimpoc V, Goss LP (1989) SiC-Based thin-filament pyrometry: Theory and thermal properties. *Symposium (International) on Combustion* 22: 1907-1914 DOI [http://dx.doi.org/10.1016/S0082-0784\(89\)80205-X](http://dx.doi.org/10.1016/S0082-0784(89)80205-X)
109. Pautin S, Giovannini A, Bédard B (1994) Thin filament infrared pyrometry: instantaneous temperature profile measurements in a weakly turbulent hydrocarbon premixed flame. *Experiments in fluids* 17: 397-404 DOI 10.1007/bf01877042
110. M.PITTS W (1996) Thin-filament pyrometry in flickering laminar diffusion flames *Twenty-Sixth Symposium on Combustion*, pp. 1171-1179.
111. Struk P, Dietrich D, Valentine R, Feier I Comparisons of gas-phase temperature measurements in a flame using thin-filament pyrometry and thermocouples, pp. 853.
112. Kuhn PB, Ma B, Connelly BC, Smooke MD, Long MB (2011) Soot and thin-filament pyrometry using a color digital camera. *Proceedings of the Combustion Institute* 33: 743-750 DOI <http://dx.doi.org/10.1016/j.proci.2010.05.006>
113. Ma B, Wang G, Magnotti G, Barlow RS, Long MB (2014) Intensity-ratio and color-ratio thin-filament pyrometry: Uncertainties and accuracy. *Combustion and Flame* 161: 908-916 DOI <http://dx.doi.org/10.1016/j.combustflame.2013.10.014>

114. Cook J (2008) *Flames in Tubes* Mechanical Engineering University of Sheffield, Sheffield.
115. Coward HF, Payman W (1937) Problems in Flame Propagation. *Chemical Reviews* 21: 359-366
116. Simon M (2011) *Flames in Tubes* Mechanical Engineering University of Sheffield, Sheffield.
117. Mossa FMS, Woolley R (2011) The propagation of propane/air flames in tubes European Council Meeting.
118. Yang J, Mossa FMS, Huang HW, Wang Q, Woolley R, Zhang Y (2015) Oscillating flames in open tubes. *Proceedings of the Combustion Institute* 35: 2075-2082
119. Wu M-h, Burke MP, Son SF, Yetter RA (2007) Flame acceleration and the transition to detonation of stoichiometric ethylene/oxygen in microscale tubes. *Proceedings of the Combustion Institute* 31: 2429-2436 DOI <https://doi.org/10.1016/j.proci.2006.08.098>
120. Yu G, Law CK, Wu CK (1986) Laminar flame speeds of hydrocarbon+ air mixtures with hydrogen addition. *Combustion and Flame* 63: 339-347
121. Wu F, Kelley AP, Zhu D, Law CK (2011) Further Study on Effects of Hydrogen Addition on Laminar Flame Speeds of Fuel-Air Mixtures 7th US National Combustion Meeting, Atlanta, GA.
122. Kee RJ, Grcar JF, Smooke MD, Miller JA (1985) PREMIX: a Fortran program for modeling steady laminar one-dimensional premixed flames. Sandia National Laboratories Report
123. M. Guenoche, Gouy H (1954). *Rev Inst Franc Petrole* vol. 9: pp. 562
124. Henderson HT, Hill GR (1956) A kinetic study of methyl chloride combustion. *The Journal of Physical Chemistry* 60: 874-878
125. Holman J (2002) *Heat transfer*, 9th edn McGraw-Hill
126. Linnett JW (1953) Methods of measuring burning velocities Symposium (International) on Combustion Elsevier, pp. 20-35.
127. Hamins A, Heitor M, Libby P (1988) Gravitational effects on the structure and propagation of premixed flames. *Acta Astronautica* 17: 503-514

128. Strehlow R, Reuss D (1981) Flammability limits in a standard tube. *Combustion Experiments in a Zero Gravity Laboratory* 73: 61-89
129. Kuo KK (2005) *Principles of combustion*: 732
130. Turns SR (2000) *An Introduction to Combustion*, 2nd McGraw-Hill.
131. Ma Z, Zhang Y, Li Y, Zheng Y (2014) High temperature measurement using very high shutter speed to avoid image saturation, 1 edn AIP, pp. 246-253.
132. Ma.Z. ECE, Zhang Y., and Woolley R. (2016) Measuring the temperature of a flame propagating through a quartz tube using high speed colour imaging and thin SiC filament based two colour method 12th International Conference on Heat Transfer, Fluid Mechanics and Thermodynamics (HEFAT2016), Costa Del Sol, Spain.
133. McIntosh AC (1995) Pressure-driven disturbances in fluid dynamic interactions with flames. In: Buckmaster J, Takeno T (eds) *Modeling in Combustion Science: Proceedings of the US-Japan Seminar Held in Kapaa, Kauai, Hawaii, 24–29 July 1994* Springer Berlin Heidelberg, Berlin, Heidelberg, pp. 176-192.
134. G. A. Batley ACM, J. Brindley (1996) Baroclinic distortion of laminar flames. *Proceedings of the Royal Society of London Series A: Mathematical, Physical and Engineering Sciences* 452: 199
135. Batley GA, McIntosh AC, Brindley J, Falle SAEG (1994) A numerical study of the vorticity field generated by the baroclinic effect due to the propagation of a planar pressure wave through a cylindrical premixed laminar flame. *Journal of Fluid Mechanics* 279: 217-237 DOI Doi: 10.1017/s0022112094003897
136. Kadowaki S, Hasegawa T (2005) Numerical simulation of dynamics of premixed flames: flame instability and vortex–flame interaction. *Progress in Energy and Combustion Science* 31: 193-241
137. Higgins B, McQuay M, Lacas F, Rolon J-C, Darabiha N, Candel S (2001) Systematic measurements of OH chemiluminescence for fuel-lean, high-pressure, premixed, laminar flames. *Fuel* 80: 67-74
138. Muruganandam T, Kim B-H, Morrell M, Nori V, Patel M, Romig B, Seitzman J (2005) Optical equivalence ratio sensors for gas turbine combustors. *Proceedings of the combustion institute* 30: 1601-1609

APPENDICES

Appendix A: Python Code MATLAB Script

```
#THIS IS A PROGRAM TO READ AND PROCESS FLAME IMAGE FILES
```

```
# Install the following packages compatible with python2.7.6
```

```
# numpy, PIL, six, dateutil, Scipy, matplotlib, pyparsing
```

```
from PIL import Image, ImageDraw, ImageFont, ImageEnhance, ImageFilter
```

```
from numpy import *
```

```
import matplotlib.pyplot as plt
```

```
import numpy as np
```

```
import os.path
```

```
from scipy.integrate import quad
```

```
import math
```

```
from math import *
```

```
from scipy import stats
```

```
# initialise the arrays
```

```
x = []
```

```
y = []
```

```
x1 = []
```

```
y1 = []
```

```
xfront = []
```

```
yfront = []
```

```
xframe = []
```

```
yframe = []
```

```
name = "info.txt"
```

```
input_file = open (name,"r")
```

```
input_file.readline()
```

```
root = input_file.readline(6)
```

```
#print 'root',root
```

```

input_file.readline()
input_file.readline()
#print 'tmp',tmp
tmp = input_file.readline()
begin, end = (int(val) for val in tmp.split(","))
print 'begin,end',begin,end
input_file.readline()
tmp = input_file.readline()
threshold = int(tmp)
print 'threshold',threshold
input_file.readline()
tpp = input_file.readline()
special=int(tpp)
input_file.readline()
psf = input_file.readline()
scale = (float(psf))/(22400)
input_file.readline()
tubedia = input_file.readline()
tube_diameter=int(tubedia)
input_file.close()
name = "front.txt"
output_file1 = open(name,"w")
name = "flamex.txt"
output_file2 = open(name,"w")
name = "flamey.txt"
output_file3 = open(name,"w")

for k in range(begin, end+1, 1):
    if k < 10:
        file_name = root + "0" + str(k) + ".bmp"
        #print 'file_name1',file_name1

```

```

else:
    file_name = root + str(k) + ".bmp"
    #print 'file_name1',file_name1

#PIL routines
# open image
img = Image.open(file_name)
# covert image to single channel
img = img.convert("L")
img = img.point(lambda p: p > threshold and 255)
# find image sizes
width = img.size[0]
height = img.size[1]
#print 'width,height',width,height

#img.show()

# this seems to be needed otherwise it crashes
width = width - 1

# start on the right and move left
for j in range(2, height, 1):
    # flag is use to indicate front of flame
    flag = 1
    # top of image working down
    for i in range(width, 2, -1):
        #interrogate image to find white cells
        if img.getpixel((i,j)) == 255:
            x.append(i)
            y.append(j)
            if flag == 1:

```

```

    xfront.append(i)
    yfront.append(j)
    # Check for the required special frame
    if k == special:
        xframe.append(i)
        yframe.append(j)
    flag = 0

    #this prints the leading edge distance
    output_file1.write('{:03d}\n'.format(max(xfront)))
    y1.append(int('{:03d}'.format(max(xfront))))

# Generate the total number of flame
n = len(y1)
# Generate data for the leading edge distance in meters covered by the flame
y1 = [(j * scale) for j in y1]
# Generate data for the time in seconds required for the distance
x1 = [(i+1)* (0.002380952)) for i in xrange(n)]
# Generate the linear equation that models the flame speed
coefficients = np.polyfit(x1, y1, 1)
polynomial = np.poly1d(coefficients)
print ""
print polynomial
uo = coefficients[0]

# Calculate the Standard Error
slope, intercept, r_value, p_value, std_err = stats.linregress(x1,y1)
# To get coefficient of determination (r_squared)
#print "r-squared:", r_value**2
#print "p-value:", p_value
print ""
print "Standard-Error:", std_err

```



```

# FLAME SURFACE AREA CALCULATION
# Generate data for the flame x-coordinate
xa = [(i * scale) for i in xframe]
# Generate data for the flame y-coordinate
ya = [(j * scale) for j in yframe]
# Generate the polynomial equation that models the flame shape
coefficients1 = np.polyfit(ya, xa, 8)
polynomial1 = np.poly1d(coefficients1)
print ""
#print polynomial1

# Generating the measurement parameter of the flame
cy=(max(ya))
cx=polynomial1(cy)
fy=(min(ya))
fx=polynomial1(fy)
d=(max(xa))
amid = (cy+fy)/2
bmid = (cx+fx)/2
aa = amid-fy
bb = d-bmid
if aa > bb:
    a=bb
    b=aa
else:
    a=aa
    b=bb
print a
print b
# Calculate the radius of the tube

```

```

c=(float(tube_diameter)/2000.0)
# Calculate the value of pi
pi=math.pi
#value of phi
phi = math.acos(c/a)
#squared K equation
k = (a**2)*((b**2)-(c**2)) / (b**2)*((a**2)-(c**2))
#first kind elliptical integral
def integrand(x):
    return int(1/(math.sqrt(1 - ((k*k) * (np.sin (x)) *(np.sin (x))))))
ff, err = quad(integrand, 0, phi)
#second kind elliptical integral
def integrand(x):
    return int((math.sqrt(1 - ((k*k) * (np.sin (x)) *(np.sin (x))))))
ee, err = quad(integrand, 0, phi)
# Area of the half-surface of the ellipsoid
SF = (pi * (c**2)) + ((pi * b * (c**2) * (1/((a**2) - (c**2)))**(1/2)) * ff) + ((pi * b *
((a**2) - (c**2))**(1/2)) * ee)
# Generate the flame speed
uo = coefficients[0]
# Calculate the gas velocity
ug = (0.4107*(uo))-0.0784
# Calculate the
ec = (math.sqrt(1-((a**2)/(b**2))))
a2 = ((2*pi*(a**2))*(1+((b/(a*ec))*(math.asin(ec)))))/2)
tarea = pi*(c**2)
#af = (SF)-a2
af = a2
print ug
print SF
print a2

```

```

#pc = (((a*b)**1.6)+((a*c)**1.6)+((c*b)**1.6))
#SF2 = (2*pi)*(pc/3)**(1/1.6)
#af = SF2-a2
uf = float(((uo)-ug)*(tarea/af))
print "Flame Speed:", uo
print ""
print "Burning Velocity:", uf

# Plot the leading edge distance against time
plt.figure(1)
plt.plot(x1, y1, 'k')
plt.xlabel('Time (s)')
plt.ylabel('Leading Edge Distance (m)')
plt.text(0.05,0.06,polynomial)
plt.grid(True)
plt.savefig("Figure1")
# Plot the flame coordinates
plt.figure(2)
plt.plot(ya, xa, 'r--')
plt.xlabel('x-coordinate')
plt.ylabel('y-coordinate')
plt.grid(True)
plt.savefig("Figure2")

#This prints the flame front and its co-ordinates
output_file2.write("%s\n" % xframe)
output_file2.write("%s\n" % yframe)
output_file3.write("%s\n" % x1)
output_file3.write("%s\n" % y1)
output_file3.write("%s\n" % coefficients)
output_file3.write("%s\n" % coefficients1)

```

plt.show()

output_file1.close()

output_file2.close()

output_file3.close()

```
% Get the file directory
file = dir('H:\Celestine_toclosedend\MATLAB\All_0.7_1\ma\*.jpg');
% Determine the total length of images
NF = length(file);
% creat a loop for all images from one to the total number of Image
for k = 1 : NF
    % read the image
    img =
imread(fullfile('H:\Celestine_toclosedend\MATLAB\All_0.7_1\ma',
file(k).name));
    % determine image with pixel less than or equal to 20 and change
them
    % to white
img(img<=20)=255;
    % change all non-white pixel to black
img(img==255)=0;
    %show the figure
figure, imshow(img)
    % find all pixel that is not black
b=find(img>0);
    % determine the total number of all pixel not black
c(k,1)=length(b);
    % the total pixel that is not black as a string
disp(num2str(c(k,1)));
    % move to next image
end
% Close all opened images
close all
```

Appendix B: Volume of Fuel Calculation

The fuel/air ratio or air/fuel ratio is not a better parameter for defining mixture composition because:

- The composition of combustion products is significantly different for fuel-lean and fuel-rich mixtures,
- The stoichiometric fuel/air ratio depends on fuel composition,

Therefore, the equivalence ratio (ϕ) which is the ratio of the actual fuel/air ratio to the stoichiometric ratio (or its inverse) is a more informative parameter for defining mixture composition.

$$\phi = \frac{(F/A)_{actual}}{(F/A)_{stoic}} \quad (B1)$$

Or

$$\phi = \frac{(A/F)_{stoic}}{(A/F)_{actual}} \quad (B2)$$

For fuel-lean mixtures: $\phi < 1$

For stoichiometric mixtures: $\phi = 1$

For fuel-rich mixtures: $\phi > 1$

Where

$$(F/A)_{stoic} = \left(\frac{m_f}{m_a}\right)_{stoic} \quad \text{and} \quad (F/A)_{actual} = \left(\frac{m_f}{m_a}\right)_{actual} \quad \text{or}$$
$$(A/F)_{stoic} = \left(\frac{m_a}{m_f}\right)_{stoic} \quad \text{and} \quad (A/F)_{actual} = \left(\frac{m_a}{m_f}\right)_{actual}$$

For the actual combustion process, assume the fuel/air to be an ideal gas at constant temperature

$$PV = mRT$$

And

$$m = \frac{PV}{RT}$$

For fuel, the mass of fuel,

$$m_f = \frac{PV_f}{R_f T}$$

For air, mass of air,

$$m_a = \frac{PV_a}{R_a T}$$

$$(A/F)_{actual} = \left(\frac{m_a}{m_f} \right)_{actual} = \left(\frac{PV_a}{R_a T} \right) / \left(\frac{PV_f}{R_f T} \right)$$

$$(A/F)_{actual} = \left(\frac{R_f V_a}{V_f R_a} \right)$$

Where

V is the volume, R is the specific gas constant and a, f represents air and fuel respectively.

For the Rig, let the total volume be V_T

$$V_T = V_f + V_a$$

$$V_a = V_T - V_f$$

Therefore

$$(A/F)_{actual} = \left(\frac{R_f (V_T - V_f)}{V_f R_a} \right)$$

$$V_f = \left\{ \frac{R_f V_T}{\left(((A/F)_{actual}) R_a + R_f \right)} \right\}$$

Equivalence ratio

$$\phi = \frac{(A/F)_{stoic}}{(A/F)_{actual}}$$

$$(A/F)_{actual} = \frac{(A/F)_{stoic}}{\phi}$$

Therefore

$$V_f = \left\{ \frac{R_f V_T}{\left(\left(\frac{(A/F)_{stoic}}{\phi} \right) R_a + R_f \right)} \right\} \quad (B3)$$

Also, since the specific gas constant (R) is

$$R = \frac{R_u}{\bar{M}}$$

Where R_u is the universal gas constant (8.314 kJ/kmol.K and \bar{M} is the molar mass of the gas.

Equation B3 becomes

$$V_f = \left\{ \frac{V_T}{\left(\left(\frac{\bar{M}_f (A/F)_{stoic}}{\phi \bar{M}_a} \right) + 1 \right)} \right\} \quad (B4)$$

Also,

$$\phi = \left\{ \frac{\bar{M}_f (A/F)_{stoic}}{\bar{M}_a \left(\frac{V_T}{V_f} - 1 \right)} \right\} \quad (B5)$$

Volume of Fuel, Hydrogen and Air required at varying Equivalence ratio for the Experiment.

In a fuel-air mixture with hydrogen addition there are two fuels and one oxidizer in the system, therefore we need two parameters to represent its composition, respectively designating the fuel-oxidizer ratio and the amount of hydrogen addition. The parameters used by most previous researchers are the overall equivalence ratio, ϕ , and the mole fraction of hydrogen in the fuel mixture, α_H , respectively defined as

$$\phi = \frac{C_F/C_A}{(C_F/C_A)_{st}} + \frac{C_H/C_A}{(C_H/C_A)_{st}} \quad (B6)$$

$$\alpha_H = \frac{C_H}{C_H + C_F} \quad (B7)$$

where C_F , C_H and C_A , are the mole concentrations of the dominant fuel, hydrogen and air respectively; and the subscript *st* designates the value at the stoichiometric condition. These definitions imply that the oxidizer is equally available to both the dominant fuel and hydrogen; in other words, they have the same priority to react with oxygen. However, hydrogen as a fuel is special from any other fuel in two aspects: (1) it is highly reactive; (2) it is highly diffusive. Therefore it is reasonable to assume that hydrogen has a stronger tendency to react with oxygen, especially considering that in most studies the amount of hydrogen addition is small in terms of the oxygen consumption.

Thus if the mole fraction of fuel, hydrogen and air are respectively C_F , C_H and C_A , with $C_F + C_H + C_A = 1$, following Law's concept, Equations (B8) and (B9) were used for determining the composition parameters for the mixture.

$$\phi_F = \frac{C_F/[C_A - (C_H/(C_H/C_A)_{st})]}{(C_F/C_A)_{st}} \quad (B8)$$

$$R_H = \frac{C_H + (C_H/(C_H/C_A)_{st})}{C_F + [C_A - (C_H/(C_H/C_A)_{st})]} \quad (B9)$$

Where the subscript st represent the mole concentration of the mixture at stoichiometric condition, ϕ_F represent the effective equivalence ratio of the main fuel and R_H represent the amount of hydrogen addition, i.e., the ratio of the total mole concentration of the hydrogen-air mixture to the total mole concentration of the main fuel-air mixture. The method assumes there is a complete oxidation of hydrogen but in practical term, complete oxidation of hydrogen cannot be justified.

Therefore, solving equations (B8) and (B9) simultaneously with $C_F + C_H + C_A = 1$, we have:

Let's represent $(C_F/C_A)_{st}$ as x and $(C_H/C_A)_{st}$ as y , which are the stoichiometric fuel-to-air molar ratio and hydrogen-to-air molar ratio respectively. Equations (B8) and (B9) becomes

$$\phi_F = \frac{C_F/[C_A - (C_H/y)]}{x} \quad (B10)$$

$$R_H = \frac{C_H + (C_H/y)}{C_F + [C_A - (C_H/y)]} \quad (B11)$$

$$C_F + C_H + C_A = 1 \quad (B12)$$

Making C_F the subject of the formula from Equation (B12) and substituting the result into equation (B11), then simplified to give:

$$C_H = \frac{R_H}{1 + \frac{1}{y} + \frac{R_H}{y} + R_H} \quad (B13)$$

Then,

$$C_A = \frac{1 - C_H(1 - (\phi_F x/y))}{\phi_F x + 1} \quad (B14)$$

and

$$C_F = 1 - C_H - C_A \quad (B15)$$

To get the required volume for the experiment, you multiply the mole concentrations by the total volume of the rig.

NOTE: $(C_H/C_A)_{st} = 0.418$ for hydrogen, $(C_F/C_A)_{st} = 0.105$ for methane-air and $(C_F/C_A)_{st} = 0.0418$ for propane-air.

Appendix C: Flame Surface Area

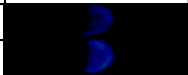
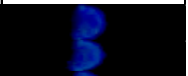
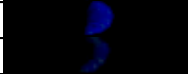










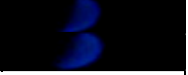









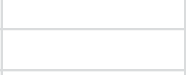


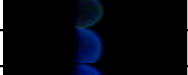
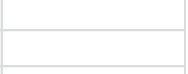

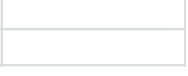


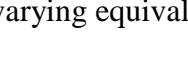






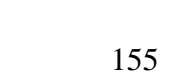


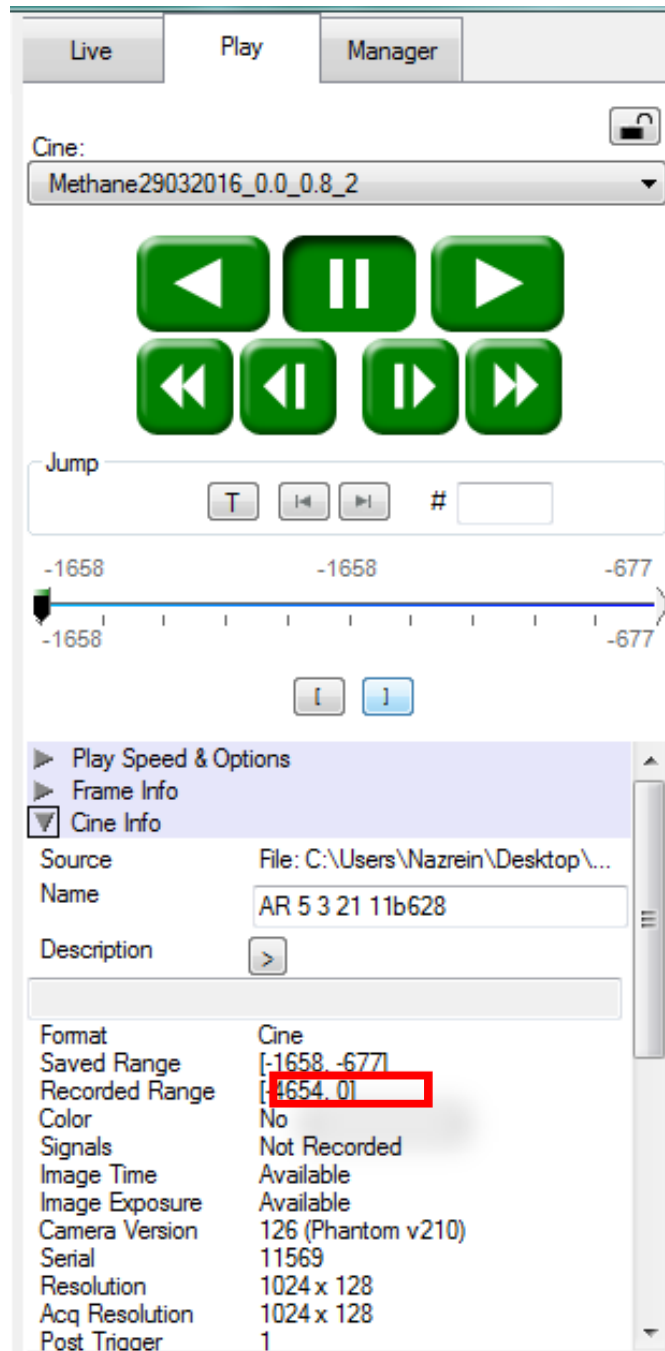
RH	0.9 EQUIVALENCE RATIO		1.0 EQUIVALENCE RATIO	
	Surface Area (m ²)	Picture	Surface Area (m ²)	Picture
0	0.00052		0.00049	
0.1	0.00041		0.00046	
0.2	0.00039		0.00051	
0.3	0.00047		0.00049	
0.4	0.00049		0.00051	
0.5	0.00050		0.00046	
RH	1.1 EQUIVALENCE RATIO		1.2 EQUIVALENCE RATIO	
	Surface Area (m ²)	Picture	Surface Area (m ²)	Picture
0	0.00054		0.00054	
0.1	0.00049		0.00047	
0.2	0.00047		0.00058	
0.3	0.00045		0.00052	
0.4	0.00053		0.00053	
0.5	0.00046		0.00049	
RH	1.3 EQUIVALENCE RATIO		1.4 EQUIVALENCE RATIO	
	Surface Area (m ²)	Picture	Surface Area (m ²)	Picture
0	0.00056		0.00052	
0.1	0.00047		0.00051	
0.2	0.00058		0.00052	
0.3	0.00050		0.00049	
0.4	0.00054		0.00054	
0.5	0.00047		0.00045	
RH	1.5 EQUIVALENCE RATIO			
	Surface Area (m ²)	Picture		
0	0.00040			
0.1	0.00051			
0.2	0.00051			
0.3	0.00048			
0.4	0.00052			
0.5	0.00045			

Figure C1: Flame surface Area at varying equivalence ratio and RH

Appendix D: Data synchronisation steps

1. Process the distance data as usual.
2. Take note of the original number of frames.



The frame recorded is **-4654 to 0**, in this case.

3. Take note the processed frame number from the excel file,

	A	B	C	D	E	F
1	ImageNr.	TimeFromTrig.	Synced Time	X0	Y0	Absolute Time
2	1635	-1.08996	1.771333333	0	-0.0242287	Tue Mar 29 2016 17:06:25.861391.89
3	-1634	-1.08929	1.772	0.000950147	-0.0242287	Tue Mar 29 2016 17:06:25.862058.55
4	-1633	-1.08863	1.772666667	0.00142522	-0.0242287	Tue Mar 29 2016 17:06:25.862725.21
5	-1632	-1.08796	1.773333333	0.00190029	-0.0237537	Tue Mar 29 2016 17:06:25.863391.87
6	-1631	-1.08729	1.774	0.00190029	-0.0242287	Tue Mar 29 2016 17:06:25.864058.54

The first frame, -1635 in this case.

952	-685	-0.456632	2.404666667	0.48315	-0.0247038	Tue Mar 29 2016 17:06:26.494719.57
953	-684	-0.455966	2.405333333	0.483625	-0.0251789	Tue Mar 29 2016 17:06:26.495386.23
954	-683	-0.455299	2.406	0.484575	-0.0251789	Tue Mar 29 2016 17:06:26.496052.89
955	-682	-0.454632	2.406666667	0.48505	-0.0251789	Tue Mar 29 2016 17:06:26.496719.55
956	-681	-0.453966	2.407333333	0.485525	-0.0251789	Tue Mar 29 2016 17:06:26.497386.21
957	-680	-0.453299	2.408	0.486	-0.0251789	Tue Mar 29 2016 17:06:26.498052.87

The last frame, -680 in this case.

4. Process the pressure data, delete rows with 0 from the second row, and get the time for each row.

	B	C
	0.00112892	-0.001152581
	0.001454848	-0.000174795
	0.000802991	-0.000826652
	0.00112892	-0.001804438
	0.001454848	-0.001152581
	0.00112892	-0.000826652
	0.001454848	-0.000826652
	0.001780777	-0.000174795
	0.001454848	-0.000826652
	0.001454848	4.72155392
	0.002106706	4.722205777
	0.000802991	4.717968704
	0.002106706	4.72155392
	0.001780777	4.720250205
	0.00112892	4.717642776
	0.001454848	4.72155392
	0.000802991	4.720250205
	0.001454848	4.716990918
	0.001780777	4.719924276
	0.001454848	4.717968704

5. Take the final time from the pressure data.

A	B	C
2.853333	0.001454848	4.717968704
2.854	0.002106706	4.724813207
2.854667	0.002432634	4.720576134
2.855333	0.001454848	4.718294633
2.856	0.001780777	4.722205777
2.856667	0.001454848	4.720576134
2.857333	0.001454848	4.718294633
2.858	0.001454848	4.717968704
2.858667	0.001780777	4.720576134
2.859333	0.001454848	4.717642776
2.86	0.000802991	4.717316847
2.860667	0.001780777	4.718294633
2.861333	0.001454848	4.715687204

6. Use the frame sync calculator, insert the starting phantom frame, which is -4654, and the end, 0 in this case, followed by the frames with flame, -1635 to -680 in this case. Leave the Normalised frame number alone, it is automated, and it is there for the calculation of the time.

	A	B	C	D
1		Phantom Frame Number	Normalized Frame Number	Time
2	First Frame	-4653	1	-3.102
3	Start of Cropped frame	-1635	3019	-1.09
4	End of Cropped Frame	-680	3974	-0.453333333
5	Last Frame	0	4654	
6				
7	Total Frames	4654		

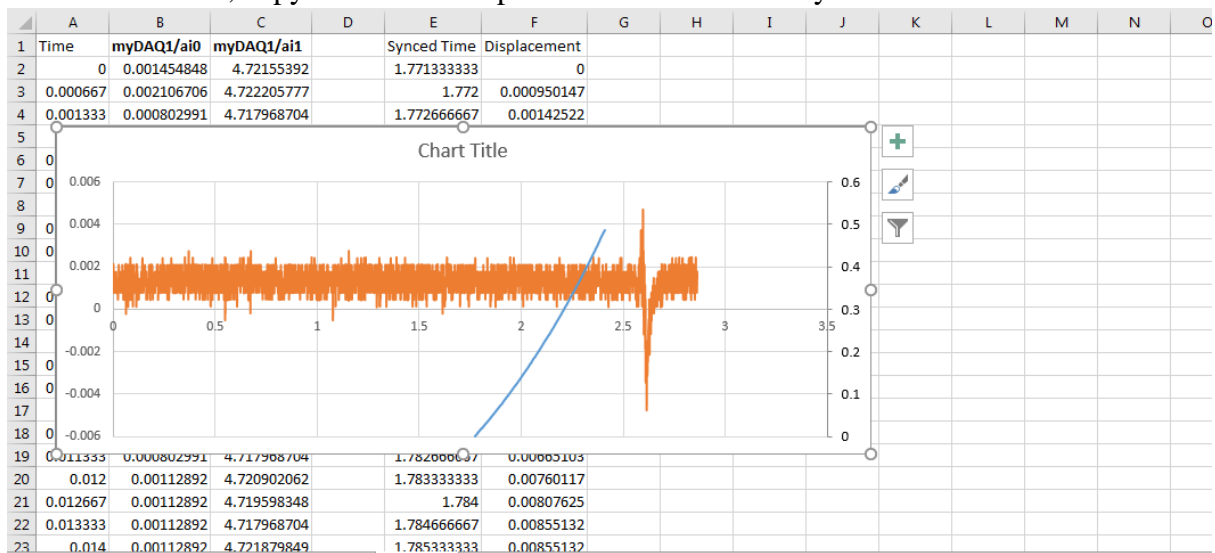
7. Use the **final time of the pressure data**, -2.861333 in this case, and match it with the **final frame of the phantom data**, which is at frame 0.

	A	B	C	D
1		Phantom Frame Number	Normalized Frame Number	Time
2	First Frame	-4653	1	-0.240666667
3	Start of Cropped frame	-1635	3019	1.771333333
4	End of Cropped Frame	-680	3974	2.408
5	Last Frame	0	4654	2.861333333
6				
7	Total Frames	4654		

8. Take the start time, and use it on the displacement data sheet, and do the usual time increment thing we always do, $=X+(1/1500)$.

	A	B	C	D	E	F
1	ImageNr.	TimeFromTrig.	Synced Time	X0	Y0	Absolute Time
2	-1635	-1.08996	1.771333333	0	-0.0242287	Tue Mar 29 2016 17:06:25.861391.89
3	-1634	-1.08929	1.772	0.000950147	-0.0242287	Tue Mar 29 2016 17:06:25.862058.55
4	-1633	-1.08863	1.772666667	0.00142522	-0.0242287	Tue Mar 29 2016 17:06:25.862725.21
5	-1632	-1.08796	1.773333333	0.00190029	-0.0237537	Tue Mar 29 2016 17:06:25.863391.87
6	-1631	-1.08729	1.774	0.00190029	-0.0242287	Tue Mar 29 2016 17:06:25.864058.54
7	-1630	-1.08663	1.774666667	0.00285044	-0.0242287	Tue Mar 29 2016 17:06:25.864725.20
8	-1629	-1.08596	1.775333333	0.00285044	-0.0242287	Tue Mar 29 2016 17:06:25.865391.86
9	-1628	-1.08529	1.776	0.00332551	-0.0242287	Tue Mar 29 2016 17:06:25.866058.52
10	-1627	-1.08463	1.776666667	0.00332551	-0.0242287	Tue Mar 29 2016 17:06:25.866725.18
11	-1626	-1.08396	1.777333333	0.00380059	-0.0247038	Tue Mar 29 2016 17:06:25.867391.84
12	-1625	-1.08329	1.778	0.00427566	-0.0247038	Tue Mar 29 2016 17:06:25.868058.50
13	-1624	-1.08263	1.778666667	0.00427566	-0.0242287	Tue Mar 29 2016 17:06:25.868725.16
14	-1623	-1.08196	1.779333333	0.00475073	-0.0242287	Tue Mar 29 2016 17:06:25.869391.82
15	-1622	-1.08129	1.78	0.00522581	-0.0242287	Tue Mar 29 2016 17:06:25.870058.48
16	-1621	-1.08063	1.780666667	0.00570088	-0.0242287	Tue Mar 29 2016 17:06:25.870725.14
17	-1620	-1.07996	1.781333333	0.00665103	-0.0242287	Tue Mar 29 2016 17:06:25.871391.80
18	-1619	-1.07929	1.782	0.00665103	-0.0242287	Tue Mar 29 2016 17:06:25.872058.46
19	-1618	-1.07863	1.782666667	0.00665103	-0.0232786	Tue Mar 29 2016 17:06:25.872725.12
20	-1617	-1.07796	1.783333333	0.00760117	-0.0237537	Tue Mar 29 2016 17:06:25.873391.79
21	-1616	-1.07729	1.784	0.00807625	-0.0237537	Tue Mar 29 2016 17:06:25.874058.45
22	-1615	-1.07663	1.784666667	0.00855132	-0.0242287	Tue Mar 29 2016 17:06:25.874725.11

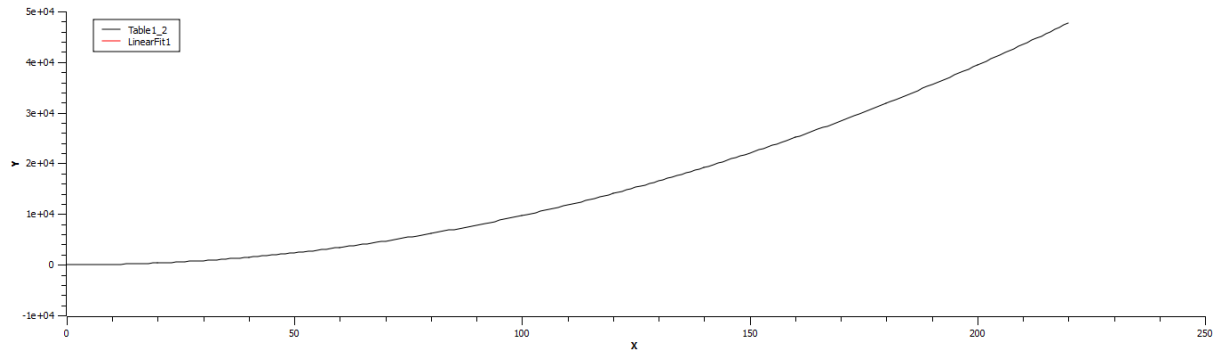
9. Plot them, copy them onto the pressure data. It is now synced.



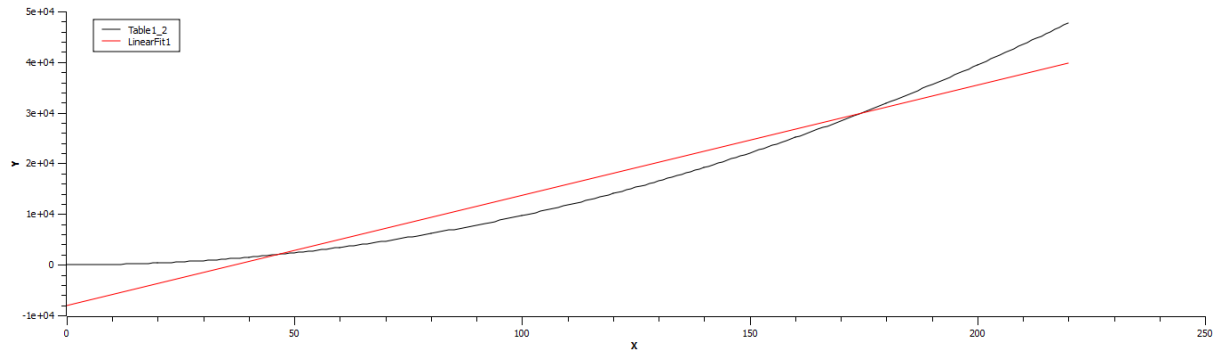
Appendix E: Data Analysis steps and example

Example 1

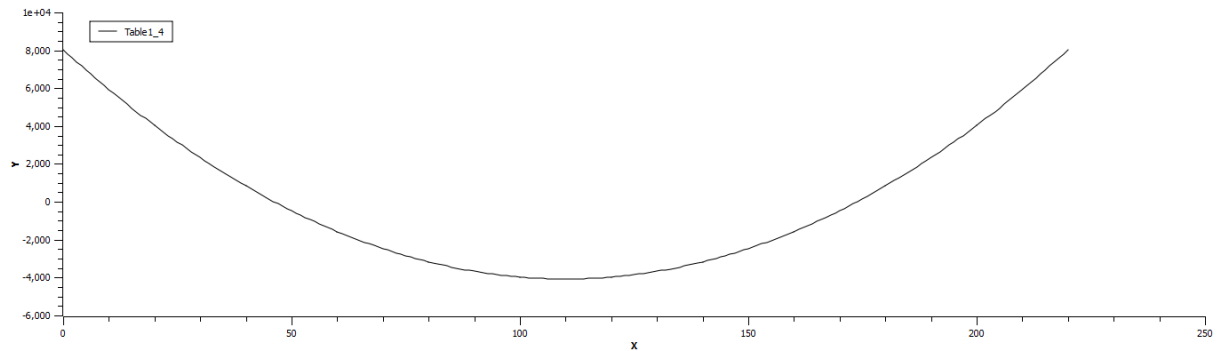
To test our flame processing method, we created a dummy equation ($y = x^2 - 3x + 2$), and generate data for this equation for $x = 0$ to 220. Figure 4.2a shows the plot of y against x . The other plots are as shown in Figure 4.2b to 4.2d.



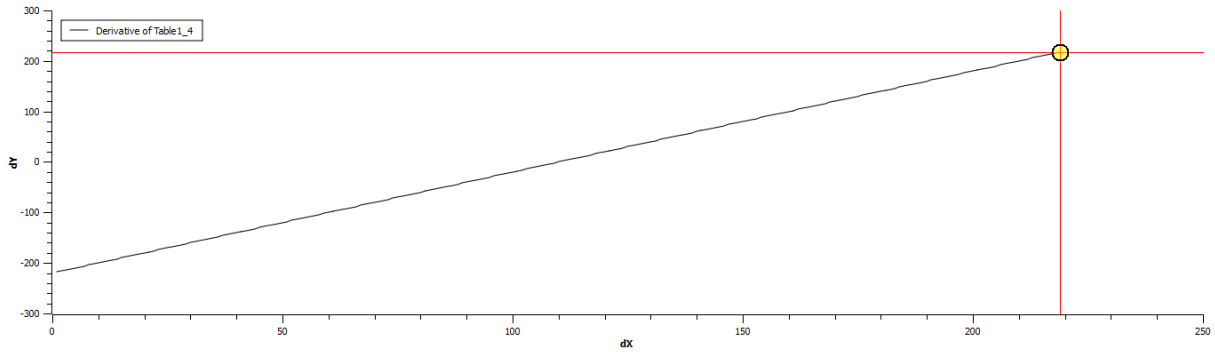
(a)



(b)



(c)



(d)

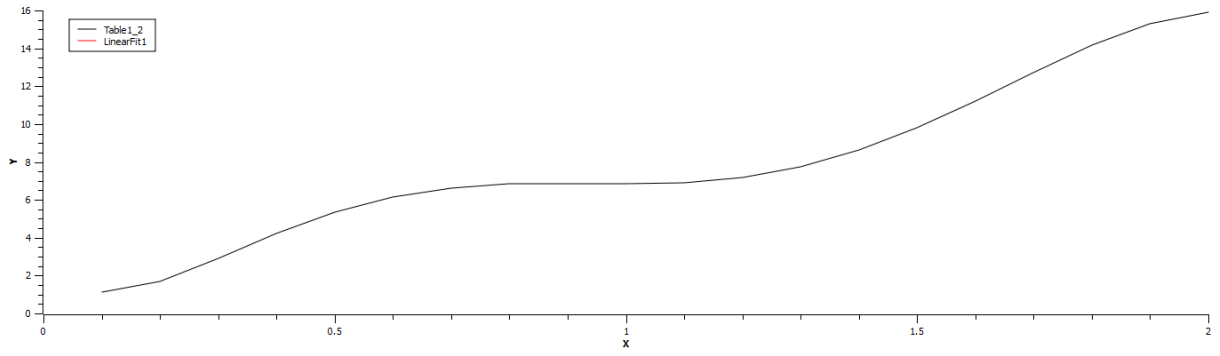
Figure 4.2: Graph of Y against X and the derivate of Y against X

- (1) Plot the distance (flame front distance) against time(4.2a)
- (2) Draw a linear Fit to the graph to get the linearized equation of the original data (Figure 4.2b)
- (3) Generate distance data for the linear equation generate in (2) above
- (4) Subtract the generated distance data in (3) from the original flame front distance data
- (5) Plot the result from (4) against time (Figure 4.2c)
- (6) Differentiate the result from (4) to get the derivative (Figure 4.2d)
- (7) Add the slope from (2) to the maximum derivative value from (6) to get the derivative(speed) of the original flame

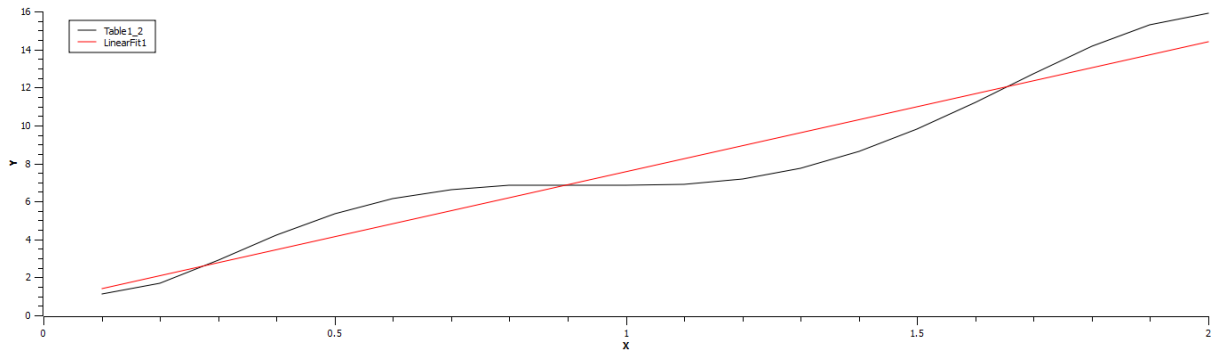
Using the steps above, we get the linear slope to be 217 and the maximum derivative value as 218 at $x=219$, which sums up to 435. The derivative of the equation at point $x=219$ numerically is 435.

Example 2

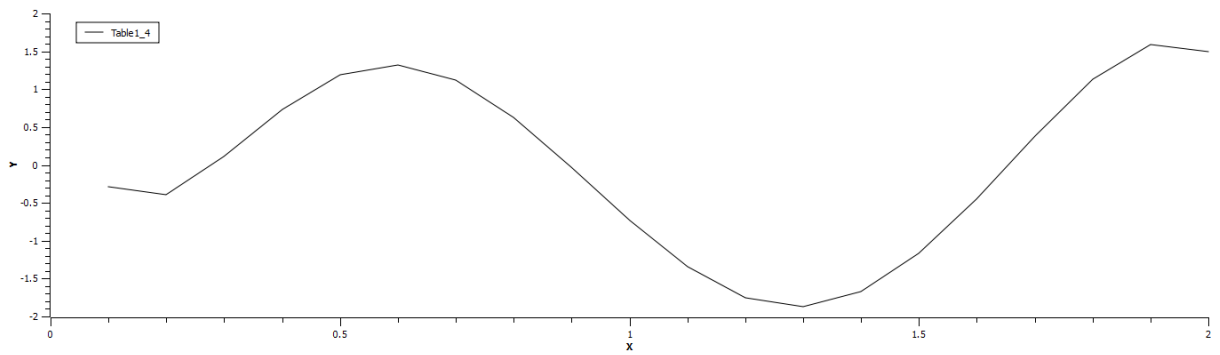
To be confident of our method and result, we tried it on another equation $y = 5.5918x^6 - 47.841x^5 + 147.16x^4 - 200.85x^3 + 118.78x^2 - 17.945x + 19357$ with values of x ranging from $x=0$ to 2. Figure 4.3a the plot of y against x . The other plots are as shown in Figure 4.3b to 4.3d.



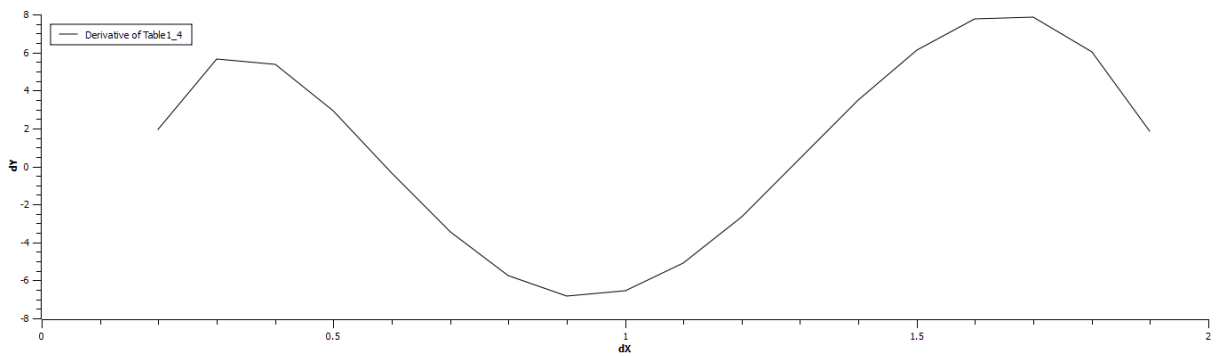
(a)



(b)



(c)



(d)

Figure 4.3: Graph of Y against X and the derivate of Y against X

Using the steps above, we get the linear slope to be 6.8 and the maximum derivative value as 8.0 at $x=1.7$, which sums up to 14.8. The derivative of the equation at point $x=1.7$ numerically is 15.

Appendix F: Harmonic Analysis (Fast Fourier Transform/FFT)

To estimate the frequency value of a function/data, the Fourier Transform is a fundamental mathematical method to convert a signal from its original time/space domain onto the frequency domain. A fast Fourier transform (FFT) algorithm computes the discrete Fourier transform (DFT) of a sequence or its inverse. An FFT rapidly computes such transformations by factorizing the DFT matrix into a product of sparse (mostly zero) factors [147].

The function $f(t)$, assumed to be periodic, can be represented by an infinite sum of sine and cosine functions, called Fourier series. For a function periodic in $[-T/2, T/2]$, the series can be written as

$$A_n = \frac{1}{T} \int_{-T/2}^{T/2} f(t) e^{-2\pi i n t / T} dt \quad (F1)$$

Where A_n is the coefficients for the Fourier series expansion. Replacing the discrete term A_n by its continuous term while $T \rightarrow \infty$, ($n/T \rightarrow f$) and the angular frequency $\omega = 2\pi f$, the generalized equation for continuous Fourier transform is as shown in Equation 3.13.

$$F(\omega) = \int_{-\infty}^{\infty} f(t) e^{-i\omega t} dt, \text{ where } |F(\omega)| = 0 \text{ and } |\omega| \geq \frac{1}{2} (2\pi/T) \quad (F2)$$

However, signals picked up by a data acquisition system are of finite extent and the integration of the Fourier transform can only be achieved by a finite summation of the finite samples. Considering signals and not functions, the infinite integration of Equation F2 is then replaced by the summation over N samples of signal as shown in Equation F3.

$$F_s(\omega) = \sum_{n=-N/2}^{N/2} f(nT) e^{-i\omega n T} \quad (F3)$$

The start point of the sampled Fourier Transform $F_s(\omega)$ can be shifted by $N/2$ without any loss of information (it only affects the phase angle of the transform). The resulting transform $F_D(\omega_k)$ is called the Discrete Fourier Transform (DFT), shown in Equation F4

$$F_D(\omega_k) = \sum_{n=0}^{N-1} f(nT)e^{-i\omega_k nT} \text{ where } \omega_k = \frac{2\pi}{NT}k \text{ with } k = 0, 1, 2, \dots, N - 1 \quad (F4)$$

Since computing the DFT contains a lot of redundancy, the first fundamental algorithm developed by Cooley and Tukey [148] is usually used by all efficient computational programs. This technique is known as the Fast Fourier Transform (FFT).